1. Report No. FHWA/TX-09/0-5255-2	2. Government Accession No.	3. Recipient's Catalog No.
4. Title and Subtitle STEEL FIBER REPLACEMENT OF MILD STEEL IN PRESTRESSED CONCRETE BEAMS		5. Report Date October 2010 Published: January 2011
		6. Performing Organization Code
7. Author(s) Padmanabha Rao Tadepalli, Norman Hoffman, Thomas T. C. Hsu, and Y. L. Mo		8. Performing Organization Report No. Report 0-5255-2
9. Performing Organization Name and Address Department of Civil & Environmental Engineering Cullen College of Engineering University of Houston 4800 Calhoun Road Houston, TX 77204-4003		10. Work Unit No. (TRAIS)
		11. Contract or Grant No. Project 0-5255
12. Sponsoring Agency Name and Address Texas Department of Transportation Research and Technology Implementation Office P.O. Box 5080 Austin, Texas 78763-5080		13. Type of Report and Period Covered Technical Report: September 2006 - August 2010
		14. Sponsoring Agency Code

15. Supplementary Notes
Project performed in cooperation with the Texas Department of Transportation and the Federal Highway Administration.
Project Title: Steel Fiber Replacement of Mild Steel in Prestressed Concrete Beams
URL: http://www.egr.uh.edu/structurallab/

16. Abstract
In traditional prestressed concrete beams, longitudinal prestressed tendons serve to resist bending moment and transverse mild steel bars (or stirrups) are used to carry shear forces. However, traditional prestressed concrete I-beams exhibit early-age cracking and brittle shear failure at the end zones despite the use of a high percentage of stirrups (4.2%). Moreover, producing and placing stirrups require costly labor and time. To overcome these difficulties, it is proposed to replace the stirrups in prestressed concrete beams with steel fibers. This replacement concept was shown to be feasible in a TxDOT project (TxDOT project 0-4819) recently completed at the University of Houston.

The replacement of stirrups by steel fibers in highway beams requires a set of shear design provisions and guidelines for prestressed Steel Fiber Concrete (PSFC) beams. The development of rational shear provisions with wide applications must be guided by a mechanics-based shear theory and must be validated by experimental tests on I- and box-beams. A rational shear theory, called the Softened Membrane Model (SMM), has been developed at the University of Houston for reinforced concrete beams. This theory satisfies Navier's three principles of mechanics of materials, namely, stress equilibrium, strain compatibility and the constitutive relationship between stress and strain for the materials.

The first phase of the research consisted of testing 10 full-size prestressed PSFC panels. This was done to establish the effect of fiber factor and the level of prestress on the constitutive models of steel fiber concrete and prestressing tendons. From this data a set of constitutive models was developed to predict the behavior of prestressed PSFC. Notable findings include the fact that increasing steel fiber content has a beneficial effect on the softening properties of prestressed PSFC. Additionally, the findings show that increasing steel fiber content increases tension stiffening in prestressed PSFC under tensile loading.

The second phase of this research project generalizes the SMM shear theory for application to prestressed PSFC beams. This was achieved by feeding the new constitutive models of fiber concrete and prestressing tendons into a finite element program (OpenSees). The accuracy of the new shear theory was evaluated by testing full-size prestressed PSFC I- and box-beams that fail in shear modes. The developed finite element program was used to simulate the shear behavior of the beams with acceptable accuracy. Finally, a design equation and recommendations were provided for use when designing PSFC beams. Using the design equations, a series of four design examples, was also provided.

17. Key Words	18. Distribution Statement
Beams, constitutive models, shear provisions, prestressed concrete, steel fiber concrete, membrane elements, full-scale tests, design equation	No restrictions. This document is available to the public through NTIS: National Technical Information Service Springfield, Virginia 22161 http://www.ntis.gov

19. Security Classif.(of this report)	20. Security Classif.(of this page)	21. No. of Pages	22. Price
Unclassified	Unclassified	192	

STEEL FIBER REPLACEMENT OF MILD STEEL IN PRESTRESSED CONCRETE BEAMS

by

Padmanabha Rao Tadepalli,
Research Assistant,

Norman Hoffman
Research Assistant,

Thomas T. C. Hsu
Moores Professor,

and

Y. L. Mo
Professor

Technical Report 0-5255-2

Research Project Number 0-5255
Steel Fiber Replacement of Mild Steel in Prestressed Concrete Beams
Performed in cooperation with the
Texas Department of Transportation
and the
Federal Highway Administration

October 2010
Published: January 2011

Department of Civil and Environmental Engineering

University of Houston

Houston, Texas

Disclaimer

This research was performed in cooperation with the Texas Department of Transportation and the U.S. Department of Transportation, Federal Highway Administration. The contents of this report reflect the views of the authors, who are responsible for the facts and accuracy of the data presented herein. The contents do not necessarily reflect the official view or policies of the FHWA or TxDOT. This report does not constitute a standard, specification, or regulation, nor is it intended for construction, bidding, or permit purposes. Trade names were used solely for information and not product endorsement.

Acknowledgments

This research, Project 0-5255, was conducted in cooperation with the Texas Department of Transportation and the U.S. Department of Transportation, Federal Highway Administration. The project monitoring committee consisted of John Vogel (Project Director), Duncan Stewart (Research Engineer), Dean Van Landuyt, John Holt (Member), Matthew Connelly (Member), Jason Tucker (Member) and Lou Triandafilou (Member)

The researchers would like to thank the Texas Concrete Company, Victoria, Texas, and Flexicore of Texas, Houston for continued co-operation during this project. The researchers are grateful to Chaparrel Steel Co. of Midlothian, Texas, for supplying the steel bars for this research, and the Bekaert Company for supplying steel fibers.

TABLE OF CONTENTS

LIST OF TABLES

Page

LIST OF FIGURES

Page

CHAPTER 1

INTRODUCTION

1.1 Overview of Research

Prestressed Steel Fiber Concrete (PSFC) is conventional concrete reinforced with mild steel bars, prestressing tendons, and discrete steel fibers of short length and small diameter. Adding steel fibers to plain concrete matrix has little effect on its pre-cracking tensile response, but does substantially enhance its post-cracking response, including greatly improved ductility, toughness, and crack-control (ACI-318, 2008; Abrishami and Mitchell, 1997; ACI 544.1R, 1996; Samarrai and Elvery, 1974; Romualdi and Mandel, 1964). Steel fiber reinforcement has the potential to reduce or in some cases eliminate the need for traditional shear reinforcement (stirrups) in some structures. Minimizing the need for traditional shear reinforcement would result in a reduction in time and labor costs associated with their placement and fabrication.

The idea of prestressing concrete structures was first applied in 1928 by Eugene Freyssinet (1956) in his effort to save the Le Veurdre Bridge over the Allier River near Vichy, France. Since then, the prestressing concrete technology has developed at a brisk rate and presently is widely used in construction practice. The primary purpose of using prestressed concrete was to eliminate/reduce cracking at service load and to fully utilize the capacity of high-strength steel. After the Second World War, prestressed concrete became prevalent due to the needs of reconstruction and the availability of high-strength steel. Today, prestressed concrete has become the predominant material in highway bridge construction. It is also widely used in the construction of buildings, underground structures, TV towers, floating storage tanks and offshore structures, power stations, nuclear reactor vessels, etc.

This research intends to test Prestressed Steel Fiber Concrete (PSFC) so that it can be designed effectively. The past three decades have seen a rapid development of knowledge in shear of reinforced concrete structures. Various rational models for reinforced/prestressed concrete elements subjected to shear have been proposed that are based on the smeared-crack

concept and can satisfy Navier's three principles of mechanics of materials, namely stress equilibrium, strain compatibility, and constitutive laws. These rational or mechanics-based models at the "smeared-crack level" (in contrast to the "discrete-crack level" or "local level") include the Compression Field Theory (CFT) (Vecchio and Collins, 1981), the Modified Compression Field Theory (MCFT) (Vecchio and Collins, 1986), the Rotating-Angle Softened Truss Model, (RA-STM) (Hsu, 1993; Belarbi and Hsu, 1995; Pang and Hsu, 1995), the Fixed-Angle Softened Truss Model, (FA-STM) (Pang and Hsu, 1996; Hsu and Zhang, 1997), the Softened Membrane Model, (SMM) (Zhu, 2000; Hsu and Zhu, 2002), and the Softened Membrane Model for Prestressed Concrete (SMM-PC) (Wang, 2006). By referencing the aforementioned concrete research and analyzing the PSFC test data, a model can be proposed to predict the shear behavior of PSFC to include the contribution of the steel fibers.

Ten full-scale panels were tested to study the constitutive relationships of elements (panels) made of Prestressed Steel Fiber Concrete (PSFC). The PSFC panels were subjected to biaxial tensile-compressive loadings. The principal variables of the testing program were: (a) percent of steel fibers by volume, V_f, and (b) the prestressing force used in the panel.

Twelve full scale bridge girders made using PSFC were tested to study their behavior in web shear as well as flexural shear failure modes. The results obtained from these tests were analyzed and a simple equation was developed for the shear design of PSFC girders. To validate the constitutive models of PSFC obtained from the panel tests, they were incorporated in a finite element package known as OpenSees and the structural behavior of all the tested PSFC girders was successfully simulated.

1.2 Objectives of Research

The objectives of this research project can be summarized as follows:

(1) To investigate experimentally the structural behavior of PSFC panels subjected to sequential loading and proportional loading (pure shear).

(2) To develop the constitutive laws of PSFC in tension and compression and prestressing strands in PSFC, focusing particularly on the effect of prestress and fiber reinforcement on the stress-strain relationship of PSFC in compression.

(3) To establish a shear model to predict the shear behavior of PSFC membrane elements (panels).

(4) To perform shear tests on PSFC beams so as to validate the analytical model developed for PSFC in this project.

(5) To extend the shear design equation, previously developed for prestressed concrete beams at the University of Houston (Laskar et al. 2010), to PSFC beams based on the tests performed in this research.

1.3 Outline of Report

This report is divided into eleven chapters, which are described as follows:

Chapter-1 introduces the overview of the research, the objectives of the research, and the outline of this report.

Chapter-2 presents a literature review of shear models for reinforced, prestressed, and steel fiber concrete elements, with emphasis on the series of the models developed by the University of Houston (UH) group. There is limited research data available on prestressed steel fiber concrete membrane elements. Thus, even a thorough review of literature produced very few references on this subject.

Chapter-3 presents the mechanical properties of steel fiber concrete with different types of steel fibers.

Chapter-4 describes the test facility used in this research, namely, the Universal Panel Tester. Emphasis is placed on the servo-control system, which makes the tester unique. The loading system, the measurement setup, and the data acquisition system are also described.

Chapters-5 and -6 describe the experimental program and analysis of PSFC panels.

Chapters-7 and -8 describe the full-scale tests of twelve PSFC I- and box-beams to study the structural behavior with regard to ultimate shear strength, ductility, and failure mechanism. The results obtained from testing the I-beams are presented in Chapter-7 and the results obtained from testing the Box-beams are presented in Chapter-8.

Chapter-9 presents the analysis of the PSFC beams tested in this study using a computer program - Simulation of Concrete Structures (SCS). The SCS program was based on the constitutive laws of prestressed steel fiber concrete (SMM-PSFC) developed by analyzing the panel test results.

Chapter-10 presents a simple design equation for shear in PSFC beams. The proposed equation was based on previously available design equation for prestressed concrete beams (Laskar et al. 2010). The new equation proposed herein considers the effect of steel fibers on the shear strength of PSFC beams. Four design examples are included to illustrate the practical use of the new equation for shear design of PSFC beams.

Chapter-11 provides the conclusions of this research and suggests further studies in the area.

CHAPTER 2

BACKGROUND ON SHEAR THEORIES OF REINFORCED AND PRESTRESSED CONCRETE

2.1 Introduction

Constitutive models for concrete are being investigated by two general groups of concrete researchers. There are those models that have been developed by materials researchers and there are those models developed by researchers attempting to predict the behavior of whole structural assemblies, including reinforcing steel. The latter group of models is generally referred to as smeared models. The models overlap and indeed the materials models form the basis of the structures models. It must be clearly understood that the distinctive difference between the two sets of research is the presence of reinforcing steel such as deformed mild steel rebar or prestressing tendon. Concrete with reinforcing steel behaves differently from concrete without reinforcing steel.

The research at the University of Houston and University of Toronto has focused on structural assemblies of concrete and reinforcing steel. These assemblies are tested to determine the constitutive properties on what is called a *smeared* or average basis. Smeared model properties by definition span multiple cracks in reinforced concrete. The smeared constitutive model is a macro or full scale model which is used to model whole structural behavior, particularly shear behavior of reinforced concrete continuums such as walls, beam webs, and other membrane structures. Smeared constitutive models are designed and calibrated to full-scale structures.

The materials research models for concrete focus on the micro-level of concrete. They generally consider concrete on the single crack level, and may even model the cracks themselves. The overlap of model groups occurs at the concrete-rebar interface. Constitutive bond researchers model the bond between concrete and reinforcing steel. These models form a bridge between the materials models and the smeared model research.

The individual smeared constitutive equations cover the following aspects of behavior:

- Concrete in Tension (pre-cracking and post cracking branches)
- Concrete in Compression (ascending and descending branches)
- Stress Equilibrium Equations
- Strain Compatibility Equations
- Post-Cracking Hsu/Zhu (Poisson) Ratios
- Uniaxial – Biaxial Transformation Equations
- Embedded Mild Steel
- Embedded Prestressing Tendon

A survey of literature reveals that constitutive material models for plain concrete can be categorized into three very broad groups based on the loading situation: unixial, biaxial and triaxial models. These three types of models can be further derived based on the nature of loading, i.e. tension and compression. The basic uniaxial stress strain model for plain concrete consists of an ascending branch and a descending branch. The peak of this curve occurs at a location called the concrete compressive strength (f_c') while the corresponding strain is the peak compressive strain (ε_0). There have been numerous studies and approximations for modeling the stress-strain curve of plain concrete. Significant yet simple approximations of the stress-strain curve include the Hognestad (1952) parabola based on the model proposed by Stussi (1932), Desai and Krishnan (1964), and Wang and Shah (1978). The basic approach for researchers modeling the curve is to base the shape on key parameters that can be obtained easily from physical tests of specimens, namely the failure criteria, f_c' and ε_0.

2.2 Previous Studies by Research Group at UH

In the past 20 years, Hsu and his colleagues performed over 130 panel tests using the Universal Panel Tester (Hsu, Belarbi, and Pang, 1995) at the University of Houston. A series of

three rational models for the monotonic shear behavior of reinforced concrete elements (panels) were developed.

A reinforced concrete membrane element subjected to in-plane shear and normal stresses is shown in Fig. 2.1(a). The directions of the longitudinal and the transverse steel bars are designated as ℓ- and t- axes, respectively, constituting the $\ell - t$ coordinate system. The normal stresses are designated as σ_ℓ and σ_t in the ℓ- and t- directions, respectively, and the shear stresses are represented by $\tau_{\ell t}$ in the $\ell - t$ coordinate system. Based on the reinforced concrete sign convention for Mohr's circles, a positive shear stress $\tau_{\ell t}$ is the one that causes clockwise rotation of a reinforced concrete element (Hsu, 1993).

The applied principal stresses for the reinforced concrete element are defined as σ_2 and σ_1 based on the $2-1$ coordinate system as shown in Fig. 2.1(d). The angle between the direction of the applied principal compressive stress ($2-$axis) and the direction of the longitudinal steel ($\ell-$axis) is defined as the fixed-angle α_2, because this angle does not change when the three in-plane stresses, σ_ℓ, σ_t, and $\tau_{\ell t}$, increase proportionally. This angle α_2 is also called the steel bar angle because it defines the direction of the steel bars with respect to the applied principal stresses.

The principal stresses in concrete coincide with the applied principal stresses σ_1 and σ_2 before cracking. When the principal tensile stress σ_1 reaches the tensile strength of concrete, cracks will form and the concrete will be separated by the cracks into a series of concrete struts in the 2- direction as shown in Fig. 2.1(f). If the element is reinforced with different amounts of steel in the ℓ- and the t- directions, i.e., $\rho_\ell f_\ell \neq \rho_t f_t$ in Fig. 2.1(c), the direction of the principal stresses in concrete after cracking will deviate from the directions of the applied principal stresses. The new directions of the post-cracking principal stresses in concrete are defined by the $d-r$ coordinate system shown in Fig. 2.1(e). Accordingly, the principal

compressive stress and the principal tensile stress in the cracked concrete are defined as σ_d and σ_r, respectively.

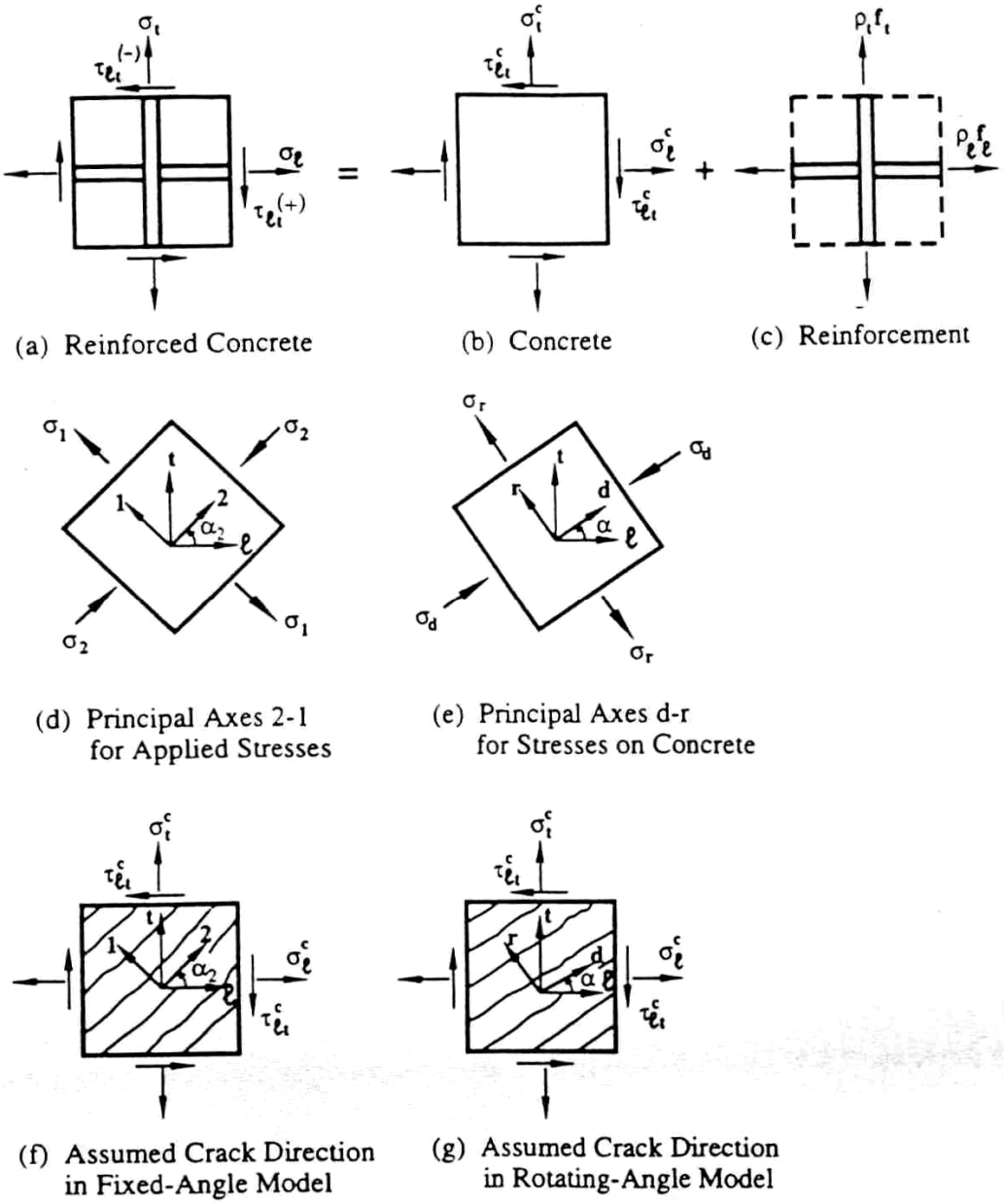

Fig. 2.1 Reinforced Concrete Membrane Elements Subjected to In-plane Stresses.

The angle between the direction of the principal compressive stress in the cracked concrete ($d-$axis) and the direction of the longitudinal steel ($\ell-$axis) is defined as the rotating-angle α. The angle α is dependent on the relative amount of "smeared steel stresses," $\rho_\ell f_\ell$ and $\rho_t f_t$, in the longitudinal and the transverse directions as shown in Fig. 2.1(c). When $\rho_\ell f_\ell > \rho_t f_t$, the $d-r$ coordinate gradually rotates away from the $2-1$ coordinate and α becomes smaller with increasing load. With increasing applied proportional stresses (σ_ℓ, σ_t and $\tau_{\ell t}$), the deviation between the angle α and the angle α_2 increases. This deviation angle β is defined as $\alpha_2 - \alpha$. When the percentages of reinforcement are the same in the ℓ- and the t- directions, the rotating angle α is equal to the fixed-angle α_2.

The rotating-angle softened-truss model (RA-STM) is based on the assumption that the direction of cracks coincides with the direction of the principal compressive stress in the cracked concrete, as shown in Fig. 2.1(g). The derivations of all the equilibrium and compatibility equations are based on the rotating-angle α. In contrast, the fixed-angle softened-truss model (FA-STM) is based on the assumption that the direction of the cracks coincides with the direction of the applied principal compressive stress as shown in Fig. 2.1(f). In the fixed-angle softened-truss model, all the equations are derived based on the fixed-angle α_2.

The three stress components σ_ℓ, σ_t, and $\tau_{\ell t}$ shown in Fig. 2.1(a) are the applied stresses on the reinforced concrete element viewed as a whole. The stresses on the concrete struts are denoted as σ_ℓ^c, σ_t^c, and $\tau_{\ell t}^c$ as shown in Fig. 2.1(b). The longitudinal and the transverse steel provide the smeared (average) stresses of $\rho_\ell f_\ell$ and $\rho_t f_t$ as shown in Fig. 2.1(c). The reinforcement is assumed to take only axial stresses, neglecting any possible dowel action. Summing the concrete stresses and the steel stresses in the $\ell-$ and $t-$directions and maintaining the equilibrium of forces and moments give the following equations:

$$\sigma_\ell = \sigma_\ell^c + \rho_\ell f_\ell , \qquad \text{(Eq. 2-1)}$$

$$\sigma_t = \sigma_t^c + \rho_t f_t , \qquad \text{(Eq. 2-2)}$$

$$\tau_{\ell t} = \tau_{\ell t}^c . \qquad \text{(Eq. 2-3)}$$

Eqs. (2-1) to (2-3) are the basic equilibrium equations for both RA-STM and FA-STM. When the three concrete stresses (σ_ℓ^c, σ_t^c, and $\tau_{\ell t}^c$) in the $\ell - t$ coordinate are transformed to the principal $d - r$ coordinate of concrete, Fig. 2.1(g) we obtain the RA-STM derived in Section 2.2.1. When the three concrete stresses (σ_ℓ^c, σ_t^c, and $\tau_{\ell t}^c$) are transformed to the principal $2-1$ coordinate of the applied stresses, Fig. 2.1(f), we obtain the FA-STM.

2.2.1 Softened Membrane Model (SMM)

The RA-STM and the FA-STM are two rational models that can satisfy Navier's three principles of mechanics of materials. Although these two models are successful in predicting the pre-peak behavior of reinforced concrete membrane elements subjected to monotonic shear stresses, they cannot explain the existence of the post-peak load-deformation curves (descending branches). The reason, as pointed out by Hsu and Zhu (2002), is because the Poisson effect is neglected in those theories.

In order to predict the descending branches of the shear stress-strain curves of membrane elements, a new theory known as the softened membrane model (SMM) was developed by Hsu and Zhu (2002) that did consider the Poisson effect. In this model, two Hsu/Zhu ratios, ν_{12} and ν_{21}, were obtained from tests (Zhu and Hsu, 2002) to characterize the Poisson effect of cracked concrete in the $2-1$ coordinate system using the smeared crack concept. Hsu/Zhu ratio ν_{12} is defined as the ratio $\Delta\varepsilon_1/\Delta\varepsilon_2$, where $\Delta\varepsilon_1$ is the resulting increment of strain in 1 direction and $\Delta\varepsilon_2$ is the source increment of strain in 2- direction. Similarly, Hsu/Zhu ratio ν_{21} is defined as the ratio $\Delta\varepsilon_2/\Delta\varepsilon_1$, where $\Delta\varepsilon_2$ is the resulting increment of strain in 2- direction

and $\Delta\varepsilon_1$ is the source increment of strain in 1- direction. It is to be mentioned that the 1-direction is the direction of the applied principal tensile stresses, and the 2- direction is the direction of the applied principal compressive stresses.

The SMM is an extension of the FA-STM with two improvements. One is the inclusion of the two Hsu/Zhu ratios to consider the Poisson effect, and the other is the derivation of a simple, but rational, shear modulus of concrete.

2.2.2 Softened Membrane Model for Prestressed Concrete (SMM-PC)

Reinforced concrete structures can be visualized as assemblies of membrane elements, and their behavior can be predicted using the finite element method once the constitutive relationships of the elements are established. At the University of Houston, Zhong (2005) developed a nonlinear finite element program, named Simulation of Concrete Structures (SCS) for reinforced concrete structures. In that program, based on the Cyclic Softened Membrane Model (CSMM) (Mansour, 2001; Mansour and Hsu, 2005a and 2005b), a 2D reinforced concrete plane stress material module and three uniaxial material modules of steel and concrete were developed and implemented into the object-oriented finite element framework OpenSees (Fenves 2001). SCS is proven to successfully predict the behavior of reinforced concrete plane stress structures subjected to static, reversed cyclic, and dynamic loading. The Softened Membrane Model for Prestressed Concrete (SMM-PC) was developed by Wang (2006) to predict the response of prestressed concrete membrane elements under shear loading.

2.3 Softened Membrane Model for Prestressed Steel Fiber Concrete (SMM-PSFC)

2.3.1 Steel Fibers

Steel fibers used in this research were high performance fibers and were the same as used previously in a TxDOT research project 0-4819 by Dhonde et al. (2006), which investigated the end-zone cracking in PSFC I-beams. Dhonde et al. reported a considerable increase in the shear and flexural strength of the PSFC I-beams owing to the use of steel fibers. This prompted further investigation into the shear properties of PSFC through the present study.

There are many types of steel fibers commercially available in the market. Among the many steel fibers, the Dramix fiber (used by Dhonde et al. 2006) was a preliminary choice for the current research work. Tadepalli et al. (2009) tested and compared the structural properties of several types and manufactures of high performance steel fibers (reported in Chapter-3). Tadepalli et al. (2009) tested small concrete beams made using two types of hooked and one type of twisted steel fibers. They also investigated the effects of different type and dosage of steel fibers on the mechanical properties of concrete, such as the compressive strength, first-crack flexural strength, ultimate flexural strength, modulus of elasticity, flexural toughness, and ductility.

2.3.2 Effect of Adding Steel Fibers to Concrete

The addition of steel fibers to plain concrete has beneficial effects on the engineering properties of concrete. Steel fibers improve the following mechanical properties of concrete (Tadepalli et al. 2009, Thomas et al. 2007, Traina 1991):

(a) Unixial Compressive Strength of concrete, $f_c^{'}$

(b) Uniaxial Peak strain of concrete at $f_c^{'}$, ε_0

(c) Modulus of Elasticity of concrete, E_c

(d) Uniaxial Tensile Strength of concrete, f_t

(e) Modulus of Rupture

(f) Ductility

(g) Poisson's Ratio, ν

Therefore, it is reasonable to assume that steel fibers can alter the fundamental constitutive laws of concrete.

Steel fibers affects most significantly the tensile strength and ductility of concrete. Thomas et al. (2007) reported a 38% increase in the split tensile cylinder strength using just 1.5% steel fiber content by volume of concrete. Tadepalli et al. (2009) tested steel fiber concrete beam specimens (6 in. wide x 6 in. deep x 20 in. long) under a four-point loading assembly (Modulus of Rupture test) to get the load-deflection characteristic of fibrous concrete. The tests revealed a noticeable

improvement in the post-peak load carrying capacity (residual strength) of the steel fiber concrete beam specimens when compared to the plain concrete specimens. The plain concrete beam specimens failed suddenly (i.e. in brittle mode) upon reaching a peak load, while the steel fiber concrete specimens sustained significant residual load indicating enhanced ductility, energy absorption and toughness. This enhanced post-peak residual strength in steel fiber concrete beam is due to the bridging effect of fibers across the tensile crack (ACI 544.R1, 1996; Thomas et al., 2007 and Tadepalli et al. 2009).

The effect of steel fibers on uniaxial compressive strength of concrete cylinder is modest; in comparison to the fiber's pronounced effect on the tensile strength of concrete. Thomas et al. (2007) reported a linear increase in the compressive strength of concrete up to 8% with increasing fiber dosage up to 1.5% by volume of fibers. Thus, in compression, the ultimate strength of concrete is only slightly affected by the presence of steel fibers, with observed increases ranging from 0 to 15% for up to 1.5 % by volume of fibers (ACI 544.R1, 1996).

Although there is only a modest increase in the compressive strength of fibrous concrete, there is a substantial increase in the compressive strain, ε_0. Thomas et al. attributes the gain in strain to the 'confinement' effect of the fibers within the concrete matrix. Again, the increase in ε_0 was found to be linear up to a maximum of 29% over plain concrete, with increasing fiber content up to 1.5% by volume of fibers. Thomas et al. (2007) also found only a slight gain (of about 8%) in the modulus of elasticity (E_c) and negligible change in Poisson's ratio of fibrous concrete with increasing fiber content, up to 1.5% by volume. In practice, when the volume percentage of fibers is less than 2%, the modulus of elasticity and Poisson's ratio of fibrous concrete are generally taken as equal to those of a similar non-fibrous concrete (ACI 544.R1, 1996).

Key investigations into the biaxial behavior of fiber reinforced concrete were performed by Kupfer (1969), Traina (1991) and Yin (1989). These researchers established the basic failure envelope for fiber concrete, with respect to plain concrete. These studies showed that the material and structural behavior of fibrous and non-fibrous concrete is fairly different. The

primary difference under biaxial loading is the increase in compressive strength of fiber concrete over the plain concrete, for all stress ratios. Furthermore, when compared to the uniaxial strength, the biaxial strength increases by as much as 85% with 1.5% fiber volume over plain concrete (Traina, 1991). Relevant constitutive models for fiber concrete include biaxial models developed by Tan et al. (1993) and Hu et al.(2003) based on the experimental work of Traina (1991) and Yin (1989). The model proposed by Tan considered only compression-compression biaxial loading, while the Hu model considered both compression and tension loading. Hu et al. presented a single smooth biaxial failure curve for the fiber concrete.

The development of Softened Membrane Model for Prestressed Steel Fiber Concrete (SMM-PSFC) to predict the response of prestressed concrete membrane elements under shear loading is discussed in Chapter-6.

CHAPTER 3

MECHANICAL PROPERTIES OF STEEL FIBER CONCRETE

3.1 Introduction

Steel fibers of various shapes (i.e. straight, crimped, hooked single, hooked collated, twisted etc.) are available in market, intended for structural use. Steel fiber concrete has been studied for more than five decades, but very little literature is available on the performance of different types of steel fibers in concrete with different compressive strength i.e. normal strength and high strength concrete.

It is well know that addition of steel fibers in concrete reduces workability. Therefore, practical dosage of steel fibers in normal concrete varies from 0.5 to a maximum of 3 percent by volume (Bayasi and Soroushiah 1992). Workability of steel fiber concrete can be enhanced by using supplementary cementitious materials such as fly ash, slag, silica fume, etc (ACI 544.1R 1996). Steel fiber concrete mixes with good workability can be made by using supplementary cementitious materials up to 15% by weight of cement (Balaguru et al. 1993 and ACI 544.1R 1996).

The beneficial influence of fibers in concrete depends on many factors such as type, shape, length and cross-section of fibers, strength and bond characteristics of fiber, fiber content, matrix strength, mix design and mixing of concrete. Fibers are known to enhance the mechanical performance of concrete with regard to its tensile and shear strength, toughness, ductility, durability, fatigue and shrinkage resistance (Shah 1991 and ACI 544.1R 1996). Bayasi and Soroushaih (1992) demonstrated that hooked fibers perform better than straight or crimped steel fibers in terms of flexural strength and energy absorption capacity. Balaguru et al. (1992) reported that for steel fibers with hooked ends, the length of fibers did not affect the toughness significantly.

The purpose of this experimental study was to determine and compare the structural performance of different types and dosage of steel fibers in normal and high strength concrete.

3.2 Experimental Program

The experimental program included flexural testing of small-sized steel fiber concrete beam specimens made using different concrete strengths, fiber type and fiber dosage. The Modulus of

Rupture (MOR) beam test (Fig. 3.1(a)), in accordance with ASTM C 1609, was carried out owing to its popularity, quick test set–up assembly and easy to prepare specimens. This test method evaluates the flexural performance of fiber concrete using parameters derived from the load-deflection curve obtained by testing a simply supported beam under third-point loading.

This test method provides for the determination of first-peak loads and the corresponding stresses. It also requires determination of residual loads (i.e. post-crack loads) at specified beam deflections (Fig. 3.1(b)). The test also includes the determination of specimen toughness based on the area under the load-deflection curve up to a prescribed deflection and the corresponding equivalent flexural strength ratio. Specimen toughness expressed in terms of the area under the load-deflection curve is an indication of the energy absorption capability of the particular test specimen (ASTM C 1609).

The first-peak strength characterizes the flexural behavior of the fiber-reinforced concrete up to the onset of cracking, while residual strengths at specified deflections characterize the residual capacity after cracking. Specimen toughness is a measure of the energy absorption capacity of the test specimen. Fiber concrete is influenced in different ways by the amount and type of fibers in the concrete. In some cases, fibers may increase the residual load and toughness capacity at specified deflections while producing a first-peak strength equal to or only slightly greater than the flexural strength of the concrete without fibers. In other cases, fibers may significantly increase the first-peak and peak strengths while affecting a relatively small increase in residual load capacity and specimen toughness at specified deflections (ASTM C 1609).

The first-peak strength, peak strength, and residual strengths determined by this test method reflect the behavior of fiber-reinforced concrete under static flexural loading. The absolute values of energy absorption obtained in this test are of little direct relevance to the performance of fiber-reinforced concrete structures since they depend directly on the size and shape of the specimen and the loading arrangement. But, the results of this test method may be used for comparing the performance of various fiber concrete mixtures.

In all 39 beam specimens of 6 in x 6 in. x 20 in. size were tested under a four point loading system. The MOR test evaluates the maximum tensile bending stress in a beam at failure. The action of fibers bridging a tension crack that normally form during the beam test is observed in this test. Thus, the results from the beam tests can be correlated to shear failure of beams that typically demonstrates similar diagonal tension cracking.

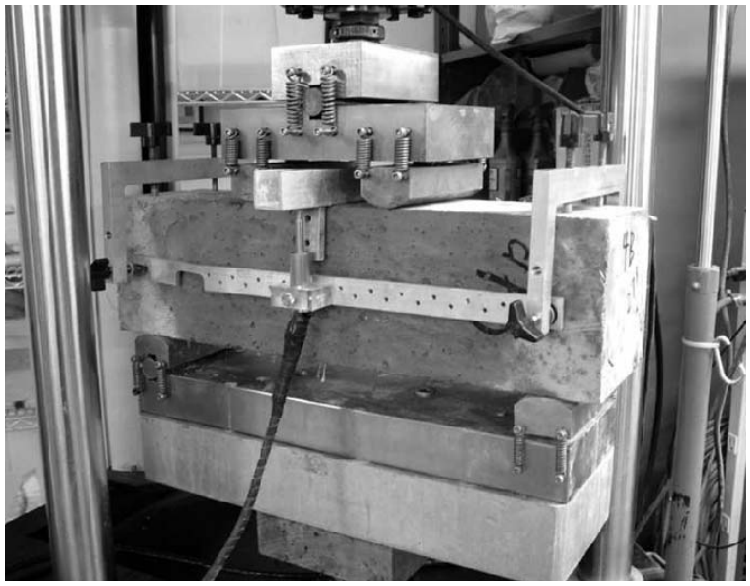

(a)

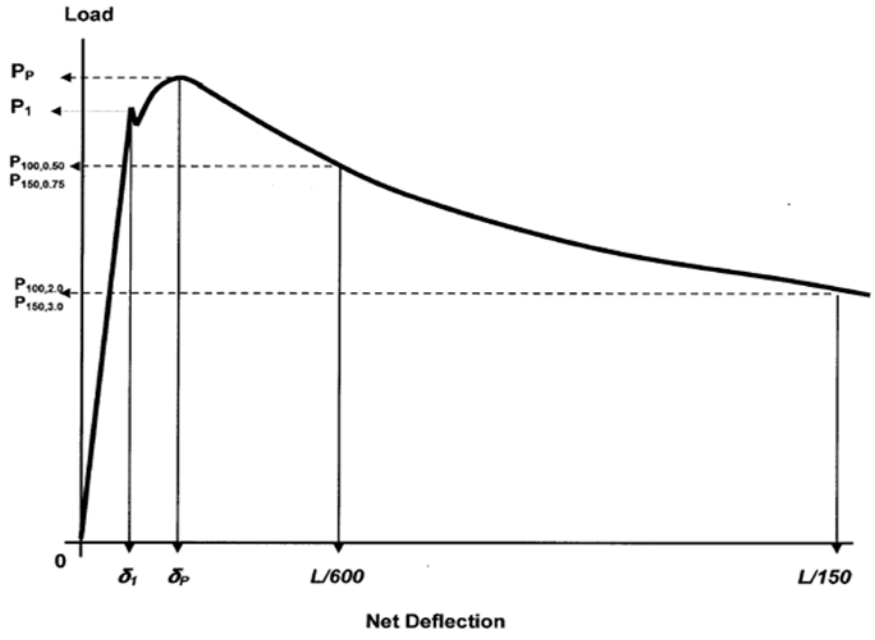

L = Test Span
P_P = Peak Load
P_1 = First-Peak Load
f_P = Peak Strength
f_1 = First-Peak Strength
δ_P = Net deflection at Peak Load
δ_1 = Net deflection at First-Peak Load
$P_{100,0.50}$ or $P_{150,0.75}$ = Residual Load at Span / 600
$f_{100,0.50}$ or $f_{150,0.75}$ = Residual Strength at Span / 600
$P_{100,2.0}$ or $P_{150,3.0}$ = Residual Load at Span / 150
$f_{100,2.0}$ or $f_{150,3.0}$ = Residual Strength at Span / 150
$T_{100,2.0}$ or $T_{150,3.0}$ = Area under L-D curve 0 to Span / 150

(b)

Fig. 3.1 (a) Beam Set-up for Modulus of Rupture Test (ASTM C 1609) (b) Example for Calculation of Various Load-Deflection Parameters in MOR Test (ASTM C 1609)

A total of thirteen concrete mixes based on the concrete mix proportions used by TxDOT to manufacture prestressed concrete beams were investigated. The typical nomenclature used to differentiate the thirteen concrete mixes is given in Table 3.1.

Table 3.1 – Concrete Mix Nomenclature and Description for Modulus of Rupture Test

Mix Nomenclature	Description
TTC	This mix is traditionally used by TxDOT to cast I-girders. This mix served as the *'control mix'* for various concrete mixes with steel fibers
TTCDL1 **TTCDL2**	**T**xDOT **T**raditional **C**oncrete mix with **D**ramix **L**ong fibers
TTCDS1 **TTCDS2**	**T**xDOT **T**raditional **C**oncrete mix with **D**ramix **S**hort fibers
TTCR1 **TTCR2**	**T**xDOT **T**raditional **C**oncrete mix with **R**oyal fibers
TTCH1 **TTCH2**	**T**xDOT **T**raditional **C**oncrete mix with **H**elix fibers
MIXDL1 **MIXDL2**	Mix with Dramix Long fibers used to cast panels
MIXDS1 **MIXDS2**	Mix with Dramix Short fibers used to cast panels

3.2.1 Test Specimens

Three beam specimens were prepared and tested with each of the thirteen mix designs shown in Table 3.1. The beams were 6 in. square in cross section and had an overall length of 20 in. with 18 in. of test span. To determine the compressive strength of concrete mix, three 6 in. diameter by 12 in. long test cylinders were cast along with the beam specimens for each of the thirteen mixes. Three beam specimens were cast and tested corresponding to each of the concrete mixes.

3.2.2 Materials and Concrete Mixes

3.2.2.1 Concrete

Locally available materials, which were traditionally used by TxDOT in manufacturing their beams, were used to prepare the concrete mixes for MOR beam specimens.

Cement – High early strength cement was used in all the mixes, since it was necessary to develop high release strengths at an early age in the prestressed concrete beams. Portland cement

(Type-III) conforming to ASTM C150 and fly ash (Type-F) conforming to ASTM C618 were the only powder materials used. Fly ash was added to the mix to enhance workability, curtail rise in temperature and reduce cost.

Coarse and Fine Aggregates –The mixes utilized uniformly-graded, rounded, river-bed, coarse aggregates of 3/4 inch nominal size (AASHTO T27 1996) and well-graded, river-bed sand with a fineness modulus of 2.55 (AASHTO M43 1998). The specific gravity of the coarse aggregates was 2.6 and that of the fine aggregates was 2.63.

Admixtures - A Polycarboxylate-based High Range Water Reducing (HRWR) agent conforming to ASTM C 494-1999, Type F was used to achieve workable concrete mixes. A retarder conforming to ASTM C 494-1999, Type-B was added to the mixes as required to delay the initial setting of the mix.

3.2.2.2 Steel Fibers

Steel fibers manufactured by three different companies and readily available in the local market were used in this study. The Dramix steel fibers were hooked-collated with long and short lengths. The Royal steel fibers were hooked-single and the Helix steel fibers were twisted in shape. Two different steel fiber dosage were used, i.e. 0.5% and 1.5% by volume of concrete. Table 3.2 present the detail specifications of the steel fibers used in this experimental study.

Table 3.2 – Details of Steel Fibers Used in Concrete Mixes

Fiber Type		**Length** (inch) L_f	**Diameter** (inch) D_f	**Aspect Ratio** L_f/D_f	**Tensile Strength** (ksi)
Dramix	Long Fiber	2.4	0.03	80	150
	Short Fiber	1.2	0.022	55	160
Royal		1.6	0.03	53	150
Helix		1.0	0.02	50	350

Two types of concrete mixes i.e. with and without fly ash were used in this research. Concrete mixes without fly ash were used to cast panels, while the one with fly ash were used to cast beams. Table 3.3 summarizes the mix proportions used for various concrete mixes in this work.

Table 3.3 – Mix Proportions for Modulus of Rupture Beam Specimens

Component (lb/yd.^{3})*	[TTCDL1, TTCDS1, TTCH1, TTCR1]^X	[TTCDL2, TTCDS2, TTCR2, TTCH2]$^+$	**TTC** (Control)	[MIXDL1, MIXDS1]^X	[MIXDL2, MIXDS2]$^+$
Cement	628	628	628	575	575
Fly ash	157	157	157	-----	-----
Cementitious material	785	785	785	575	575
Water/Cement ratio (w/c)	0.39	0.39	0.39	0.60	0.60
Water/Cementitious ratio	0.32	0.32	0.32	0.60	0.60
Coarse aggregate (CA)	1900	1900	1900	1614	1614
Fine aggregate (FA)	1193	1193	1193	1516	1516
CA/FA ratio	1.59	1.59	1.59	1.07	1.07
HRWR (fl.oz./cwt)	6.4 (13)	6.4 (13)	6.4 (13)	-----	-----
Fibers	66	200	-----	66	200
Retarder	2.5	2.5	2.5	-----	-----

*Each concrete mix had a batch-yield of 0.08 yd.^{3}

^{X} – Steel fiber dosage of 0.5% by volume. $^+$- Steel fiber dosage of 1.5% by volume.

3.2.3 Experimental Setup

The MOR beam tests were performed according to the guidelines of ASTM C 1609, using a two-point loading system and a total span of 18 inches (Fig. 3.2). Steadily increasing static load was applied on top of the beam using a displacement control at a rate of 0.005 in/min up to a net vertical deflection of 0.03 inch. After that, the rate of loading was changed to 0.01 in/min. Beam deflections were continuously recorded throughout the test using two Linear Variable Differential Transformers (LVDTs) mounted at its mid-span on either side of the beam. A load cell was used to obtain the applied load values throughout the test. Both the LVDTs and load cell were connected to a data acquisition system to record the load and displacement values during the test. Fig. 3.2 shows a typical beam set-up for MOR test.

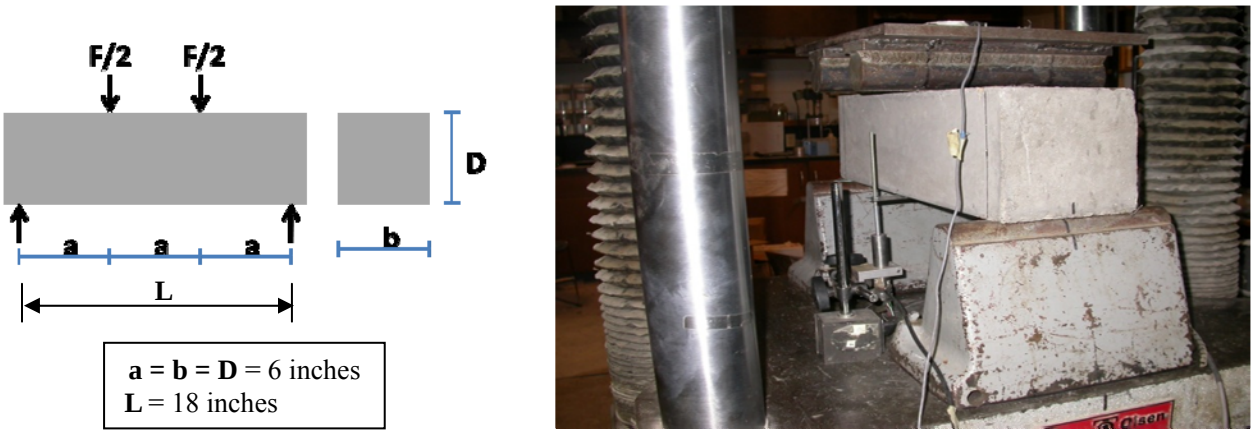

Fig. 3.2 Modulus of Rupture Beam Test Setup

3.3 Results and Discussion

The average compressive strengths of all the concrete mixes are shown in Table 3.4. The table also presents the first-peak load (F) and MOR strength of each concrete mix tested. The percentage increase in MOR strength for a particular concrete mix with 1.5% dosage of steel fibers with respect to a 0.5% dosage of steel fibers is also shown in this table. It can be observed that the short Dramix steel fibers with 1.5% dosage (i.e. the TCCDS mix) yielded the maximum gain in the percentage MOR strength in comparison with other series of concrete mixes. Generally, all the concrete mixes showed a reasonable increase in the percentage MOR strength, except the TTCDL series. This may be due to the fact that the TTCDL mix with 1.5% dosage of long fibers had poor workability, which was also evident in its reduced compressive strength.

Table 3.4 – Results of Compressive and Flexural Strength (MOR) of Beam Specimens

Beam/Mix ID	Compressive Strength (psi)	First-Peak Load F (lbs)	MOR FL/bD^2 (psi)	% Increase in Flexural Strength
TTC	10,200	11,600	966	-----
MIXDL1[x]	5910	12,100	1008	} 29
MIXDL2[+]	6250	15,630	1302	
MIXDS1[x]	5310	8580	715	} 71
MIXDS2[+]	5950	14,680	1223	
TTCDL1[x]	11,310	17,530	1460	-----
TTCDL2[+]	9560	16,040	1336	
TTCDS1[x]	10,250	12,100	1008	} 121
TTCDS2[+]	13,360	26,730	2227	
TTCH1[x]	10,600	15,560	1296	} 68
TTCH2[+]	5380	26,100	2174	
TTCR1[x]	8600	12,170	1014	} 74
TTCR2[+]	11,820	21,150	1762	

[x] – Steel fiber dosage of 0.5% by volume. [+]- Steel fiber dosage of 1.5% by volume.

The Load -Vs- Displacement curves for beam specimens with 0.5% and 1.5% dosage of steel fibers are shown in Fig. 3.3 and Fig. 3.4, respectively. From these figures it can be seen that the concrete mixes with higher compressive strength showed greater stiffness. This can be attributed to the fact that young's modulus of concrete is dependent on its compressive strength.

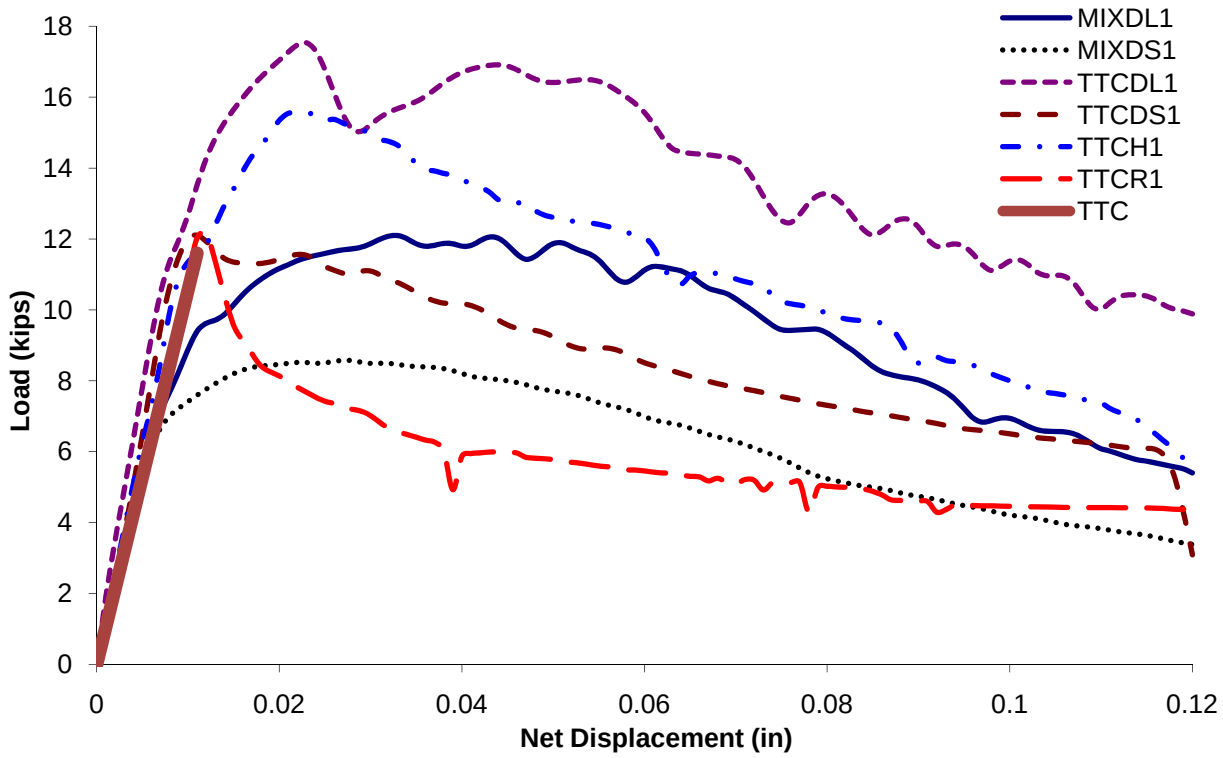

Fig. 3.3 Load vs. Displacement Curves for Beam Specimens with 0.5% Fiber Content

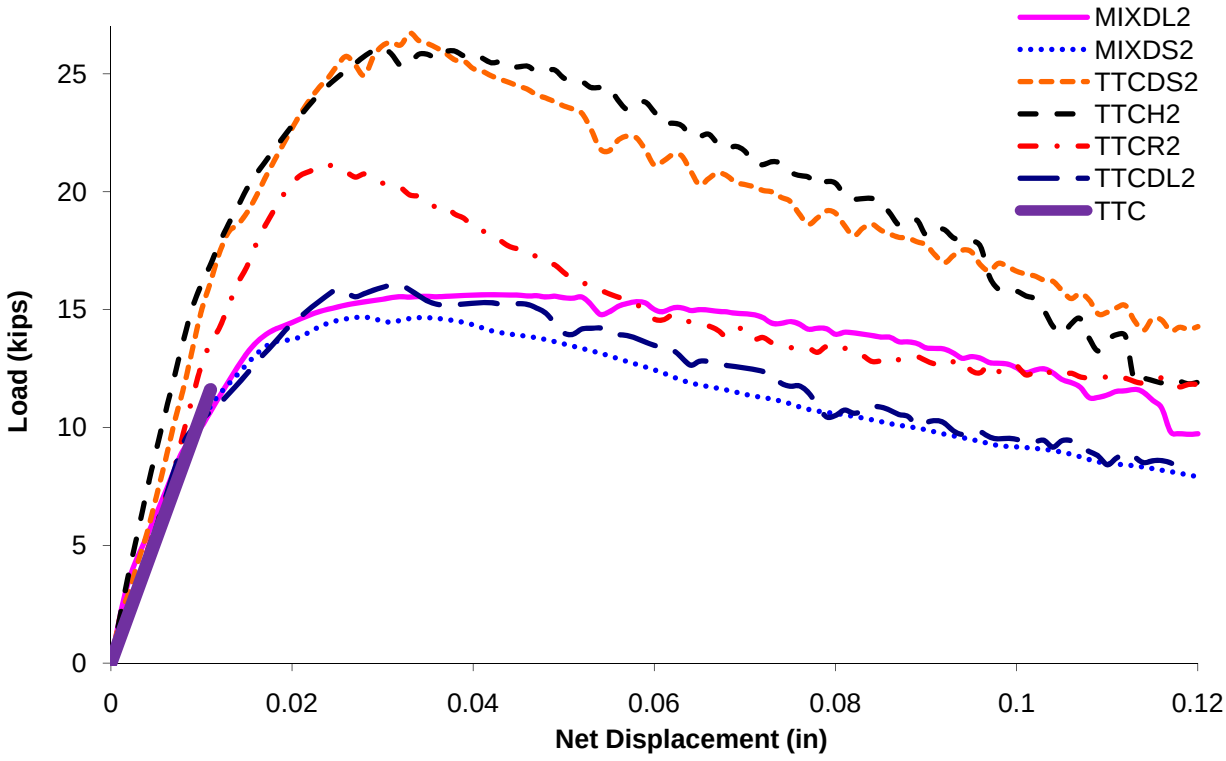

Fig. 3.4 Load vs. Displacement Curves for Beam Specimens with 1.5% Fiber Content

In order to facilitate better comparison, the load values in the Load-vs.-Displacement results are normalized using the corresponding cylinder compressive strength for each concrete mix. These normalized displacement curves for beam specimens with 0.5% and 1.5% dosage of steel fibers are shown in Figs. 3.5 and 3.6, respectively.

The normalized load was determined by dividing the applied external moment with resisting moment of the beam. From Fig. 3.2 it is clear that $\frac{Fa}{2}$ is the applied external moment. From the Euler-Bernoulli's beam bending theory, $\sqrt{f_c'}\frac{bD^2}{6}$ is the resisting moment in case of tension failure.

So the normalized load can be written as $\frac{\frac{Fa}{2}}{\sqrt{f_c'}\frac{bD^2}{6}}$ (Eq. 3-1)

Where, F = Total load applied, lbs.

a = Distance of the applied load from support, in.

f_c' = Concrete compressive strength, psi

b = Width of the beam, in., and

D = Depth of the beam, in.

After normalization the stiffness of all the curves matches very well, which supports the normalization technique used. Figs. 3.5 and 3.6 depict that the maximum normalized MOR strengths for concrete mixes with 1.5% dosage of steel fibers is higher than the mixes with 0.5% dosage of steel fibers. Considering the normalized MOR strength for concrete mixes with 0.5% dosage of steel fibers in Fig. 3.5, the long-Dramix fibers had the highest strength, followed by the Helix, short-Dramix and Royal fibers. Also, comparing the normalized MOR strength for concrete mixes with 1.5% dosage of steel fibers in Fig. 3.6, the short and long Dramix fiber out-performed the other fibers.

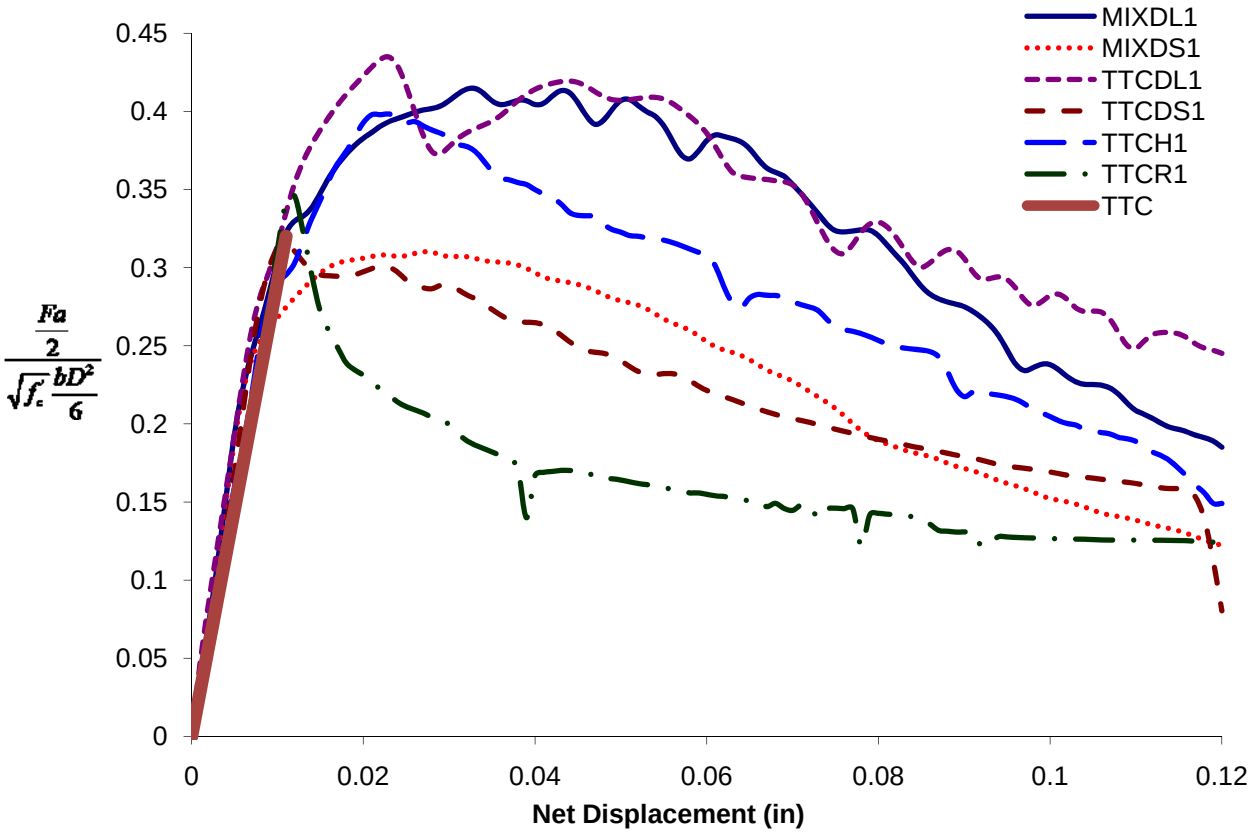

Fig. 3.5 Normalized Load vs. Displacement Curves for Beam Specimens with 0.5% Fiber Content

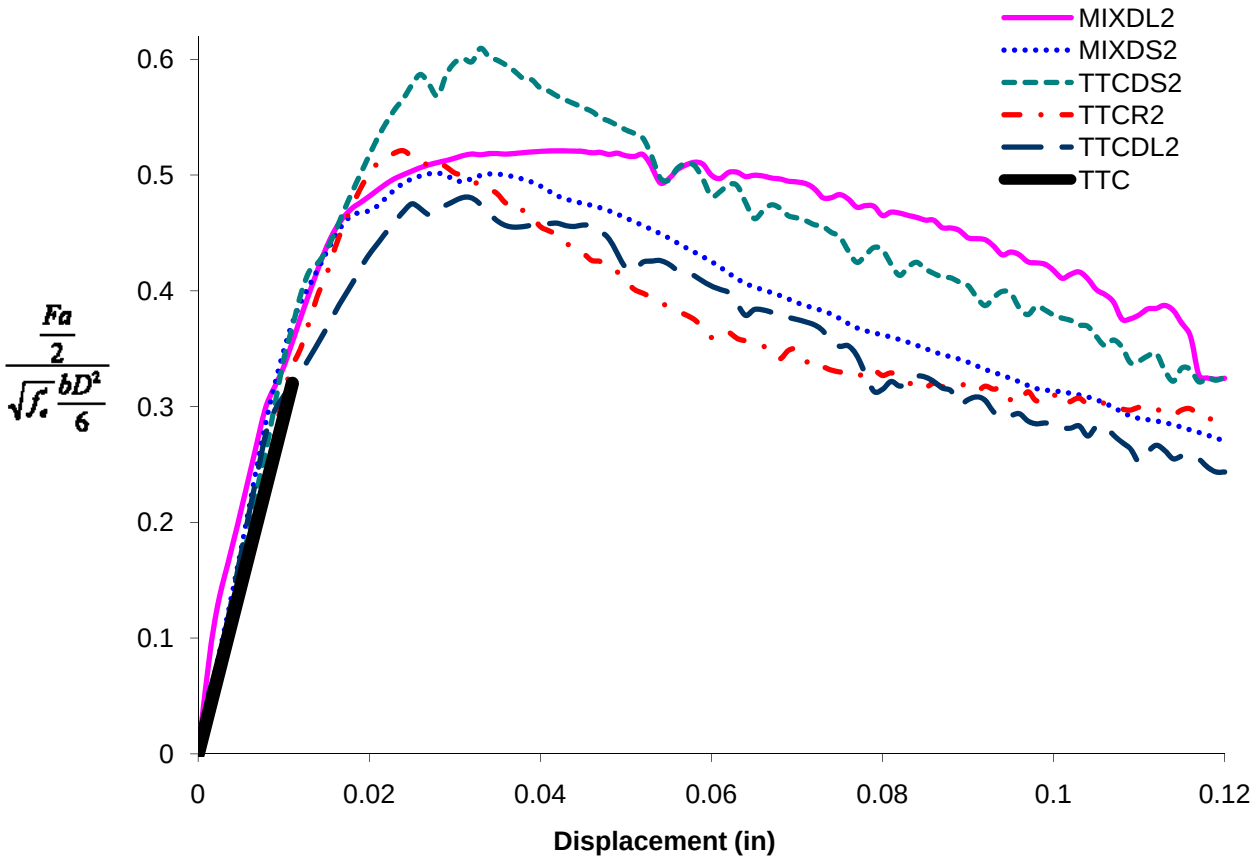

Fig. 3.6 Normalized Load vs. Displacement Curves for Beam Specimens with 1.5% Fiber Content

From the above figures it can be observed that Dramix long fibers, when used in either low (i.e. concrete without fly ash) or high strength concrete (i.e. concrete with fly ash) mixes behaved better than Royal or Helix fibers. At higher dosage of fibers, both Dramix long and short fibers showed almost the same strength and similar structural behavior (Fig. 3.6). This was not true in case of lower dosage of fibers (Fig. 3.5). Hence, the effect of fiber length on enhancing the MOR strength diminished with an increase in the dosage of fibers.

Table 3.5 – Flexural Toughness Values at Beam Displacements of 0.12 in. and 0.03 in.

Beam/Mix ID	Toughness at a displacement of 0.12 in ($Tough_{0.12}$) kip-in	% Increase	Toughness at a displacement of 0.03 in ($Tough_{0.03}$) kip-in	% Increase
MIXDL1[x]	1.187	38.2	0.301	21.9
MIXDL2[+]	1.641		0.367	
MIXDS1[x]	0.751	90	0.223	61.4
MIXDS2[+]	1.427		0.360	
TTCDL1[x]	1.670		0.423	
TTCDS1[x]	1.024	126	0.311	74.3
TTCDS2[+]	2.314		0.542	
TTCH1[x]	1.280		0.352	
TTCR1[x]	0.688	154.4	0.228	94.3
TTCR2[+]	1.750		0.443	

[x] – Steel fiber dosage of 0.5% by volume. [+]- Steel fiber dosage of 1.5% by volume.

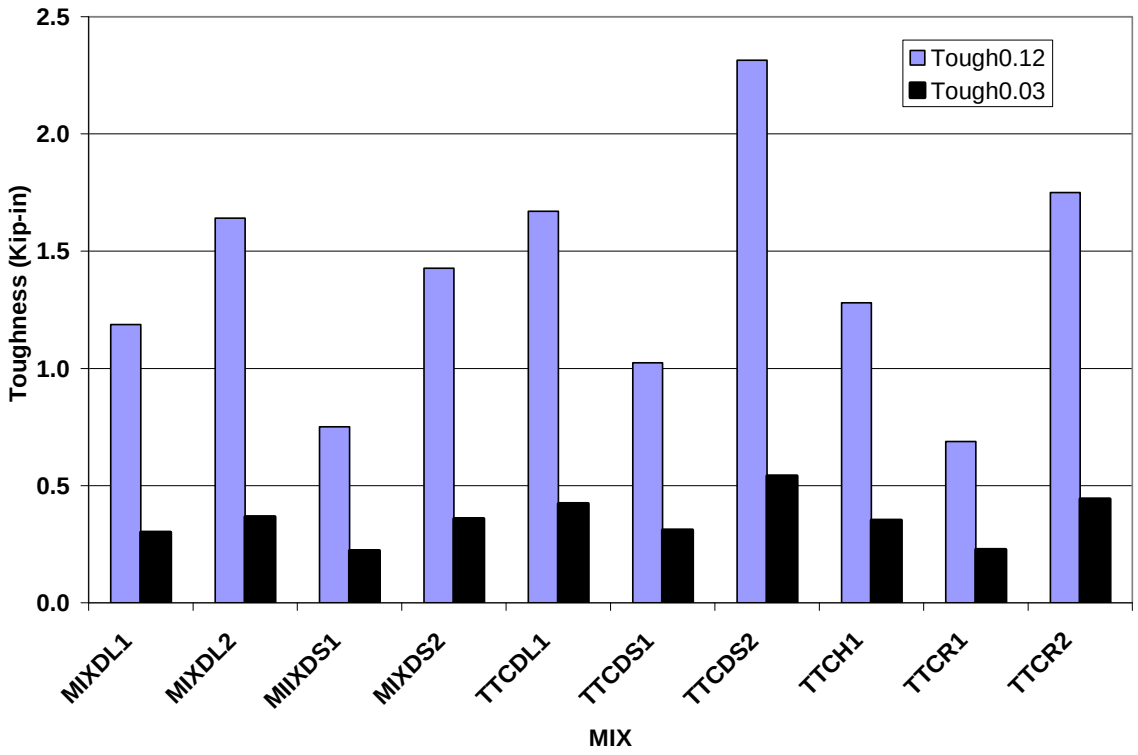

Fig. 3.7 Flexural Toughness Values at Beam Displacements of 0.12 in. and 0.03 in. for Various Concrete Mixes

The beam toughness is represented by the area under the Load-vs.-Displacement curve, in a MOR test. The average toughness values were calculated for all the beam specimens and are presented in Table 3.5 and also plotted in Fig. 3.7. Additionally, in order to better compare the MOR results, the average normalized toughness values were also calculated, as shown in Table 3.6 and are also plotted in Fig. 3.8.

Table 3.6 – Normalized Flexural Toughness Values at Beam Displacements of 0.12 in. and 0.03 in.

Beam/Mix ID	Normalized Toughness at a displacement of 0.12 in ($NTough_{0.12}$)	% Increase	Normalized Toughness at a displacement of 0.03 in ($NTough_{0.03}$)	% Increase
MIXDL1^{x}	0.0407	34.4	0.0103	18.4
MIXDL2^{+}	0.0547		0.0122	
MIXDS1^{x}	0.0272	79	0.0081	51.8
MIXDS2^{+}	0.0487		0.0123	
TTCDL1^{x}	0.0414		0.0105	
TTCDS1^{x}	0.0267	97.8	0.0081	53
TTCDS2^{+}	0.0528		0.0124	
TTCH1^{x}	0.0328		0.0090	
TTCR1^{x}	0.0196	120.4	0.0065	67.7
TTCR2^{+}	0.0432		0.0109	

^{x} – Steel fiber dosage of 0.5% by volume. $^{+}$- Steel fiber dosage of 1.5% by volume.

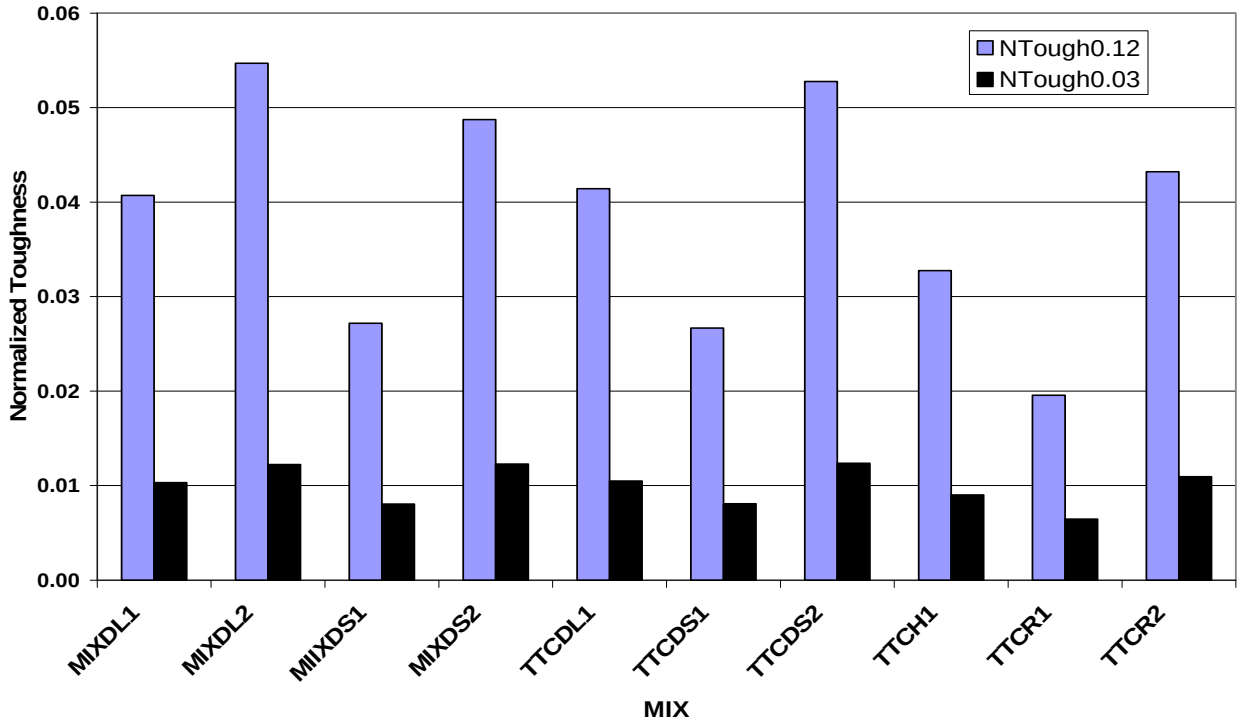

Fig. 3.8 Normalized Flexural Toughness Values at Beam Displacements of 0.12 in. and 0.03 in. for Various Concrete Mixes

It is to be noted that the plain or non-fibrous concrete (TTC) mix did not demonstrate residual strength and hence did not yield any toughness values. From the above results it can be observed that for the concrete mixes with 0.5% fiber dosage, the beams with Dramix long fiber had the highest toughness values followed by the beams with Helix fibers. Mixes with Royal fibers had the least toughness values at both 0.5% and 1.5% fibers dosage. Among all the mixes, the TTC mix with Dramix short fibers at 1.5% dosage had the maximum toughness value at displacements of 0.12 in and 0.03 in. Royal fibers showed the maximum increase in toughness value when fiber content changed from 0.5% to 1.5%. Dramix long fibers showed the least increase, implying that long fibers are good when used in lower dosage.

The mechanical properties of the steel fiber concrete beams, calculated in accordance with ASTM-C 1609, are given in Table 3.7.

Table 3.7 – Properties of Fiber Reinforced Beams in Accordance with ASTM C1609

Beam/Mix ID	First-Peak load F (kips)	First-peak deflection (in)	Peak Load (kips)	Peak Load deflection (in)	Residual Load $P_{0.12}$ (kips)	Residual strength $f_{0.12} = \frac{FL}{bD^2}$ (psi)	Residual Load $P_{0.03}$ (kips)	Residual strength $f_{0.03} = \frac{FL}{bD^2}$ (psi)
TTC	11.6	0.013	11.6	0.013	0	0	0	0
MIXDL1[x]	9.62	0.012	12.10	0.033	5.400	450	11.870	989
MIXDL2[+]	15.63	0.041	15.63	0.041	9.734	811	15.437	1286
MIXDS1[x]	8.58	0.027	8.58	0.027	3.379	281	8.491	708
MIXDS2[+]	14.68	0.028	14.68	0.028	7.909	659	14.506	1208
TTCDL1[x]	17.53	0.023	17.53	0.023	9.885	824	15.223	1269
TTCDS1[x]	12.10	0.011	12.10	0.011	3.088	257	11.094	924
TTCDS2[+]	25.74	0.026	26.73	0.033	14.278	1190	26.197	2183
TTCH1[x]	15.56	0.023	15.56	0.023	5.824	485	14.969	1247
TTCR1[x]	12.17	0.012	12.17	0.012	4.373	364	7.020	585
TTCR2[+]	21.15	0.024	21.15	0.024	11.830	986	20.365	1697

[x] – Steel fiber dosage of 0.5% by volume. [+]- Steel fiber dosage of 1.5% by volume.

The MOR tests of beams showed that the non-fibrous beams had no ductility. In these beams, once the maximum tensile stress was reached, the beams failed suddenly without any warning. The addition of steel fibers changed the failure characteristics of the beams in flexure. After the onset of initial crack at the beam bottom, the specimen did not fail suddenly, but demonstrated considerable residual strength.

The randomly oriented steel fibers, crossing or bridging the crack, resisted the propagation of the crack and hence prevented sudden failure. In many beam specimens, this caused an increase in the load-carrying capacity beyond the first crack. The applied load reached a peak value which can be correlated to a function of fiber dosage, tensile strength of fiber, fiber shape and fiber bond strength. Beyond the peak value, the applied load decreased progressively and localized peaks and valleys were observed.

This can be attributed to the progressive fiber failure in bond from bottom (i.e. at crack opening) to the top of the section (i.e. at crack arrest). Failure occurred due to bond failure between concrete and fiber through straightening of fibers, as shown in Fig. 3.9. At the failure

flexural-tension crack in beam specimens, steel fibers were observed to be de-bonded (i.e. pulled-out) from the concrete and very few actually showed tensile-rupture. This means that steel fibers having good bond strength in concrete are expected to structurally perform better. Therefore, since the Dramix fibers with elongated hooked ends and Helix fibers with twisted-wavy shape demonstrated higher mechanical strength (i.e. MOR strength and toughness) than the Royal fibers, which had relatively smaller hooked ends.

Fig. 3.9 Straightening (De-bonding) of Steel Fibers in Beam Specimen after Failure

For the concrete mixes with 0.5% fiber content, the TTCDL1 mix with Dramix long fibers showed the largest ultimate (peak) load. The ultimate load values of all the beams with 0.5% fiber content are tabulated in Table 3.4 and plotted in Fig. 3.10.

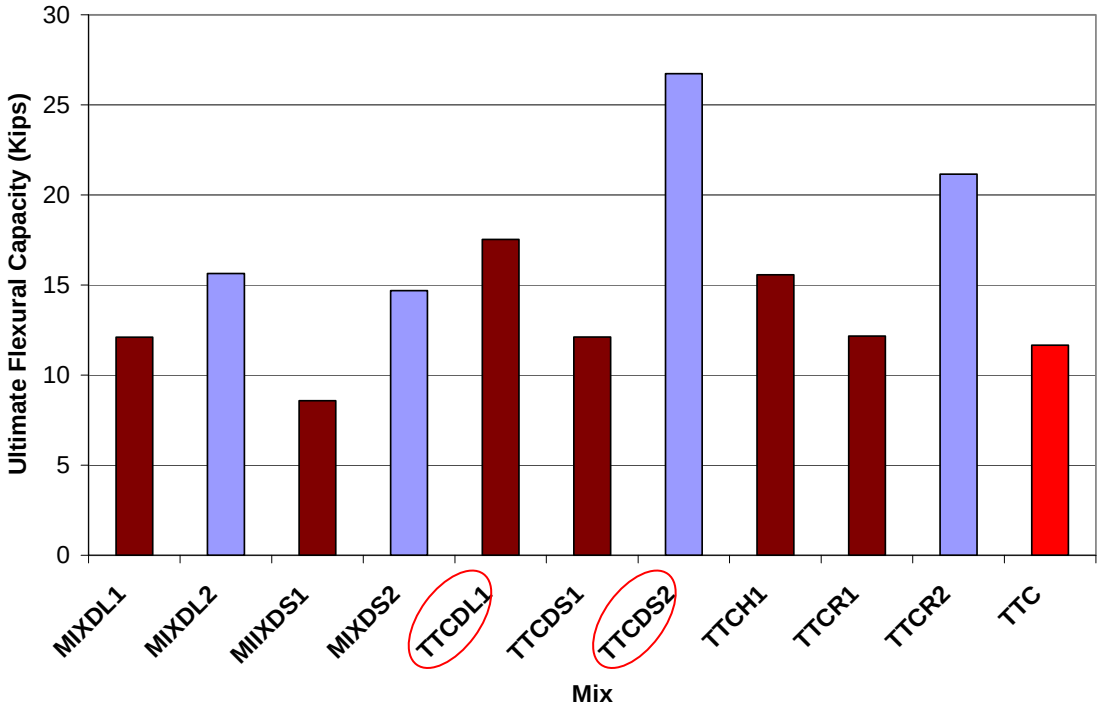

Fig. 3.10 Ultimate (Peak) Load of All Beam Specimens in MOR Test

Among all the mixes with 1.5% fiber content, TTCDS2 mix with Dramix short fibers showed the largest ultimate (peak) load among all the other beams. Poor workability was demonstrated while casting the concrete containing 1.5% fiber dosage in case of both the Dramix long and Helix fibers. Therefore, fiber contents greater than 1.5% by volume most likely may have been completely unworkable and therefore impractical. It is therefore recommended, that to achieve a stable and workable fibrous concrete mix, the maximum percentage of Dramix long or Helix fibers be limited to 1.5% by volume of concrete and that the water/cementitious ratio should never be less than 0.30.

The ultimate load values of all the mixes with 1.5% fiber dosage are presented in Table 3.4 and are plotted in Fig. 3.10. The percentage increase in flexural capacity of the beams when fiber content is enhanced from 0.5% to 1.5% is shown in Table 3.4. The results point out that the percent increase in the flexural capacity of the beams was most prominent in case of the short fibers.

Table 3.8 depicts the percentage increase in the ultimate flexural load capacities of beam specimens made with Dramix fibers. The beams with Dramix long fibers had better flexural

strength than beams with the same dosage of short fibers. This holds true for both high strength and normal strength concrete. The increase in the ultimate flexural load capacities of beam specimens is more pronounced with the 0.5% dosages than with the 1.5% dosages. The reason for this was the detrimental effect of higher dosage of fibers on workability and stability of the fibrous concrete. Stability and workability of the Dramix fiber mix was observed to be reduced with larger dosage of steel fibers, which invariably decreased the mechanical strength of beams with 1.5% dosage.

Table 3.8 - Increase in Flexural Capacity of Beam Specimens with Dramix Fibers

Beam/Mix ID	Ultimate Flexural Capacity (kips)	% Increase in Flexural Capacity
MIXDS1[x]	8.58	41
MIXDL1[x]	12.10	
TTCDS1[x]	12.10	45
TTCDL1[x]	17.53	
MIXDS2[+]	14.68	6.5
MIXDL2[+]	15.63	

[x] – Steel fiber dosage of 0.5% by volume. [+]- Steel fiber dosage of 1.5% by volume.

Considering only the Dramix fiber beam specimens, the percentage increase in flexural toughness values with increased fiber length and same fiber dosage are shown in Table 3.9. Additionally, the percentage increase in the normalized flexural toughness values for beam specimens with Dramix fibers corresponding to the data in Table 3.9 are shown in Table 3.10.

Table 3.9 - Increase in Flexural Toughness of Beam Specimens with Fiber Length (Dramix)

Beam/Mix ID	Toughness at a displacement of 0.12 in ($Tough_{0.12}$) kip-in	% Increase	Toughness at a displacement of 0.03 in ($Tough_{0.03}$) kip-in	% Increase
MIXDS1[x]	0.751	} 58	0.223	} 35
MIXDL1[x]	1.187		0.301	
MIXDS2[+]	1.427	} 15	0.360	} 2
MIXDL2[+]	1.641		0.367	
TTCDS1[x]	1.024	} 63	0.311	} 36
TTCDL1[x]	1.670		0.423	

[x] – Steel fiber dosage of 0.5% by volume. [+]- Steel fiber dosage of 1.5% by volume.

Table 3.10 - Increase in Normalized Flexural Toughness of Beam Specimens with Fiber Length (Dramix)

Beam/Mix ID	Normalized Toughness at a displacement of 0.12 in ($NTough_{0.12}$)	% Increase	Normalized Toughness at a displacement of 0.03 in ($NTough_{0.03}$)	% Increase
MIXDS1[x]	0.0272	} 49.6	0.0081	} 27
MIXDL1[x]	0.0407		0.0103	
MIXDS2[+]	0.0487	} 12.3	0.0123	} -0.8
MIXDL2[+]	0.0547		0.0122	
TTCDS1[x]	0.0267	} 55	0.0081	} 29.6
TTCDL1[x]	0.0414		0.0105	

[x] – Steel fiber dosage of 0.5% by volume. [+]- Steel fiber dosage of 1.5% by volume.

From Tables 3.9 and 3.10, it can be concluded that the increase in flexural toughness is significant when the fiber length is increased at lower dosages of fibers. At higher fiber dosage, the flexural toughness is unaffected by the fiber length, but is found to be dependent on fiber type and dosage.

3.4 Summary

Flexural tests (ASTM C 1609) on small-sized steel fiber concrete beam specimens made using different concrete strengths, fiber type and fiber dosage were carried out in this study. This test method evaluates the flexural performance of fiber concrete using parameters derived from the load-deflection curve obtained by testing a simply supported beam under third-point loading. The Modulus of Rupture (MOR) and flexural toughness values of different beam specimens were determined through this experimental study. The primary focus of this experimental program was to determine and compare the structural behavior of different types and dosage of steel fibers in normal and high strength concrete. Based on the test results, suitable mix designs - including an appropriate choice of the type and dosage of steel fiber, will be selected to cast large-scale prestressed concrete beams in the next phase of this research project.

Following conclusions can be drawn from the above test results:

1. Addition of steel fibers in concrete increased the load carrying capacity, ductility and energy absorption capability (i.e. flexural toughness) of the beam.

2. An increase of 30% to 120% was observed in the ultimate flexural capacities of beam specimens, when steel fiber content was increased from 0.5% to 1.5% by volume of concrete.

3. Dramix long fibers structurally performed better than any other fibers when used in small quantities (i.e. 0.5% dosage). At higher fiber dosage (i.e. 1.5%), both Dramix short and Helix fiber mixes showed similar results. However, the concrete mixes with Helix fiber were found to be practically unworkable. Hooked collated steel fibers (Dramix) performed better than hooked single fibers (Royal). The mechanical performance of Dramix short fibers and Helix fibers was found to be similar at all fiber dosages, in the flexural tests.

4. In the beam specimens with 0.5% dosage of Dramix fibers, an increase in the fiber length (i.e. from short to long fibers) attributed to a significant increase (of about 30%)

in the flexural toughness values. The beneficial effect of fiber length on flexural toughness became less significant at higher dosage of steel fibers in the beam specimens.

5. Based on the flexural test results of small beam specimens, the Dramix steel fibers were selected to cast the prestressed concrete beams. In this case, the recommended maximum dosage of Dramix steel fibers to be used in the concrete mix is as below;

    (a) Dramix Long Fibers - Dosage of 0.5% by volume of concrete
    (b) Dramix Short Fibers - Dosage of 1.5% by volume of concrete

PART I:

PRESTRESSED STEEL FIBER CONCRETE ELEMENTS

CHAPTER 4

TEST FACILITIES OF PANELS

4.1 General Description

The tests to find constitutive models of PSFC were carried out using the Universal Panel Tester (Hsu, Belarbi, and Pang, 1995) at the University of Houston. The Universal Panel Tester was built in 1988 to study the behavior of reinforced concrete membrane elements subjected to any combination of in-plane and out-of-plane forces. The reinforced concrete panels were 55 inches square and up to 16 inches thick. Such panels can be considered as full-size specimens because they can be reinforced with deformed bars up to one inch in diameter. The South and North end views of the Universal Panel Tester are shown in Fig. 4.1 and 4.2, respectively.

This versatile equipment consists of a giant 15.7 ft. x 15.7 ft. vertical steel frame that houses 37 in-plane jacks of 100-ton capacity each and 3 in-plane rigid links. The out-of-plane frame contains 3 rigid links and has a space available for 17 additional out-of-plane hydraulic jacks of 60-ton capacity each. Every jack can be precisely controlled in force or strain mode using a servo-valve that is equipped with a sophisticated hydraulic distribution system so that any conceivable stress conditions encountered in actual structures can be simulated. These stress conditions include any combinations of in-plane and out-of-plane normal stresses (tension and compression) and shear stresses.

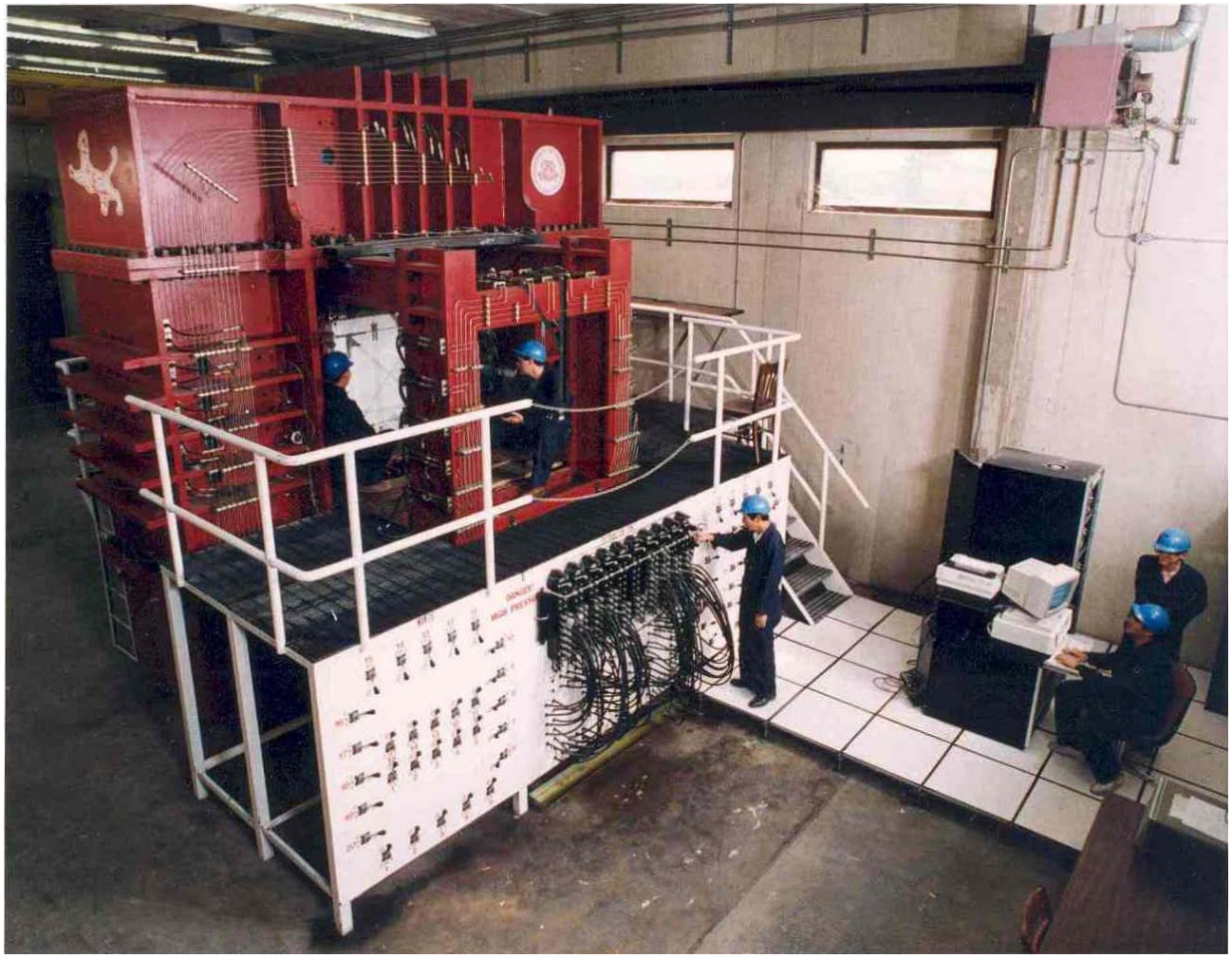

Fig. 4.1 South End View of the Universal Panel Tester at the University of Houston

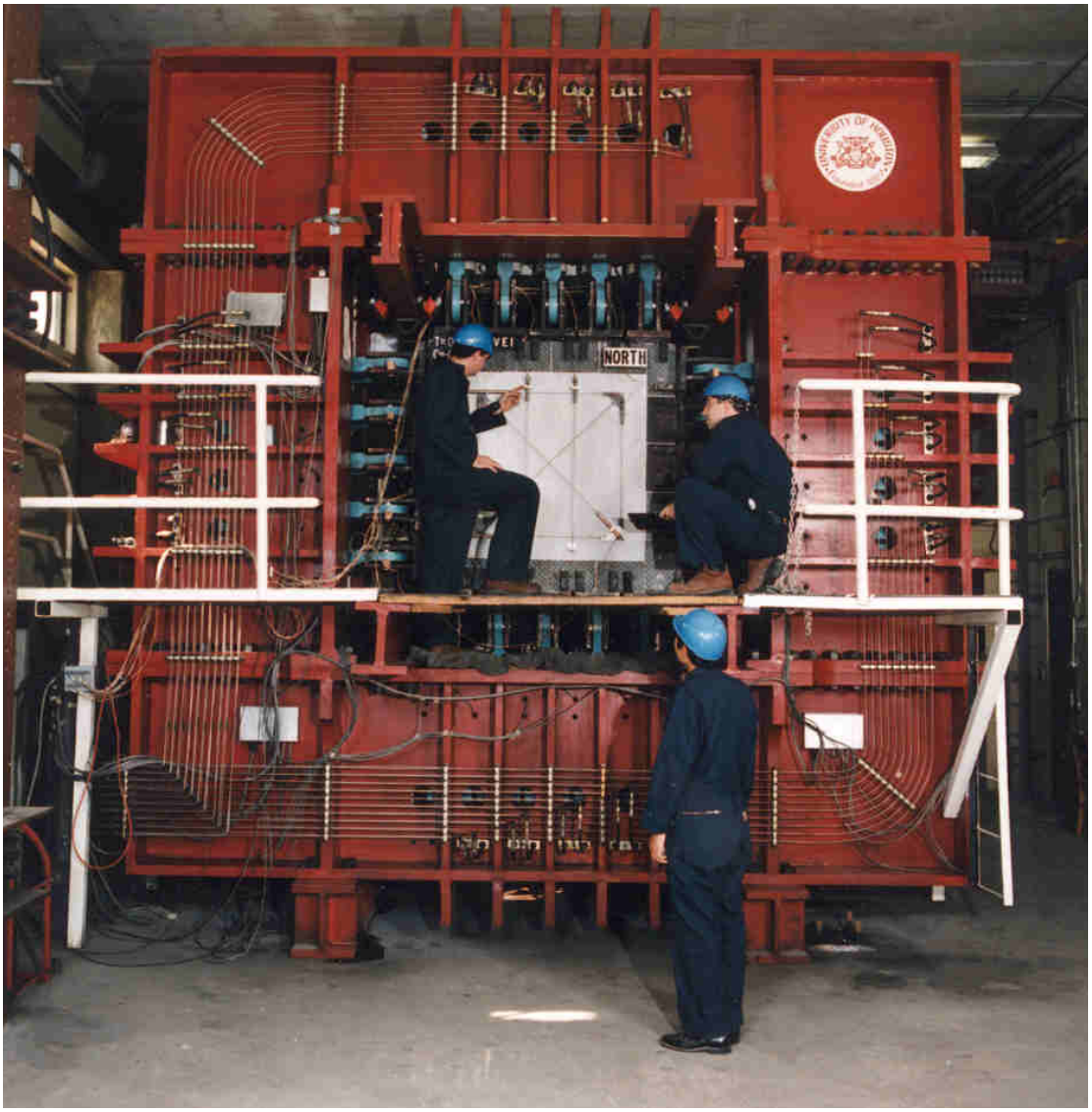

Fig. 4.2 North End View of the Universal Panel Tester at the University of Houston

Until 1993, an Edison load maintainer and distribution unit was used to control the oil pressures of the hydraulic jacks in the Universal Panel Tester. Consequently, the panels could be tested only in load-control mode. Although such tests have produced the constitutive laws of normal strength concrete panels, serious drawbacks were observed in the original tests. First, the post-yielding branch of the shear stress-strain curve of reinforced concrete panels could not be accurately obtained because the increase of strain in the post-yielding range was accompanied by an unstable reduction of load, which was difficult to manually control. This drawback was particularly serious for reinforced concrete with low percentages of reinforcement. Second, the behavior of the test panels in the post-peak range could not be reliably obtained due to the brittle failure of concrete in the descending portion, which frequently occurred in high-strength concrete and prestressed concrete panels.

In order to provide the deformation-control capability, a closed-loop servo-control system was installed in the Universal Panel Tester in 1993. The upgrade made it feasible to perform tests in the strain-control mode, in addition to the load-control mode. This automated servo-control system has ten servo-valves with ten independent programming capabilities and is suitable for many complex applications. The upgraded panel tester is much more versatile than the one in Canada (Kirschner and Collins, 1986), which has no servo-control system and where the five pairs of jacks on each side of a panel must have the same force. Thus, this Universal Panel Tester at the University of Houston is the only one in the world that can perform full-size panel tests in the strain-control mode and with any prescribed stresses at the four edges of the specimen. The above mentioned strain-control feature was utilized in this research to investigate the behavior of prestressed steel fiber concrete membrane elements under pure shear stresses.

CHAPTER 5

EXPERIMENTAL PROGRAM OF PSFC PANELS: GROUP-TEF

5.1 General Description of Group-TEF Specimens

The purpose of testing the five Prestressed Steel Fiber Concrete (PSFC) panels in Group-TEF was to obtain the constitutive laws of Steel Fiber Concrete (SFC) and steel tendons in prestressed concrete membrane elements and to make direct comparisons between PSFC panels and non-fibrous Prestressed Concrete (PC) panels. The system of post-tensioning and grouting used herein was shown to be equal to true prestressing by Wang (2006). The prestressing tendons in both the series of panels were aligned along the horizontal direction. These full-size PSFC panels (elements) were subjected to biaxial tension-compression loads along their edges. The panels were designed with three variables: (1) percentage of prestressing tendons $\rho_{\ell p}$ in the panels, (2) fiber-factor $(L_f/D_f)V_f$, and (3) tensile strain in the horizontal direction $\overline{\varepsilon}_1$, which was held constant during the second stage of the loading in each panel. The primary difference between series TEF and Wang's (2006) TE series was the presence of Dramix fiber in series TEF. This was intended to simplify comparison of results and highlight the effect of fiber on constitutive laws of prestressed concrete. All the panels were subjected to sequential loading. Tensile forces were first applied in the horizontal direction. After attaining the desired smeared (average) tensile strain in the panels, compressive stresses were gradually applied in the vertical direction until failure. During the first stage of the tensile loading, the constitutive laws of PSFC in tension and prestressing tendons embedded in SFC were obtained. In the second stage of the compressive loading, the stress-strain relationships of concrete in compression were recorded, from which the experimental softening coefficients were determined.

5.2 Tensile Stress-Strain Relationships

Table 5.1 summarizes the reinforcement details in various panel specimens (Group-TE) used in Wang's (2006) tests and indicates the corresponding Group-TEF PSFC panels. To describe the panel behavior the horizontal principal stress, σ_1, is plotted against the horizontal principal strain, ε_1. Two series of panels TEF- 1, 2, 3 and TEF-3, 4, 5 are shown in Fig. 5.1 and 5.2, respectively. Also plotted in these figures are the results for prestressed panels with no fiber,

from Wang (2006). As shown in Fig. 5.1, the panels in the first series (TEF-1, 2, and 3) all had the same amount of prestress. These are compared to corresponding equivalent non-fibrous PC panels TE-3, TE-4, and TE-5. From these results it can be seen that the post-cracking tensile stiffness of PSFC enhanced with an increase in the fiber-factor.

Table 5.1 – Details of Various Panel Specimens

Group-TEF (Fiber-Factor) PSFC Panels	**Group-TE** PC Panels without steel fiber, Wang (2006)	**Steel Reinforcement in ℓ- direction**		**Prestress Force** (ksi)
		Tendons (Low-Relaxation)	$\rho_{\ell p}$	
TEF-1 (0.28)	TE-5	2-ϕ0.6 @10.5 in.	0.59%	0.8
TEF-2 (0.55)	TE-4	2-ϕ0.6 @10.5 in.	0.59%	0.8
TEF-3 (0.83)	TE-3	2-ϕ0.6 @10.5 in.	0.59%	0.8
TEF-4 (0.80)	TE-7	4-ϕ0.6 @10.5 in.	1.18%	1.6
TEF-5 (0.28)	TE-6	1-ϕ0.6 @10.5 in.	0.30%	0.4

In the second series of panels TEF-3, 4, and 5, Fig. 5.2, the tensile loads carried by the panels increased with the increase in prestressing force. The measured tensile stresses of 900, 1700, and 3300 psi at a strain of 0.01 for panels TEF-5, 3, and 4, respectively, were approximately proportional to the prestressing steel of 0.30%, 0.59%, and 1.18%, respectively. For Group-TEF, the corresponding cracking stresses (un-normalized) were found to be 450, 1000, and 1700 psi, respectively. Fig. 5.2 shows the corresponding Group-TE panels, it can be seen that the steel fiber increased the panel stiffness and tensile stress capacity.

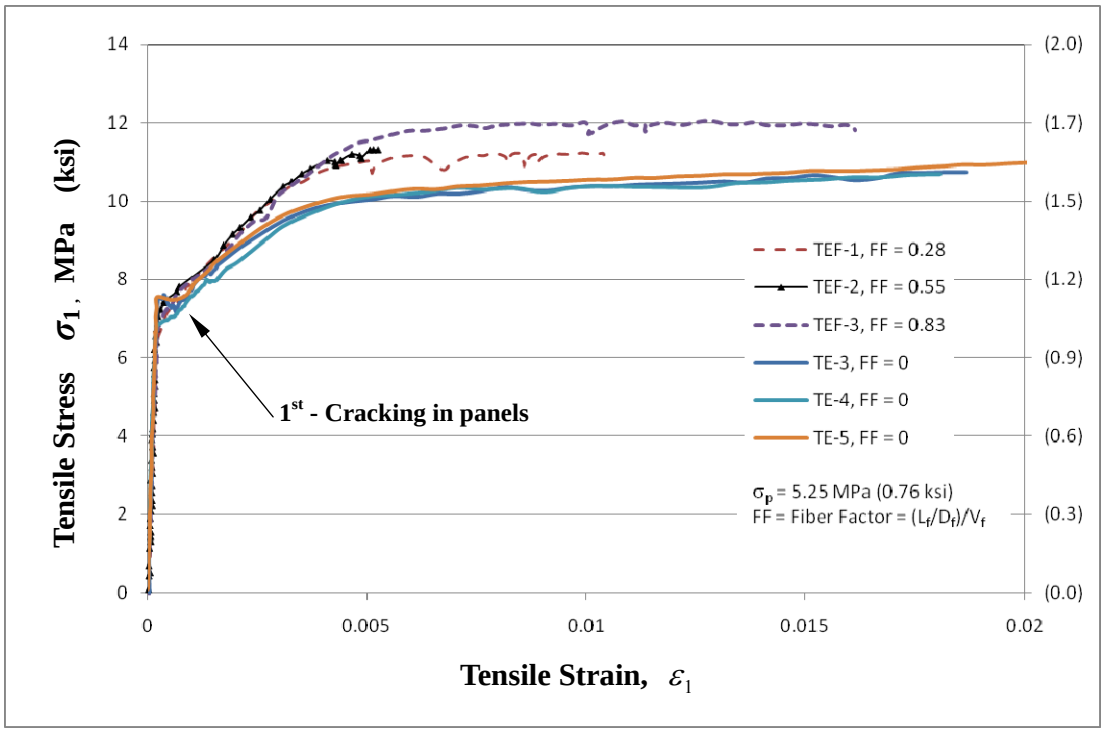

Fig. 5.1 $\sigma_1 - \varepsilon_1$ Relationships in panels TEF-1, 2, and 3

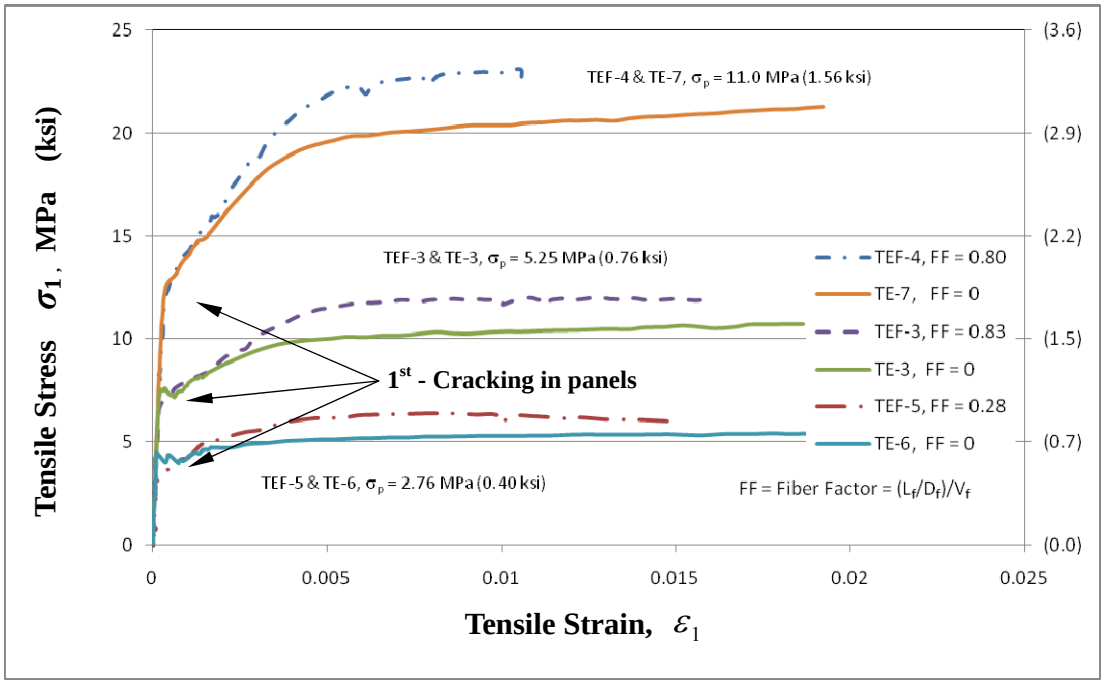

Fig. 5.2 $\sigma_1 - \varepsilon_1$ Relationships in panels TEF-3, 4, and 5

5.3 Smeared (Average) Stress-Strain Relationships of SFC in Tension

Plain concrete cannot resist any tensile stresses after tensile cracks are formed, but the concrete between these cracks in reinforced concrete can still resist some tensile stress. This contribution of concrete to resist tension between cracks is known as "tension stiffening" (Carreira and Chu, 1986). Taking into account this phenomenon, the smeared (average) stress-strain relationships of concrete and mild steel were studied (Hsu and Belarbi, 1994; Hsu and Zhang, 1996). Tension stiffening can also be observed in prestressed concrete (Wang 2006), and its behavior is very similar to reinforced concrete after cracking.

5.3.1 Pre-Decompression Behavior

Before applying loads, initial compressive stress and strain exist in the concrete due to the prestress. Upon applying a tensile load, the first stage of the stress-strain relationship of concrete, called "decompression" begins. The initial stress and the initial uniaxial strain in SFC are denoted as σ_{ci} and $\bar{\varepsilon}_{ci}$, respectively, while the initial stress and the initial uniaxial strain of prestressing tendons are f_{pi} and $\bar{\varepsilon}_{pi}$, respectively. These stresses are in equilibrium as follows

$$\sigma_{ci} A_c + f_{pi} A_{ps} = 0, \tag{5-1}$$

where,

A_c, A_{ps} = cross-sectional areas of PSFC panel and tendons, respectively, in.^{2}

Prior to concrete cracking, both the PSFC and the prestressing tendons can be considered as elastic materials. When stretched to the same strain ε_1, the SFC stress σ_c and the tendon stress f_{ps} are given as follows:

$$\sigma_c = \sigma_{ci} + E_c' \varepsilon_1, \tag{5-2}$$

$$f_{ps} = f_{pi} + E_{ps} \varepsilon_1, \tag{5-3a}$$

where,

E_{ps} = modulus of prestressing steel tendons, psi and

E_c' = decompression modulus of SFC, given as $2f_c'/\varepsilon_0$, psi

The total load resisted, P is the sum of the forces in PSFC and the tendon

$$P = A_c \sigma_c + A_{ps} f_{ps} = \left(E_c' A_c + E_{ps} A_{ps}\right)\varepsilon_1 + \left(\sigma_{ci} A_c + f_{pi} A_{ps}\right). \tag{5-3b}$$

In view of Eq. (5-1),

$$P = \left(E_c' A_c + E_{ps} A_{ps}\right)\varepsilon_1 . \tag{5-4}$$

Substituting the cross-sectional area of tendons $A_{ps} = \rho_{\ell p} A_c$ into Eq. (5-4) and rearranging the terms, a general form of equilibrium equation before cracking is given as

$$E_c'\varepsilon_1 = \frac{P}{A_c} - \rho_{\ell p} E_{ps}\varepsilon_1 . \tag{5-5}$$

Substituting Eq. (5-5) into Eq. (5-2), the PSFC stress, σ_c, is obtained as follows

$$\sigma_c = \sigma_{ci} + \frac{P}{A_c} - \rho_{\ell p} E_{ps}\varepsilon_1 . \tag{5-6}$$

The SFC uniaxial strain $\bar{\varepsilon}_c$ is given by

$$\bar{\varepsilon}_c = \bar{\varepsilon}_{ci} + \varepsilon_1 . \tag{5-7}$$

Using Eqs. (5-6) and (5-7), the experimental stress-strain relationship of concrete in decompression can be plotted as shown in Fig. 5.3. By inspection, the relationship is close to a straight line.

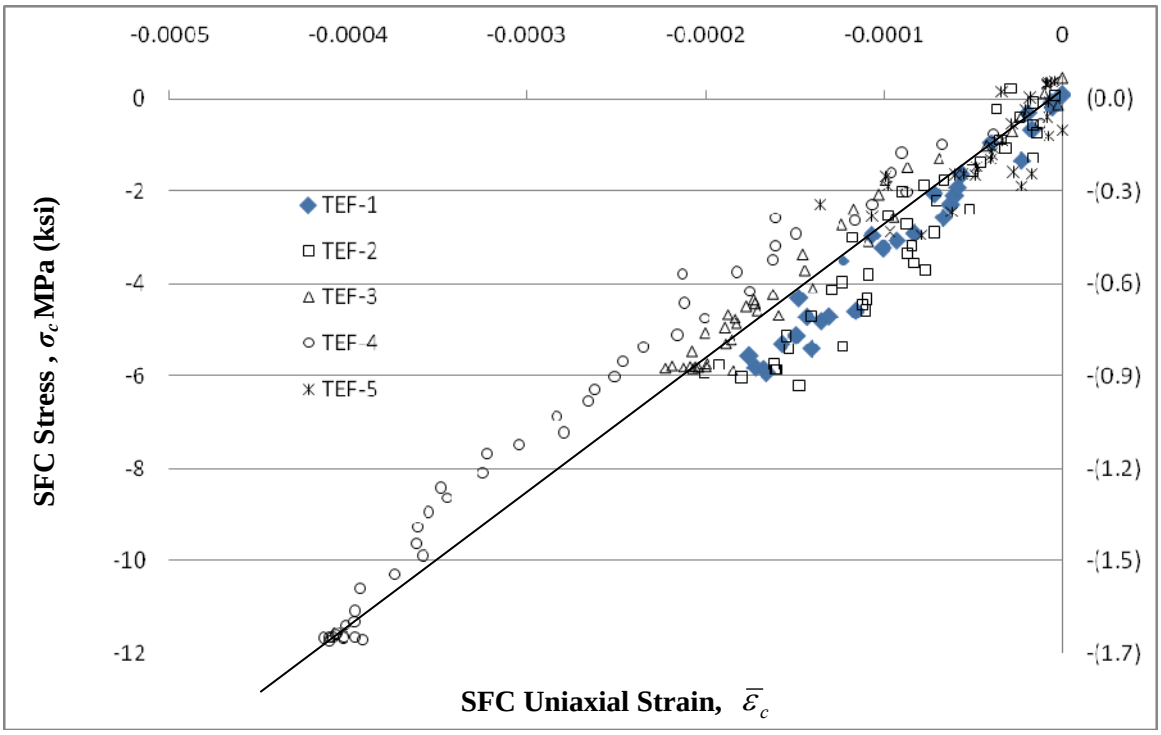

Fig. 5.3 Experimental $\sigma_c - \bar{\varepsilon}_c$ Relationships of PSFC in Decompression

5.3.2 Post-Decompression Behavior

After the decompression of the concrete and before the yielding of the tendons, Eqs. (5-6) and (5-7) can still be applied to obtain the experimental stress-strain relationship of the PSFC. After cracking, the applied strain ε_1 becomes the smeared (average) strain. Fig. 5.4 shows the stress-strain curves of the PSFC in tension. The stresses are normalized by dividing the cracking strength of the PSFC by $\sqrt{f'c}$. The effect of the steel fiber can clearly be seen in Fig 5.4 by observing the behavior as the tensile strain increases past the cracking strain. For normal concrete without steel fibers, as the tensile strain increases past the cracking strain, the concrete tensile stress decreases sharply per Eq. 5-8 as described by Wang (2006) for prestressed normal concrete.

$$\sigma_c = f_{cr}\left(\frac{\varepsilon_{cr}}{\bar{\varepsilon}_c}\right)^{0.5}, \qquad \bar{\varepsilon}_c > \varepsilon_{cr}, \tag{5-8}$$

For PSFC, however, after the initial drop in concrete tensile stress just after cracking, there is a marked increase in tensile stress which is sustained well past cracking. The stress peaks at a point, σ_{cp}, and thereafter decreases gradually. This was described in research by Limsuwan (2006) for PSFC reinforced with mild steel. For PSFC, the behavior in tension is different from concrete without fibers. Examination of Fig. 5.4 indicates there is an increase in post-decompression tensile stress as tensile strain increases, or tensile strain hardening, rather than a decrease, as with the Equation 5-8. This strain hardening curve can be characterized as a three part curve, defined by two points, herein called the steel fiber concrete tensile yield point, f_{cy} and the associated strain, e_{cy}, and the steel fiber concrete ultimate tensile stress and corresponding ultimate tensile strain.

Table 5.4 indicates that f_{cy} and e_{cy} do not vary appreciably with either the fiber-factor or longitudinal reinforcing ratio. Therefore, an average value will be use for each and will be treated as constants. Such is not the case with $f_{c,ult}$ and $e_{c,ult}$., i.e. the ultimate concrete stress and strain. Both $f_{c,ult}$ and $e_{c,ult}$ vary with both fiber-factor and longitudinal reinforcing ratio. To simplify the analytic model, $e_{c,ult}$ will be treated simply as a function of initial prestess, with a value of (0.01 – e_{pi}). Where, e_{pi} is the initial prestress strain in the tendon.

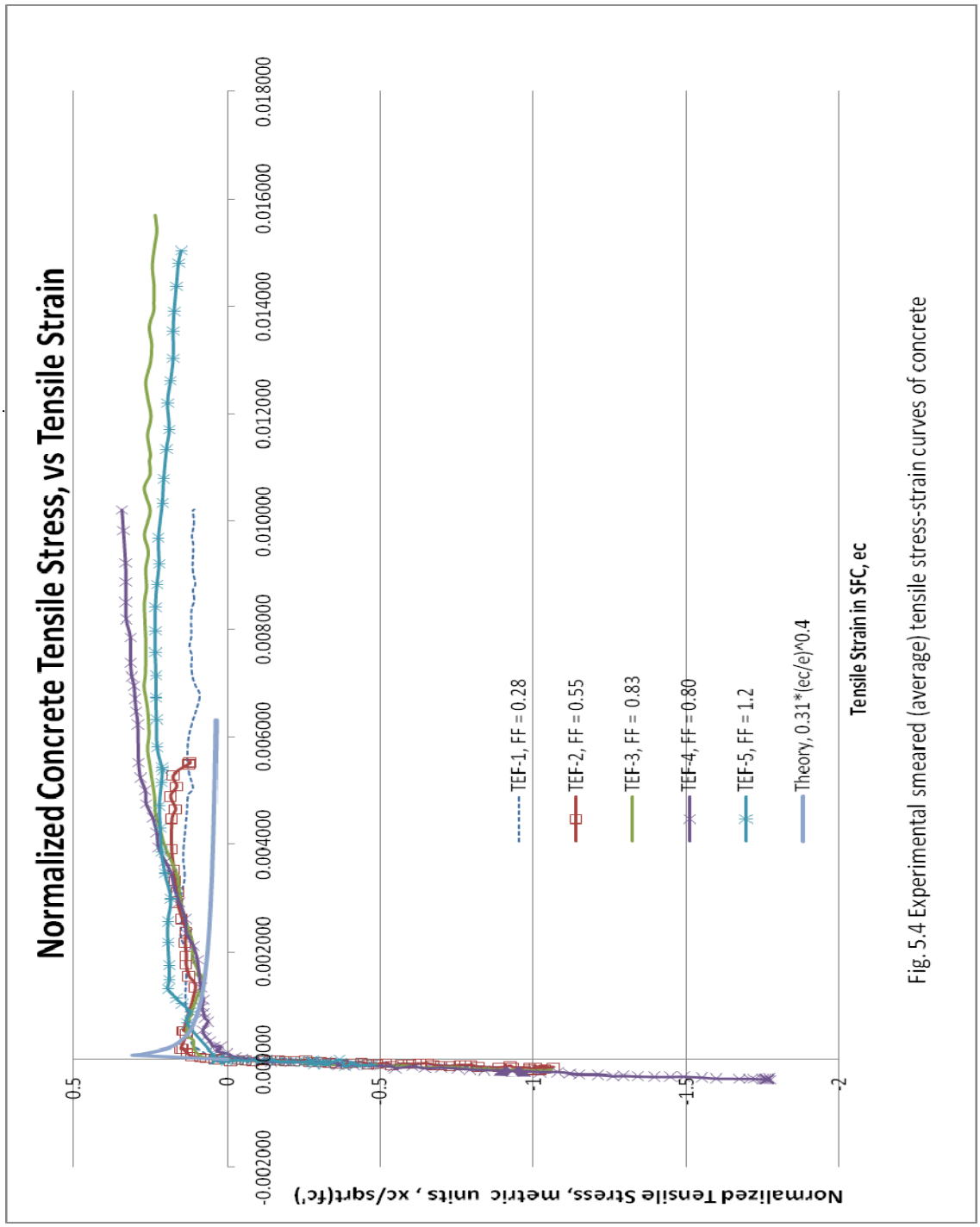

Fig. 5.4 Experimental smeared (average) tensile stress-strain curves of concrete

Table 5.2 (a) – Average Normalized Yield Stress for Panels TEF-1, -2, -3, -4, -5

			At Yield	
Panel	ρ_l	**Fiber-Factor**	e_{cy}	$f_{cy}/\text{sqrt. } f_{c'}$
TEF-1	0.0059	0.280	0.000558	0.110
TEF-2	0.0059	0.550	0.000479	0.132
TEF-3	0.0059	0.830	0.000476	0.130
TEF-4	0.0118	0.800	0.000546	0.077
TEF-5	0.0030	1.200	0.000671	0.128
	AVERAGE	➔	**0.0005**	**0.120**

Table 5.2 (b) – Normalized Ultimate Tensile Stress for Panels TEF-1, -2, -3, -4, -5

			At Ultimate	
Panel	ρ_l	**Fiber-Factor**	$e_{c\,ult}$	$f_{c\,ult}/\text{sqrt. } f_{c'}$
TEF-1	0.0059	0.280	0.002290	0.149
TEF-2	0.0059	0.550	0.004885	0.185
TEF-3	0.0059	0.830	0.006920	0.270
TEF-4	0.0118	0.800	0.010216	0.344
TEF-5	0.0030	1.200	0.007965	0.234
TEF-x	0.003	0.800	-	0.227

The fiber-factor and longitudinal prestress, do have significant impact on the value of $f_{c,ult}$. Due to the limited amount of data with only five test panels, the function for $f_{c,ult}$ is based on a created sixth data point. The sixth data point was created by extrapolating the data for panels TEF-3 and TEF-4 which had fiber-factors of 0.8 and 0.83 respectively and longitudinal reinforcing ratios of 0.0059 and 0.0118, respectively; thereby creating an $f_{c,ult}$ for a fictitious panel with a fiber-factor of 0.8 and a longitudinal reinforcing ratio of 0.003. Note that panel TEF-5 has been excluded from inclusion in the empirical data analysis. This specimen was unloaded and reloaded after initial cracking and the precise cracking point became indistinct due to locally de-bonded fibers within a dominant crack. These six data points were fit to an equation for a plane in the form:

$$A \times FF + B \times \rho_l + C \times f_{cult} + D = 0 \qquad (5.8a)$$

where, A, B, C and D are empirical constants which are determined by combining the individual equations for $f_{c,ult}$ -vs.- Fiber-Factor (FF) from Fig. 5.6 and $f_{c,ult}$ –vs.- ρ_l from Fig. 5.5 as;

$$f_{c,ult} / f_{c'} = [0.2198 \text{ x FF} + 0.0799] \qquad (5.9)$$

$$f_{c,ult} / \text{sqrt } f_{c'} = [13.145 \text{ x } \rho_l + 0.1898] \qquad (5.10)$$

Combining these equations yields the expression

$$f_{c,ult}/\text{sqrt } f_{c'} = [12.44\, \rho_l + 0.223 \text{ FF } -0.0069] \qquad (5.11)$$

The constant -0.069 is negligible, and rounding the other factors for simplification yields the equation;

$$f_{c,ult} = (12.0\, \rho_l + 0.2 \text{ FF}) \sqrt{f_c'} \qquad (5.12)$$

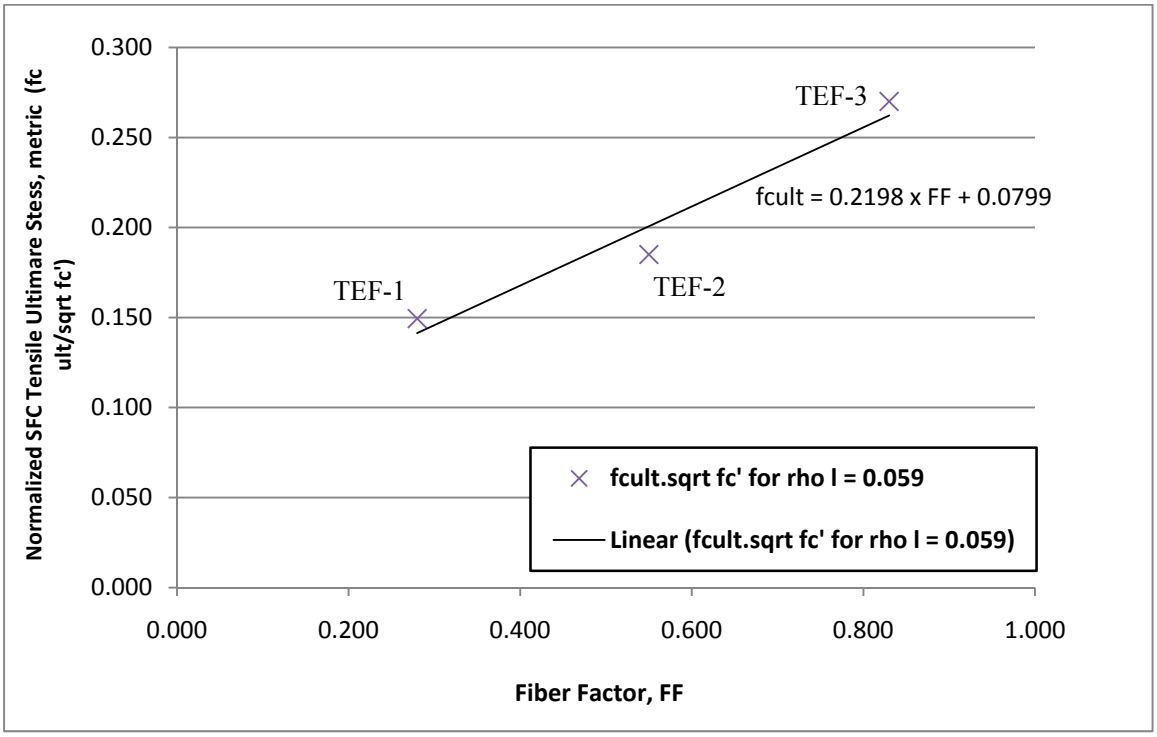

Fig. 5.5 Normalized Ultimate Tension ($f_{c,ult}$) vs. Fiber-Factor for ρ_l = 0.059 in PSFC Panels

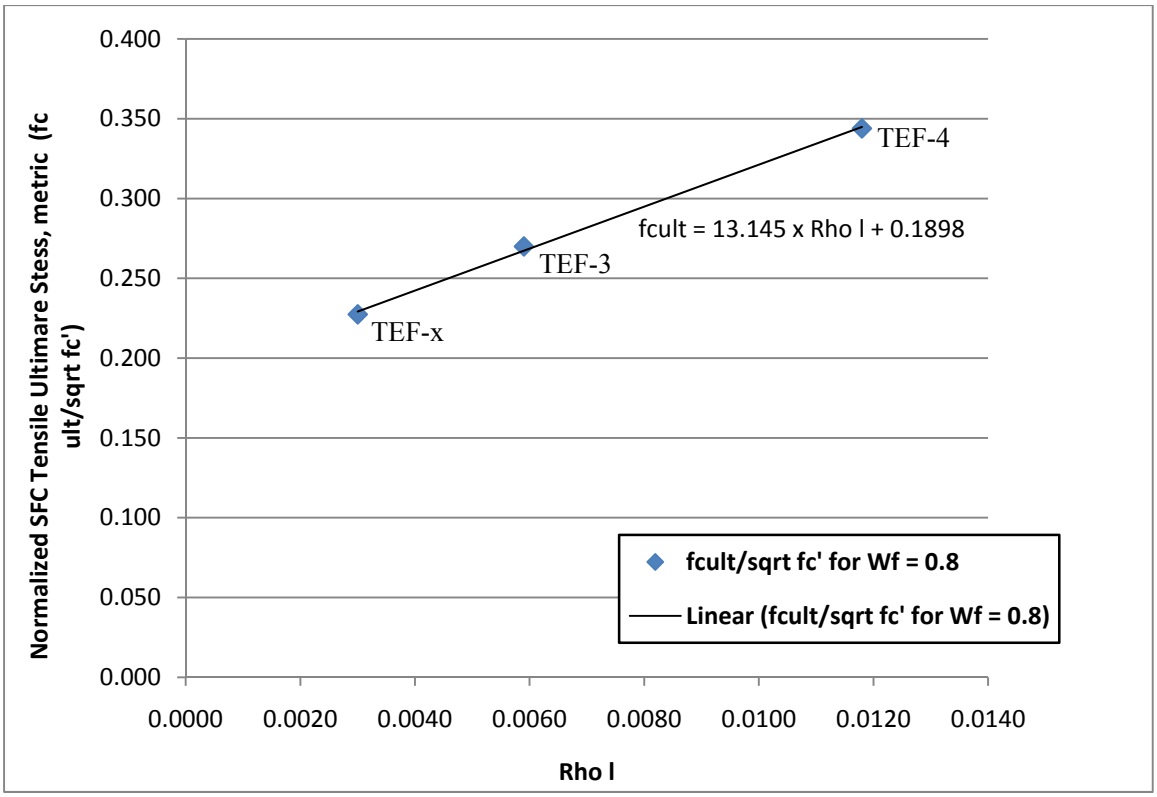

Fig. 5.6 Normalized Ultimate Tension ($f_{c,ult}$) vs. ρ_l for Fiber-Factor = 0.80 in PSFC Panels

Thus, the relationships of the tensile stress σ_1^c versus the uniaxial tensile strain $\bar{\varepsilon}_1$ of PSFC are given as follows for the TEF series of panel tests:

Stage UC: $\sigma_1^c = E_c'\bar{\varepsilon}_1 + \sigma_{ci}$, $\bar{\varepsilon}_1 \le (\bar{\varepsilon}_{cx} - \bar{\varepsilon}_{ci})$, (5-13a)

Stage T1: $\sigma_1^c = E_c''(\bar{\varepsilon}_1 + \bar{\varepsilon}_{ci})$, $(\bar{\varepsilon}_{cx} - \bar{\varepsilon}_{ci}) < \bar{\varepsilon}_1 \le (\varepsilon_{cy} - \bar{\varepsilon}_{ci})$, (5-13b)

Stage T2: $\sigma_1^c = E_c'''(\bar{\varepsilon}_1 + \bar{\varepsilon}_{ci})$, $(\bar{\varepsilon}_{cy} - \bar{\varepsilon}_{ci}) < \bar{\varepsilon}_1 \le (\varepsilon_{cult} - \bar{\varepsilon}_{ci})$, (5-13c)

Stage T3: $\sigma_1^c = E^{IV}{}_c(\bar{\varepsilon}_1 + \bar{\varepsilon}_{ci})$, $\bar{\varepsilon}_1 > (\varepsilon_{cult} - \bar{\varepsilon}_{ci})$, (5-13d)

where,

E_c' = decompression modulus of concrete taken as $\frac{2f_c'}{\varepsilon_0}$, (5-13e)

$\bar{\varepsilon}_{ci}$ = initial strain in concrete due to prestress,

σ_{ci} = initial stress in PSFC,

$\bar{\varepsilon}_{cx}$ = extra strain in concrete after decompression calculated by $\bar{\varepsilon}_{ci} - \frac{\sigma_{ci}}{E'_c}$,

$\varepsilon_{c\max}$ = PSFC maximum strain taken as 0.04 - ε_{pi}

ε_{cult} = PSFC ultimate strain taken as 0.01- ε_{pi}

f_{cult} = PSFC ultimate stress strain taken as $(0.2FF + 12\rho_l)\sqrt{f'_c}$

ε_{cy} = PSFC yield strain taken as 0.0005,

f_{cy} = PSFC effective "yield" stress for Sequential Loading taken as $0.12\sqrt{f'_c}$

(f'_c and $\sqrt{f'_c}$ are in MPa) where:

E''_c = modulus of PSFC taken as $\frac{f_{cy}}{\varepsilon_{cy} - \bar{\varepsilon}_{cx}}$,

E'''_c = modulus of PSFC taken as $\frac{f_{cult} - f_{cy}}{\varepsilon_{cult} - \varepsilon_{cy}}$,

E_c^{IV} = modulus of PSFC taken as $\frac{-f_{cult}}{\varepsilon_{\max} - \varepsilon_{cult}}$,

These expressions are plotted along with the test data in Figs. 5.7 through 5.11 and the results compare favorably with the experimental data.

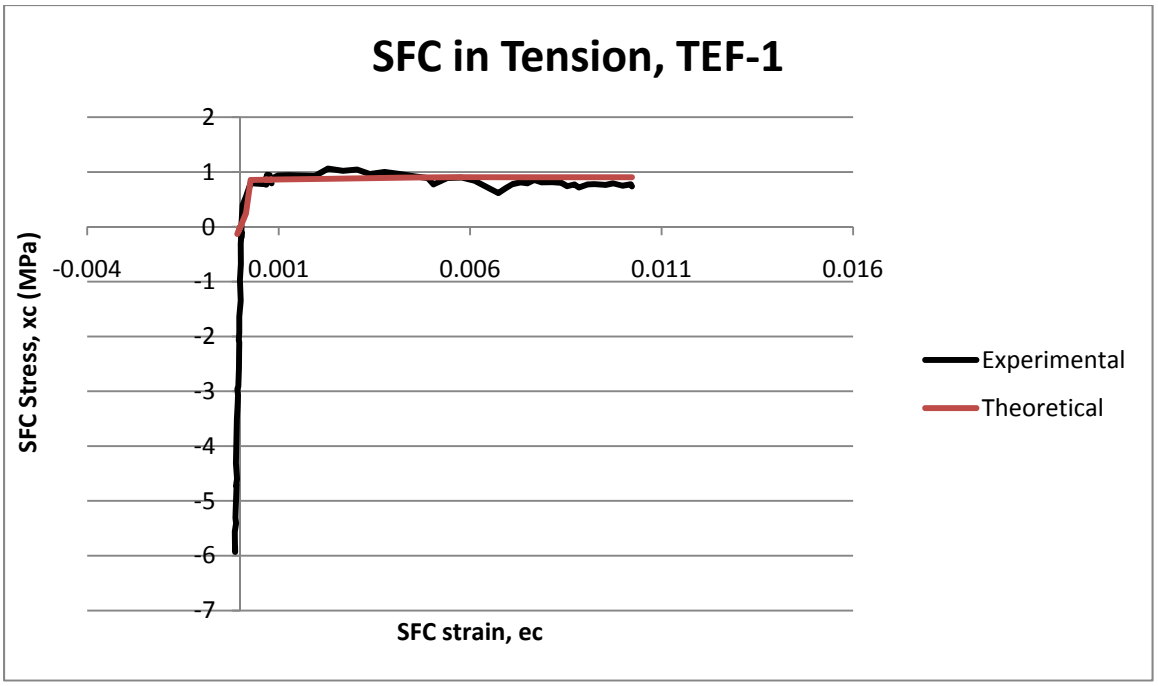

1 MPa =145 psi

Fig. 5.7 Experimental and Analytic Comparison for PSFC Panel TEF-1

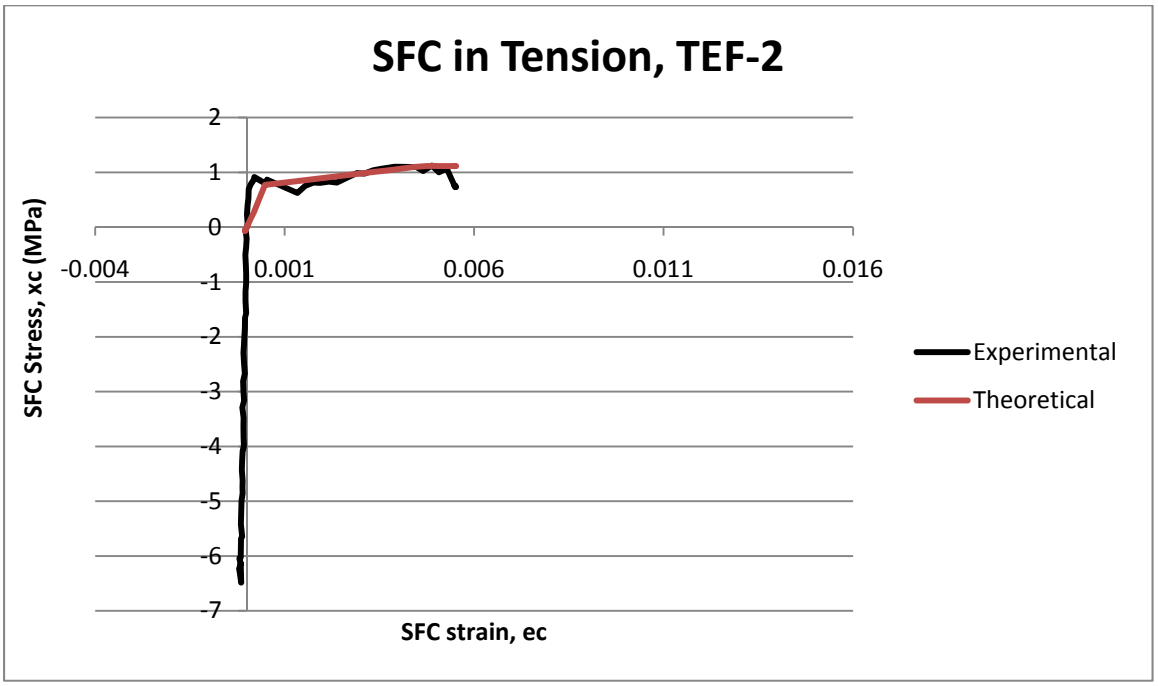

1 MPa =145 psi

Fig. 5.8 Experimental and Analytic Comparison for PSFC Panel TEF-2

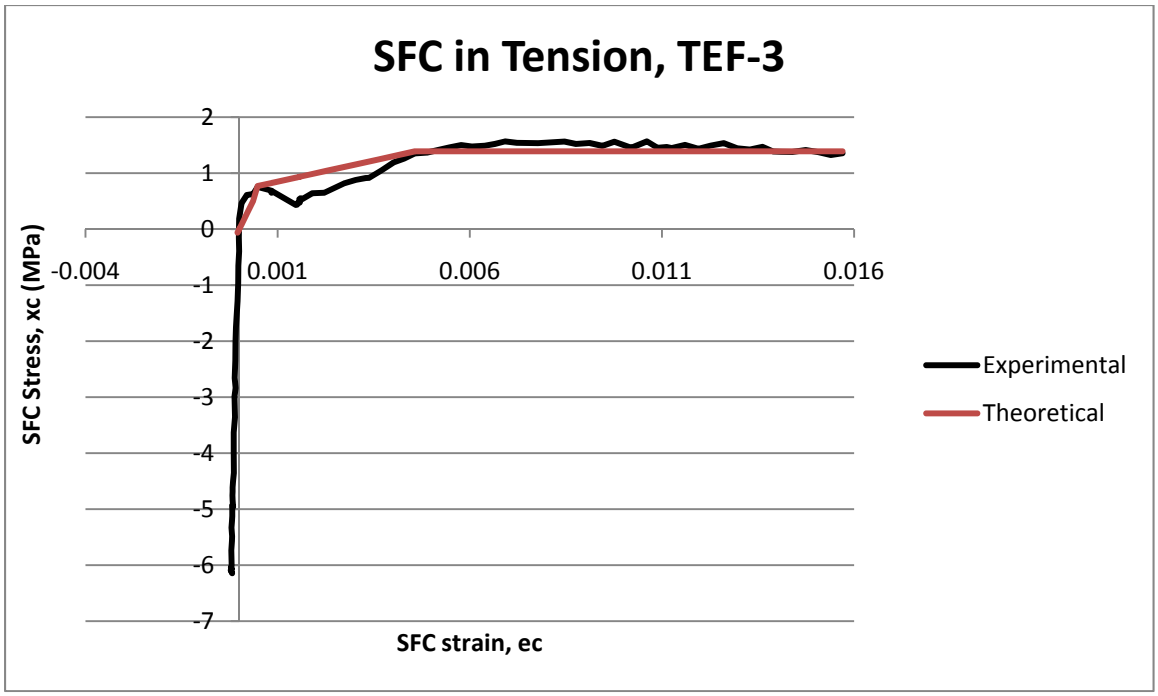

1 MPa =145 psi

Fig. 5.9 Experimental and Analytic Comparison for PSFC Panel TEF-3

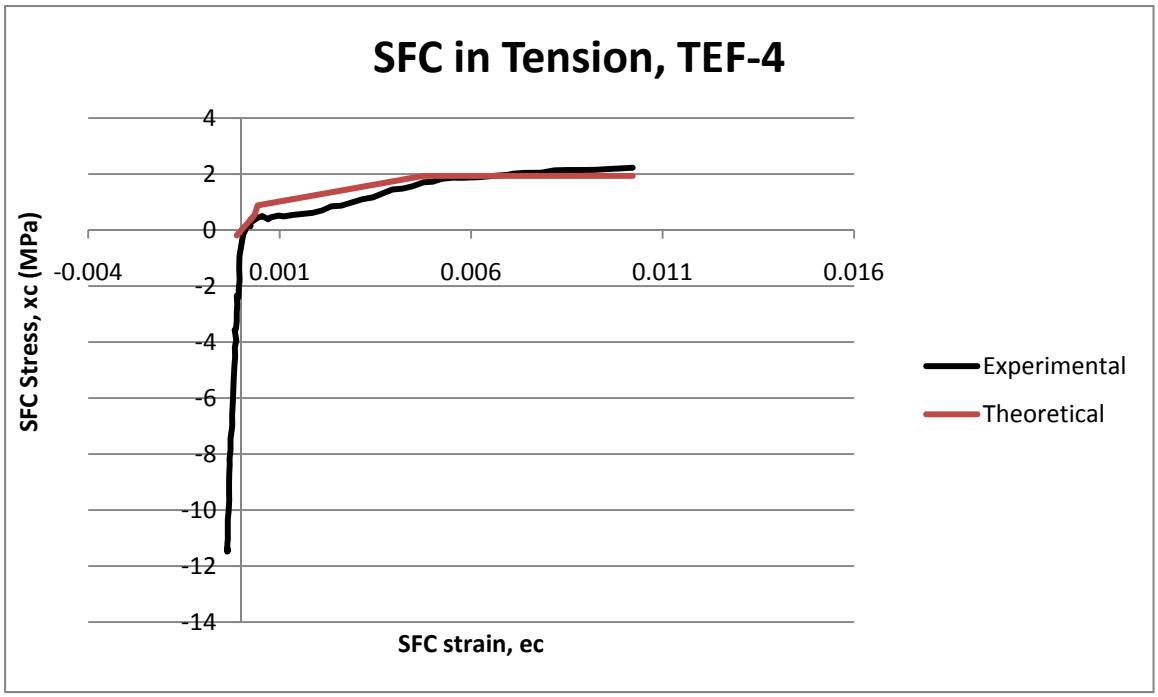

1 MPa =145 psi

Fig. 5.10 Experimental and Analytic Comparison for PSFC Panel TEF-4

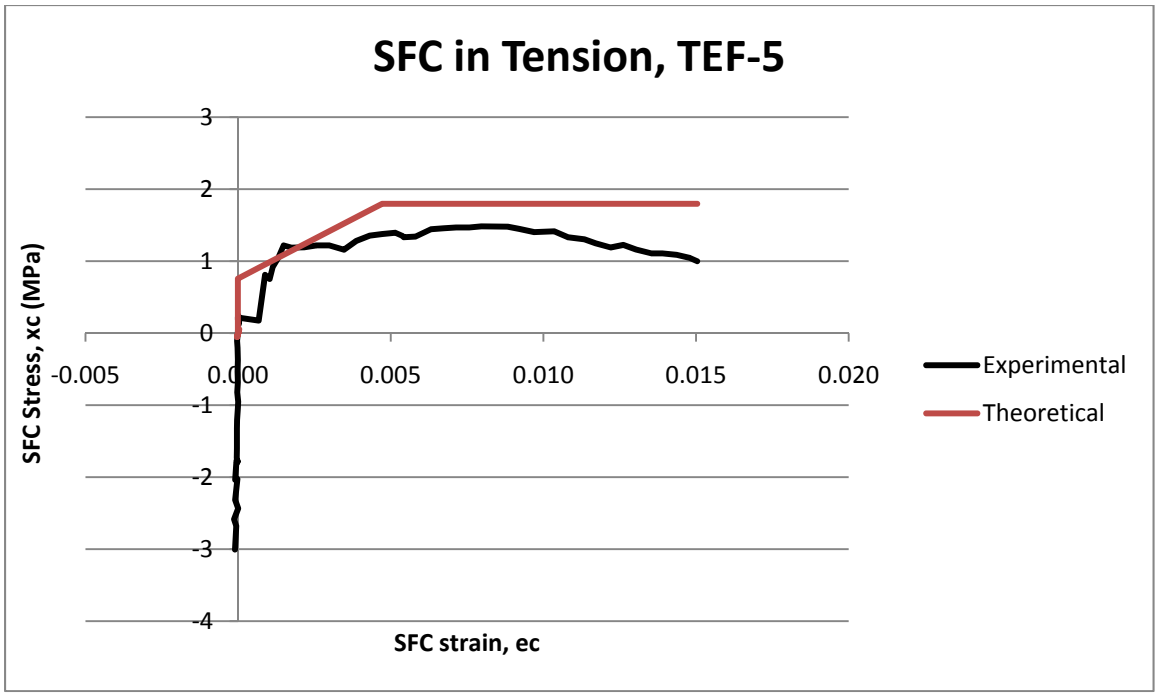

1 MPa =145 psi

Fig. 5.11 Experimental and Analytic Comparison for PSFC Panel TEF-5

5.3.3 Experimental Methods for Determining the Tensile Stress-Strain Curve for PSFC.

Experimental methods for determining the descending tensile branch of concrete include:

- Direct tensile loading of Dog-bone Specimens
- Direct tensile loading of prismatic specimens reinforced with a single rebar or tendon

The PSFC tensile stress-strain curves derived from these tests differ in several respects with the ones derived from the above methods.

5.4 Compressive Stress-Strain Relationship in PSFC Panels

The applied compressive stress-strain relationships of the panels in Group-TEF are given in Fig. 5.12 and 5.13. In these figures, the applied compressive stresses, σ_2, in the vertical axis, have been normalized with respect to the square root of the specimen cylinder compressive strength, $\sqrt{f'_C}$. This was done to facilitate interpretation of the graphs. Softening is a function of $\sqrt{f'_C}$. These plots are provided for information purposes regarding the applied loading.

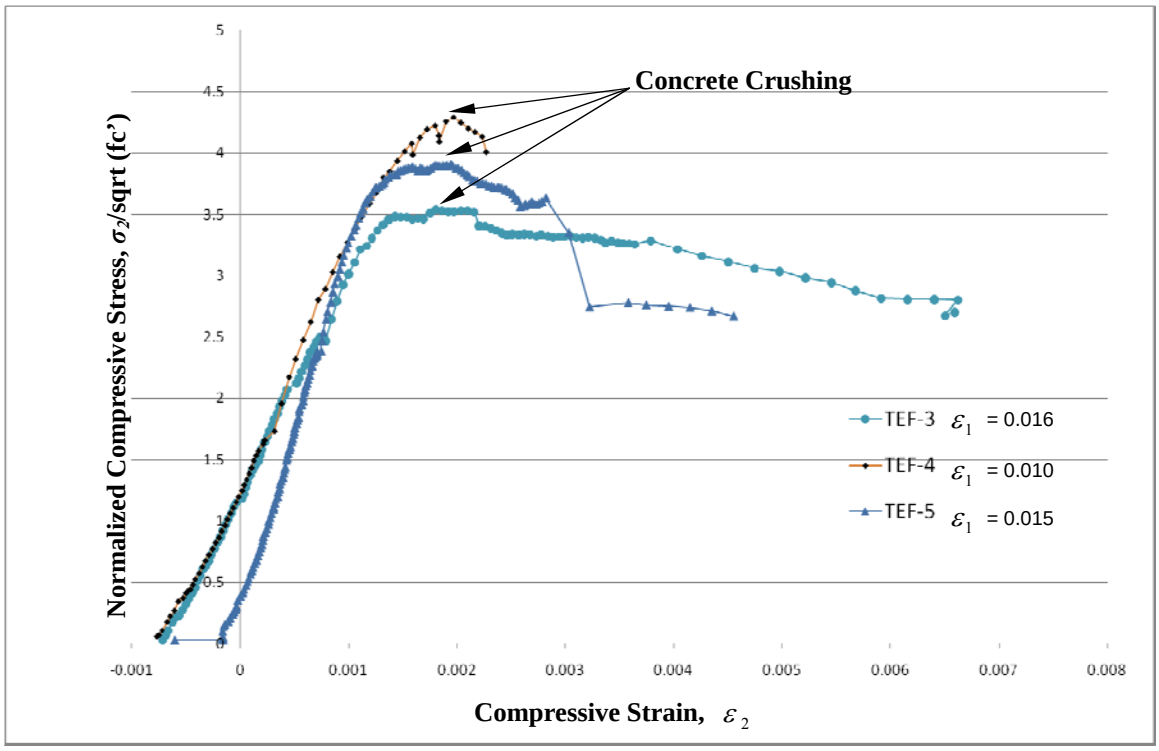

Fig. 5.12 Applied $\sigma_2 - \varepsilon_2$ Relationships in PSFC Panels TEF-4, 3, and 5

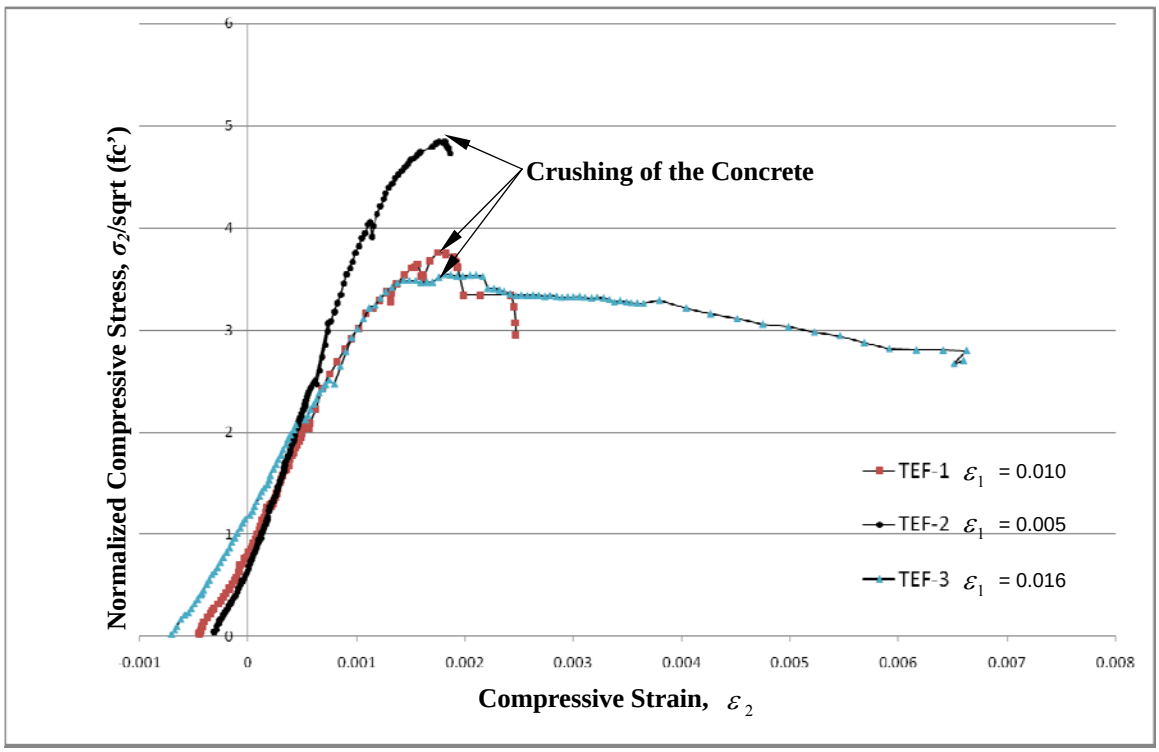

Fig. 5.13 Applied $\sigma_2 - \varepsilon_2$ Relationships in PSFC Panels TEF-1, 2, and 3

Generally, panels with lower tensile strain had the higher crushing strength; however the effect of fiber still needs to be extracted.

5.5 Smeared-(Average) Stress-Strain Relationships of PSFC in Compression

The experimental smeared (average) stress-strain curves of the PSFC in compression are shown in Fig. 5.14 and 5.15. In these figures, the PSFC compressive stresses, σ_c, in the vertical axis, have been normalized with respect to the square root of the specimen cylinder compressive strength, $\sqrt{f'c}$. This was done to facilitate interpretation of the graphs. Softening transitions to a function of $\sqrt{f'c}$ as $f'c$ approaches 6 ksi, which was the target concrete strength level.

To obtain the compressive stress-strain relationship of the PSFC, the mild steel stresses are subtracted from the applied stresses in Fig. 5.14 and Fig. 5.15, while the strains remain the same. The stress-strain relationship of mild steel bars in compression is the same as that of a bare steel bar. That is, the stress is proportional to the strain with the slope of E_s until yielding and becomes a constant of 60.20 ksi after yielding.

Based on experiments by Wang (2006), for prestressed concrete (no steel fiber), a parabolic equation was developed for the compressive stress-strain curve of prestressed concrete:

$$\sigma_c = \zeta_\sigma f_c' \left[2\left(\frac{\varepsilon_c}{\zeta_\varepsilon \varepsilon_0}\right) - \left(\frac{\varepsilon_c}{\zeta_\varepsilon \varepsilon_0}\right)^2 \right], \qquad \frac{\varepsilon_c}{\zeta_\varepsilon \varepsilon_0} \le 1, \tag{5-14a}$$

or

$$\sigma_c = \zeta_\sigma f_c' \left[1 - \left(\frac{\varepsilon_c/\zeta_\varepsilon \varepsilon_0 - 1}{4/\zeta_\varepsilon - 1} \right)^2 \right], \quad \frac{\varepsilon_c}{\zeta_\varepsilon \varepsilon_0} > 1, \tag{5-14b}$$

where

ε_0 = concrete cylinder strain corresponding to cylinder strength, f_c', and

ζ_σ, ζ_ε = stress and strain softening coefficients, respectively.

and

$$\zeta_\sigma = f(F) f(f_c') f(\bar{\varepsilon}_1) f(\beta) W_p \le 0.9, \tag{5-15}$$

$$f(f_c') = \frac{5.8}{\sqrt{f_c'}} \le 0.9 \quad (f_c' \text{ in MPa}), \tag{5-16}$$

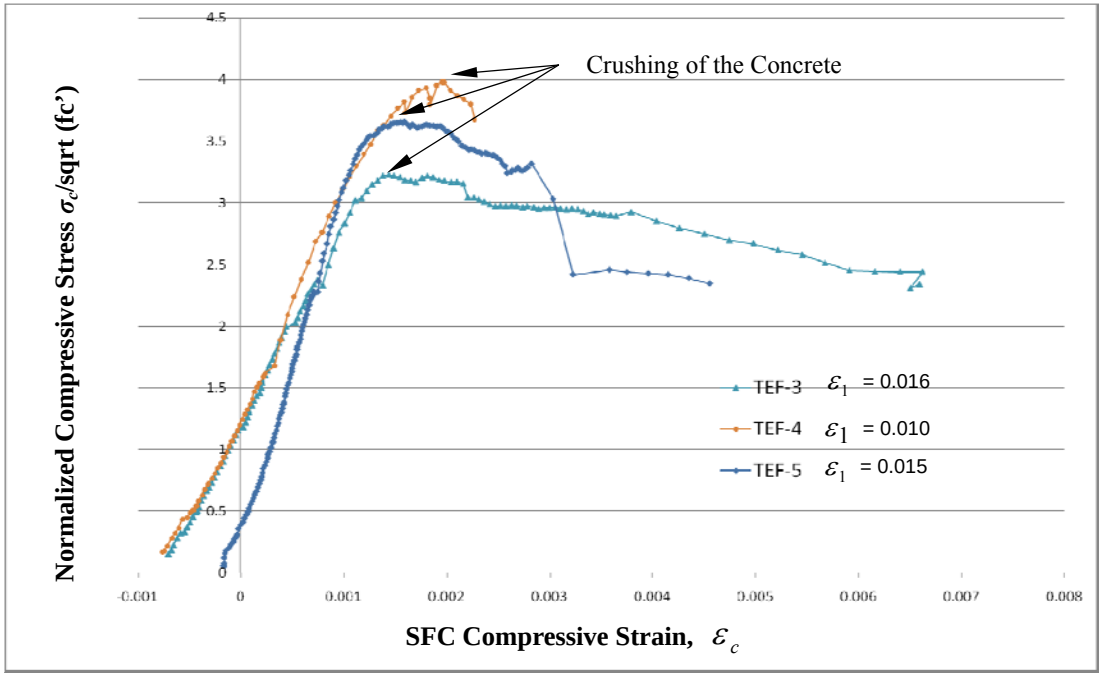

Fig. 5.14 Smeared Stress-Strain Relationships of PSFC Panels TEF-3, 4, and 5 in Compression

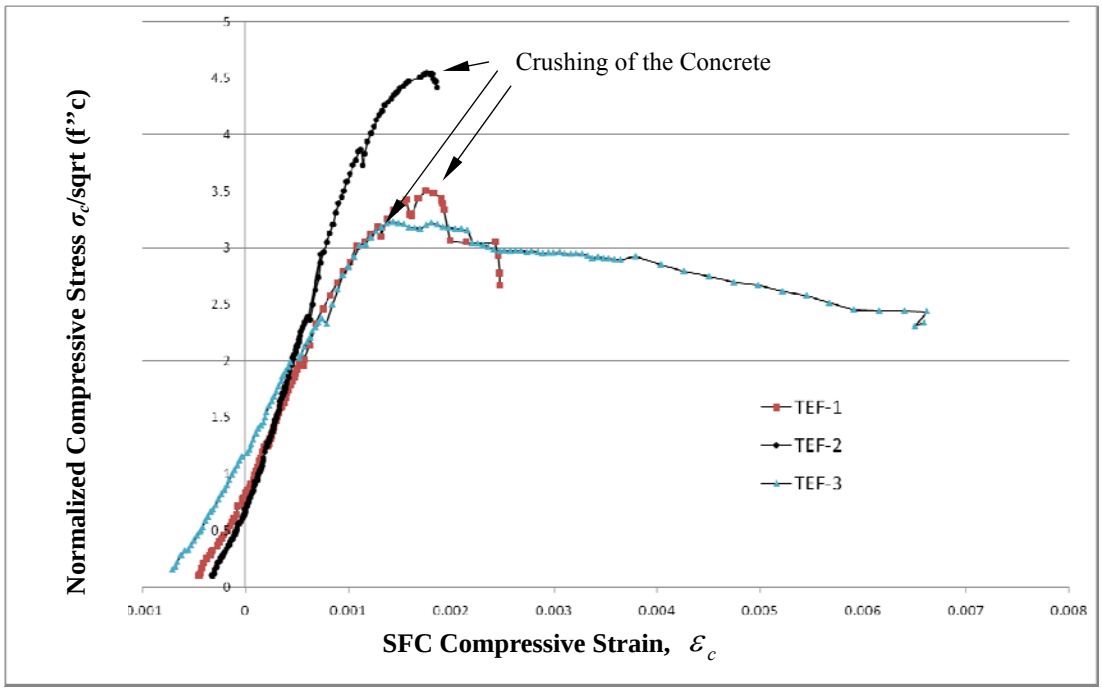

Fig. 5.15 Smeared Stress-Strain Relationships of PSFC Panels TEF-1, 2, and 3 in Compression

$$f(\bar{\varepsilon}_1) = \frac{1}{\sqrt{1+250\bar{\varepsilon}_1}}, \tag{5-17}$$

$$f(\beta) = 1 \quad \text{because} \quad \beta = 0, \tag{5-18}$$

and
$$W_p = 1.15. \tag{5-19}$$

Based on the experimental research conducted by Belarbi and Hsu (1994 and 1995), the strain softening coefficient ζ_ε for 90° panels under sequential loading is equal to unity. The same phenomenon was also observed for prestressed concrete panels (Wang, 2006). The discussion in this section, however, focuses on the stress softening coefficient, ζ_σ.

The stress softening coefficient ζ_σ is defined as the ratio of the peak compressive concrete stress σ_p of the panel to the companion cylinder strength f_c' as follows

$$\zeta_\sigma = \frac{\sigma_p}{f_c'}. \tag{5-20}$$

Based on the above equation, the experimental softening coefficients ζ_σ of the panels are calculated and listed in Table 5.5 for Group-TEF and for Group TE (Wang, 2006). Table 5.6 shows the relationship between softening coefficient and fiber-factor. The calculated softening coefficient is shown in column [7] and the experimental softening coefficient is shown in column [8]. The calculated softening coefficient is the ratio of experimental softening coefficient to the calculated softening coefficient, as shown in the last column of the table; to show the effect of fiber addition. This ratio is plotted in Fig. 5.16 with respect to fiber-factor. With no fiber, the average ratio of experimental to calculated softening is 1.0, as shown by Wang (2006). As can be seen from this plot, the ratio increased as fiber-factor increased. The TEF data shows a consistent increasing trend which can be expressed as follows:

$$\frac{\zeta_{\sigma,\exp}}{\zeta_{\sigma,calc.}} = W_f = 1 + 0.2FF \quad , \tag{5-21}$$

where, FF = fiber-factor.

Table 5.3 – Experimental Softening Coefficients for PC and PSFC Panels

Panel No.	$\rho_{\ell p}$	$\bar{\varepsilon}_1$	f'_c **(MPa)**	σ_p **(MPa)**	ζ_σ **(exp.)**
[1]	[2]	[3]	[4]	[5]	[6]=[5]/[4]
TEF-1	0.59%	1.0%	50.6	24.92	**0.493**
TEF-2	0.59%	0.5%	37.1	27.70	**0.747**
TEF-3	0.59%	1.6%	33.8	18.80	**0.556**
TEF-4	1.18%	1.0%	41.9	25.76	**0.615**
TEF-5	0.30%	1.5%	40.1	23.15	**0.577**
TE-4	0.59%	1.5%	38.69	18.65	0.482
TE-3	0.59%	1.9%	32.52	15.98	0.492
TE-5	0.59%	2.9%	34.76	13.55	0.390
TE-6	0.295%	2.0%	36.81	21.42	0.582
TE-7	1.18%	2.1%	42.39	15.13	0.357

1 MPa =145 psi

Table 5.4 - Softening Coefficient as a Function of Fiber-Factor in PC and PSFC Panels

Panel No.	f'c (MPa)	$\bar{\varepsilon}_1$	F	$\frac{5.8}{\sqrt{f'_c}}$	$\frac{1.15}{\sqrt{1+250\bar{\varepsilon}_1}}$	ζ_σ (calc.)	ζ_σ (exp.)	$\zeta_{\sigma(\exp)}/\zeta_{\sigma(\text{calc})}$
[1]	[2]	[3]	[4]	[5]	[6]	[7]=[5][6]	[8]	[8]/[7]
TEF-1	50.6	1.0%	0.28	0.82	0.615	0.501	0.493	0.98
TEF-2	37.1	0.5%	0.55	0.95	0.767	0.690	0.747	1.08
TEF-3	33.8	1.6%	0.83	1.0	0.514	0.463	0.556	1.20
TEF-4	41.9	1.0%	0.8	0.9	0.615	0.551	0.615	1.12
TEF-5	40.1	1.5%	1.2	0.92	0.528	0.475	0.577	1.22
TE-4	18.7	1.5%	0	0.9	0.533	0.480	0.482	1.00
TE-3	15.9	1.9%	0	0.9	0.475	0.428	0.492	1.15
TE-5	13.6	2.9%	0	0.9	0.435	0.392	0.390	1.00
TE-7	15.1	2.1%	0	0.89	0.465	0.414	0.357	0.86

1 MPa =145 psi

Panels TEF-4 and -5 used long aspect fibers, whereas TEF-1, -2, and -3 used short aspect fibers. Wang's results show some scatter which is attributable to the higher tensile strain levels used. Higher tensile strain means greater cracking and thus introduces the possibility of more scatter when testing the cracked panel in compression. The TEF panels were tested in compression at tensile strain levels roughly half of Wang's. Lower target tensile strain levels

were necessary to prevent premature tendon failure due to the increased post-cracking stiffness of PSFC.

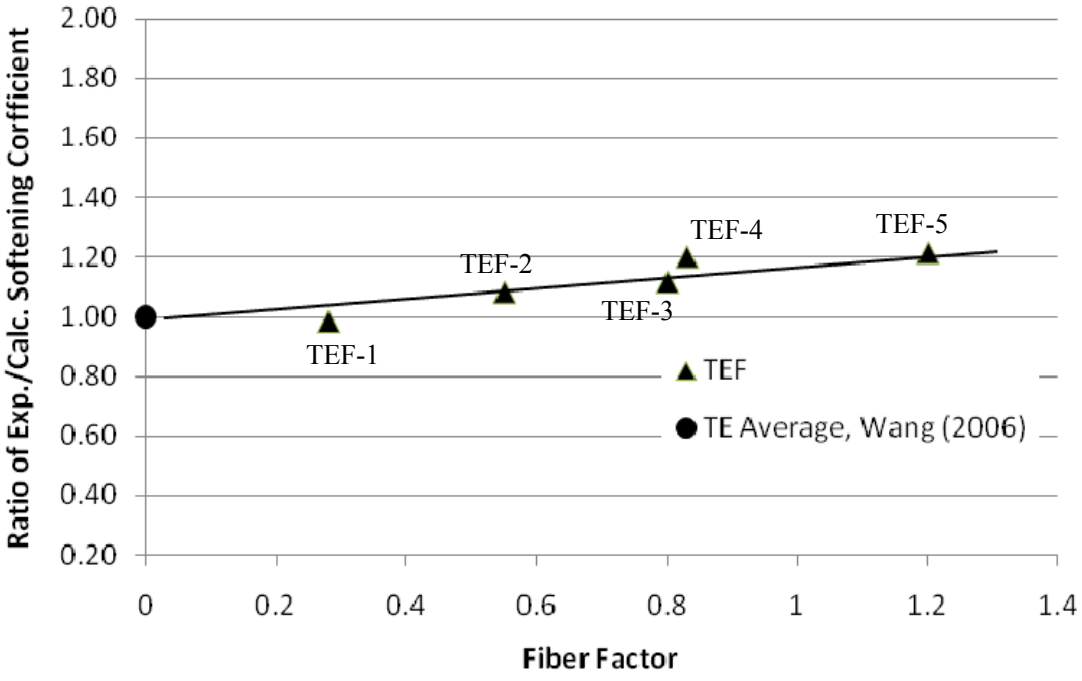

Fig. 5.16 Effect of Fiber-Factor on Softening Coefficient in PSFC and PC Panels

An attempt was made to analytically quantify the descending branch of the PSFC in compression curve. However, the results exhibit inconsistent post-peak ductility that it is difficult to make a reasonable interpretation. The final mode of failure for panel TEF-2, was sudden and was accompanied by an uncharacteristically loud bang which rocked the panel testing machine's steel frame. The sudden failure can be attributed to the very low tensile strain target of only 0.5%. Panels TEF-1, -3, -4, and -5, with tensile strain targets of at least 1%, exhibited a slow post peak crushing and spalling failure. Otherwise, there does not appear to be any relationship between post-peak ductility and either fiber-factor or tensile strain level. Due to this, the descending branch analytic model used by Wang (2006) for prestressed concrete will be utilized for PSFC (Eq. 5.13b). The only difference being that the peak will reflect the PSFC softening expression. A plot of the descending branches only is shown in Fig. 5.17.

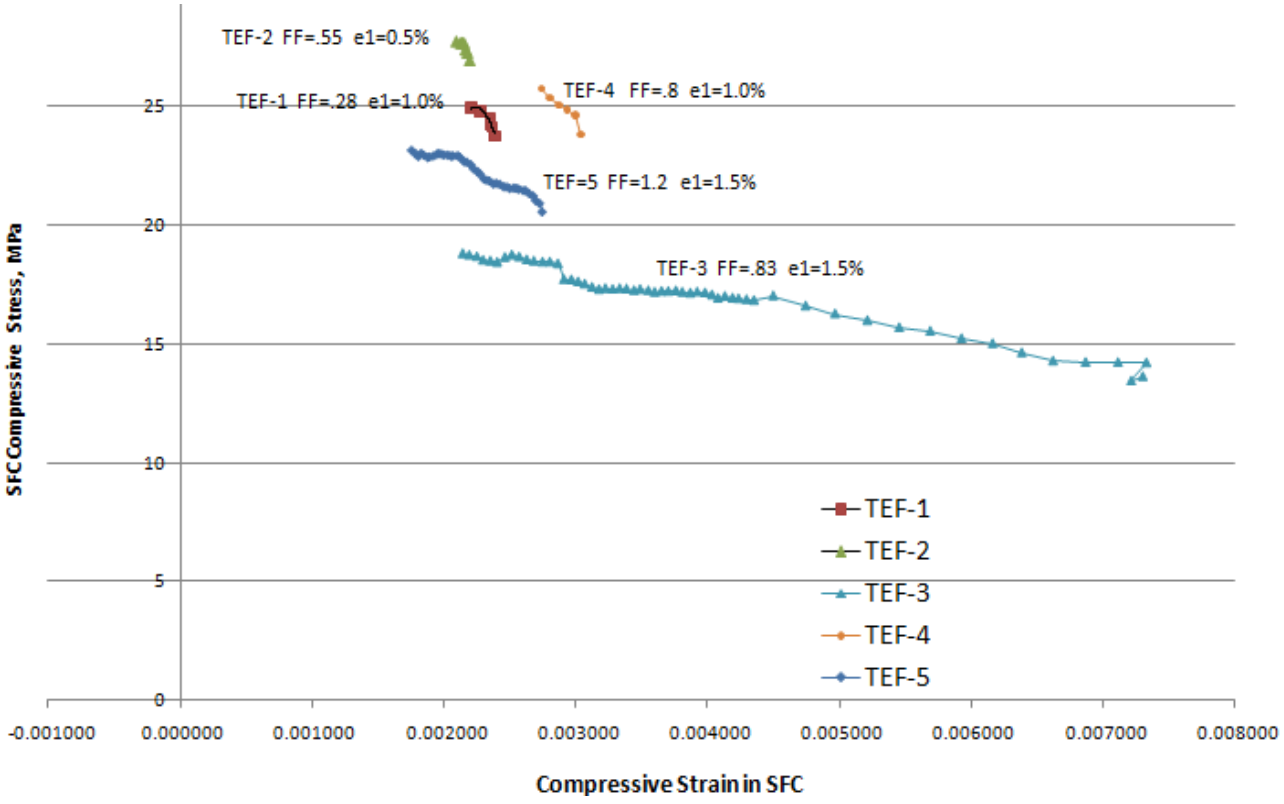

Fig. 5.17 Compressive Stress-Strain Curves (Descending Branches) of PSFC Panels

5.6 Tensile Behavior of Embedded Tendon

The characteristics of the bare steel tendon were determined from the results of direct tensile tests from three bare bar tendon specimens. The tendon can be characterized as low relaxation strand. From the test data, a complete empirical curve (power formula) can be fit to the data using the technique of Tadros (1992) by defining curve parameters A, B, C, and D in (Eq. 5-22).

$$f_{ps} = \varepsilon_{ps}\left[A + \frac{B}{\left\{1+\left(C\varepsilon_{ps}\right)^{D}\right\}^{1/D}}\right] \le 270ksi \qquad \text{(Eq. 5-22)}$$

This is done in Table 5.5, the average parameters of the three curves are used to define the bare steel curve. The same technique is used in Table 5.6 to determine the curve fit parameters for the Embedded Tendon. The results for the bare tendon curves are plotted in Fig. 5.18. In this research, the elastic limit of prestressing tendons embedded in concrete is approximately 70% of

the ultimate strength f_{pu}, which is lower than that of bare prestressing strands. Therefore, the stress-strain relationship of prestressing tendons prior to $0.7f_{pu}$ is given by;

$$f_{ps} = E_{ps}\bar{\varepsilon}_s, \quad \bar{\varepsilon}_s < \frac{0.7f_{pu}}{E_{ps}}, \tag{5-23}$$

where,

E_{ps} = elastic modulus of prestressing tendons taken as 29,000 ksi, and

f_{pu} = ultimate strength of prestressing tendons taken as 270 ksi.

After the cracking of the concrete, the experimental stress and strain of prestressing tendons can be obtained by the following derivation;

The total load is given as

$$P = A_c\sigma_c + A_{ps}f_{ps}. \tag{Eq. 5.24}$$

The smeared (average) stress of concrete σ_c can be obtained from Eq. (5-13c). Substituting Eqs. (5-13b), (5-13c), or (5-13d) into Eq. (5-4), rearranging the terms, and then using Eq. (5-7), the stress of prestressing tendons is given as;

$$f_{ps} = \frac{P}{A_{ps}} - \frac{f_c}{\rho_{lp}} \tag{5-25}$$

The strain in the tendons is,

$$\bar{\varepsilon}_s = \bar{\varepsilon}_{pi} + \varepsilon_1. \tag{5-26}$$

The fitted average bare tendon curves, experimental embedded tendon curves, and theoretical embedded tendon curves are plotted in Figs. 5.19 through 5.23. Also plotted is the curve for embedded tendon in concrete without steel fiber from Wang (2006). As can be seen in the figures, there is no substantial difference between the Wang (2006) embedded tendon curves and the empirical embedded curves from this research. Therefore, for simplicity, Wang's expressions will be used.

$$f_{ps} = \frac{E''_{ps}\bar{\varepsilon}_s}{\left[1+\left(\frac{E''_{ps}\bar{\varepsilon}_s}{f'_{pu}}\right)^5\right]^{\frac{1}{5}}}, \quad \bar{\varepsilon}_s \geq \frac{0.7f_{pu}}{E_{ps}}, \tag{5-27}$$

where

E''_{ps} = modulus of prestressing tendons taken as 30,345 ksi, and

f'_{pu} = revised strength of prestressing tendons taken as 260 ksi

Table 5.5 – Tensile Stress-Strain Curve Parameters for Bare Tendon

Load Deformation Curve Parameter	Tendon T1	Tendon T2	Tendon T3	Avg.
Pult (kips)	55.9	59.8	58.7	
fpu (ksi)	257.6	275.6	270.6	**273**
Pult (kN)	249	266	261	
Max. %e	0.016019	0.043432	0.043432	
Yield @ 1% Elongation (kips)	54.6	54.3	54.1	
fpy (ksi)	251.6	250.3	249.5	
Yield @ 1% Elongation (kN)	243	242	241	
fpy (MPa)	1734	1725	1719	
f,,/f,,	-	0.91	0.92	
ACI Eq. 18-3, gamma p	-	0.28	0.28	
P.L. (kips)	47	47	47	
P.L. (kN)	209	209	209	
fp p.l/fpu	0.84	0.79	0.80	
e @ P.L.	0.007	0.007	0.007	
E (ksi) Determined Graphicaly at P.L.	29865	29865	29865	**29865**
E (kN)	132840	132840	132840	
fn (ksi) determined graphically or can use 1.04*fpy	253	253	253	
C = E/fn	118	118	118	**118**
A = Ep (ksi) Modulus in Plastic	557	633	489	**560**
B = E-Ep	29308	29232	29376	**29305**
D = n (m) determined by trial and	12	10.2	9.7	**10**

Table 5.6 – Tensile Stress-Strain Curve Parameters for Embedded Tendon from PSFC Panel TEF-1, -2, and -3 Tests

Load Deformation Curve Parameter	TEF-1	TEF-2	TEF-3
Pult (kips)	55.9	59.8	58.7
fpu (ksi)	257.6	275.6	270.6
Pult (kN)	249	266	250
Max. %e	0.016019	0.043432	0.043432
Yield @ 1% Elongation (kips)	54.6	54.3	55.1
fpy (ksi)	251.6	250.3	253.7
Yield @ 1% Elongation (kN)	243	242	245
fpy (MPa)	1734	1725	1748
f_{py}/f_{pu}	-	0.91	0.94
ACI Eq. 18-3, gamma p	-	0.28	0.28
P.L. (kips)	47	47	47
P.L. (kN)	209	209	209
fp p.l/fpu	0.84	0.79	0.80
e @ P.L.	0.007	0.007	0.007
E (ksi) Determined Graphicaly at P.L.	29865	29865	29865
E (kN)	132840	132840	132840
fn (ksi) determined graphically or can use 1.04*fpy	253	253	250
C = E/fn	118	118	119
A = Ep (ksi) Modulus in Plastic Range	557	633	1000
B = E-Ep	29308	29232	28865
D = n (m) determined by trial and error	12	10.2	9
Trial Check fpy (ksi)	251.5	250.3	248.7

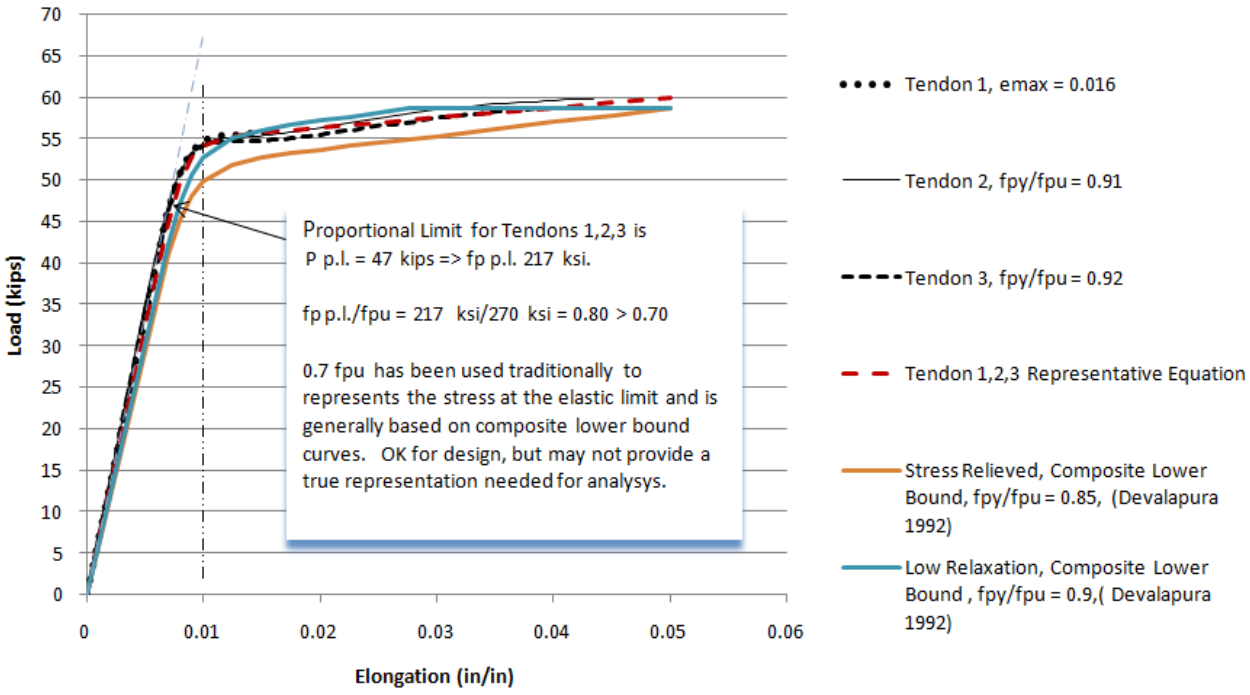

Fig. 5.18 Tensile Load vs. Elongation Curve for Bare Tendon

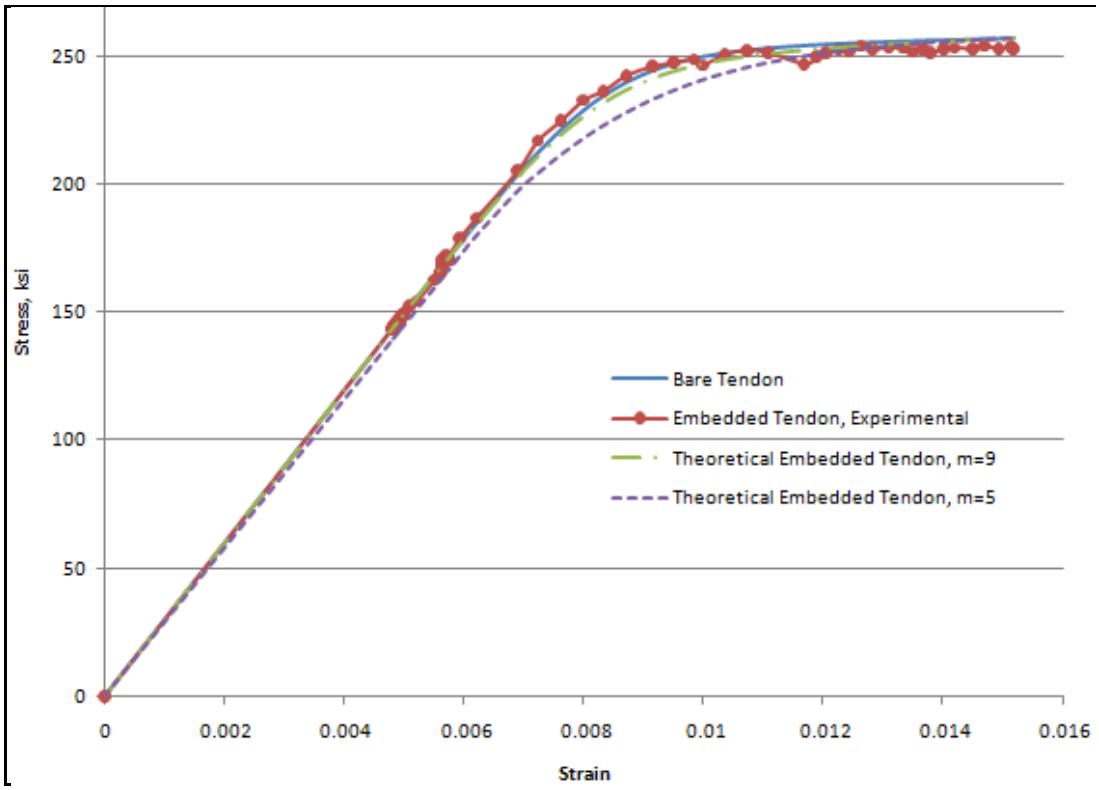

Fig. 5.19 Tendon Stress-Strain Curves in PSFC Panel TEF-1

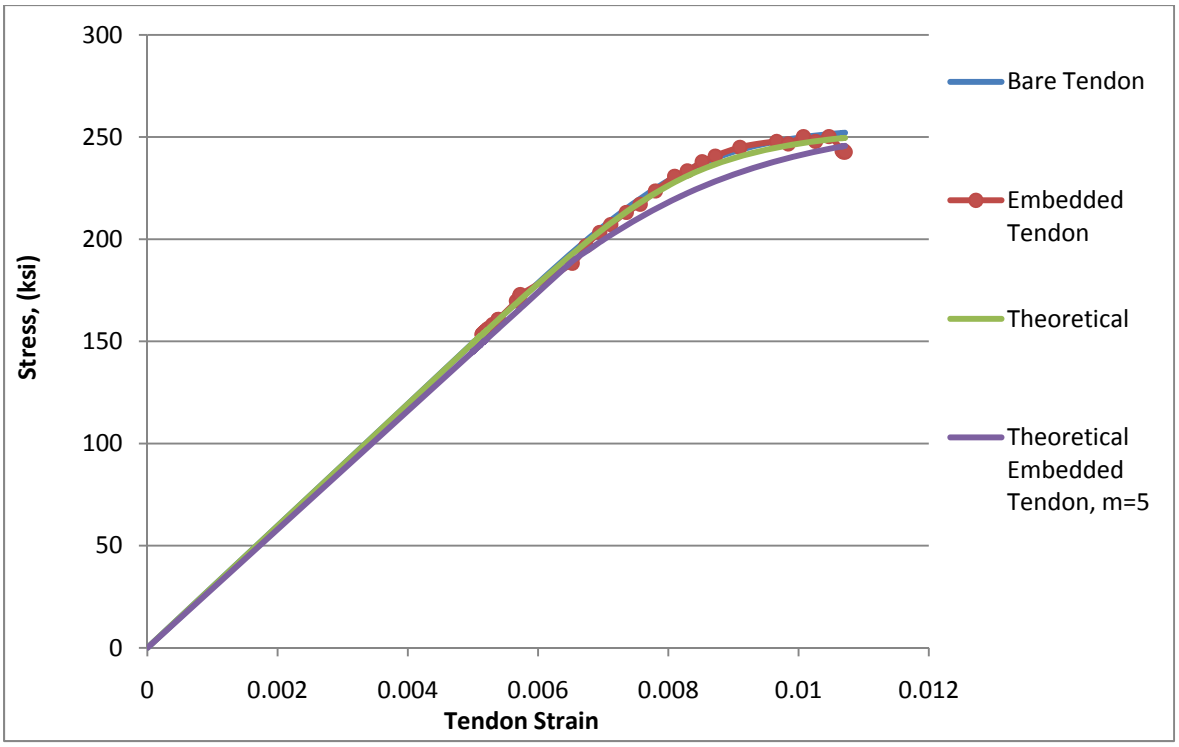

Fig. 5.20 Tendon Stress-Strain Curves in PSFC Panel TEF-2

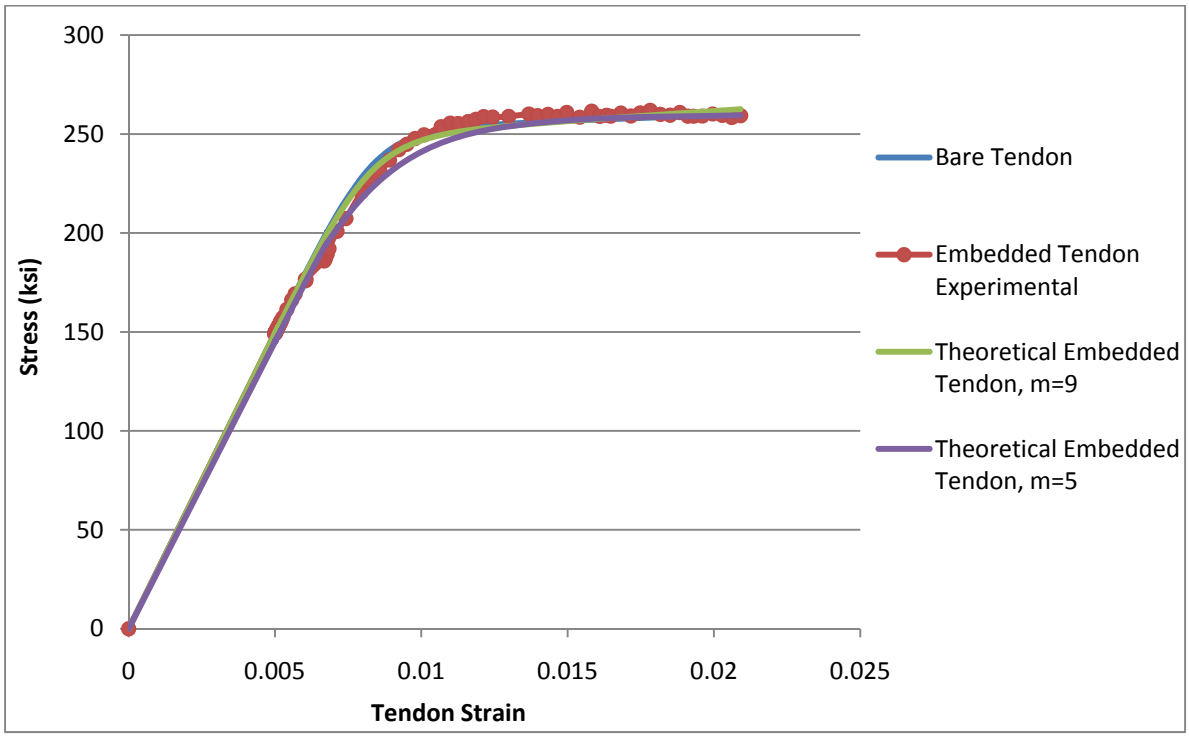

Fig. 5.21 Tendon Stress-Strain Curves in PSFC Panel TEF-3

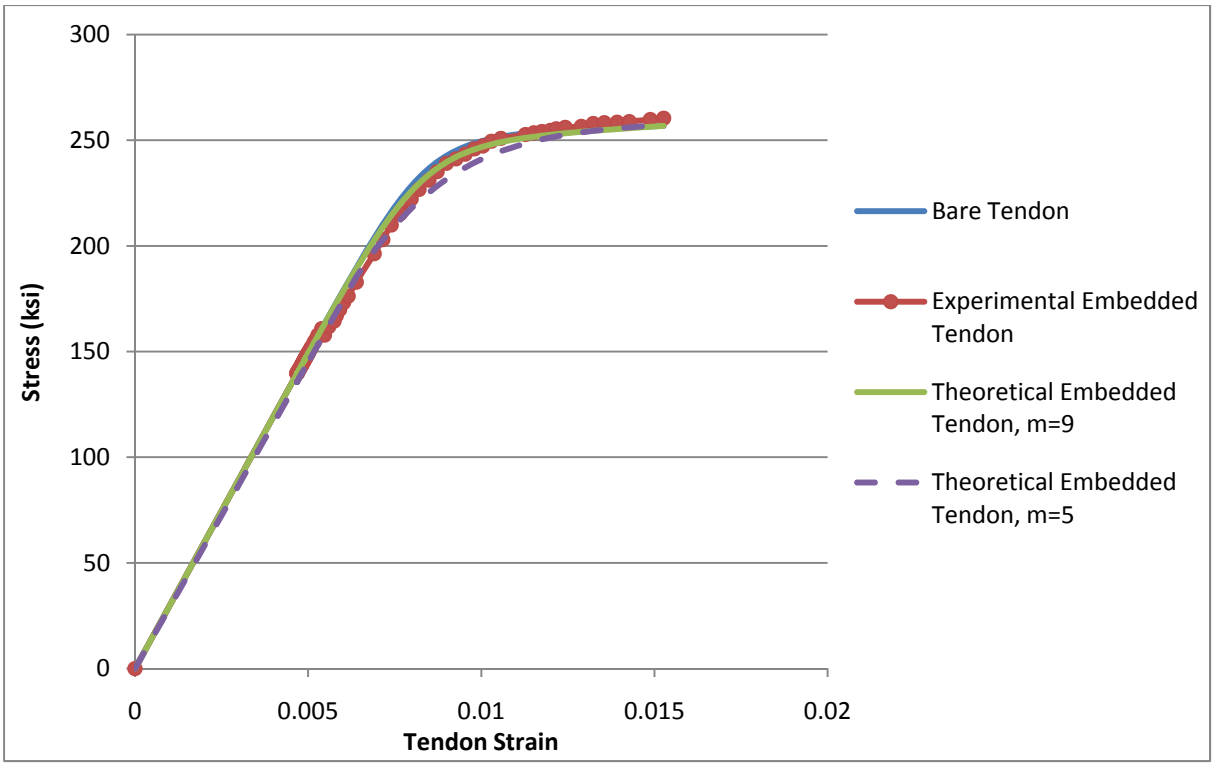

Fig. 5.22 Tendon Stress-Strain Curves in PSFC Panel TEF-4

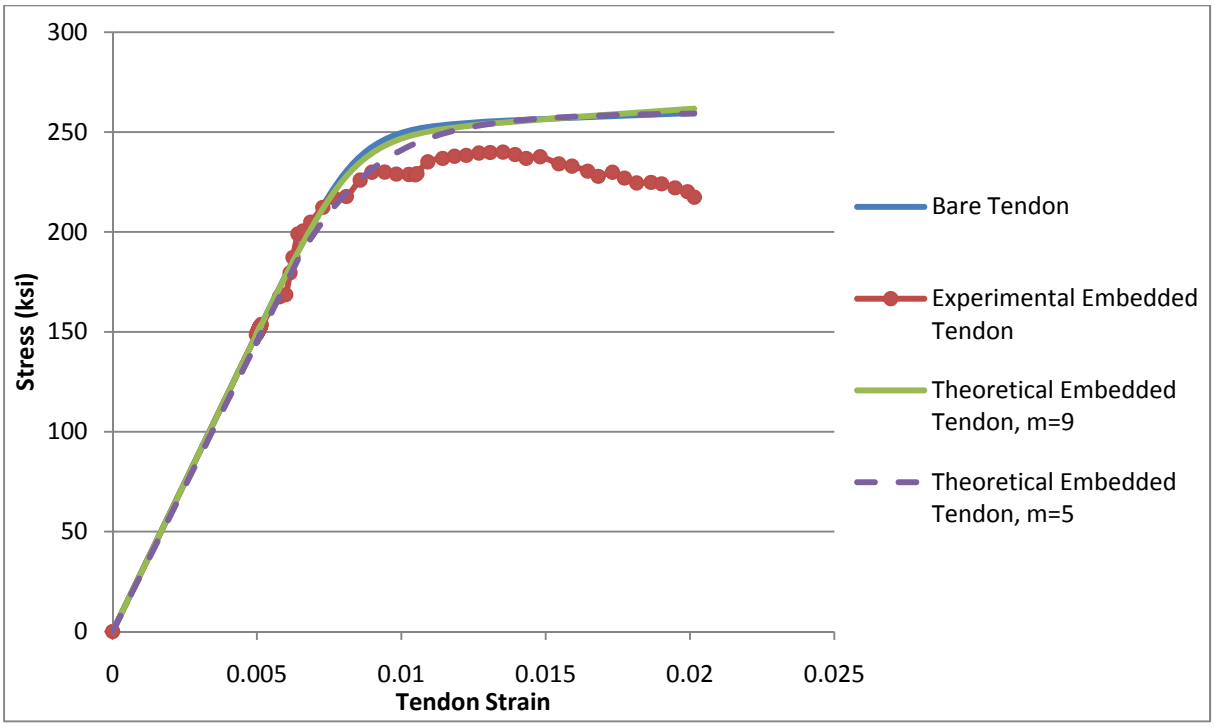

Fig. 5.23 Tendon Stress-Strain Curves in PSFC Panel TEF-5

5.7 Cracking Behavior of PSFC Panels (TEF Series)

In the first stage of tensile loading, all five panels were used to obtain the tensile constitutive laws of PSFC and prestressing tendons. In the second stage of compressive loading, the softening coefficients of prestressed PSFC were studied.

All panels exhibited relatively uniform cracking in the vertical direction under tensile loading. The number of cracks increased with the amount of prestressing steel in the longitudinal direction. This is consistent with Wang (2006) with no steel fibers. The greater the longitudinal steel ratio, the greater the number of cracks. Crack distribution was generally uniform, and primary cracking occurred within the LVDT-sensored area of the specimens. Photographs of representative crack patterns near the end of the tensile stage of loading are shown in Fig. 5.24 through Fig. 5.28 for each TEF specimen. The presence of steel fibers stiffened the response of the panels after initial cracking and before yielding of the steel (refer to Fig. 5.1 and 5.2). The effect of this stiffening was that the tendons in several trial panels failed before reaching target tensile strain levels. The steel fibers tended to hold the cracked concrete together such that it allowed a dominant crack to open. Tensile strain accumulated at this crack and, in the case of panel TEF-5, the tendon failed at this type of dominant crack.

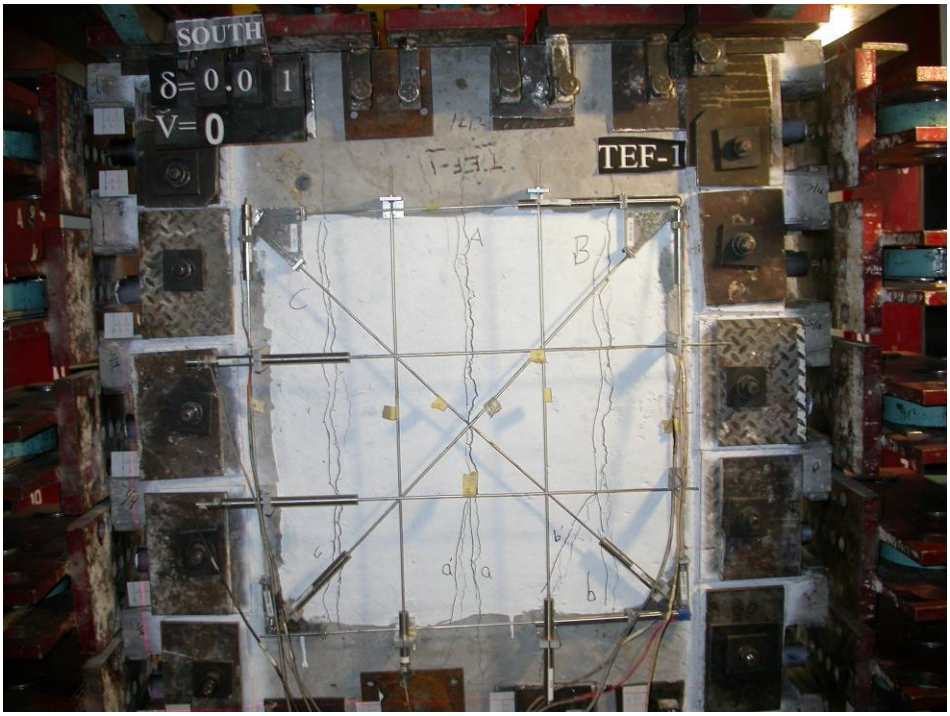

Fig. 5.24 Crack Pattern in PSFC Panel TEF-1

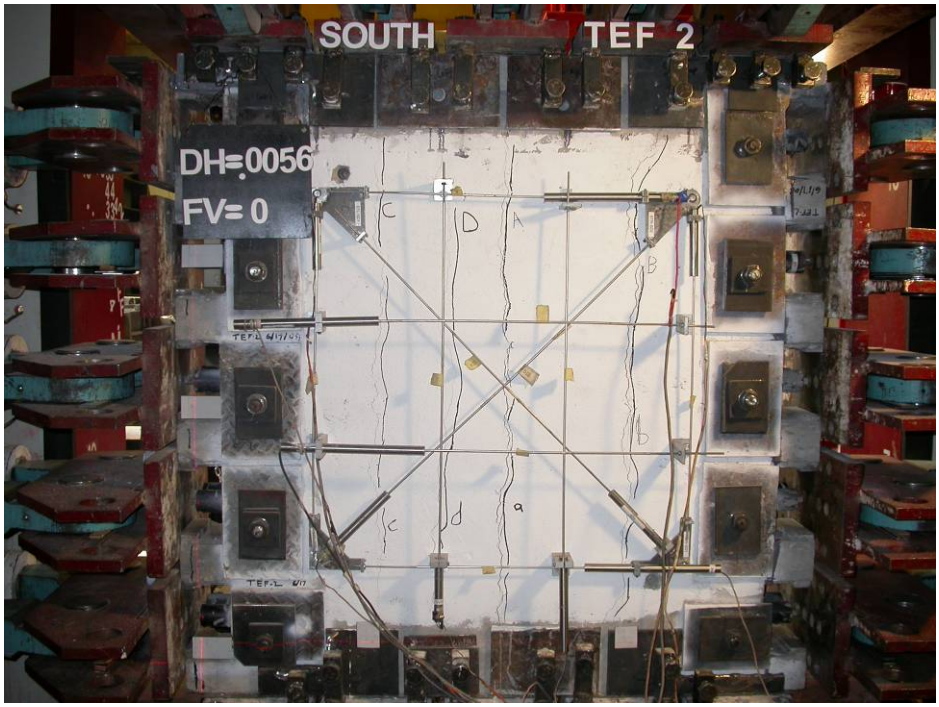

Fig. 5.25 Crack Pattern in PSFC Panel TEF-2

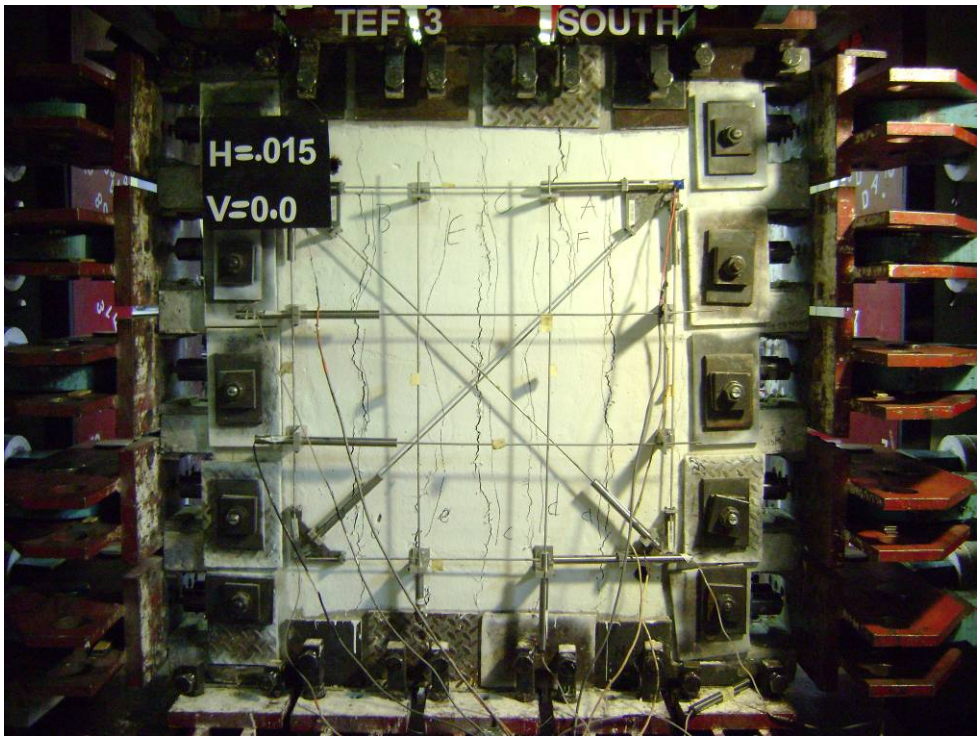

Fig. 5.26 Crack Pattern in PSFC Panel TEF-3

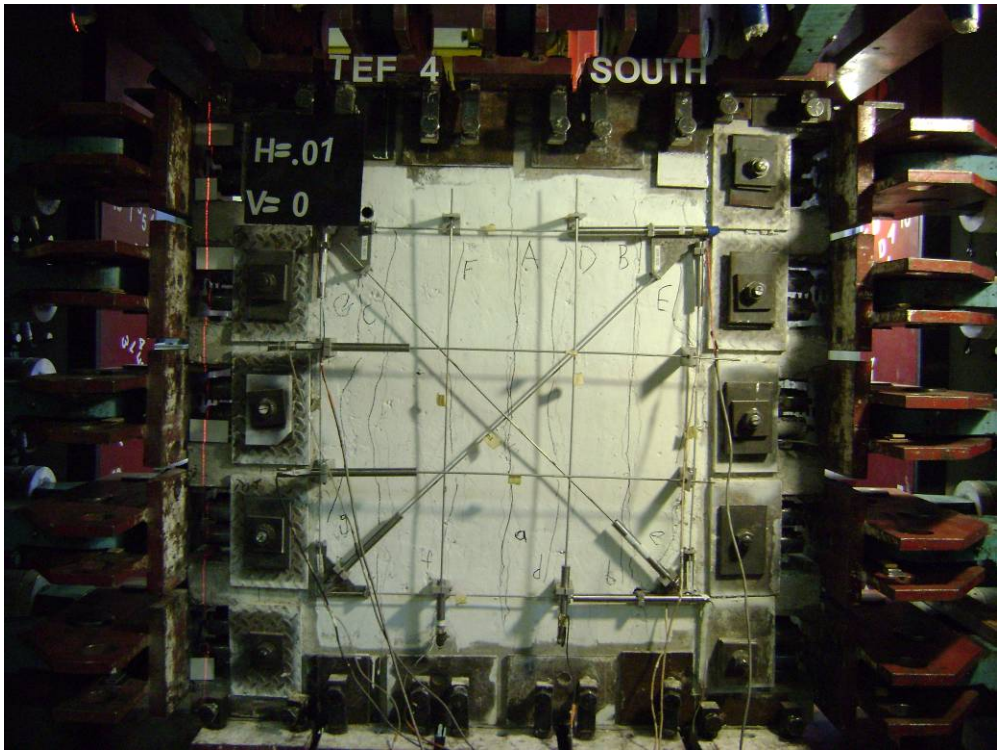

Fig. 5.27 Crack Pattern in PSFC Panel TEF-4

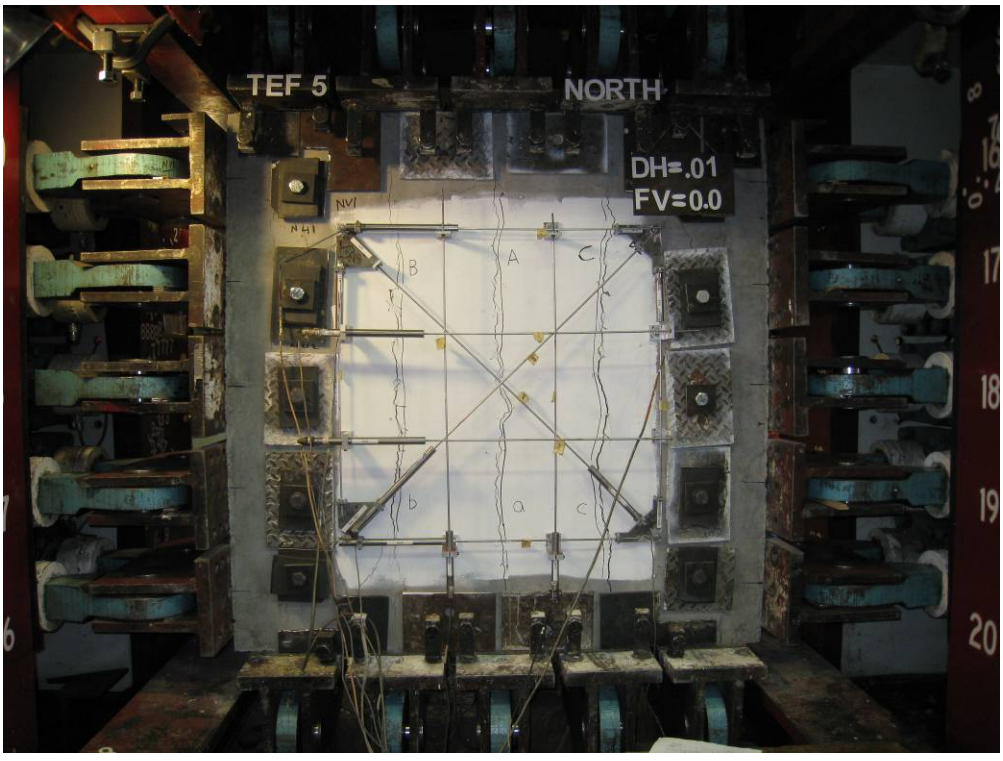

Fig. 5.28 Crack Pattern in PSFC Panel TEF-5

CHAPTER 6

EXPERIMENTAL PROGRAM OF PSFC PANELS: GROUP-TAF

6.1 General Description of Group-TAF Specimens

Five Prestressed Steel Fiber Concrete (PSFC) panels with steel oriented at 45 to the horizontal, were tested in pure shear under proportional loading. To ensure a state of pure shear stresses, equal magnitudes of principal tensile stress σ_1 and principal compressive stress σ_2 were applied on the four edges of each panel throughout the loading history. This loading scheme is referred to as proportional loading. During the test, load-control procedure was used before yielding and strain-control procedure after yielding. In the strain-control mode, the horizontal strain ε_1 was used to control the horizontal tensile stress σ_1 as well as the vertical compressive stress σ_2, using a servo-control system.

The objective of this research was to study the effect of steel fibers on the shear behavior of PSFC membrane elements. To achieve the goal, the panels were designed to have various properties based on three primary variables: (1) percentage of steel fibers by volume, V_f, (2) aspect ratio of steel fibers, ℓ_f/d_f, and (3) longitudinal prestressing steel ratio, $\rho_{\ell p}$. The specimens were designed to simplify comparison with the panels tested by Wang (2006). The primary difference between Group-TAF and Wang's (2006) Group-TA panels is the presence of Dramix steel fiber. Details of the TAF series of panels is shown in Table 6.1.

6.2 Cracking Behavior of PSFC Panels (TAF Series)

The test panels in this research were subjected to principal tensile stress in the horizontal direction and principal compressive stress in the vertical direction. With increasing applied stresses, the tensile stress in the Steel Fiber Concrete (SFC) increased. When this tensile stress reached the cracking strength of SFC, off-vertical cracks started to form perpendicularly to the direction of the principal applied tensile stress. With increasing load, additional vertical cracks formed in between the previous cracks. Once the applied stresses reached the yielding stress of the steel, no additional vertical cracks were formed, but the crack widths kept increasing in size. Note that for panel TAF-2, a series of cracks, inclined at 45 degrees from vertical (2-direction), appeared on the north side of the panel upon reaching the tensile cracking load. As load

increased, a series of cracks quickly developed which emanated from these 45 degree cracks. The angle of these rotated cracks was about 15 degrees from vertical.

Photographs of representative crack patterns prior to ultimate load are shown in Fig. 6.1 through Fig. 6.5 for each TAF specimen.

Table 6.1 – Details of Various Panel Specimens

Group-TAF (Fiber-Factor) PSFC Panels	**Steel Reinforcement in ℓ- direction**		**Prestress Force** (ksi)
	Tendons (Low-Relaxation)	$\rho_{\ell p}$	
TAF-1 (0.28)	2-ϕ0.6@7.5 in.	0.84%	1.2
TAF-2 (0.55)	2-ϕ0.6@7.5 in.	0.84%	1.2
TAF-3 (0.83)	2-ϕ0.6@7.5 in.	0.84%	1.2
TAF-4 (0.80)	2-ϕ0.5@7.5 in.	0.59%	0.84
TAF-5 (1.2)	1-ϕ0.6@7.5 in.	0.42%	0.60

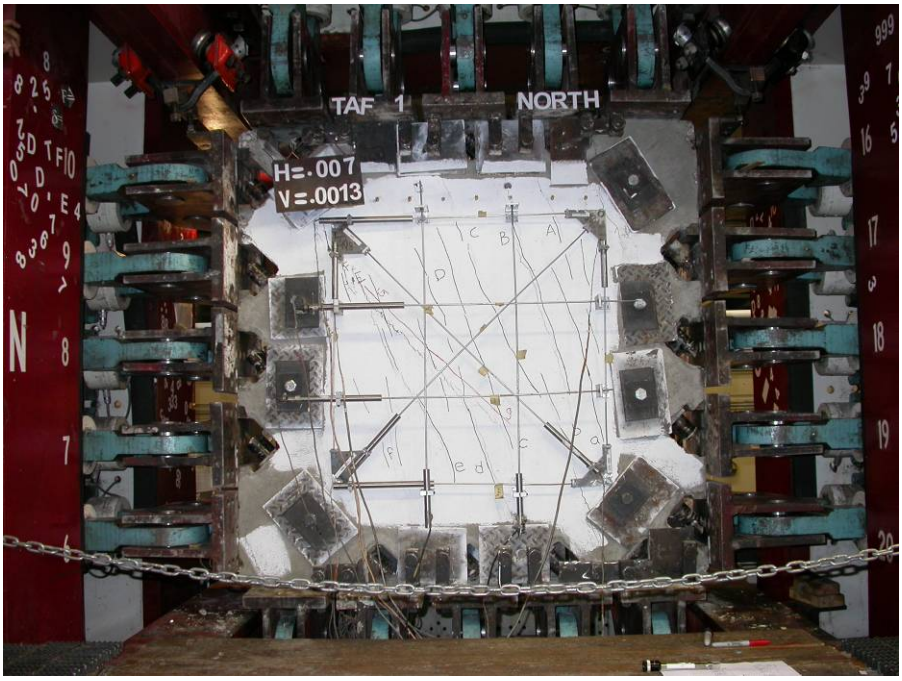

Fig. 6.1 Crack Pattern in PSFC Panel TAF-1

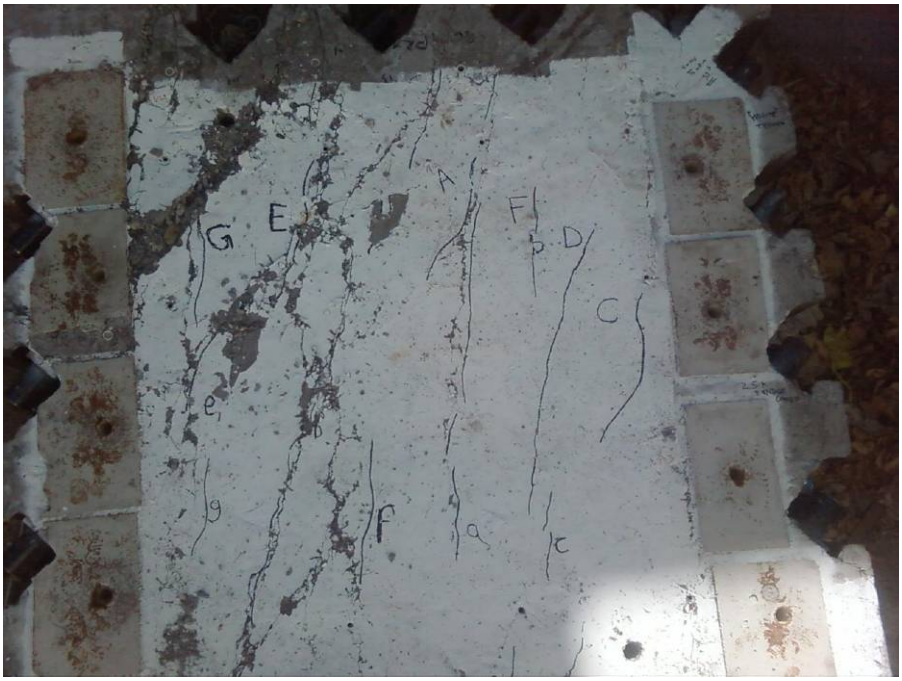

Fig. 6.2 Crack Pattern in PSFC Panel TAF-2

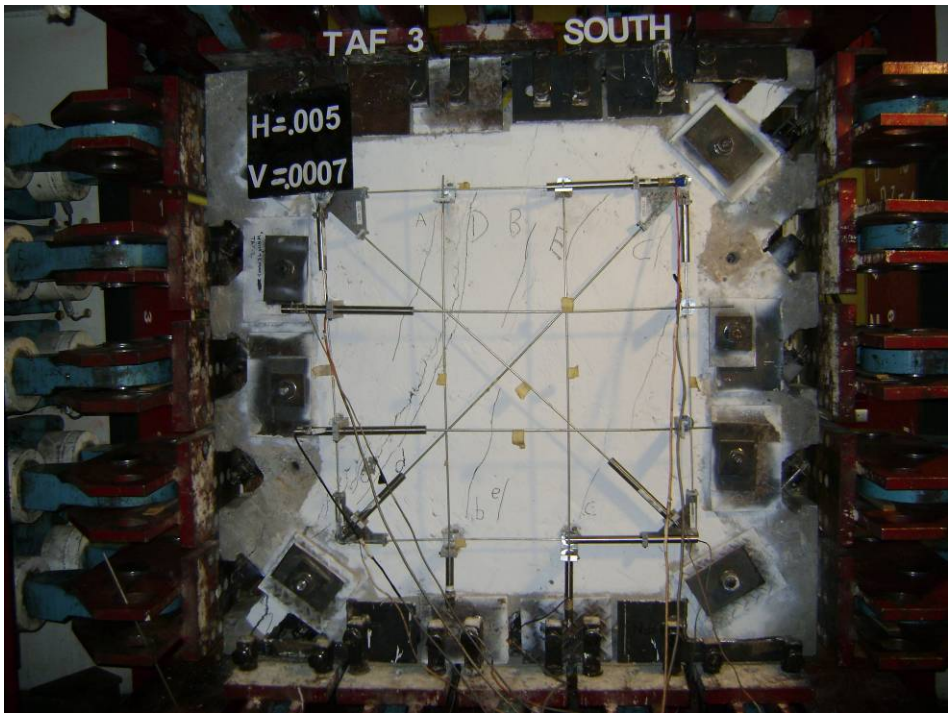

Fig. 6.3 Crack Pattern in PSFC Panel TAF-3

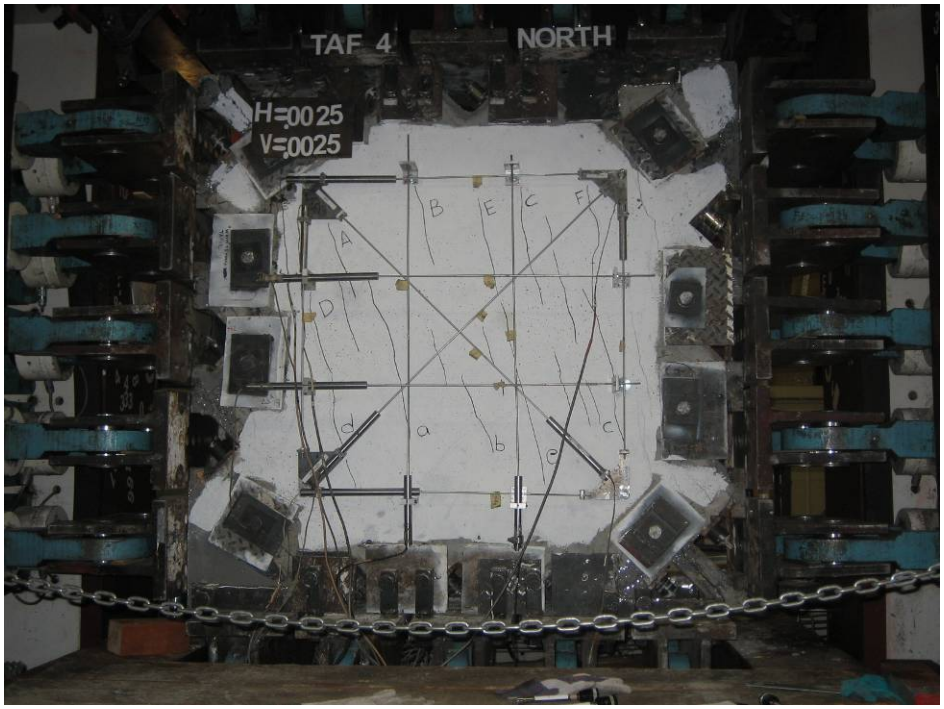

Fig. 6.4 Crack Pattern in PSFC Panel TAF-4

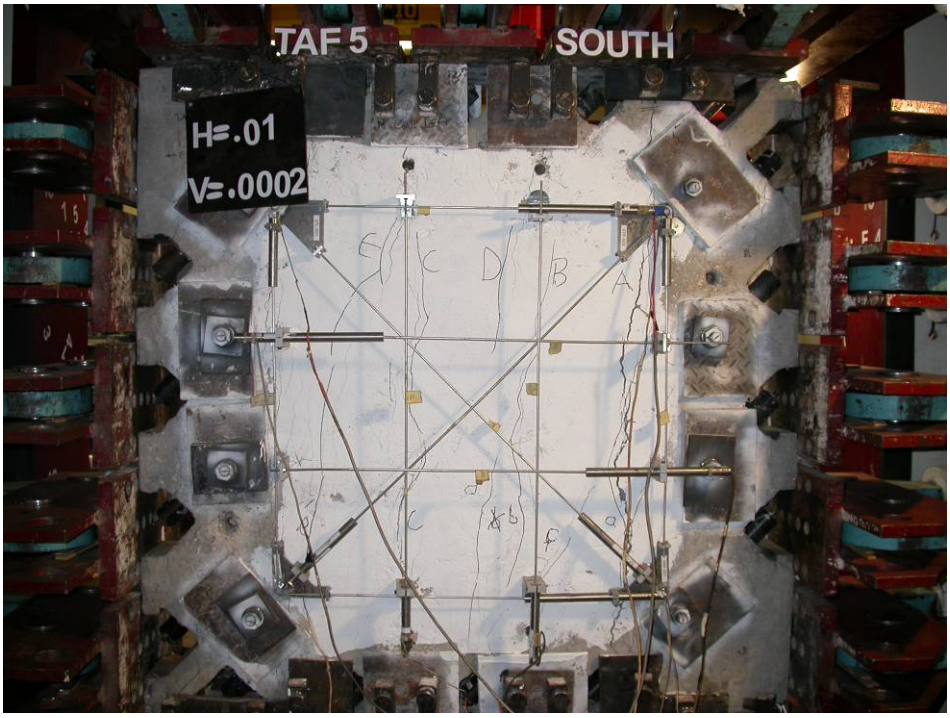

Fig. 6.5 Crack Pattern in PSFC Panel TAF-5

6.3 Shear Stress-Strain Curves

In the five panels, TAF-1 to TAF-5, the prestressing tendons and the mild steel were oriented at an angle of 45° to the principal $2-1$ coordinate of the applied stresses, i.e. $\alpha_2 = 45^\circ$. The stress transformation equations of the element in terms of principal applied stresses are given as:

$$\sigma_\ell = \sigma_2 \cos^2 \alpha_2 + \sigma_1 \sin^2 \alpha_2 , \tag{6-1}$$

$$\sigma_t = \sigma_2 \sin^2 \alpha_2 + \sigma_1 \cos^2 \alpha_2 , \tag{6-2}$$

$$\tau_{\ell t} = (-\sigma_2 + \sigma_1) \sin \alpha_2 \cos \alpha_2 . \tag{6-3}$$

The strain transformation equations of the element in terms of principal strains are given as:

$$\varepsilon_\ell = \varepsilon_2 \cos^2 \alpha_2 + \varepsilon_1 \sin^2 \alpha_2 , \tag{6-4}$$

$$\varepsilon_t = \varepsilon_2 \sin^2 \alpha_2 + \varepsilon_1 \cos^2 \alpha_2 , \tag{6-5}$$

$$\gamma_{\ell t} = (-\varepsilon_2 + \varepsilon_1) \sin \alpha_2 \cos \alpha_2 . \tag{6-6}$$

Substituting $\alpha_2 = 45^\circ$ into Eqs. (6-3) and (6-6), the shear stress $\tau_{\ell t}$ and the shear strain $\gamma_{\ell t}$ of the element can be calculated by the following simple equation in terms of the principal stresses and strains (σ_2, σ_1, ε_2, and ε_1):

$$\tau_{\ell t} = \frac{1}{2}\left(-\sigma_2 + \sigma_1\right), \tag{6-7}$$

$$\gamma_{\ell t} = \frac{1}{2}\left(-\varepsilon_2 + \varepsilon_1\right). \tag{6-8}$$

The principal stresses and strains were calculated using the readings from jack load cells and LVDTs, respectively. The shear stress-strain curves of the panels in the two series are plotted in Fig. 6.6 and Fig. 6.7, respectively. Results are presented and summarized in Table 6.2. Each of the curves for panels TAF-1, 2, 4, and 5 exhibits three critical points, namely, cracking of concrete, yielding of transverse mild steel, and crushing of concrete. Before the cracking of the concrete, the shear behavior of the panels was elastic and the $\tau_{\ell t} - \gamma_{\ell t}$ curves were essentially linear. After cracking, the approximately linear increase of the shear stresses continued with smaller slopes until the yielding of the mild steel. After the mild steel yielded, the shear strains increased dramatically with a very small increase of shear stresses. The prestressed concrete panels reached their peak shear strengths when the crushing of the concrete occurred. The shear stresses started to decline with increase of deformation beyond the peak

Comparison to Group-TA panels tested by Wang (2006) is also shown in the curves of Fig. 6.6 and 6.7. It can be observed that in general the TAF panels were generally stiffer and provided better shear strength in the region between cracking and first yielding of steel.

Table 6.2 Shear Stress at Cracking and Crushing for PSFC TAF Panels

Panel	Shear Stress at Cracking (ksi)	Shear Stress at Crushing (ksi)	$f'c$ (ksi)	$(L_f/D_f)V_f$
TAF-1	0.454	0.771	5.45	0.28
TAF-2	0.557	1.02	6.38	0.55
TAF-3	0.678	0.838	5.52	0.83
TAF-4	0.630	0.754	8.17	0.80
TAF-5	0.496	0.629	4.80	1.20

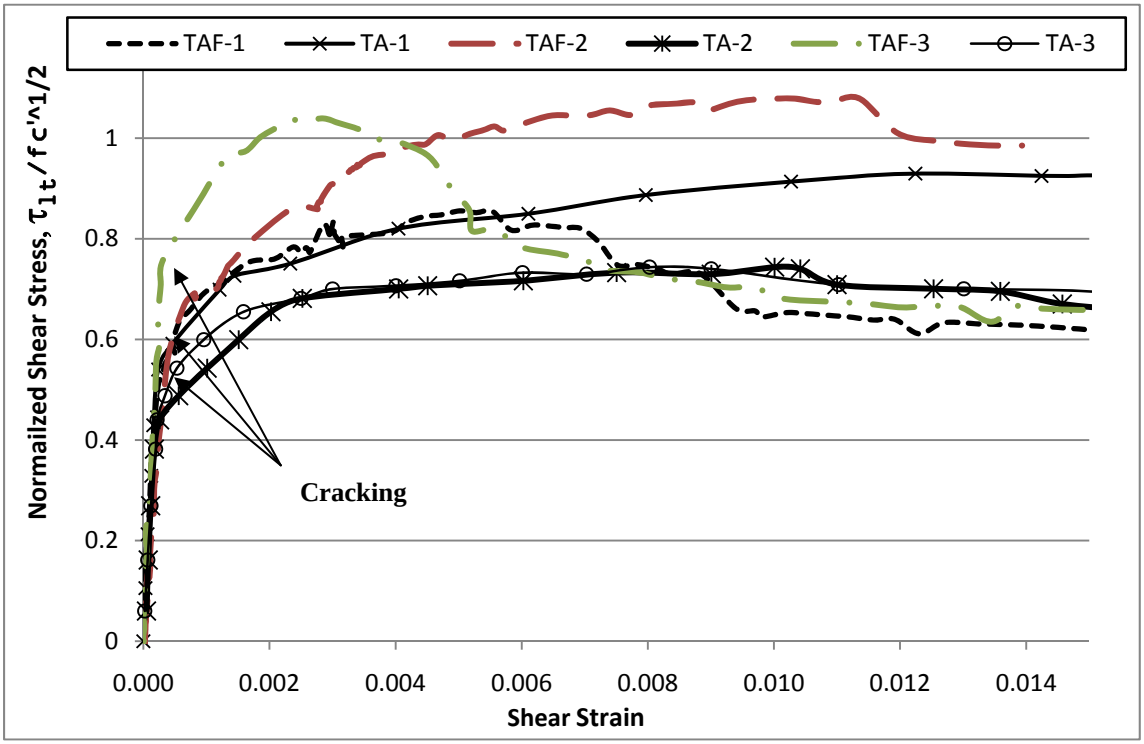

Fig. 6.6 Shear Stress-Strain in PSFC Panels TAF-1, -2, -3 and TA-1, -2, -3

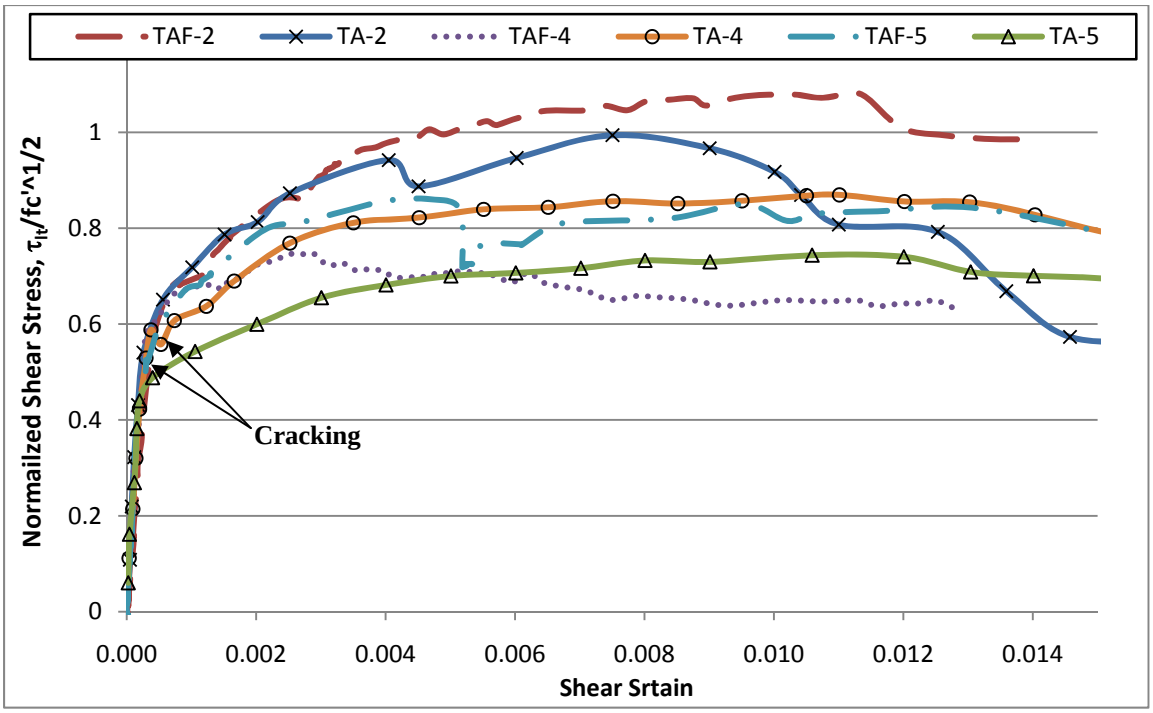

Fig. 6.7 Shear Stress-Strain in PSFC Panels TAF-2, -4, -5 and TA-2, -4, -5

6.4 Fundamentals of the Softened Membrane Model for PSFC (SMM-PSFC)

To analyze and extract meaningful information from the series TAF experimental data, an analytic model was developed based on the constitutive properties that were developed from the series TEF experimental results. The starting point for the analytic model is the SMM-PC analysis tool developed by Wang (2006) and described in section 2.2.4. This model, however, requires modification so that it can be used for SFC. The major modifications include:

(1) Modifying the SFC in tension curve after cracking to account for increased tensile toughness and stiffening.

(2) Accounting for the effects of fiber on the softening coefficient

(3) Modifying the descending branch of the SFC in compression curve to account for increased toughness after concrete crushing.

(4) Modifying the smeared tensile stress-strain curve of prestressing strand embedded in SFC.

The three equilibrium equations and three compatibility equations which form the basis of the model are summarized in Section 6.4.1; the relationships between the biaxial strains and the uniaxial strains are given in Section 6.4.2; and the framework for the constitutive laws of the materials are presented in Section 6.4.3. The algorithm to solve all the equations is shown in Section 6.4.4.

Fig. 6.8(a) shows a PSFC element subjected to in-plane stresses. As in the SMM in section 2.2.1 and the SMM-PC in section 2.2.2, two reference Cartesian coordinates are used in the SMM-PSFC, as shown in Fig. 6.8(e). The first reference Cartesian $\ell - t$ coordinate system represents the directions of the longitudinal and transverse reinforcement. The second reference Cartesian $2-1$ coordinate system represents the directions of the applied principal compressive ($2-$axis) and tensile ($1-$axis) stresses.

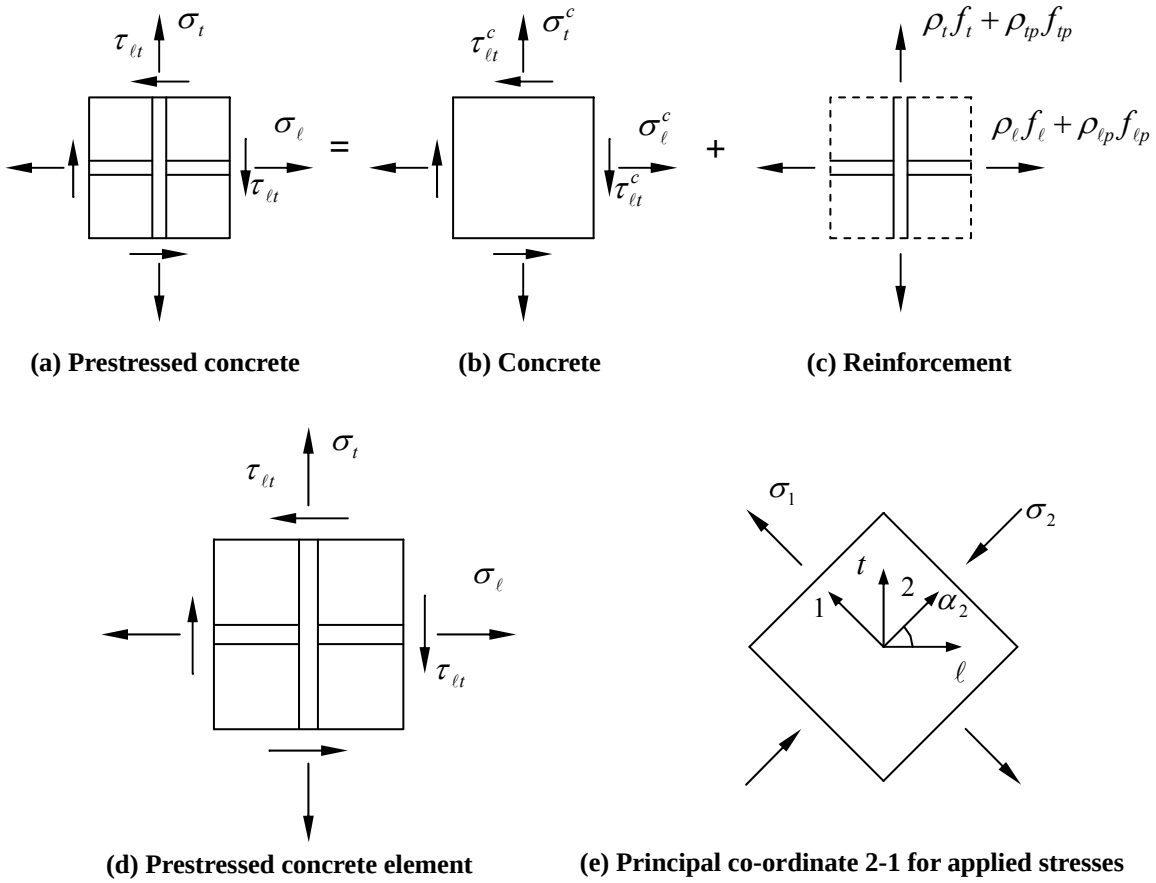

(a) Prestressed concrete **(b) Concrete** **(c) Reinforcement**

(d) Prestressed concrete element **(e) Principal co-ordinate 2-1 for applied stresses**

Fig. 6.8 Coordinate System in a PSFC Membrane Element

6.4.1 Equilibrium and Compatibility Equations

The three equilibrium equations, which relate the applied stresses (σ_ℓ, σ_t and $\tau_{\ell t}$) to the internal stresses of SFC (σ_2^c, σ_1^c and τ_{21}^c), mild steel (f_ℓ and f_t), and prestressing steel ($f_{\ell p}$ and f_{tp}) in a membrane element, are expressed as:

$$\sigma_\ell = \sigma_2^c \cos^2\alpha_2 + \sigma_1^c \sin^2\alpha_2 + \tau_{21}^c 2\sin\alpha_2\cos\alpha_2 + \rho_\ell f_\ell + \rho_{\ell p} f_{\ell p}, \qquad (6\text{-}1)$$

$$\sigma_t = \sigma_2^c \sin^2\alpha_2 + \sigma_1^c \cos^2\alpha_2 - \tau_{21}^c 2\sin\alpha_2\cos\alpha_2 + \rho_t f_t + \rho_{tp} f_{tp}, \qquad (6\text{-}2)$$

$$\tau_{\ell t} = (-\sigma_2^c + \sigma_1^c)\sin\alpha_2\cos\alpha_2 + \tau_{21}^c(\cos^2\alpha_2 - \sin^2\alpha_2). \qquad (6\text{-}3)$$

The three compatibility equations, which represent the relationship between the strains (ε_ℓ, ε_t, and $\gamma_{\ell t}$) in the $\ell - t$ coordinate of the reinforcement and the strains ($\varepsilon_1, \varepsilon_2$, and γ_{21}) in the $2-1$ coordinate of the principal applied stress, are expressed as follows (Pang and Hsu, 1996):

$$\varepsilon_\ell = \varepsilon_2 \cos^2\alpha_2 + \varepsilon_1 \sin^2\alpha_2 + \frac{\gamma_{21}}{2} 2\sin\alpha_2\cos\alpha_2, \qquad (6\text{-}4)$$

$$\varepsilon_t = \varepsilon_2 \sin^2\alpha_2 + \varepsilon_1 \cos^2\alpha_2 - \frac{\gamma_{21}}{2} 2\sin\alpha_2\cos\alpha_2, \qquad (6\text{-}5)$$

$$\frac{\gamma_{\ell t}}{2} = (-\varepsilon_2 + \varepsilon_1)\sin\alpha_2\cos\alpha_2 + \frac{\gamma_{21}}{2}(\cos^2\alpha_2 - \sin^2\alpha_2). \qquad (6\text{-}6)$$

6.4.2 Biaxial Strains vs. Uniaxial Strains

To solve the equilibrium and compatibility equations, the stress-strain relationships of SFC and reinforcement have to be provided. As mentioned in Section 2.2.3, the set of strains in the compatibility equations, ε_1, ε_2, ε_ℓ, and ε_t, are biaxial strains, which are functions of the Hsu/Zhu ratios. The constitutive laws between the stresses and the biaxial strains cannot be determined directly from experiments. Therefore, a "bridge" is required to relate the biaxial strains and the uniaxial strains. The relationships between the uniaxial strains ($\bar{\varepsilon}_1$, $\bar{\varepsilon}_2$, $\bar{\varepsilon}_\ell$, and $\bar{\varepsilon}_t$) and the biaxial strains (ε_1, ε_2, ε_ℓ, and ε_t) are given as follows (Zhu, 2000):

$$\bar{\varepsilon}_1 = \frac{1}{1-\nu_{12}\nu_{21}}\varepsilon_1 + \frac{\nu_{12}}{1-\nu_{12}\nu_{21}}\varepsilon_2, \qquad (6\text{-}7)$$

$$\bar{\varepsilon}_2 = \frac{\nu_{21}}{1-\nu_{12}\nu_{21}}\varepsilon_1 + \frac{1}{1-\nu_{12}\nu_{21}}\varepsilon_2, \qquad (6\text{-}8)$$

$$\bar{\varepsilon}_\ell = \bar{\varepsilon}_2 \cos^2 \alpha_2 + \bar{\varepsilon}_1 \sin^2 \alpha_2 + \frac{\gamma_{21}}{2} 2 \sin \alpha_2 \cos \alpha_2 , \tag{6-9}$$

$$\bar{\varepsilon}_t = \bar{\varepsilon}_2 \sin^2 \alpha_2 + \bar{\varepsilon}_1 \cos^2 \alpha_2 - \frac{\gamma_{21}}{2} 2 \sin \alpha_2 \cos \alpha_2 . \tag{6-10}$$

The Hsu/Zhu ratios are given by:

$$\nu_{12} = 0.2 + 850 \varepsilon_{sf} , \qquad \varepsilon_{sf} \le \varepsilon_y , \tag{6-11a}$$

$$\nu_{12} = 1.9 , \qquad \varepsilon_{sf} > \varepsilon_y , \tag{6-11b}$$

$$\nu_{21} = 0 , \tag{6-12}$$

where

ε_{sf} = smeared (average) tensile strain of steel bars in the ℓ and the t directions, whichever yields first, taking into account the Hsu/Zhu ratios.

6.4.3 Constitutive Relationships of SFC in Prestressed Elements

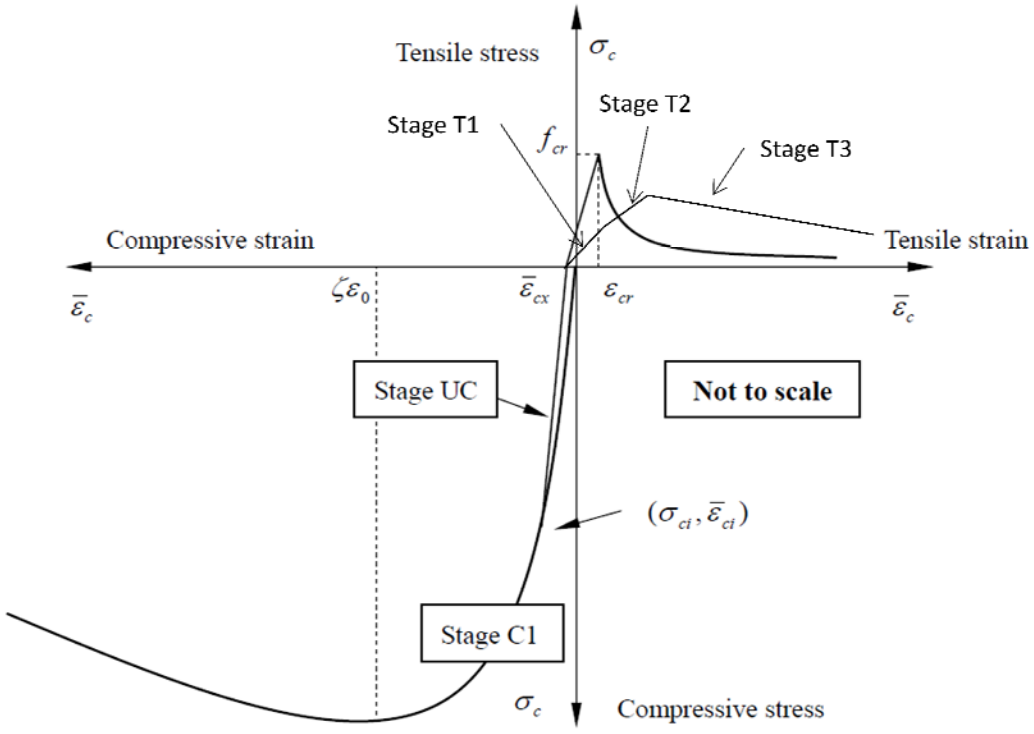

Fig 6.9 Constitutive Model for SFC

The constitutive model for prestressed SFC along with the factors that will effect prestressed SFC are summarized in this section, including the constitutive relationships of cracked SFC in tension, compression, and shear. The results are plotted in Fig. 6.9. Note that in the discussion that ensues, the tensile stress is applied in $1-$ direction and the compressive stress in $2-$ direction.

6.4.3.1 SFC in Tension

The relationships of the tensile stress σ_1^c versus the uniaxial tensile strain $\bar{\varepsilon}_1$ of prestressed SFC are given as follows:

Stage UC: $\sigma_1^c = E_c'\bar{\varepsilon}_1 + \sigma_{ci}$, $\bar{\varepsilon}_1 \le (\bar{\varepsilon}_{cx} - \bar{\varepsilon}_{ci})$, (6-13a)

Stage T1: $\sigma_1^c = E_c''(\bar{\varepsilon}_1 + \bar{\varepsilon}_{ci})$, $(\bar{\varepsilon}_{cx} - \bar{\varepsilon}_{ci}) < \bar{\varepsilon}_1 \le (\varepsilon_{cy} - \bar{\varepsilon}_{ci})$, (6-13b)

Stage T2: $\sigma_1^c = E_c'''(\bar{\varepsilon}_1 + \bar{\varepsilon}_{ci})$, $(\bar{\varepsilon}_{cy} - \bar{\varepsilon}_{ci}) < \bar{\varepsilon}_1 \le (\varepsilon_{cult} - \bar{\varepsilon}_{ci})$, (6-13c)

Stage T3: $\sigma_1^c = E^{IV}{}_c(\bar{\varepsilon}_1 + \bar{\varepsilon}_{ci})$, $\bar{\varepsilon}_1 > (\varepsilon_{cult} - \bar{\varepsilon}_{ci})$, (6-13d)

where,

E_c' = decompression modulus of concrete taken as $\frac{2f_c'}{\varepsilon_0}$, (6-13e)

$\bar{\varepsilon}_{ci}$ = initial strain in concrete due to prestress,

σ_{ci} = initial stress in SFC,

$\bar{\varepsilon}_{cx}$ = extra strain in concrete after decompression calculated by $\bar{\varepsilon}_{ci} - \frac{\sigma_{ci}}{E_c'}$,

$\varepsilon_{c\max}$ = SFC maximum strain taken as 0.04 - ε_{pi}

ε_{cult} = SFC ultimate strain taken as 0.01 - ε_{pi}

f_{cult} = SFC ultimate stress strain taken as $(0.2FF + 12\rho_l)\sqrt{f_c'}$

ε_{cy} = SFC yield strain taken as 0.0005,

f_{cy} = SFC effective "yield" stress for Proportional Loading, taken as $0.4 * FF * CF\sqrt{f_c'}$, (f_c' and $\sqrt{f_c'}$ are in MPa) where:

CF = 1 for SFC tensile volume confined (sandwiched) by two or more tendons, or

CF = ½ for SFC tensile volume unconfined by tendons

E_c'' = modulus of SFC taken as $\dfrac{f_{cy}}{\varepsilon_{cy}-\bar{\varepsilon}_{cx}}$,

E_c''' = modulus of SFC taken as $\dfrac{f_{cult}-f_{cy}}{\varepsilon_{cult}-\varepsilon_{cy}}$,

E_c^{IV} = modulus of SFC taken as $\dfrac{-f_{cult}}{\varepsilon_{\max}-\varepsilon_{cult}}$,

6.4.3.2 SFC in Compression

The smeared (average) constitutive relationships of SFC compressive stress σ_2^c and the uniaxial compressive strain $\bar{\varepsilon}_2$ are given as follows:

$$\sigma_2^c = \zeta f_c'\left[2\left(\frac{\bar{\varepsilon}_2}{\zeta\varepsilon_0}\right)-\left(\frac{\bar{\varepsilon}_2}{\zeta\varepsilon_0}\right)^2\right], \qquad \frac{\bar{\varepsilon}_2}{\zeta\varepsilon_0}\le 1, \tag{6-14a}$$

or

$$\sigma_2^c = \zeta f_c'\left[1-\left(\frac{\bar{\varepsilon}_2/\zeta\varepsilon_0-1}{4/\zeta-1}\right)^2\right], \qquad \frac{\bar{\varepsilon}_2}{\zeta\varepsilon_0}>1, \tag{6-14b}$$

where ζ is the softening coefficient.

The softening coefficient in Eq. (6-14) can be determined as follows

$$\zeta_\sigma = f(f_c')f(\bar{\varepsilon}_1)f(\beta)W_p Wf \le 0.9, \tag{6-15}$$

where

$$f(f_c') = \frac{5.8}{\sqrt{f_c'}} \le 0.9 \quad (f_c' \text{ in MPa}), \tag{6-16}$$

$$f(\bar{\varepsilon}_1) = \frac{1}{\sqrt{1+400\bar{\varepsilon}_1}}, \tag{6-17}$$

$$f(\beta) = 1-\frac{|\beta|}{24^\circ}, \tag{6-18}$$

$$W_p = 1.15+\frac{|\beta|(0.09|\beta|-1)}{6}, \tag{6-19}$$

$$\beta = \frac{1}{2}\tan^{-1}\left[\frac{\gamma_{21}}{(\varepsilon_2-\varepsilon_1)}\right], \tag{6-20}$$

and

$$Wf = 1+0.2FF \tag{6-20a}$$

6.4.3.3 SFC in Shear

The equation relating the shear stress of SFC τ_{21}^{c} and the shear strain γ_{21} in the $2-1$ coordinate is given by

$$\tau_{21}^{c} = \frac{\sigma_1^c - \sigma_2^c}{2(\varepsilon_1 - \varepsilon_2)}\gamma_{21}. \qquad (6\text{-}21)$$

6.4.3.4 Prestressing Tendons Embedded in SFC

The smeared (average) stress-strain relationships of prestressing tendons embedded in SFC are given as follows:

$$f_{ps} = E_{ps}\bar{\varepsilon}_s', \qquad \bar{\varepsilon}_s < \frac{0.7 f_{pu}}{E_{ps}}, \qquad (6\text{-}22a)$$

or

$$f_{ps} = \frac{E_{ps}''\bar{\varepsilon}_s'}{\left[1+\left(\frac{E_{ps}''\bar{\varepsilon}_s'}{f_{pu}'}\right)^5\right]^{\frac{1}{5}}}, \qquad \bar{\varepsilon}_s \geq \frac{0.7 f_{pu}}{E_{ps}}, \qquad (6\text{-}22b)$$

where

E_{ps} = elastic modulus of prestressing tendons taken as $200\,\text{GPa}$ $(29000\,\text{ksi})$,

$\bar{\varepsilon}_s'$ = $\bar{\varepsilon}_s + \varepsilon_{dec}$, uniaxial steel strain including the decompression strain,

f_{pu} = ultimate strength of prestressing tendons taken as $1862\,\text{MPa}$ $(270\,\text{ksi})$,

E_{ps}'' = modulus of prestressing tendons, used in plastic region (Eq. 6-22b), taken as $209\,\text{GPa}$ $(30345\,\text{ksi})$,

f_{pu}' = revised strength of prestressing tendons taken as $1793\,\text{MPa}$ $(260\,\text{ksi})$, and,

In the above equations, ℓp replaces *ps* in the subscript of symbols for the longitudinal tendons, and tp replaces *ps* for the transverse tendons.

6.4.3.5 Mild Steel Embedded in SFC

The smeared (average) tensile stress-strain relationships of mild steel embedded in concrete in the $\ell - t$ coordinate are the same in SMM. They can be expressed as follows:

Stage 1: $f_s = E_s\bar{\varepsilon}_s$, $\bar{\varepsilon}_s \leq \bar{\varepsilon}_n$, (6-23)

Stage 2: $f_s = f_y\left[(1-0.096FF)(0.91-2B)+(0.2FF+1)(0.02+0.25B)\frac{\bar{\varepsilon}_s}{\varepsilon_y}\right], \quad \bar{\varepsilon}_s > \bar{\varepsilon}_n,$ (6-24)

Stage 3 (unloading): $f_s = f_p - E_s(\bar{\varepsilon}_p - \bar{\varepsilon}_s), \quad \bar{\varepsilon}_s < \bar{\varepsilon}_p,$ (6-25)

where

$\bar{\varepsilon}_n = \varepsilon_y(0.93-2B),$ (6-25a)

$B = \frac{1}{\rho}\left(\frac{f_{cr}}{f_y}\right)^{1.5},$ (6-25b)

ε_{cr} = concrete cracking strain taken as 0.00008, and

f_{cr} = concrete cracking stress taken as $0.31\sqrt{f_c'}$ (f_c' and $\sqrt{f_c'}$ are in MPa) (6-25c)

In the above equations, ℓ replaces *s* in the subscript of symbols for the longitudinal steel, and t replaces *s* for the transverse steel.

6.4.4 Solution Algorithm

The solution procedure for the SMM-PSFC is given in the flow chart of Fig. 6.10. Similar to the SMM-PC, two equilibrium equations, Eqs. (6-26) and (6-27), are also used to make the solution procedure more efficient. Eqs. (6-26) and (6-27) are derived from Eqs. (6-1) and (6-2):

$$\rho_\ell f_\ell + \rho_{\ell p} f_{\ell p} + \rho_t f_t + \rho_{tp} f_{tp} = (\sigma_\ell + \sigma_t) - (\sigma_2^c + \sigma_1^c), \quad (6\text{-}26)$$

$$\rho_\ell f_\ell + \rho_{\ell p} f_{\ell p} - \rho_t f_t - \rho_{tp} f_{tp} = (\sigma_\ell - \sigma_t) - (\sigma_2^c - \sigma_1^c)\cos 2\alpha_2 - 2\tau_{21}^c \sin 2\alpha_2. \quad (6\text{-}27)$$

Defining $[\rho f]_\ell = \rho_\ell f_\ell + \rho_{\ell p} f_{\ell p}$ and $[\rho f]_t = \rho_t f_t + \rho_{tp} f_{tp}$, the above two equations become:

$$[\rho f]_\ell + [\rho f]_t = (\sigma_\ell + \sigma_t) - (\sigma_2^c + \sigma_1^c), \quad (6\text{-}28)$$

$$[\rho f]_\ell - [\rho f]_t = (\sigma_\ell - \sigma_t) - (\sigma_2^c - \sigma_1^c)\cos 2\alpha_2 - 2\tau_{21}^c \sin 2\alpha_2. \quad (6\text{-}29)$$

The solution procedure can also be described as follows (Fig. 6.9):

Step 1: Select a value of strain in the $2-$direction, ε_2.

Step 2: Assume a value of shear strain in the $2-1$ coordinate, γ_{21}.

Step 3: Assume a value of strain in the $1-$direction, ε_1.

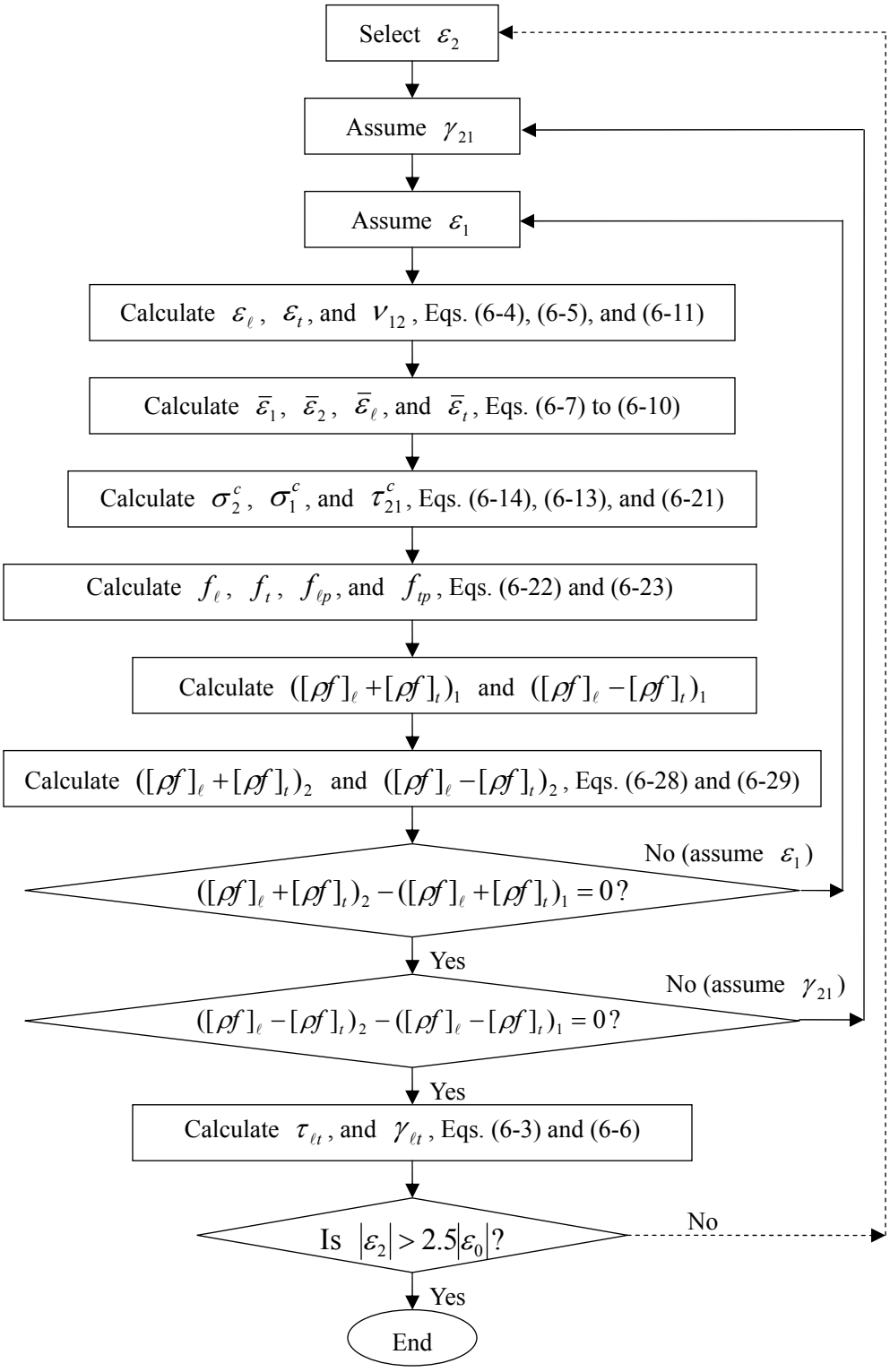

Fig. 6.10 Flow Chart of Solution Procedure for SMM-PSFC

Step 4: Calculate steel strains ε_ℓ, ε_t, and ν_{12} from Eqs. (6-4), (6-5), and (6-11), respectively. Hsu/Zhu ratio ν_{21} is taken as zero.

Step 5: Calculate uniaxial strains $\bar{\varepsilon}_1$, $\bar{\varepsilon}_2$, $\bar{\varepsilon}_\ell$, and $\bar{\varepsilon}_t$ from Eqs. (6-7) to (6-10).

Step 6: Calculate the concrete stresses σ_2^c, σ_1^c and τ_{21}^c from Eqs. (6-14), (6-13), and (6-21), respectively.

Step 7: Calculate the reinforcement stresses f_ℓ, f_t, $f_{\ell p}$, and f_{tp} from Eqs. (6-22) and (6-23).

Step 8: Calculate $([\rho f]_\ell + [\rho f]_t)_1$ and $([\rho f]_\ell - [\rho f]_t)_1$.

Step 9: Calculate $([\rho f]_\ell + [\rho f]_t)_2$ and $([\rho f]_\ell - [\rho f]_t)_2$, from Eqs. (6-28) and (6-29), respectively.

Step 10: Compare $([\rho f]_\ell + [\rho f]_t)_1$ with $([\rho f]_\ell + [\rho f]_t)_2$. When $([\rho f]_\ell + [\rho f]_t)_2$ is larger than $([\rho f]_\ell + [\rho f]_t)_1$, increase the tensile strain ε_1. Otherwise, decrease ε_1. Repeat steps 3 to 10 until $([\rho f]_\ell + [\rho f]_t)_1$ and $([\rho f]_\ell + [\rho f]_t)_2$ are close enough within the specified accuracy.

Step 11: Compare $([\rho f]_\ell - [\rho f]_t)_1$ with $([\rho f]_\ell - [\rho f]_t)_2$. When $([\rho f]_\ell - [\rho f]_t)_2$ is larger than $([\rho f]_\ell - [\rho f]_t)_1$, increase the value of shear strain γ_{21}. Otherwise, decrease the shear strain γ_{21}. Repeat steps 2 to 11 until $([\rho f]_\ell - [\rho f]_t)_1$ and $([\rho f]_\ell - [\rho f]_t)_2$ are close enough within the specified accuracy.

Step 12: Calculate the applied shear stress $\tau_{\ell t}$ and the corresponding shear strain $\gamma_{\ell t}$ from Eq. (6-3) and (6-6), respectively. This will provide one point on the $\tau_{\ell t}$ versus $\gamma_{\ell t}$ curve.

Step 13: Select another value of ε_2 and repeat steps 2 to 12. Calculations for a series of ε_2 values will provide the whole $\tau_{\ell t}$ versus $\gamma_{\ell t}$ curve.

6.4.5 Comparison of Analytic Results to Experimental Data

Figs. 6.11 through 6.15 show the analytic model plots for each TAF series panel plotted against the experimental data. The graphs indicate good correlation between the model and the experimental results along the initial parts of the curve. For panels TAF-1 and TAF-3 there was a shear slide failure in the experimental panels prior to reaching the analytic peak load.

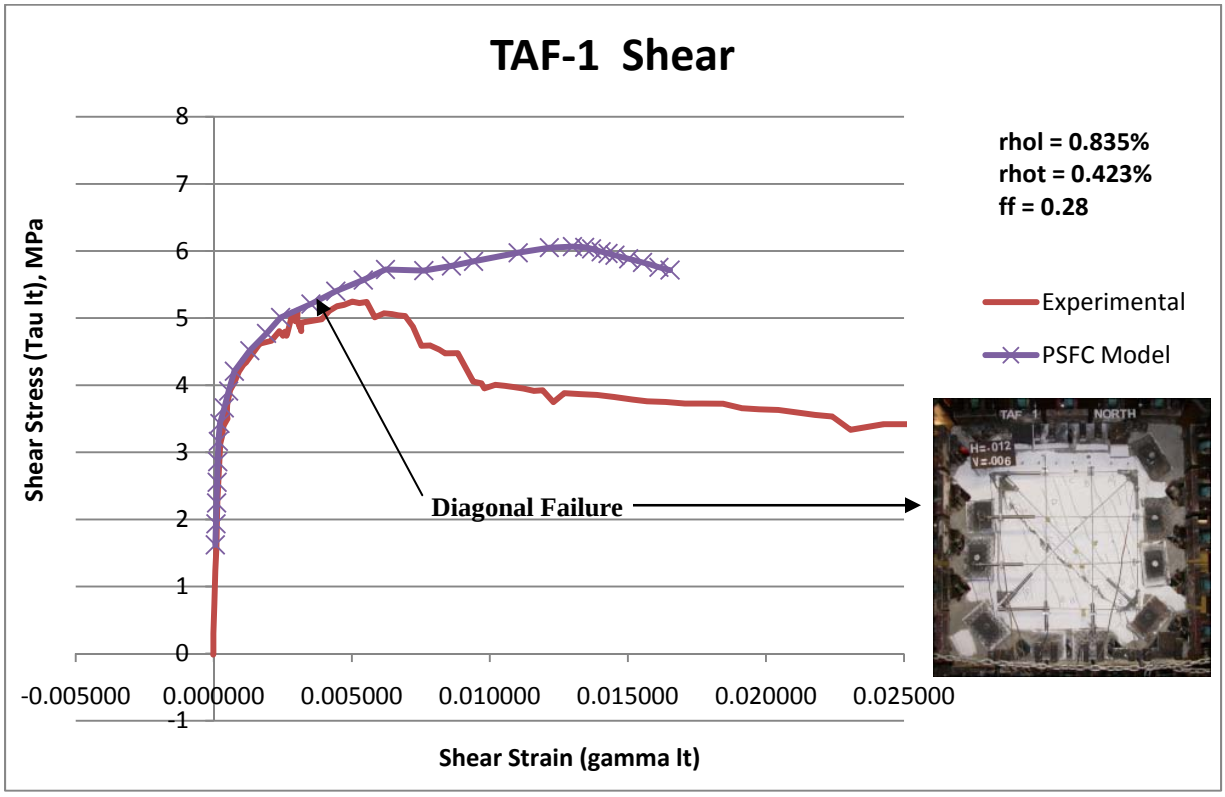

1 MPa =145 psi

Fig. 6.11 Experimental and Analytic Comparison for PSFC Panel TAF-1

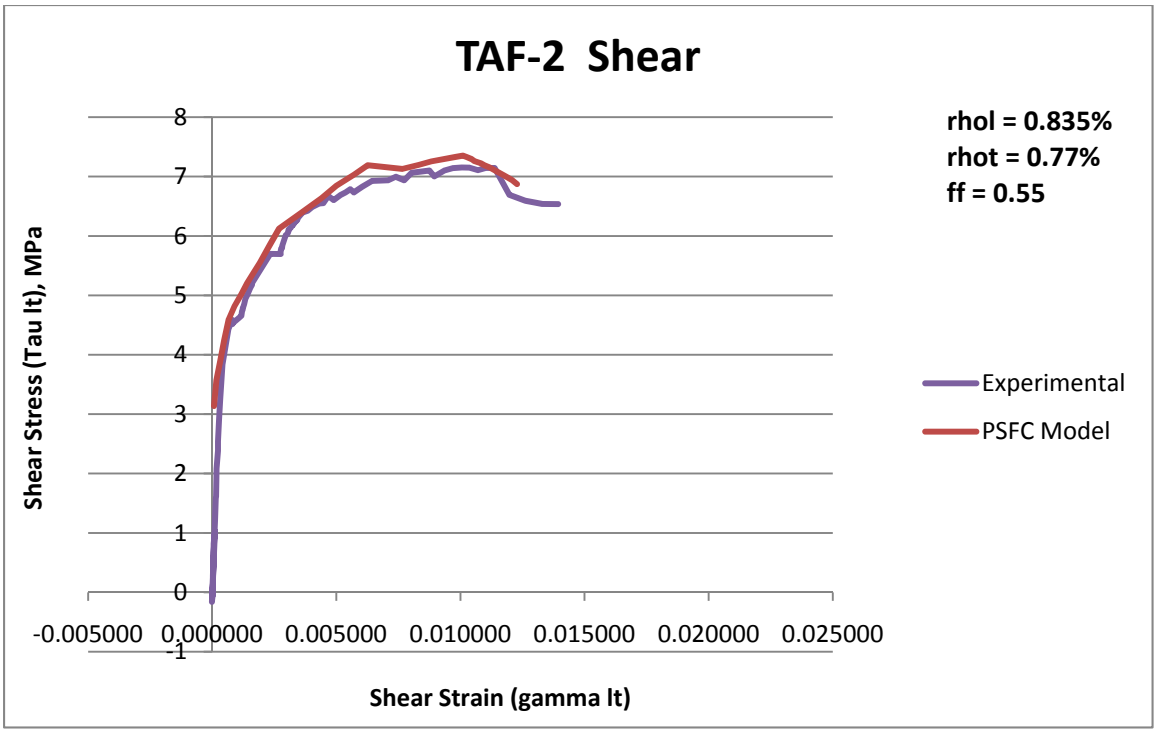

1 MPa =145 psi

Fig. 6.12 Experimental and Analytic Comparison for PSFC Panel TAF-2

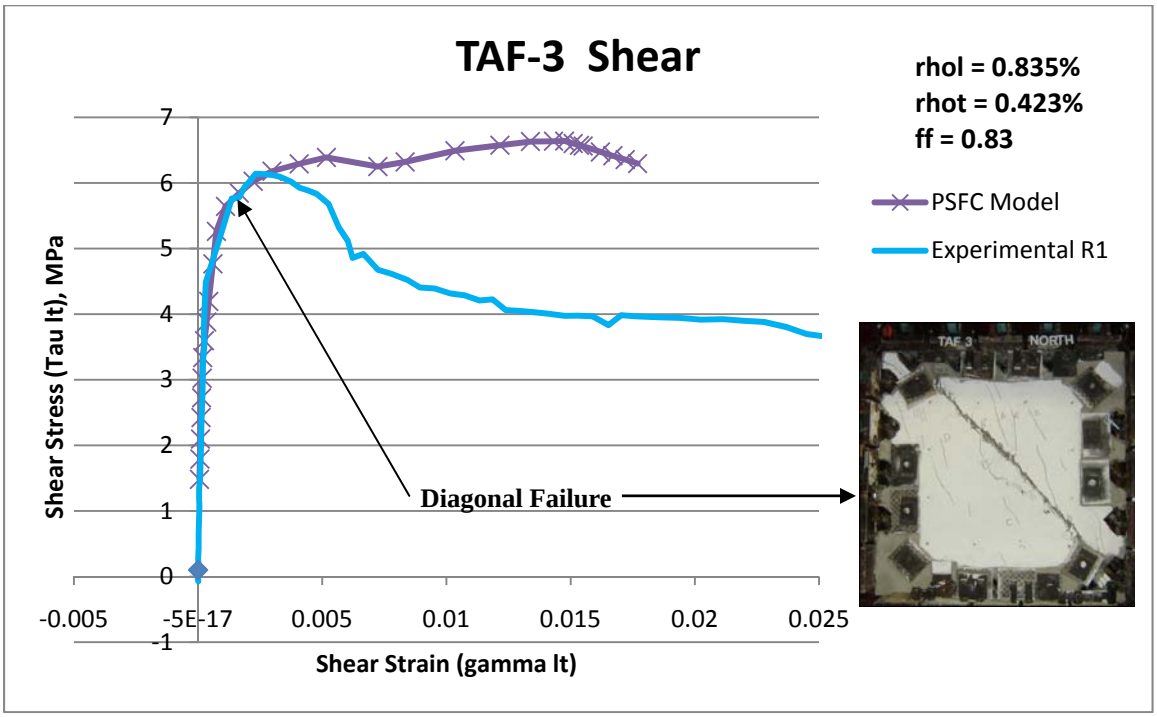

1 MPa =145 psi

Fig. 6.13 Experimental and Analytic Comparison for PSFC Panel TAF-3

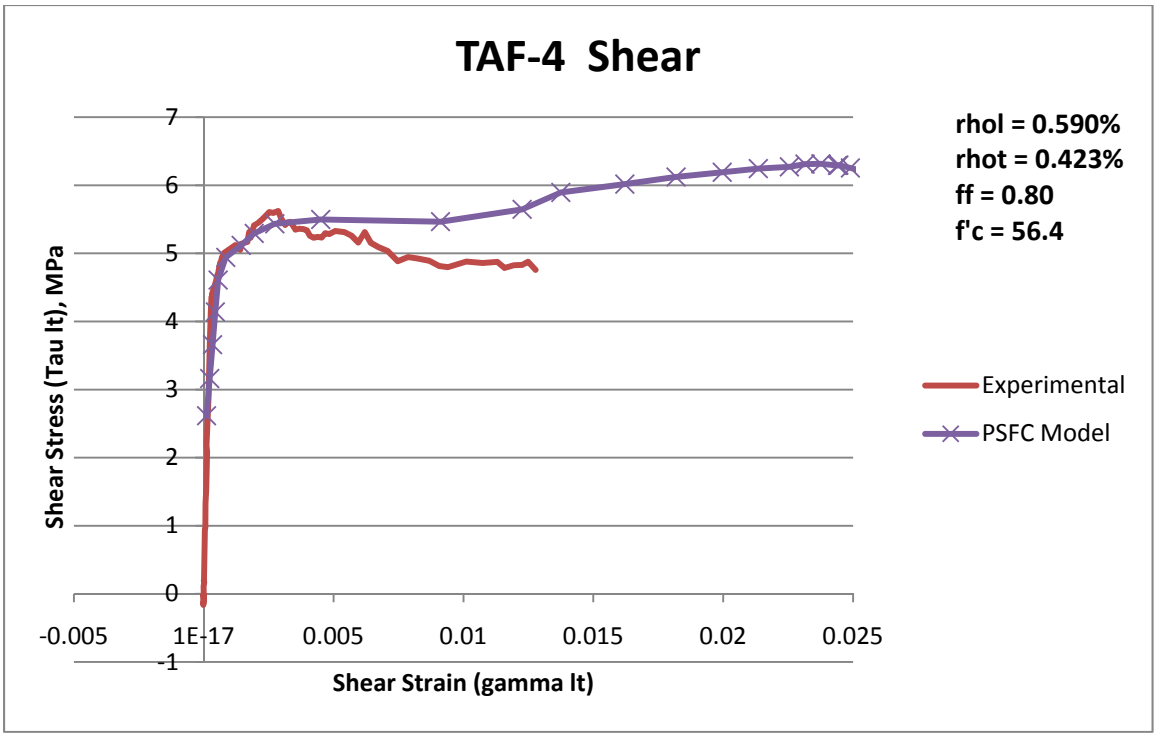

Fig. 6.14 Experimental and Analytic Comparison for PSFC Panel TAF-4

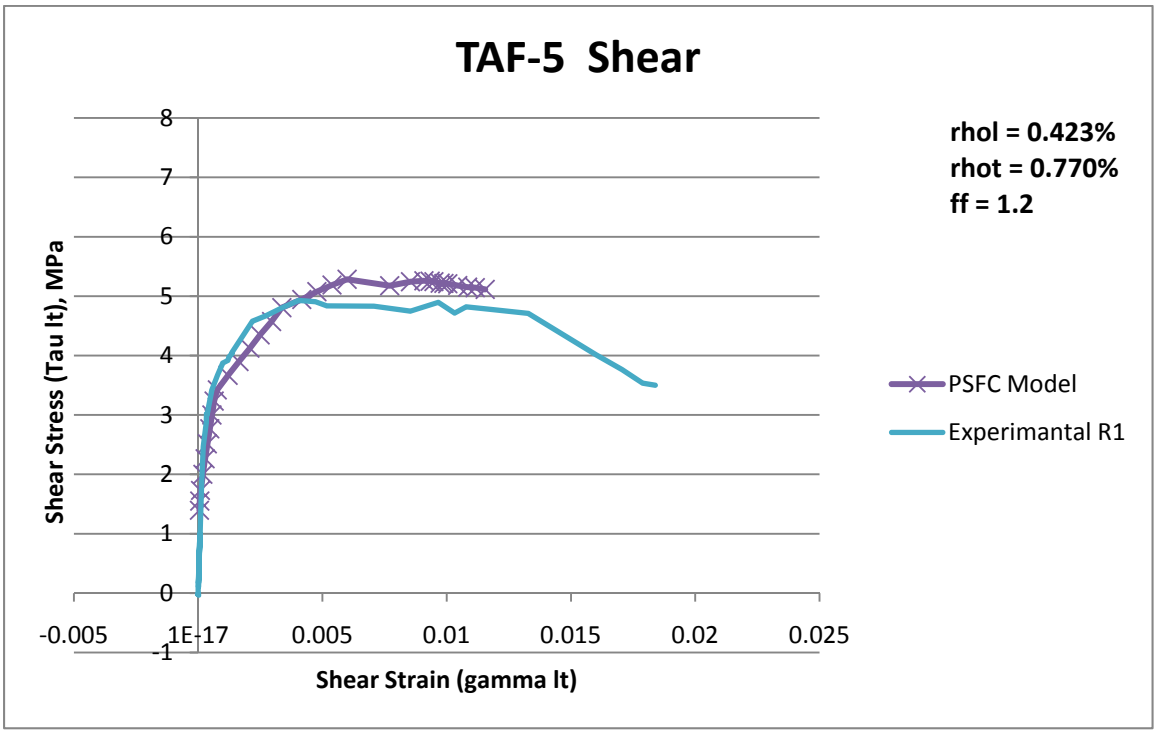

Fig. 6.15 Experimental and Analytic Comparison for PSFC Panel TAF-5

PART II:

SHEAR IN PRESTRESSED STEEL FIBER CONCRETE BEAMS

CHAPTER 7

SHEAR TESTS OF PRESTRESSED STEEL FIBER CONCRETE I-BEAMS

7.1 Introduction

The constitutive laws governing the behavior of Prestressed Steel Fiber Concrete (PSFC) were developed in Chapters 4 through 6 of this report. Chapters 7 and 8 present the results of shear test of full scale PSFC I- and Box-Beams, respectively. The constitutive model for PSFC was implemented in the finite element program (OpenSees) to predict the behavior of the tested beams in Chapter 9. Finally, Chapter 10 presents a new shear design equation and a set of guidelines for designing PSFC beams including four design examples.

7.2 Testing Program

The first series of test specimens consisted of TxDOT Type-A beams (I-Beams). Six 25-feet long beams (R1 to R6) were fabricated with PSFC to study the behavior of the beams in web-shear and flexure-shear mode of failure under monotonic loading. Dramix steel fibers, which structurally performed the best as discussed in Chapter 3, were chosen to produce the PSFC beams. The beam cross section is show in Fig. 7.1. The primary testing variables investigated were the amount of steel fiber (fiber factor) and the mode of shear failure (i.e. shear span-to-effective depth ratio, *a/d*). No traditional transverse rebars (stirrups) were used in any of the beams; the shear reinforcement consisted solely of steel fibers. Beams R1, R2, R3 and R4 were designed to fail in web-shear with *a/d* ratio of 1.6, while Beams R5 and R6 were designed to fail in flexure-shear with *a/d* ratio of 4.2.

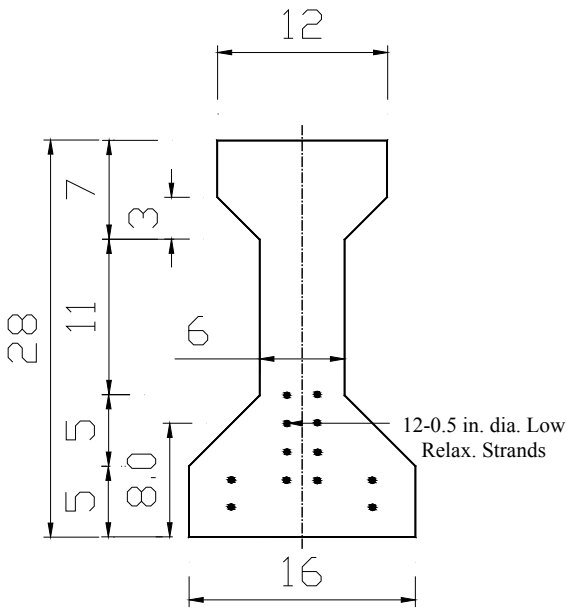

(All Dimensions are in Inches)

Fig. 7. 1 Cross Section of PSFC I-Beam

Table 7.1 – Test Variables of PSFC I-Beam

Beam ID	**Mode of Failure**	**Concrete Compressive Strength,** (ksi)	**Volume of Steel Fiber Reinforcement** V_f	**Fiber Factor** $[(L_f/D_f)V_f]/100$
R1	Web Shear	12.6	0.5% LF	**0.40**
R2	Web Shear	13.1	1% SF	**0.55**
R3	Web Shear	11.9	1.5% SF	**0.825**
R4	Web Shear	10.6	1.5% SF + 0.5% LF	0.825 + 0.40 =**1.225**
R5	Flexural Shear	12.2	0.5% LF	**0.40**
R6	Flexural Shear	12.8	1.5% SF + 0.5% LF	0.825 + 0.40 =**1.225**

LF = Dramix Long Fibers with $L_f/D_f = 80$; SF = Dramix Short Fibers with $L_f/D_f = 55$; L_f = Length of Steel Fiber; D_f = Diameter of Steel Fiber

Table 7.1 summarizes the test variables for Beams R1 to R6. Beam R1 with a fiber factor of 0.4 was designed to fail in web-shear. Beams R2, R3 and R4 were made using fiber factor of 0.55, 0.83 and 1.23, respectively and were also designed to fail in web-shear. Beam R5 and Beam R6 with a fiber factor of 0.4 and 1.23, respectively; were designed to fail in flexural-shear.

7.3 Details of PSFC I-Beams

The cross-section of the TxDOT Type A beam is shown in Fig. 7.1. The total height of the beam was 28 inches and the widths of the top and bottom flange were 12 inches and 16 inches, respectively. The width of the web was 6 inches. The prestressing tendons in all beams were straight. The location of prestressing tendons is also shown in Fig. 7.1. Twelve 0.5-inch diameter, 7-wire, low-relaxation strands were used as prestressing steel to resist flexure. The prestressing strands had an ultimate tensile strength of 270 ksi. The total length of the beams tested was 25 feet while the test span-length was 24 feet.

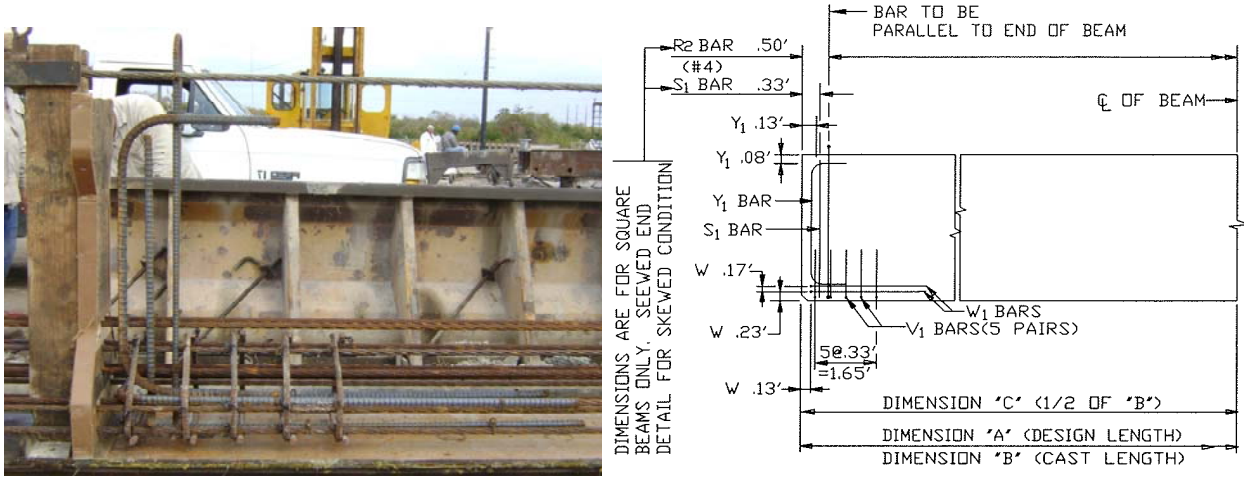

(a) Photo of End Zone Reinforcement

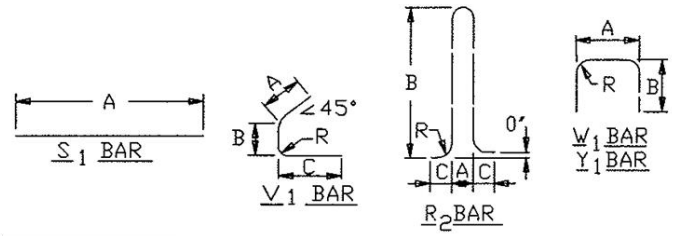

BEAM MARK						
BAR	SIZE	A	B	C	D	R
R_2	#4	3 1/4"	2'-8"	4"	———	1"
S_1	#5	———	—STRAIGHT—		———	———
W_1	#5	8 1/2"	3'-0"	———	———	1 1/4"
Y_1	#6	1'-10"	1'-0"	———	———	3"
V_1	#4	6 3/4"	3"	11 1/4"	———	1"

b) Reinforcement: Layout and Schedule

Fig. 7.2 Details of End Zone Reinforcement in PSFC I-Beams

7.4 Materials and Mix Design

The two types of steel fibers manufactured by Bekaert-Dramix® were used to cast the PSFC I-Beams. The steel fibers were 'trough' shaped with hook at both ends and were collated together. The long fiber (LF) - RC80/60BN is shown in Fig. 7.3(a) and the short fiber (SF) - ZP305 is shown in Fig. 7.3(b). The RC80/60BN fibers had a length of 2.4 inch, a diameter of 0.03 inch (aspect ratio of 80) and had a tensile strength of 150 ksi. The ZP305 fibers were 1.2 inches long and 0.022 inch in diameter (aspect ratio of 55) and had a tensile strength of 160 ksi. Table 7.2 gives out the details of the steel fiber used in this experimental study. The steel fibers were relatively stiff and glued into bundles i.e. collated. The glue dissolved in the water during mixing, thus dispersing the fibers in the mix as shown in Fig. 7.4.

Table 7.2 – Properties of Steel Fiber Used in PSFC I-Beams

Fiber Type		**Length** (inch) L_f	**Diameter** (inch) D_f	**Aspect Ratio** L_f/D_f	**Tensile Strength** (ksi)
Dramix Hooked End, Collated	Long Fiber (LF)	2.4	0.03	80	150
	Short Fiber (SF)	1.2	0.022	55	160

Table 7.3 show the details of different constituent materials of concrete used to cast the PSFC I-Beams. Locally available materials, which were traditionally utilized by TxDOT in manufacturing their beams, were used to prepare the fibrous concrete mixes.

Cement – High early strength cement was used in all the mixes, since it was necessary to develop high release strengths at an early age in the PSFC I-Beams. Portland cement (Type-III) conforming to ASTM C150 and fly ash (Type-F) conforming to ASTM C618 were the only powder materials used. Fly ash was added to the mix to enhance workability, curtail rise in temperature and reduce cost.

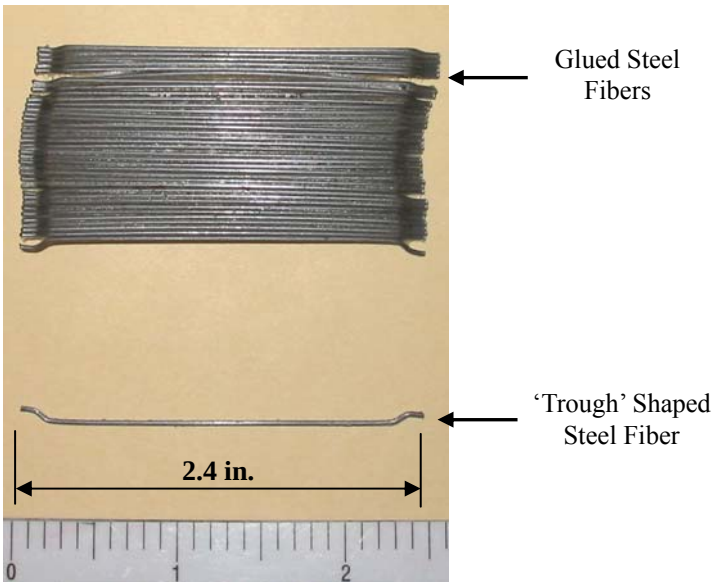

(a) Hooked Steel Fiber RC80/60BN (Bekaert-Dramix®)

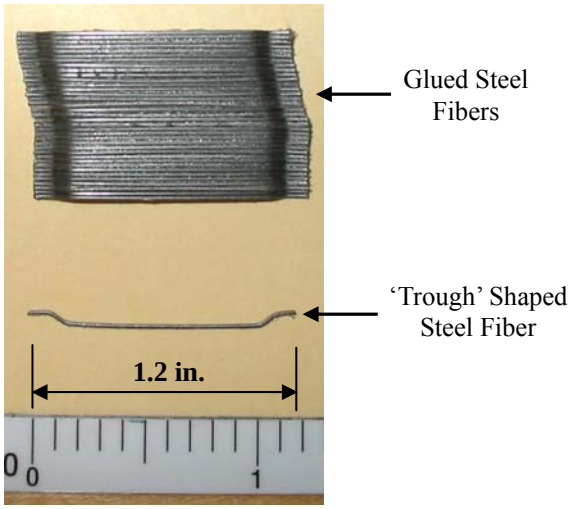

(b) Hooked Steel Fiber ZP305 (Bekaert-Dramix®)

Fig. 7.3 Steel Fibers (Bekaert-Dramix®) used in PSFC I-Beams

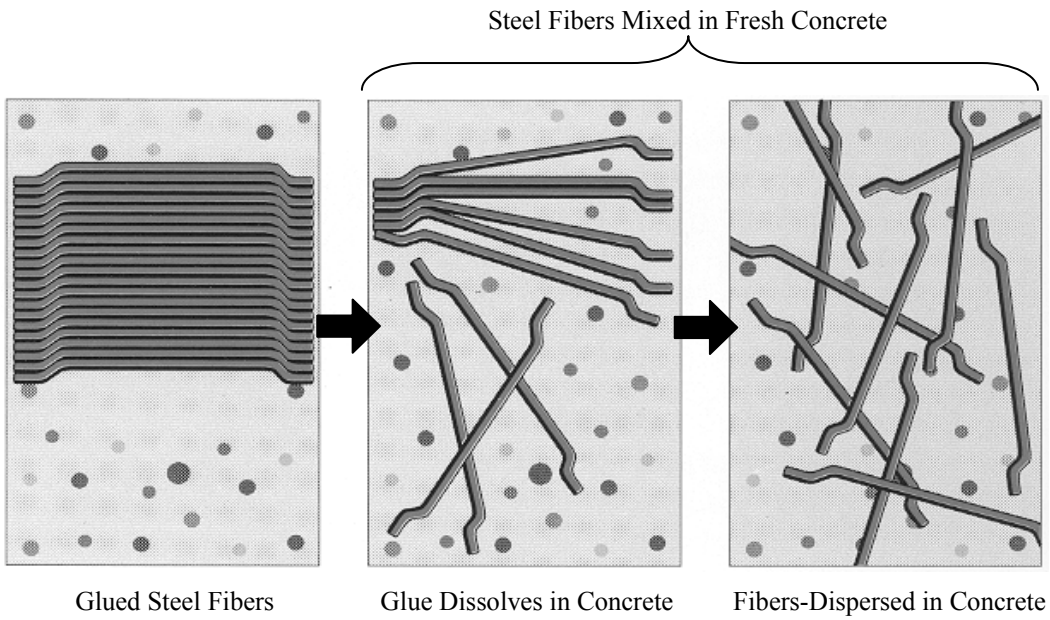

Fig. 7.4 Dispersion of Glued (Collated) Steel Fibers in Concrete

Coarse and Fine Aggregates –The mixes utilized uniformly-graded, rounded, river-bed, coarse aggregates of 3/4 inch nominal size (AASHTO T27 1996) and well-graded, river-bed sand (AASHTO M43 1998).

Admixtures - A Polycarboxylate-based High Range Water Reducing (HRWR) agent conforming to ASTM C 494-1999, Type F was used to achieve workable concrete mixes. A retarder conforming to ASTM C 494-1999, Type-B was added to the mixes as required to delay the initial setting of the mix.

Table 7.3 – Materials Used in Steel Fiber Concrete

Material	Source/Type
Cement	Alamo/ ASTM C150 Type- III
Fly Ash	Rockdale/ ASTM C618 Class F
Coarse Aggregate	Fordyce Briggs/AASHTO T27
Fine Aggregate	Fordyce Murphy/AASHTO M43

Table 7.4 – Concrete Mix Design for PSFC I-Beams

Component (lb/yd^3)	R1 and R5	R2	R3	R4 and R6
Cement	617	617	617	617
Fly ash	206	206	206	206
Cementitious material	823	823	823	823
Water	248	248	248	248
Water/Cement ratio (w/c)	0.4	0.4	0.4	0.4
Water/Cementitious ratio	0.3	0.3	0.3	0.3
Coarse aggregate (CA)	1907	1907	1907	1907
Fine aggregate (FA)	1011	1011	1011	1011
CA/FA ratio	1.88	1.88	1.88	1.88
HRWR / Superplastisizer (oz/100lbs)	11.0	11.0	11.0	11.0
Fibers	67 **LF**	134 **SF**	201 **SF**	201 **SF** +67 **LF**
Retarder (oz/100lbs)	4.0	4.0	4.0	4.0

LF = Dramix Long Fibers; SF = Dramix Short Fibers

Concrete mix design used to cast each of the PSFC beam is given in Table 7.4. The amount of fibers used in a concrete mix can also be reported as its fiber-factor, which is the product of the aspect ratio of the fibers and the volume of fibers in the mix, i.e. $(L_f/D_f)V_f$.

7.5 Fabrication of PSFC I-Beams

All steel fiber concrete mixes were mixed in a 6 yd^3 drum mixer at the Texas Concrete Company's (Victoria, Texas) precast plant. Two cubic yards of concrete was mixed for each beam. The six PSFC I-Beams were cast in two groups on two different days. Beams R2, R3 and R6 were first cast concurrently in a long-line prestressing bed using Type-A steel formwork. The strands were prestressed by hydraulic jacks against the prestressing bed ends. The second group of three Beams R1, R4 and R5 were cast one week after the first group. Concrete for both the groups was prepared in the plant's mixer, transported to the casting location (prestressing bed), and placed into the formwork using a mobile hopper, the chute of which can be seen in Fig. 7.5.

Fig. 7.5. Casting of PSFC I-Beam

During concrete placement, spud vibrators were used for compacting the fibrous concrete, (Fig. 7.5). Casting and compaction of PSFC I-Beams was relatively fast and easy in comparison with the conventional I-beams, even when the mix used large dosage of steel fibers. This was because transverse reinforcement in the beams was totally absent, causing no hindrance to the compaction of the fiber reinforced mix. Thus, fiber reinforced concrete was found to be relatively easy to compact in the absence of any traditional reinforcement. Just after mixing the steel fiber concrete (i.e. before casting the beams), slump tests were carried out for all the mixes.

Curing of the PSFC I-Beams was carried out until a minimum concrete compressive strength of 4000 psi was obtained in the beams, sufficient for release of prestress. One day after casting, the prestressing strands were slowly released and the beams were de-molded.

7.6 Test Setup

The PSFC I-Beams were placed in a vertical loading system at the University of Houston and were subjected to vertical load up to their maximum shear capacity, until failure. The testing system was a specially built steel loading frame with four actuators as depicted in Fig. 7.6. Two of the four actuators (namely actuator B and actuator C) attached to the steel frame were used to apply vertical loads on the beams. Each of the actuators had a maximum load capacity of 320

kips. Details regarding the design, layout and capabilities of the loading system can be found in Laskar et al. (2007).

Fig. 7.6 Test Set-up at University of Houston

Load application points and support locations for PSFC I-Beams are shown in Fig. 7.7. Support bearings beneath the beams were located six inches from each beam end. The applied loads from actuators B and C were 3 feet away from each of the supports for Beams R1, R2, R3 and R4, and at 8 feet from each of the supports for Beams R5 and R6. Actuator loads were applied on the beam via a steel roller and bearing plate assembly. This assembly consisted of two steel rollers (2 in. diameter and 12 in. long) sandwiched between two steel bearing plates (6 in. wide x 12 in. long x 2 in. thick), as shown in Fig. 7.8. This ensured a uniform and frictionless load transfer from the actuators to the top surface of the beam.

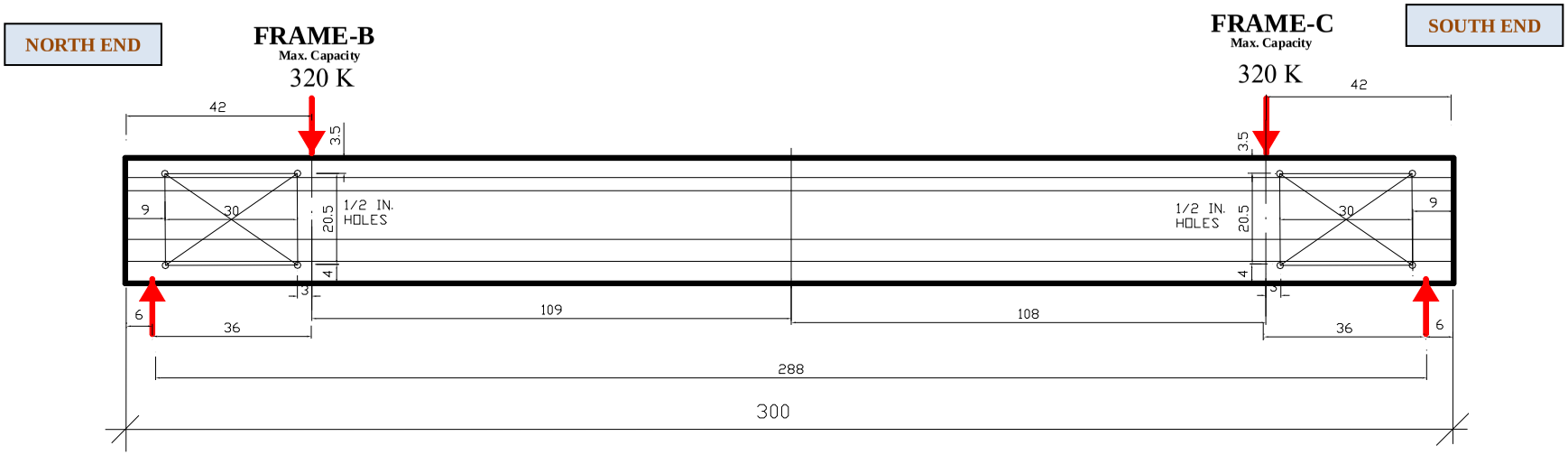

(a) Loading Points and LVDT Locations for Beams R1, R2, R3 and R4

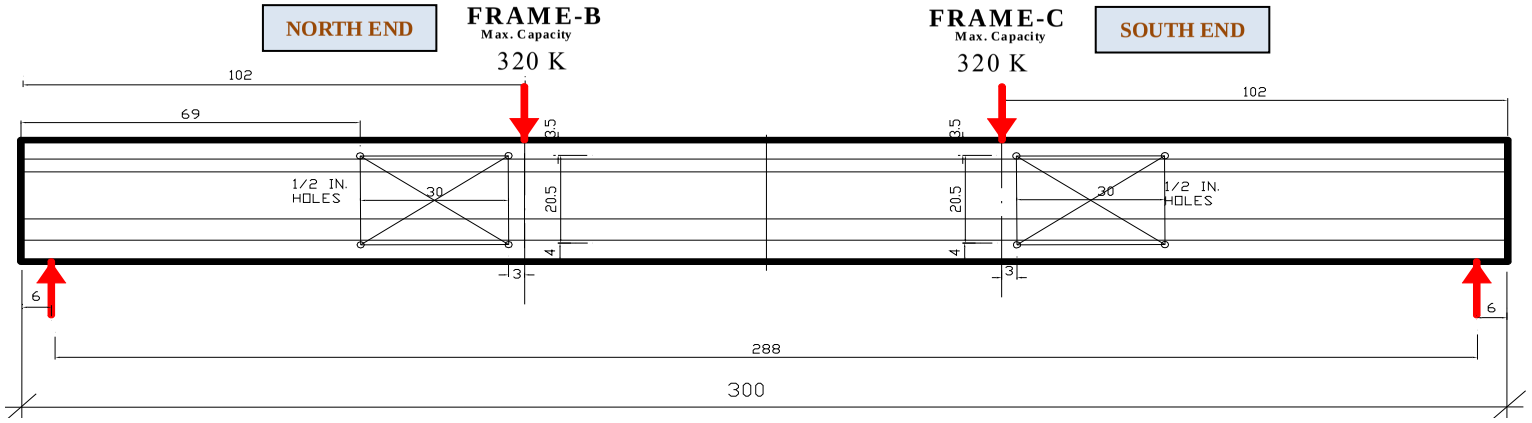

(b) Loading Points and LVDT Locations for Beams R5 and R6

(ALL DIMENSIONS ARE IN INCHES)

Fig 7.7 Loading and Support Locations in PSFC I-Beams

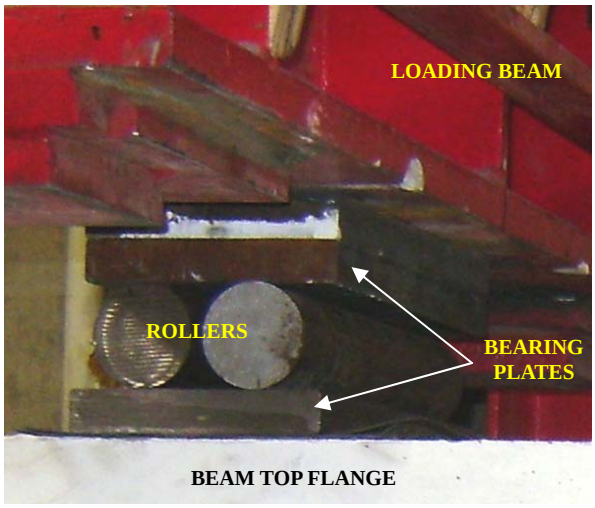

Fig 7.8 Steel Roller-Bearing Plate Assembly used to Load Beams

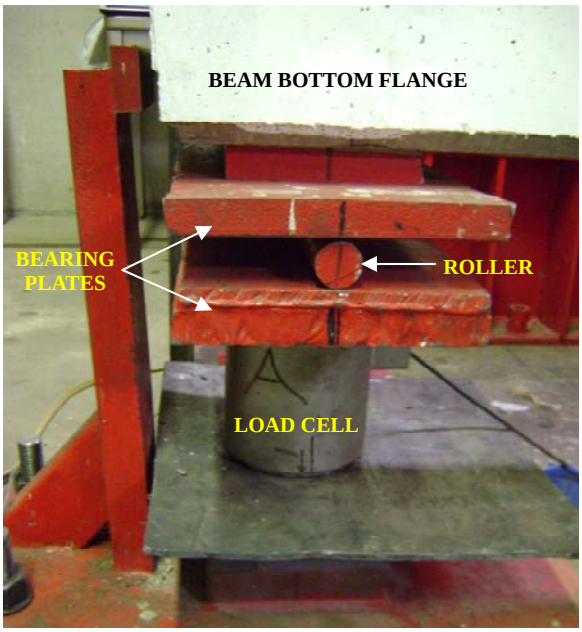

Fig 7.9 Steel Roller-Bearing Plate Assembly used to Support Beams

A typical assembly showing the bearing support arrangement at the beam end is shown in Fig 7.9. A freely movable roller assembly (roller-support) and a fixed roller assembly (hinged-support) were provided at the North and South beam ends, respectively. This enabled free rotation and longitudinal movement of the simply supported beam during test. All the steel

bearing plates and rollers were heat-treated to maximum hardness in order to minimize local deformations. Lead sheets were also used between the load bearing plates and beam surface to help distribute the load evenly.

Beam displacements and concrete strains at important locations on the beam were measured continuously throughout the load test using Linear Voltage Displacement Transducers (LVDTs). A group of seven LVDTs was used at either end and on each side of the beam to measure smeared (average) concrete strains within the beam-web. The LVDTs were arranged in a rosette form as shown in Fig. 7.10. Each rosette consisted of two vertical, three horizontal, and two diagonal LVDTs. The rosettes were mounted on the beam adjacent to the loading points where the web-shear or flexure-shear failure was anticipated (Figs. 7.7 (a), (b) and 7.10).

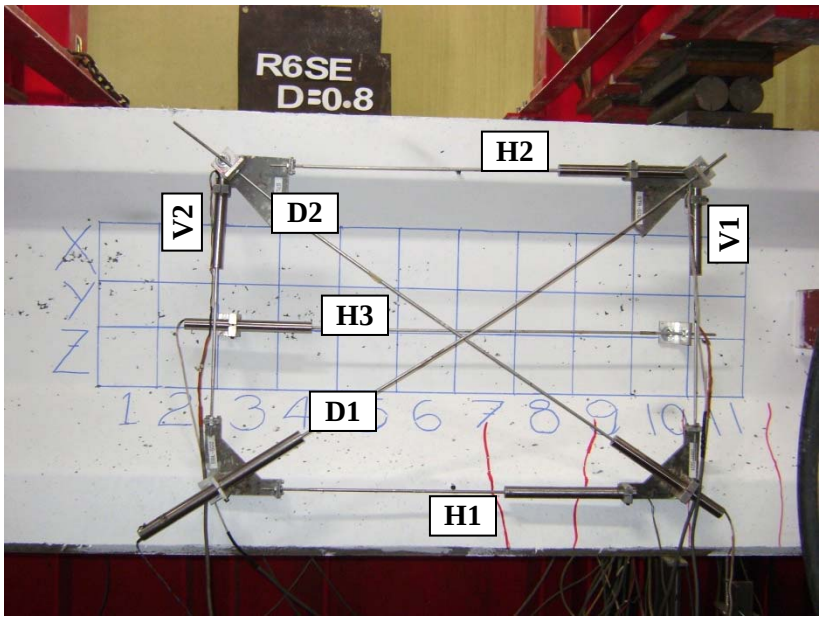

LVDT ID	Measured Smeared Strain in Concrete
H1	ε_{H1}
H2	ε_{H2}
H3	ε_{H3}
V1	ε_{V1}
V2	ε_{V2}
D1	ε_{D1}
D2	ε_{D2}

Fig. 7.10 Typical LVDT Rosette used to Measure Smeared/Average Concrete Strains in PSFC Beams

A total of six LVDTs were used to continuously monitor and measure the vertical deflections of the beam. LVDTs were placed under each beam support (North and South ends) on either sides of the beam (West and East). Two pairs of LVDTs were positioned under the beam at each of the two loading points. These LVDTs were used to measure the total and net deflections of the beam. An additional set of LVDTs was used to monitor potential lateral displacements of the beam.

Two 500 kips capacity load cells were used to monitor support reactions at each beam-end (Fig. 7.9). Two load cells, attached to the loading actuators (B and C), were used to measure the applied load on top of the beam. During a test, force equilibrium between the applied loads (actuators B and C) and the measured reactions (load cells) was always verified.

Non-stop measurement of all the experimental data (beam deflections, strains, loads, and support reactions) from the above sensors were continuously monitored and stored by the HBM 'Spider-8' Data Acquisition System, during a load test. Shear cracks, which formed on the beam web during a load test, were regularly marked on a grid, as shown in Fig. 7.10. The crack widths were measured using a hand-held microscope having a 0.001 in. measuring precision.

The two actuators were precisely controlled in force or displacement modes by the MTS 'MultiFlex' Controller System. Actuators B and C were initially used to apply shear force on the beam in force control mode at a rate of 5 kips/min. During a test, the shear load-displacement curve for a beam was continuously monitored visually on a display screen. When the slope of this load-displacement curve started to decreasing (flatten-out), the control mode of the actuators was switched to displacement control with a rate of 0.2 inch/hour. This displacement control mode was maintained until the failure occurred at either end of the beam. The displacement control feature was essential in capturing the ductility/brittleness behavior of the beam as it failed in shear.

7.7 Experimental Results

Table 7.5 shows the experimental ultimate strengths at failure for the six beams tested (R1 to R6). During the test, although application of load and support arrangements were symmetric for all the beams; only in the case of Beam R2 web-shear failures occurred simultaneous at both the ends. In all the other beams, the weaker end failed first. Even though Beam R3 ultimately failed in flexure, the shear load at failure at both the ends was close to the web-shear capacity, as indicated by the spalling of concrete struts in the web region of this beam.

While testing Beam R4 it was found that the shear capacity was surprisingly increased beyond the anticipated value due to the use of higher fiber-factor. Hence, the beam would have prematurely failed in flexure instead of the desired web-shear failure mode. Therefore, Beam R4 was reinforced with FRP sheets (installed on the beam soffit at the bottom flange) to increase its flexural capacity. The beam was then tested and eventually failed in web-shear mode at the North

end, demonstrating an unexpected high shear capacity. A large portion of the beam was still intact after the failure and therefore the South end was re-tested using a shorter span (14 ft), which failed in web-shear. This test is denoted as 'R4-Short" hereafter in the discussion.

Beams R5 and R6 failed near a region adjacent to the loading point (i.e. at one third span of the beam) in flexural-shear and flexure failure mode, respectively. As a result, both these beams did not have a sufficiently long undamaged length for another re-test in flexure-shear mode. Hence each of these two beams could provide only one failure data point. Beam R5 failed on the South side without any prior warning. The sudden brittle failure of beams subjected to flexure-shear was explained by Kani (1964). When the strength of concrete "teeth" formed between the flexural cracks is smaller than the remaining arch, the beam fails suddenly as soon as the strength of teeth is compromised. Specimen R6 apparently failed in flexure mode instead of the targeted flexure-shear mode. Beam R6 demonstrated much higher web-shear capacity than expected, owing to the use of higher fiber-factor.

Table 7.5 – Experimental Ultimate Strengths at Failure for PSFC I-Beams

Beam ID and Failed End	**Steel Fiber by Volume** (%)	**Fiber Factor**	**Concrete Compressive Strength** (ksi)	**Failure Mode**	**Ultimate Shear Capacity** (kips)	**Ultimate Moment Capacity** (kip-ft.)	**Max. Shear at Ultimate Moment** (kip)	**Max. Moment at Ultimate Shear** (kip-ft.)
R1-North	0.5% LF	0.40	12.6	Web-Shear	**264**	-	-	**793**
R2-North	1% SF	0.55	13.1	Web-Shear	**281**	-	-	**843**
R2-South	1% SF	0.55	13.1	Web-Shear	**295**	-	-	**886**
R3	1.5% SF	0.825	11.9	Flexure/ Web-Shear	-	**876**	**292**	-
R4-North	1.5% SF +0.5% LF	1.225	10.6	Web-Shear	**346**	-	-	-
R5-South	0.5% LF	0.40	12.2	Flexural-Shear	**106**	-	-	**848**
R6	1.5% SF +0.5% LF	1.225	12.8	Flexure	-	**914**	**114**	-

LF = Dramix Long Fibers; SF = Dramix Short Fibers

The comparison of shear strength of PSFC I-Beams tested in this work (Table 7.5), shows that shear capacity of beams can be significantly increased due to the addition of steel fibers in concrete. The beam test results reveal a good co-relation between the fiber-factor and shear

strength. The general trend detected was that with an increasing fiber-factor, shear strength also increased.

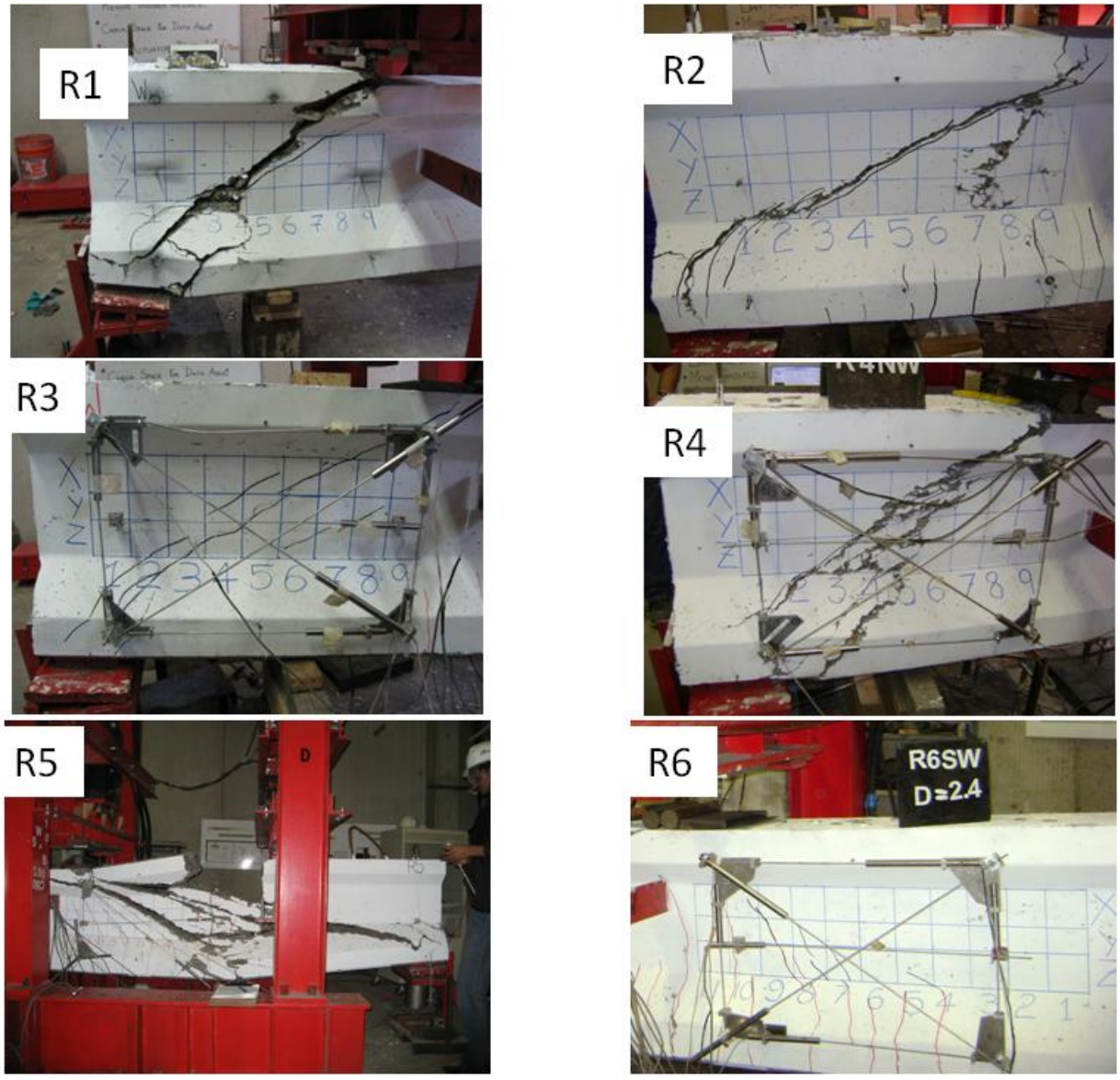

Fig. 7.11 PSFC I-Beams at Failure

The crack pattern and photograph at failure of all the PSFC I-Beams are shown in Fig 7.11. The web-shear failures in beams R1 to R4 were noticeably along a single shear crack which formed between the support and loading points at failure. Studying the failure photographs closely, it can be observed that the damage to the beams with web-shear failure mode (R1 to R4)

was less pronounced in comparison to the damage in beams with a destructive flexure-shear mode of failure (R5 and R6).

From the shape of the load-deflection curves of the PSFC I-Beams, shown in Fig. 7.12, it can be seen that the beams which failed in web-shear mode (R1 to R4) demonstrated higher shear capacities compared to the beams that failed in flexural-shear mode (R5 and R6). It is therefore evident that the shear span-to-effective depth ratio (*a/d*) has a significant effect on the web-shear and flexure-shear strengths of PSFC I-Beams. Laskar et al. (2007) reported similar results for traditional TxDOT Prestressed Concrete (PC) I-Beams. The PSFC I-Beams that failed in flexural-shear or flexure mode displayed higher ductility than the beams which failed in web-shear mode.

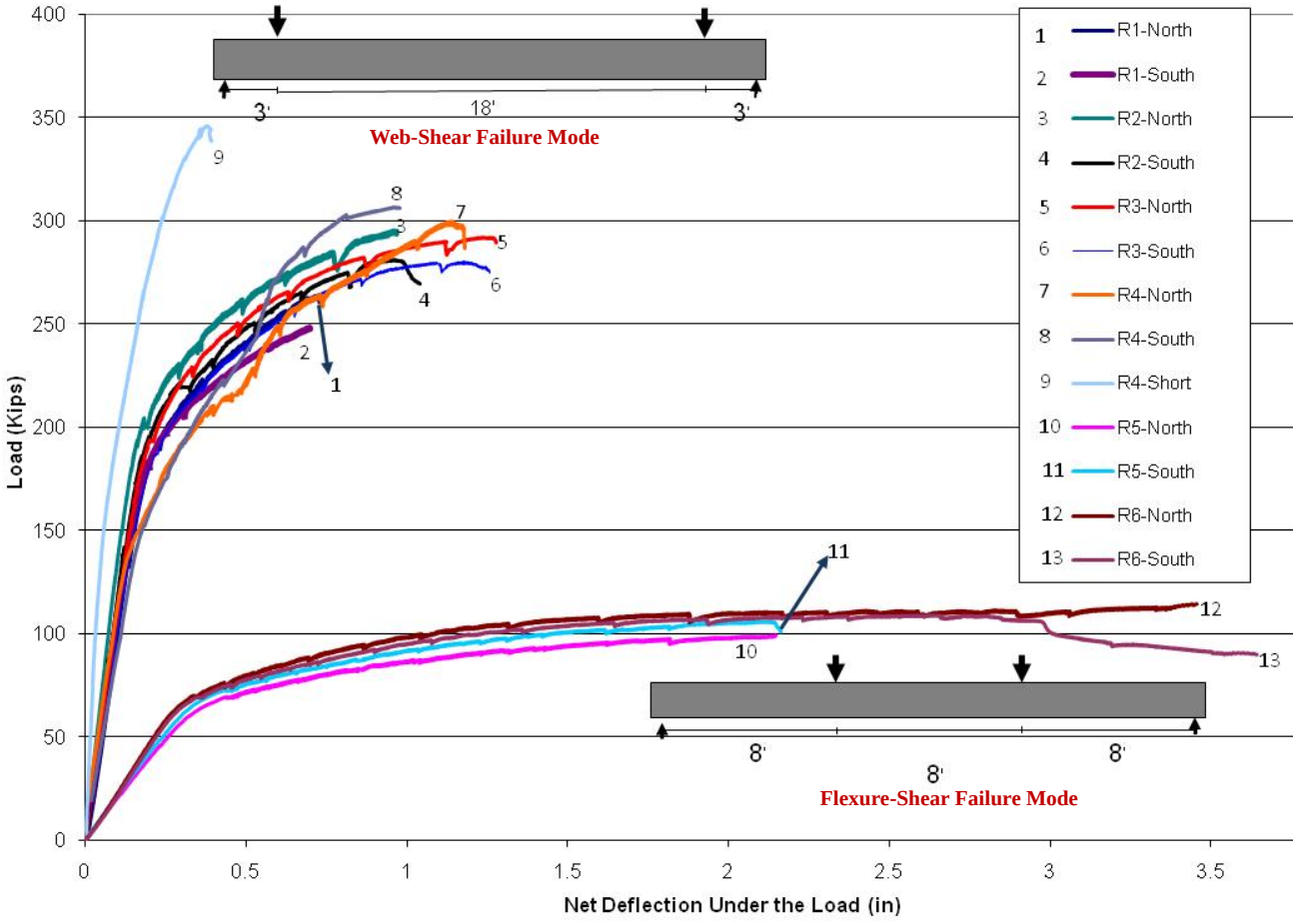

Fig. 7.12 Shear Force vs. Net Deflection Curves for PSFC I-Beams

The advantageous effect of steel fibers on shear strength of PSFC I-Beams can be observed by examining Fig. 7.12. The values of shear force plotted in this figure were obtained from the load cells under the beam's end-supports and were also verified by the load equilibrium computations. The net deflection was obtained from the difference in readings of LVDT placed under the beam at the particular actuator location and the readings of LVDT placed at the corresponding support. Hence, the beam gross deflection values were compensated for the support settlement and then used to plot the load-deflection curves (Fig. 7.12).

Since the compressive strength of concrete for various I-Beams tested were different, the beam's ultimate shear capacity was normalized with the corresponding compressive strength of concrete to better compare all beam results. Normalized shear was calculated as follows:

$$\text{Normalized Shear Force of PSFC I-Beam} = \frac{Shear\ Capacity}{bd\sqrt{f_c}}$$

where, experimental shear capacity is in lbs., f_c is in psi., b and d are in inches.

The normalized shear force vs. net deflection curves for PSFC I-Beam are shown Fig. 7.13. It can be clearly seen that the shear behavior of beams improves with increasing fiber-factor. The ductility in beams also increased with an increase in the fiber factor. This performance shows that the complete replacement of traditional transverse steel by steel fibers is very effective in resisting the shear force.

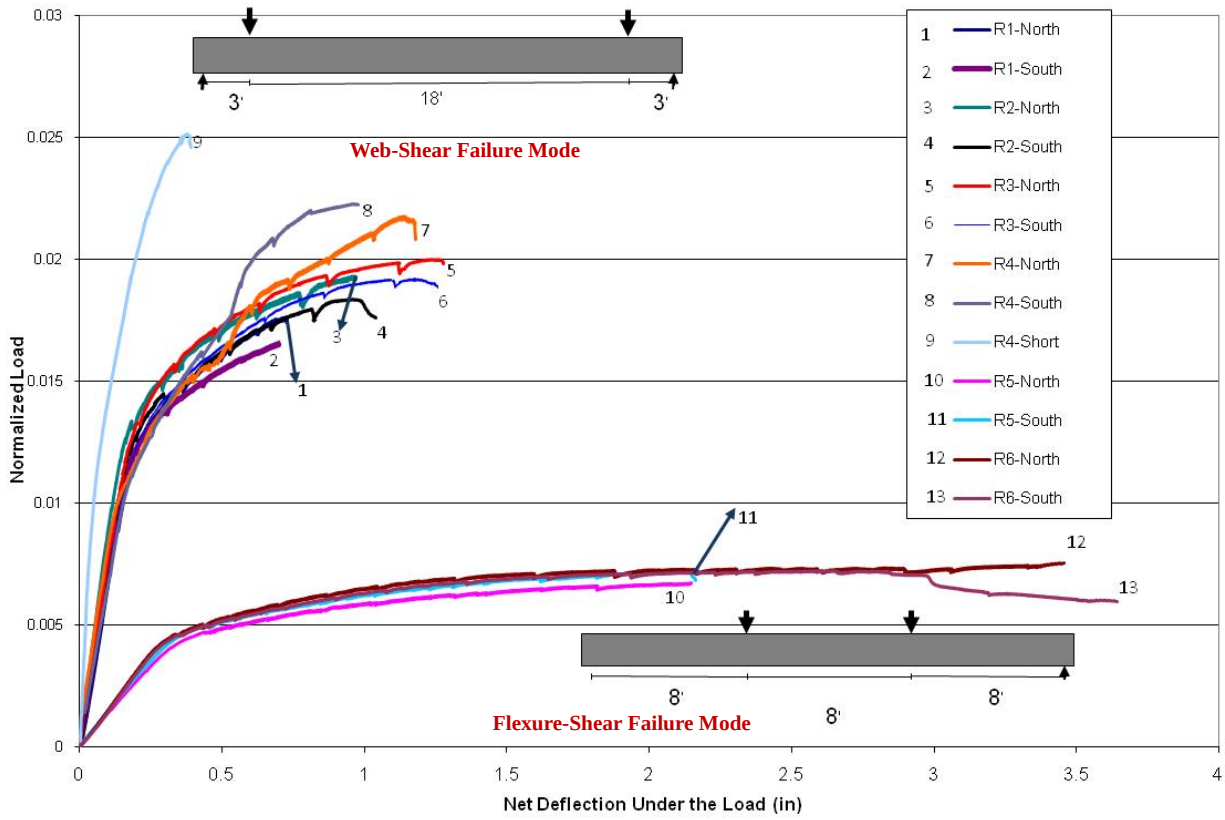

Fig. 7.13 Normalized Shear Force vs. Net Deflection Curves for PSFC I-Beams

To understand the true effectiveness of steel fibers as shear reinforcement, the results of PSFC I-Beams are compared with the results of conventional beams (LB2 and LB4) having mild steel as shear reinforcement, tested by Laskar et al. (2007). Laskar's beams had the same compressive strength of concrete, *a/d* ratios, test span and total prestressing force as the PSFC I-Beams. I-Beam LB2 had a transverse steel ratio of 1% by volume of concrete and failed in web-shear mode, while LB4 had a transverse steel ratio of 0.17% by volume of concrete and failed in flexure-shear mode. The comparisons of web-shear and flexural-shear failures for fibrous and non-fibrous PC beams are shown in Fig 7.14 and Fig 7.15, respectively.

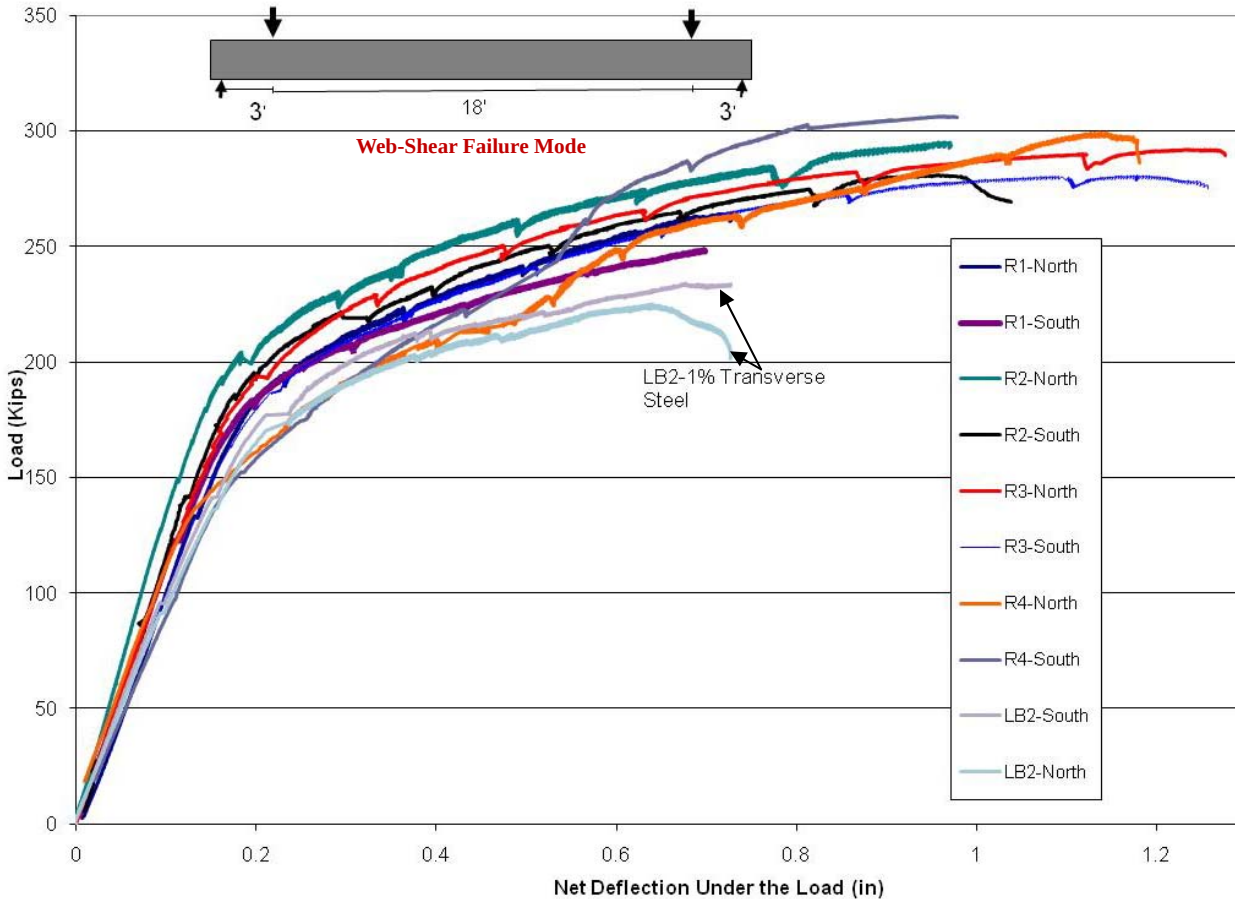

Fig. 7.14 Comparison of PSFC and PC I-Beams in Web-Shear Failure Mode

Fig. 7.14 shows that the PSFC I-Beam demonstrated superior shear performance when copmared with the traditional PC I-Beams. Not only the shear strengths, but also the ductility and stifness were greater in all the PSFC I-Beams in comparison with the PC I-Beams. The increase in shear strengths of PSFC I-Beams over the PC I-Beams due to addition of steel fibers ranged from 15% to 50% corresponding to a fiber factor of 0.40 to 1.225, respectively.

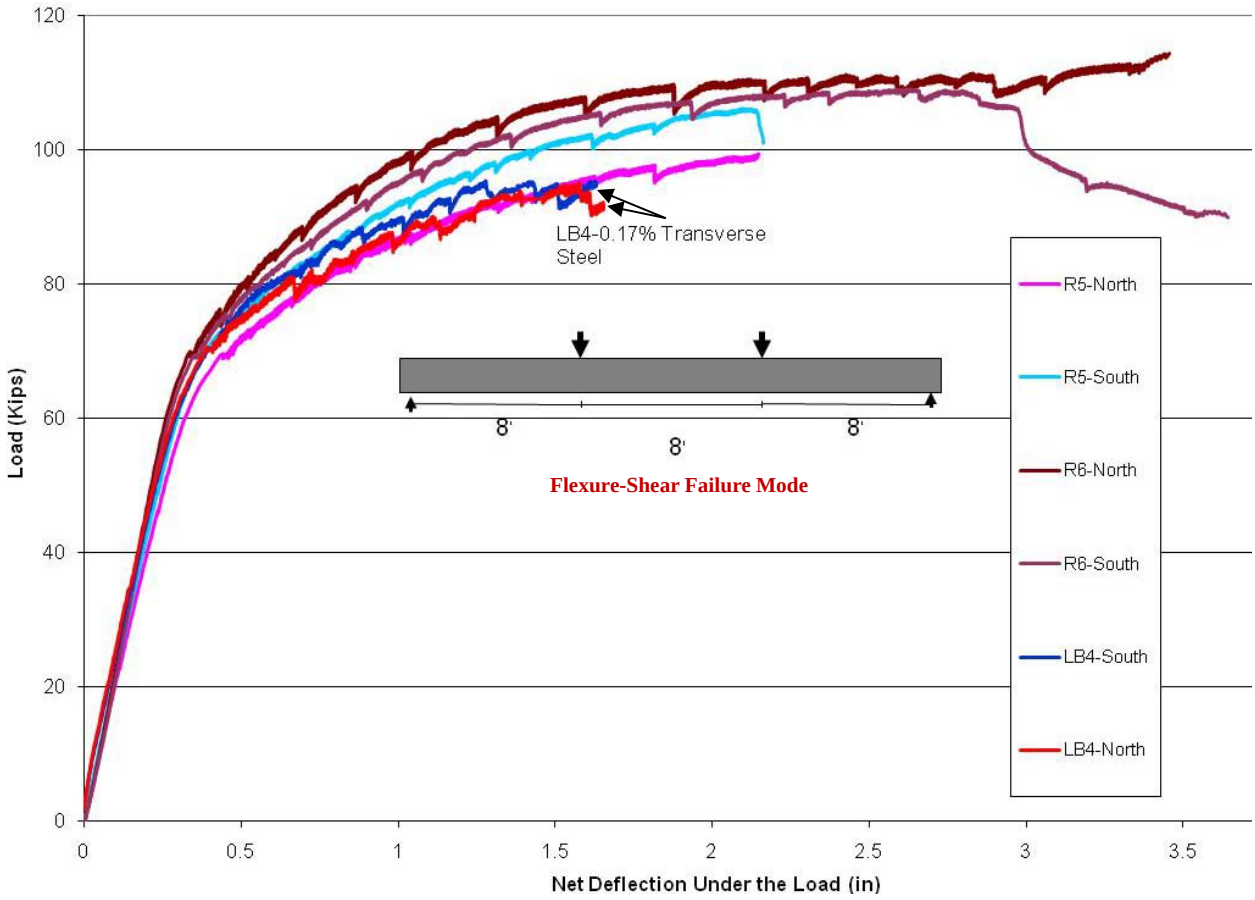

Fig. 7.15 Comparison of PSFC and PC I-Beams in Flexure-Shear Failure Mode

Fig. 7.15 shows that the PSFC I-Beam also demonstrated superior flexure-shear performance when copmared with the traditional PC I-Beams. Not only the flexure-shear strengths, but also the ductility was greater in all the PSFC I-Beams in comparison with the PC I-Beams. The increase in flexure-shear strengths of PSFC I-Beams over the PC I-Beams due to addition of steel fibers ranged from 15% to more than 24% corresponding to a fiber factor of 0.40 to 1.225, respectively. It can be clearly observed from the Fig. 7.14 and Fig 7.15 that web-shear is affected more than the flexure-shear behavior of PC beams owing to the addition of steel-fibers.

7.8 Shear Crack Widths and Crack Patterns

As mentioned earlier, shear cracks were continuously tracked and measured during the load tests of the beams. A grid was marked on the beam-web at both the beam-ends to facilitate easy identification and location of the shear cracks. Hand-held microscopes were utilized to precisely

measure the shear crack width with an accuracy of 0.001 inch. Fig. 7.16 (a) to (d) shows the plot of the normalized shear force and corresponding shear crack width in Beams R1 to R4 (having web-shear mode of failure) measured on four different sides of the beams, during the test. The represented shear crack widths for a given beam were the maximum crack widths recorded along the most dominating shear crack in a beam during the test.

The onset of shear crack formation in all the beams initiated at the mid height of the beam web and was oriented along a line joining the loading and support points. Shear cracks of this nature are referred to as "diagonal tension cracks", because the general direction of principal tension is perpendicular to this crack. The ligament of concert formed between adjacent diagonal tension cracks is referred to as a concrete compression strut. In the conventionally reinforced PC beams, the applied shear force is resisted by tension in transverse rebars and compression in the concrete strut (Schlaich et al. 1987). In the case of PSFC girders, diagonal tension is resisted solely by the steel fibers. In the test beams, the initial diagonal tension crack did not generally progress to form the failure surface, but as the load increased, other cracks appeared and further developed into a failure surface with a single dominant failure shear crack (see Fig. 7.11).

Steel fibers were clearly observed to restrict the width of the shear cracks, as seen in Fig.7.16. Generally, it was observed that as the fiber-factor increased the shear crack width for a given load decreased. Also, the load at which first visible shear crack appeared increased as the fiber-factor increased. This can be attributed to the fact that with the use of higher fiber-factor, more steel fibers are available in bridging and intersecting the shear crack. The stresses across the shear crack will therefore be shared by a larger number of steel fibers, thereby reducing the tensile strain across the crack. As the strains across the crack and in the steel fibers are reduced, the crack widths will be less.

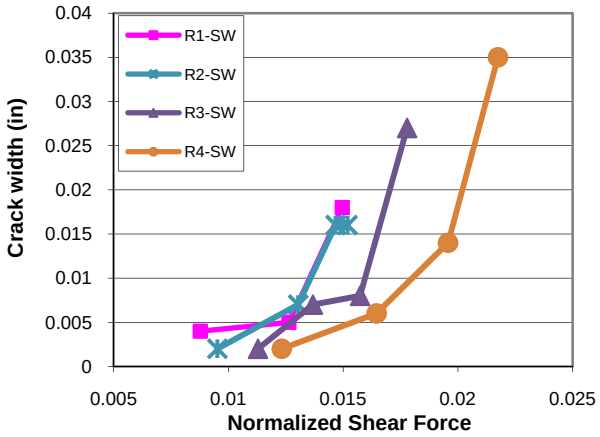

(a) Crack Widths on South-West Side

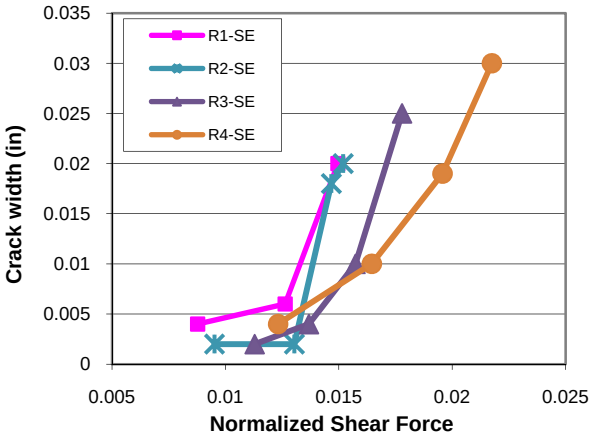

(b) Crack Widths on South-East Side

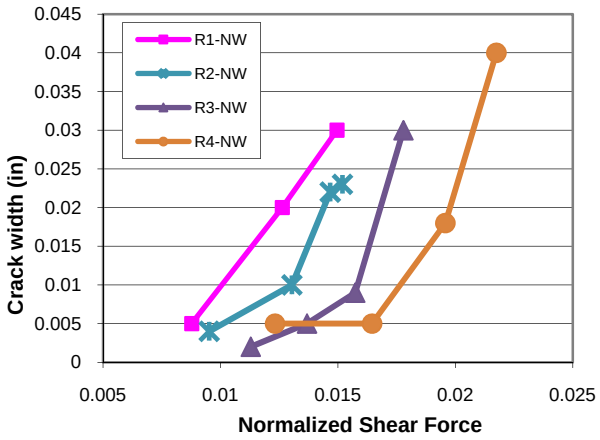

(c) Crack Widths on North-West Side

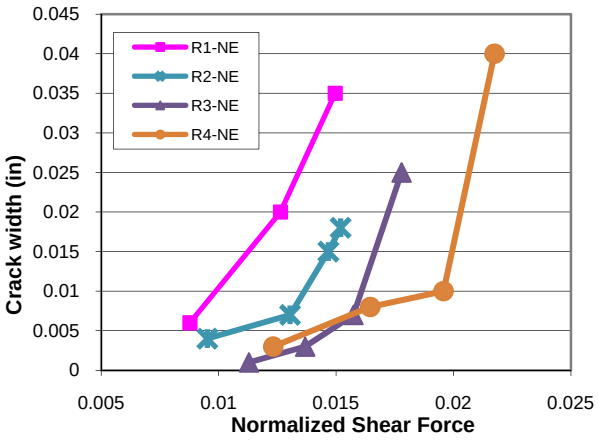

(d) Crack Widths on North-East Side

Fig.7.16 Shear Crack Widths vs. Normalized Shear Force in Beams R1 to R4

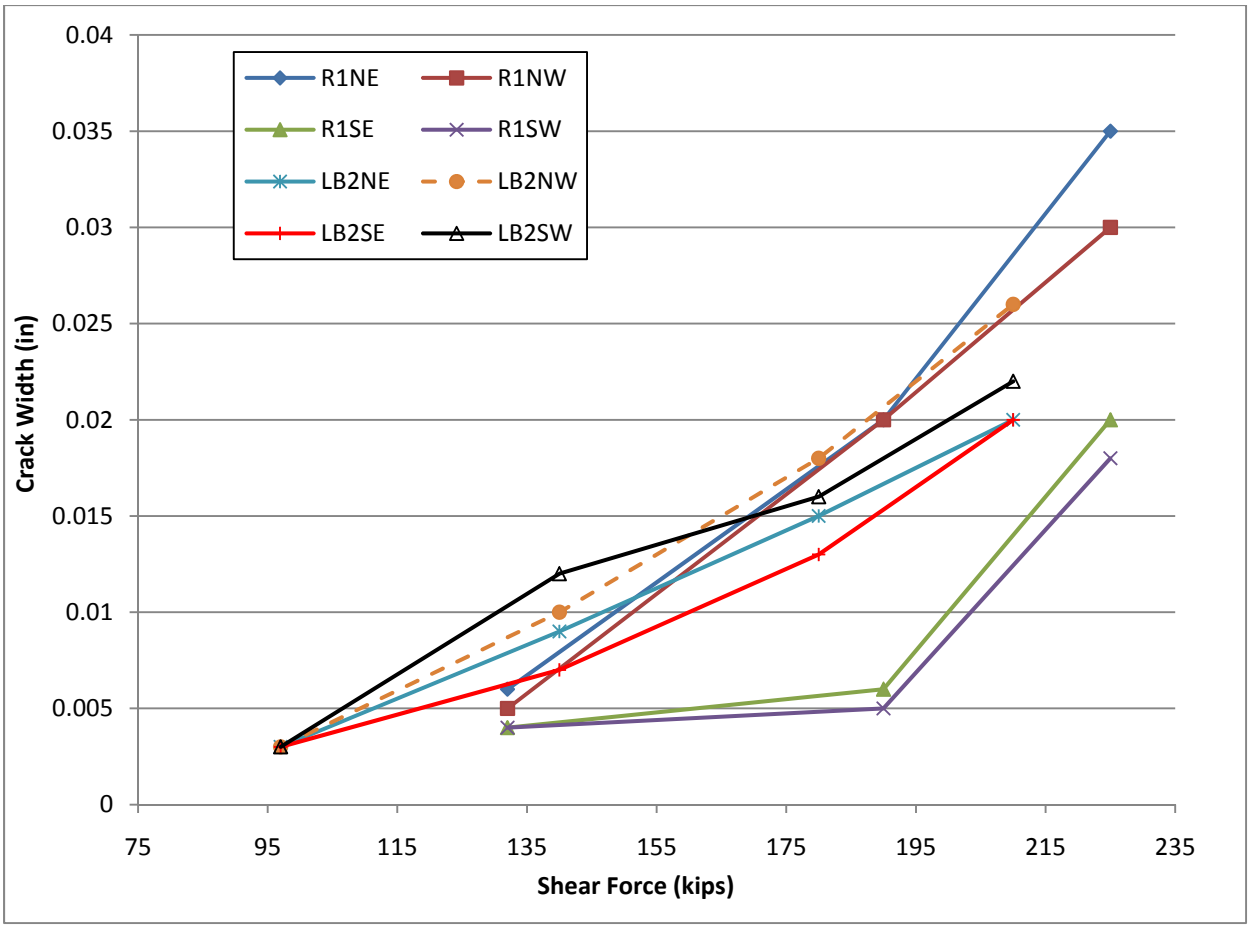

Fig.7.17 Shear Crack Widths vs. Shear Force in Beams R1 and LB2

To better understand the effectiveness of steel fibers in controlling the shear crack widths in PC beams, Fig. 7.17 is plotted depicting the crack widths of fibrous (Beam R1) and non-fibrous (Beam LB2) beams. It can be seen from Fig. 7.17 that the onset of shear cracking for beams with steel fibers occurred at a higher normalized shear force than those without steel fibers. This indicates that the addition of steel fibers in beams is helpful in preventing the development and growth of initial shear cracks. This property of steel fibers can be helpful particularly at service load level in PC highway-bridge beams.

The above discussion signify that the replacement of traditional transverse rebars with steel fibers enhance the shear crack resistance in PC beams. The test results demonstrated that steel fibers more effectively delayed the opening of cracks beyond the service load level in the PSFC I-Beams in comparison with the traditionally reinforced PC beams.

CHAPTER 8

SHEAR TESTS OF PRESTRESSED STEEL FIBER CONCRETE BOX-BEAMS

8.1 Introduction

Prestressed Box-beams are commonly used by TxDOT in bridges where higher shear and torsional resistance is required. These beams have densely reinforced webs with traditional rebars and hence are a challenge to cast. Two-stage casting of Box-beams is usually carried out by pouring the bottom flange first and then the rest of the beam. Based on the results of previous research work done at the University of Houston (UH) on Prestressed Steel Fiber Concrete (PSFC), the researcher believe that steel fiber concrete may not only ease the manufacturing, but also enhance the structural behavior of the Box-beams. Therefore, to ascertain the construction feasibility and structural performance of PSFC Box-beams, load tests on six full-size Box-beams were carried out. This chapter presents the results of the PSFC Box-beams tested at the UH.

The objective of this part of the test program was to study the local and global shear failure characteristics of the PSFC Box-beams. These beams were tested with the same strain-control procedure used for the PSFC I-Beam tests, discussed in Chapter-7. Results from the I- and Box-beam and utilizing the constitutive laws (SMM-PSFC) that were developed in this research (Chapter-6), calibration of a new analytical model - Simulation of Concrete Structures (SCS), was carried out to predict the shear behavior of PSFC beams. Chapter-9 presents the details of the unique SCS model implemented to predict the structural behavior of PSFC beams.

8.2 Testing Program

PSFC Box-beam test specimens as shown in Fig. 8.1 were used in the load tests. The original TxDOT Type-4B20 box-beam cross-section was slightly modified to suite the testing facility at the UH. All beams were designed with 19 - (0.5”oversize diameter) 7-wire, low-relaxation strands. Dramix steel fibers (which structurally performed the best as discussed in Chapter 3) that were used in the tested I-Beams (Chapter-7), were also used to produce the PSFC Box-beams. No traditional transverse rebars (stirrups) were used in any of the beams; the shear reinforcement consisted solely of steel fibers. The Box-beams were specifically designed to investigate the effects of following two variables on shear performance: (a) Shear failure modes:

web-shear and flexure-shear, (b) Fiber dosage, i.e. percent of steel fiber by volume of concrete.

The six Box-beams were divided into three groups based on the shear span-to-effective depth ratio (*a/d*) used for testing. The first group of Box-beams (RB1and RB4) was designed to fail in web-shear failure with shear span-to-effective depth ratio (*a/d*) of 1.8. The second group of Box-beams (RB2 and RB6) was designed to examine the region referred to as Kani's Valley (Kani 1964) and loaded at *a/d* ratio of 2.5. The third group of Box-beams (RB3 and RB5) was designed to fail in flexure-shear failure mode with *a/d* ratio of 4.1. Another parameter that was varied in the Box-beams tested was the amount of steel fiber dosages (V_f of 1.0% and 1.5% by volume of concrete) used as shear reinforcement. Table 8.1 shows the test variables for all six Box-beams, RB1 to RB6.

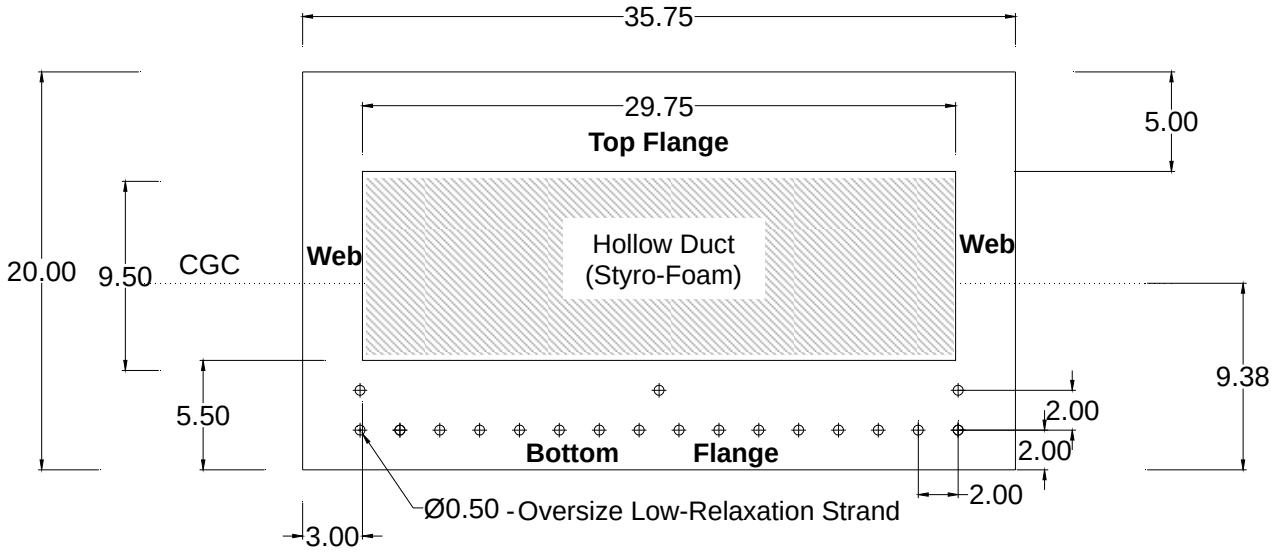

Fig. 8.1 Cross Section of PSFC Box-Beam.

(All Dimensions in inches)

Table 8.1 – Test Variables of PSFC Box-Beams

Beam ID	Mode of Failure	*a/d* Ratio	Concrete Compressive Strength, (ksi)	Volume of Steel Fiber Reinforcement V_f	Fiber Factor $[(L_f/D_f)V_f]/100$
RB1	Web-Shear	1.8	9.60	1% SF	0.55
RB2	Web/Flexure-Shear	2.5	9.56	1% SF	0.55
RB3	Flexural-Shear	4.1	9.69	1% SF	0.55
RB4	Web-Shear	1.8	10.44	1.5% SF	0.825
RB5	Flexural-Shear	4.1	10.88	1.5% SF	0.825
RB6	Web/Flexure-Shear	2.5	11.08	1.5% SF	0.825

SF = Dramix Short Fibers with $L_f/D_f = 55$; L_f = Length of Steel Fiber; D_f = Diameter of Steel Fiber

8.3 Details of PSFC Box-Beams

The total depth of the Box-beams tested was 20 inches and the thickness of the top and bottom flange were 5 inches and 5.5 inches, respectively. Total beam width was 35.75 inches. The thickness of each of the two webs was 3 inches. Prestressing strands in all the Box-beams were straight. The cross sectional area of each strand was 0.166 in^2. The prestressing strands had ultimate strength of 270 ksi. Total length of the Box-beams tested was 25 feet and the test-span length was 24 feet. Fig. 8.2 shows the typical form-work used for the Box-beam just before placing concrete. A 10 in. wide end diaphragm (i.e. block-out) was provided at both beam ends, similar to the ones typically provided in conventional box beam.

Fig. 8.2 Details of PSFC Box-Beam Before Casting.

8.4 Materials and Mix Design

Short steel fibers manufactured by Bekaert-Dramix® were used to cast the PSFC Box-beams. The steel fibers were 'trough' shaped with hook at both ends and were collated together. The short fiber (SF) - ZP305 as shown in Fig. 7.3(b) was 1.2 inches long and 0.022 inch in diameter (aspect ratio of 55) and had a tensile strength of 160 ksi. The steel fibers were relatively stiff and glued into bundles i.e. collated. The glue dissolved in the water during mixing, thus dispersing the fibers in the concrete mix. The amount of steel fibers used in the concrete mix is reported as its fiber factor, which is the product of the aspect ratio of the fibers and the volume of fibers in the mix. Sources and specification of different materials used in the concrete mix are shown in Table 8.2. Locally available materials, which were traditionally utilized by TxDOT in manufacturing their beams, were used to prepare the fibrous concrete mixes. Concrete mix design used to cast each of the PSFC Box-beams is given in Table 8.3.

Cement – High early strength cement was used in all the mixes, since it was necessary to develop high release strengths at an early age in the PSFC Box-beams. Portland cement (Type-III) conforming to ASTM C150 and fly ash (Type-F) conforming to ASTM C618 were the only powder materials used. Fly ash was added to the mix to enhance workability, curtail rise in

temperature and reduce cost.

Coarse and Fine Aggregates –The mixes utilized uniformly-graded, crushed limestone coarse aggregates of 3/4 inch nominal size (AASHTO T27 1996) and well-graded, river-bed sand (AASHTO M43 1998).

Admixtures - A High Range Water Reducing (HRWR) agent conforming to ASTM C 494-1999, Type F was used to achieve workable concrete mixes. A retarder conforming to ASTM C 494-1999, Type-B was added to the mixes as required to delay the initial setting of the mix.

Table 8.2 – Materials Used in Steel Fiber Concrete

Material	Source/Type
Cement	Capitol/ ASTM C150 Type- III
Fly Ash	Headwaters-Jewitt / ASTM C618 Class F
Coarse Aggregate	Hanson Arena /AASHTO T27
Fine Aggregate	Hanson Arena /AASHTO M43
HRWR (Superplistizer)	Sika 2110/ ASTM C 494, Type F
Retarder	Sika Plastiment/ ASTM C 494, Type-B

Table 8.3 – Concrete Mix Design for PSFC Box-beams

Component (lb/yd.^{3})*	**Box-beam RB1, RB2 and RB3**	**Box-beam RB4, RB5 and RB6**
Cement	617	617
Fly ash	206	206
Cementitious material	823	823
Water/Cement ratio (w/c)	0.39	0.39
Water/Cementitious ratio	0.29	0.29
Coarse aggregate (CA)	1690	1907
Fine aggregate (FA)	1232	1011
CA/FA ratio	1.37	1.88
HRWR (fl.oz./cwt)	3 (5.8)	5.7 (11)
Fibers	66	200
Retarder	2.1 (4)	2.1 (4)

8.5 Fabrication of PSFC Box-Beams

All steel fiber concrete mixes were mixed in a 6 yd^3 drum mixer at the Flexicore (Houston, Texas) precast plant. Two cubic yards of concrete was mixed for each beam. The six PSFC Box-beams were cast in two groups on two different days. Beams RB1 to RB5 were first cast concurrently in a long-line prestressing bed with a specially made steel formwork for the given cross section. The strands were prestressed by hydraulic jacks against the prestressing bed ends. The last beam RB6 was cast a month after the first group of beams. Concrete was prepared in the batch plant's mixer, transported to the casting site, and deposited into the formworks using a mobile hopper as shown in Fig. 8.3. During casting spud vibrators were used for consolidating the concrete, as shown in Fig. 8.4.

Fig. 8.3 Casting of PSFC Box-Beams

Fig. 8.4 First-Stage Concrete Compaction using Spud Vibrators in PSFC Box-Beams

Each beam was cast in two different monolithic stages. The concrete in first stage was used to cast the entire length of bottom flange. After finishing the first stage of casting, a styrofoam block was placed throughout the length of the beam to create the required void as shown in Fig 8.5. Hold-down rods were installed (Fig. 8.5) to restrain the movement of the styrofoam block due to concrete uplift force during casting. The second lift was then placed to fill out the web and top flanges of the beam. It was made sure that cold joint was not formed between the first and second concreting stage. Just after mixing the steel fiber concrete (i.e. before casting the beams), slump tests were carried out for all the mixes.

Fig. 8.5 Placement of Styrofoam after First-Stage of Concrete Casting in PSFC Box-Beams

Casting and compaction of PSFC Box-beams was relatively fast and easy in comparison with the conventional box beams, even though the mix used large dosage of steel fibers. This was because transverse reinforcement in the beams was totally absent, causing no hindrance to the compaction of the fibrous mix. Thus, fiber concrete was found to be relatively easy to compact in the absence of any traditional reinforcement.

Curing of the PSFC Box-beams was carried out until a minimum concrete compressive strength of 4000 psi was obtained in the beams, sufficient for release of prestress. One day after casting, the prestressing strands were slowly released and the beams were de-molded.

8.6 Test Setup

The loading frame and actuator assembly used to test the PSFC I-beams (described in Chapter-7) were also employed to carry out load tests on the PSFC Box-beams. Load was applied by actuator at either end of the beam on the top flange. This load was distributed evenly throughout the width of top flange using a steel-box beam (HSS 6 x 6 x ½ in.) as depicted in Fig.

8.6. Actuator loads were applied on top of this steel-box beam through a pair of two 12 in. long x 6 in. wide x 2 in. thick steel bearing plates and three rollers (2 inches dia.), as seen in Fig. 8.6. This arrangement ensured uniform and relatively frictionless load transfer from the actuators on to the beam surface.

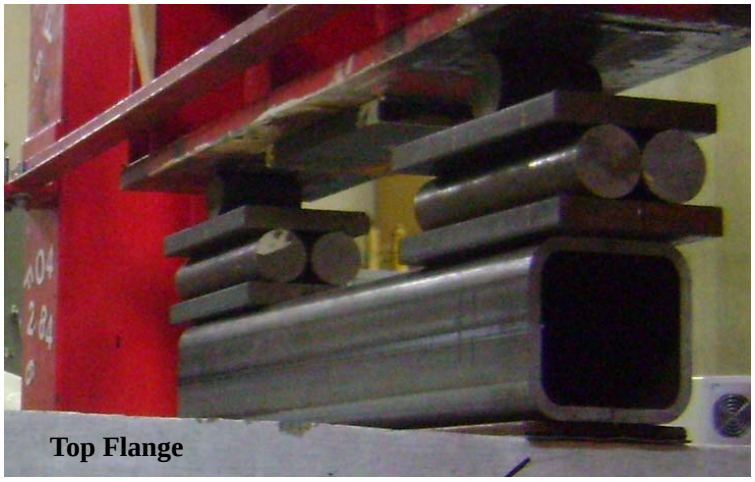

Fig. 8.6 Loading Assembly for PSFC Box-Beams

During the load testing, the Box-beam was supported on hinged supports. Two hinged-roller supports at one end and two fixed-hinged supports at the other end allowed free rotation and translation of the beam. Thus the beam acted as a simply-supported beam in a test. Since the Box-beam has two webs, the beam supports needed careful adjustments in their height and location to assure uniform loading of the webs. Thus, care was taken so as not to induce undesirable torsional forces in the web.

Beams RB1 and RB4 were supported using total of four load cells (two at each end) under the beam supports. This arrangement had the potential to create undesirable torsional restraint. Therefore, all the other Box-beams were tested with three support arrangement. Load cell-support was placed one on the North side and the other two on the South side, forming a stable and determinate simply-supported beam arrangement. The three-point support scheme simulates actual field conditions and assures the necessary torsional degree of freedom. Fig 8.7 shows the

three point support arrangement; a single support load cell can be seen on the north end and two cells can be seen on the south end.

(a) One Load Cell Support at North

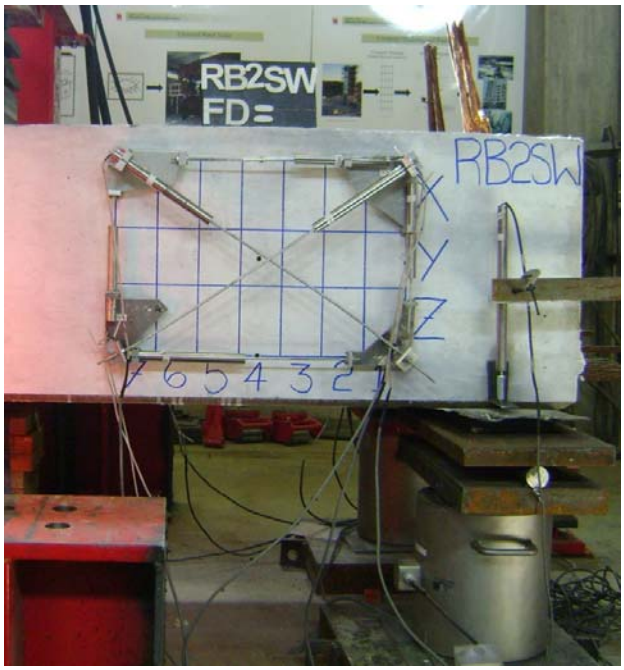

b) Two Load Cell Supports at South

Fig. 8.7 Three-point Load Cell Support System in PSFC Box-Beam

The positions of application of vertical load on the Box-beams and the support positions are shown in Fig. 8.8(a) to (c). The loads from actuators B and C were applied at 2.67 feet, 3.6 feet and 6 feet away from the supports (both north and south supports) for Box-beams with *a/d* ratios of 1.8, 2.5 and 4.1, respectively. Actuator loads and support reactions were transferred on the beam surface through steel rollers and bearing plates assemblies. All the bearing plates and rollers were heat-treated to maximum hardness, in order to minimize local deformations. Lead sheets were also used between the load bearing plates and beam surface.

The procedure adopted to control the force and displacement in the actuators was similar to the one described in Chapter-7, for I-beam tests.

Beam displacements and concrete strains at important locations on the beam were measured continuously throughout the load test using Linear Voltage Displacement Transducers (LVDTs). A group of six LVDTs was used at either end and on each outer side of the beam-web

to measure smeared (average) concrete strains within the beam-web. The LVDTs were arranged in a rosette form as shown in Fig. 8.9. Each rosette consisted of two vertical, two horizontal, and two diagonal LVDTs. The rosettes were mounted on the beam adjacent to the loading points where the web-shear or flexure-shear failure was anticipated (Figs. 8.8 (a) to (c) and Fig. 8.9).

A total of eight LVDTs were used to continuously monitor and measure the vertical deflections of the beam. LVDTs were placed under each beam support (North and South ends) on either sides of the beam (West and East). Two pairs of LVDTs were positioned under the beam corresponding to each of the two loading points. These LVDTs were used to measure the total and net deflections of the beam. An additional set of LVDTs was used to monitor potential lateral displacements of the beam. Thus, during the load test in all thirty-four LVDTs were used per beam.

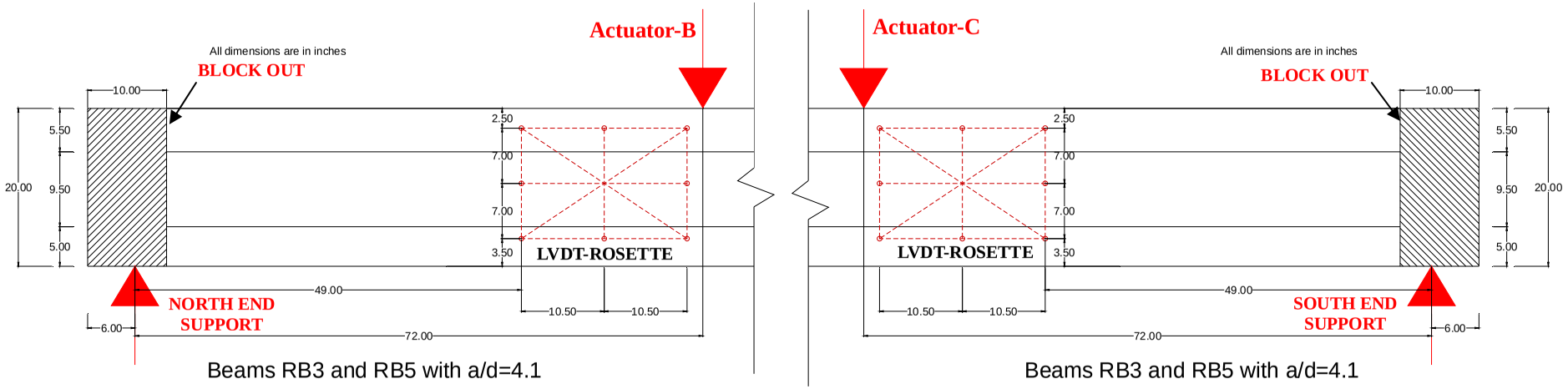

Fig. 8.8 (a): Load and Support Positions for PSFC Box-beams with *a/d* Ratio of 4.1

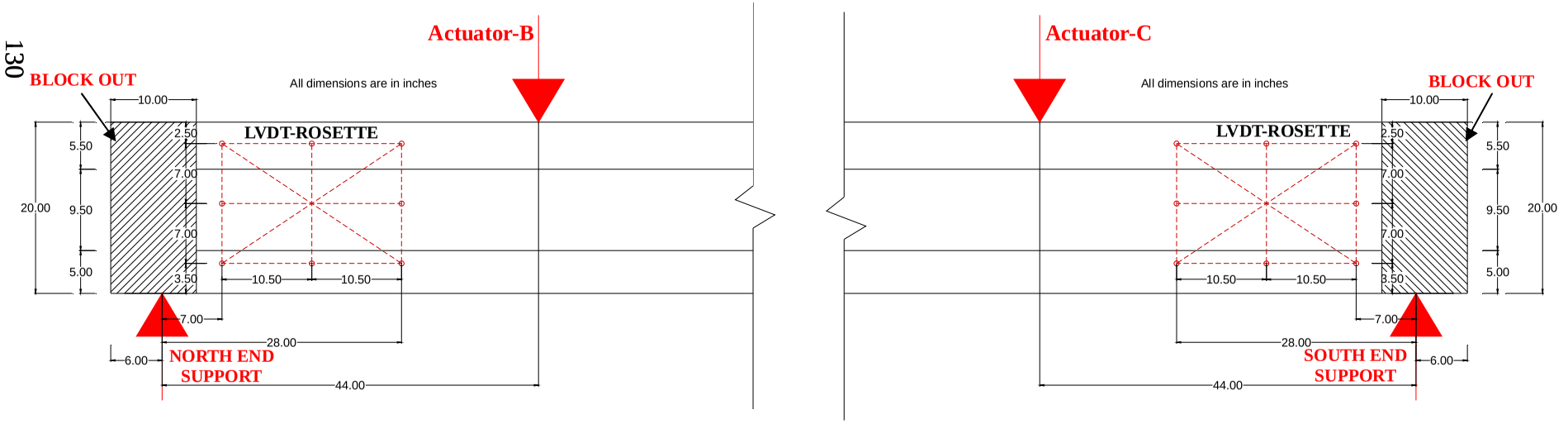

Fig. 8.8 (b): Load and Support Positions for PSFC Box-Beams with *a/d* Ratio of 2.5

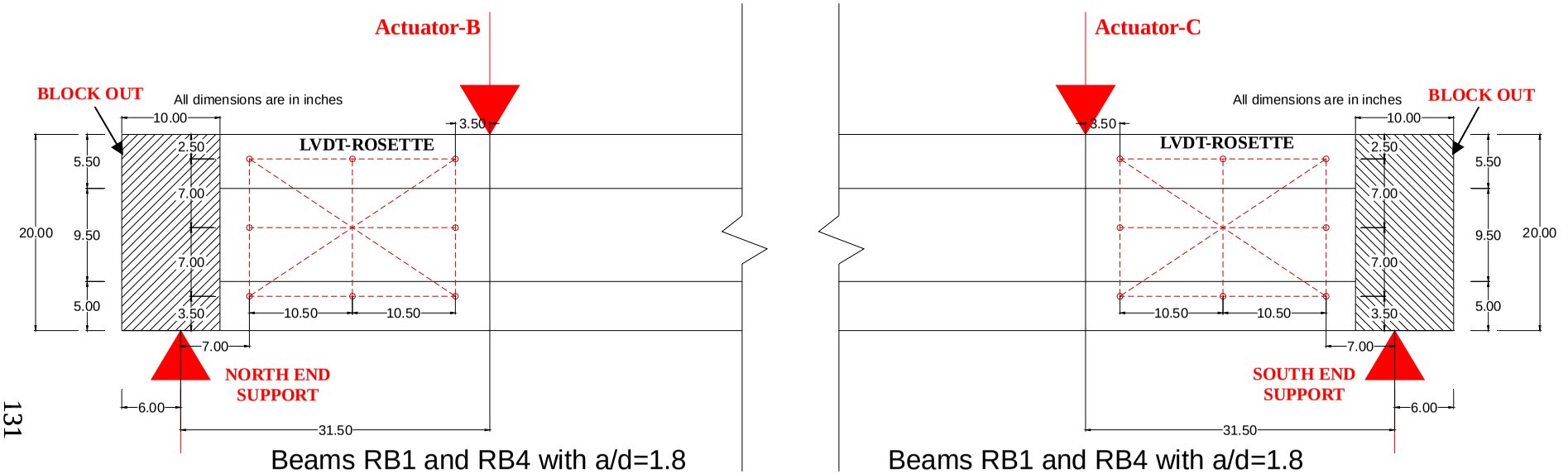

Fig. 8.8 (c): Load and Support Positions for PSFC Box-Beams with *a/d* Ratio of 1.8

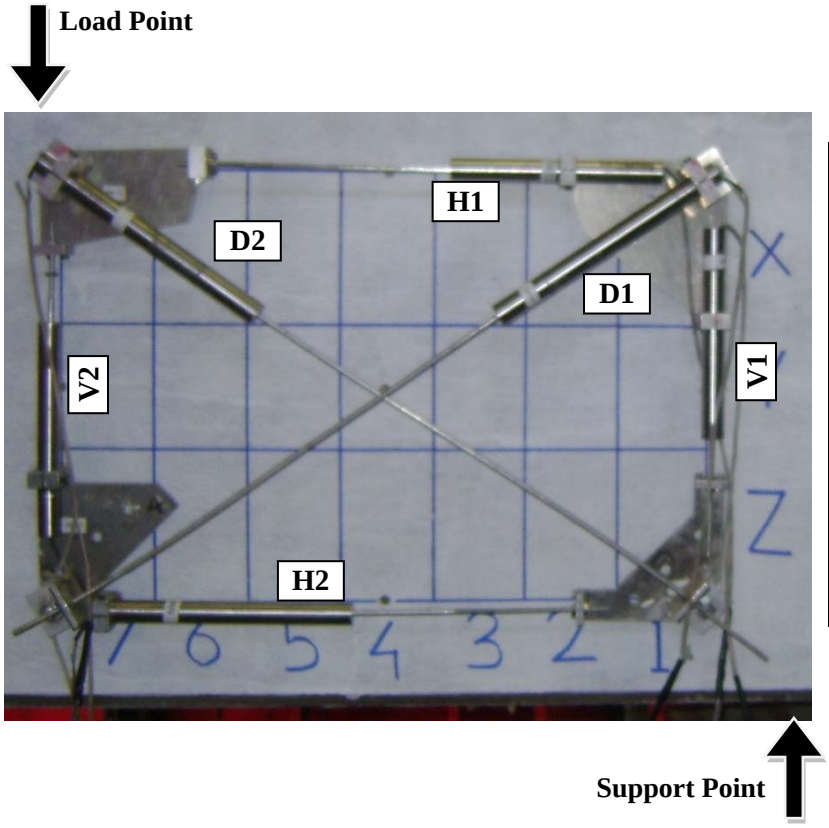

LVDT ID	Measured Smeared Strain in Concrete
H1	ε_{H1}
H2	ε_{H2}
V1	ε_{V1}
V2	ε_{V2}
D1	ε_{D1}
D2	ε_{D2}

Fig. 8.9 Typical LVDT Rosette used to Measure Smeared/Average Concrete Strains in PSFC Box-Beam

Two 1000 kips and one 500 kips capacity load cells were used to monitor support reactions at the South and North beam-ends, respectively, (Fig. 8.7). Two load cells, attached to the loading actuators (B and C), were used to measure the applied load on top of the beam. During a test, force equilibrium between the applied loads (actuators B and C) and the measured reactions (load cells) was always verified.

The data acquisition system to record the various measured data, the procedure to measure shear cracks and loading procedure during the beam tests, were the same as used in testing the I-beams and are described in Chapter-7.

8.7 Experimental Results

Table 8.4 shows the experimental ultimate shear strengths at failure for the six PSFC Box-

beams tested, i.e. RB1 to RB6. The results show that the shear capacity of PC beams can be significantly increased due to the addition of steel fibers in concrete. The beam test results reveal a good co-relation between the fiber-factor and shear strength. The general trend detected was that with an increasing fiber-factor, shear strength also increased. The tests also confirmed that as the *a/d* ratio was increased, the shear strength of the beams reduced.

Table 8.4 – Experimental Ultimate Strengths at Failure for PSFC Box-Beams

Beam ID	**Steel Fiber by Volume** (%)	**Fiber Factor**	**Concrete Compressive Strength** (ksi)	***a/d* Ratio**	**Ultimate Failure Load** (kips)				**% Difference between South and North side**
					NE	**NW**	**SE**	**SW**	
RB1	1% SF	0.55	9.60	1.8	**87.4**	**84.2**	**91.4**	**74.5**	**3.4**
RB2	1% SF	0.55	9.56	2.5	**128.6**		**77.2**	**70.3**	**12.8**
RB3	1% SF	0.55	9.69	4.1	**82.9**		**45.9**	**47.1**	**10.8**
RB4	1.5% SF	0.825	10.44	1.8	**94.7**	**82.7**	**97.6**	**87.3**	**4.0**
RB5	1.5% SF	0.825	10.88	4.1	**110.7**		**66.7**	**56.5**	**10.1**
RB6	1.5% SF	0.825	11.08	2.5	**167.2**		**91.1**	**79.1**	**1.7**

SF = Dramix Short Fibers

There was no web crushing observed during the shear failure in any of the Box-beams. This may be due to inherent redundancy in the box beam girders. The beam had two webs that transferred the applied shear load from the top flange to the beam support. During the test it was observed that even though one of the webs cracked excessively (softened) and lost its stiffness, the other web was still intact and stiff, owing to which the beam did not fail. This provided an inherent redundancy due to redistribution of load in the Box-beams during the web failure. Such phenomenon was also observed by Kani (1962) in shear tests of concrete beams.

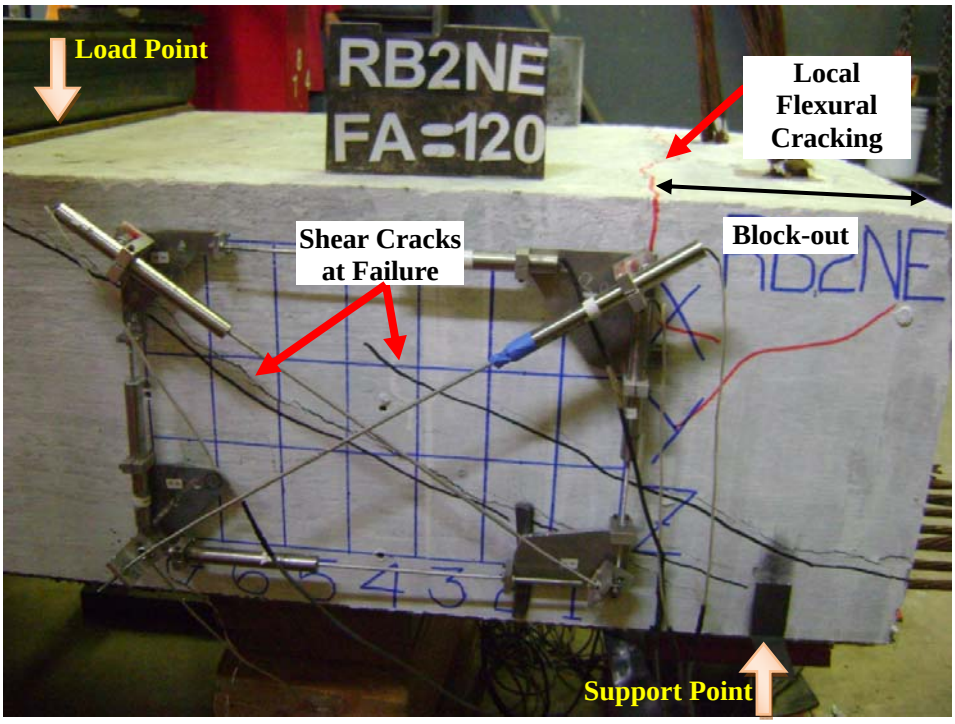

Fig. 8.10 Local Flexural Cracking at Top Flange and Block-out in PSFC Box-Beams

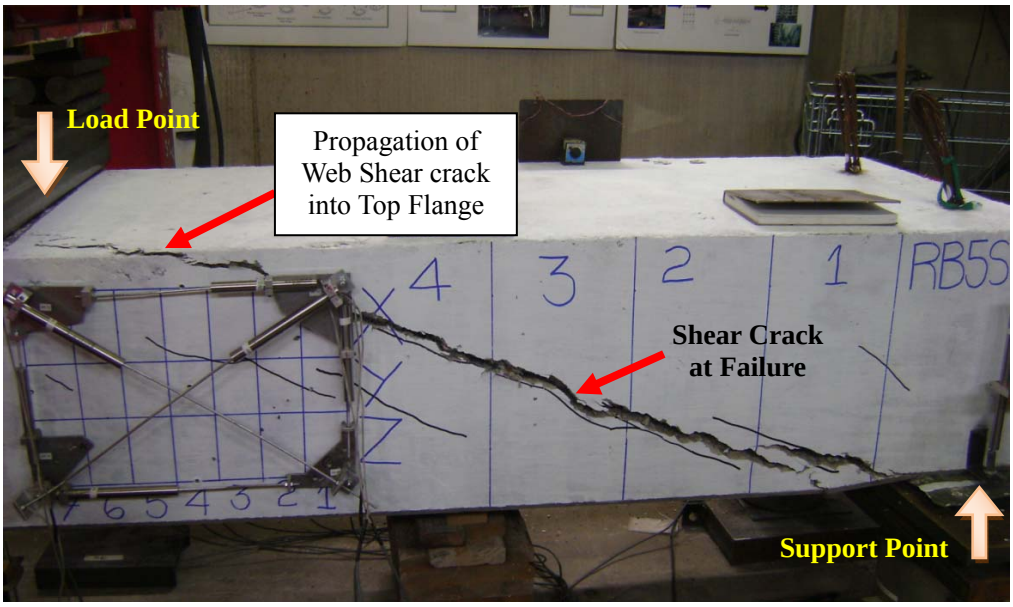

Fig. 8.11 Failure of Top and Bottom Flanges Due to Propagation of Web Shear Crack

During the tests on Box-beams, local longitudinal-flexural cracking at the connection between top flange and end diaphragm (block-out) was observed, as shown in Fig 8.10. Shear cracks developed in the beam web, propagating into the flanges is depicted in Fig 8.11. In order to avoid the local flexure failure of the top flange at end block-out in a Box-beam, longitudinal flexural steel reinforcement similar to the one provided in a conventionally box beam is recommended by the researchers to be installed in future PSFC Box-beams, as shown in Fig. 8.12.

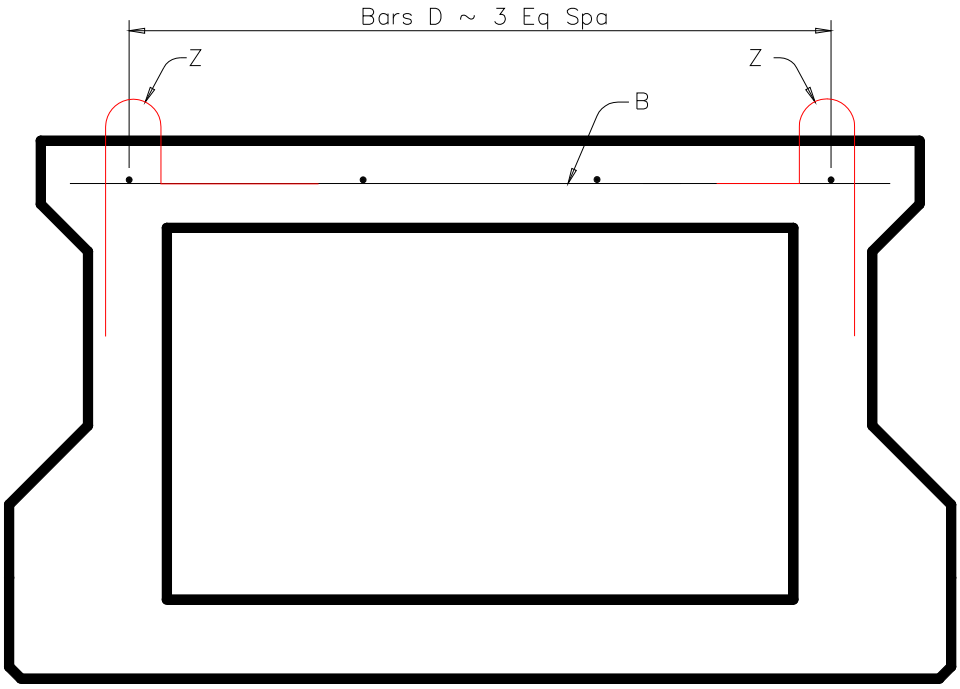

Fig. 8.12 Recommended Longitudinal Flexural Reinforcement in Future PSFC Box-Beams

As shown in Fig. 8.12, Z-rebars (hooks) should be provided to guarantee the monolithic action of top-slab and beam in horizontal shear. The top-slab's monolithic action with beam is also important in reducing the risk of local failures. Longitudinal D-rebars should be provided to resist the local flexure failure of the top flange at end block-out (as discussed before). The D-rebars can also hold the hooks in place during casting. The detailed design of the recommended flexural steel reinforcement in top flange of PSFC Box-beam will be discussed in Chapter-10.

The crack pattern and photograph at failure of all the PSFC Box-beams are shown in Fig 8.13. The web-shear failures in all beams were noticeably along a single shear crack which formed between the support and loading points at failure. Beams RB3 and RB5 displayed no

flexure cracking though they were designed to fail in flexure-shear mode. This may be due to an unexpectedly large increase in the flexural strength of the box beams because of adding steel fibers.

The load-defection curves for all Box-beams are shown in Fig. 8.14(a) through Fig. 8.14(f). The values of shear force plotted in this figure were obtained from the load cells under the beam's end-supports and were also verified by the load equilibrium computations. The net deflection was obtained from the difference in readings of LVDT placed under the beam at the particular actuator location and the readings of LVDT placed at the corresponding support. Hence, the beam gross deflection values were compensated for the support settlement and then used to plot the load-deflection curves.

It can be observed that all Box-beams had a descending branch after peak. This descending branch is primarily due to the inherent flexural redundancy of the box beam as explained previously, and hence should not be confused with structural ductility. Box-beams RB1 and RB4 were tested with four supports under them. All the other box beams were tested with only three supports i.e. one support on North side and two supports on South side, under them. In Box-beams RB2, RB3 and RB5 it was observed that the North end with one support had about 10% less shear capacity than the South end with two supports. This can be attributed to the fact that the North end had a much more complex stress flow due to single support (D-region) than the South end.

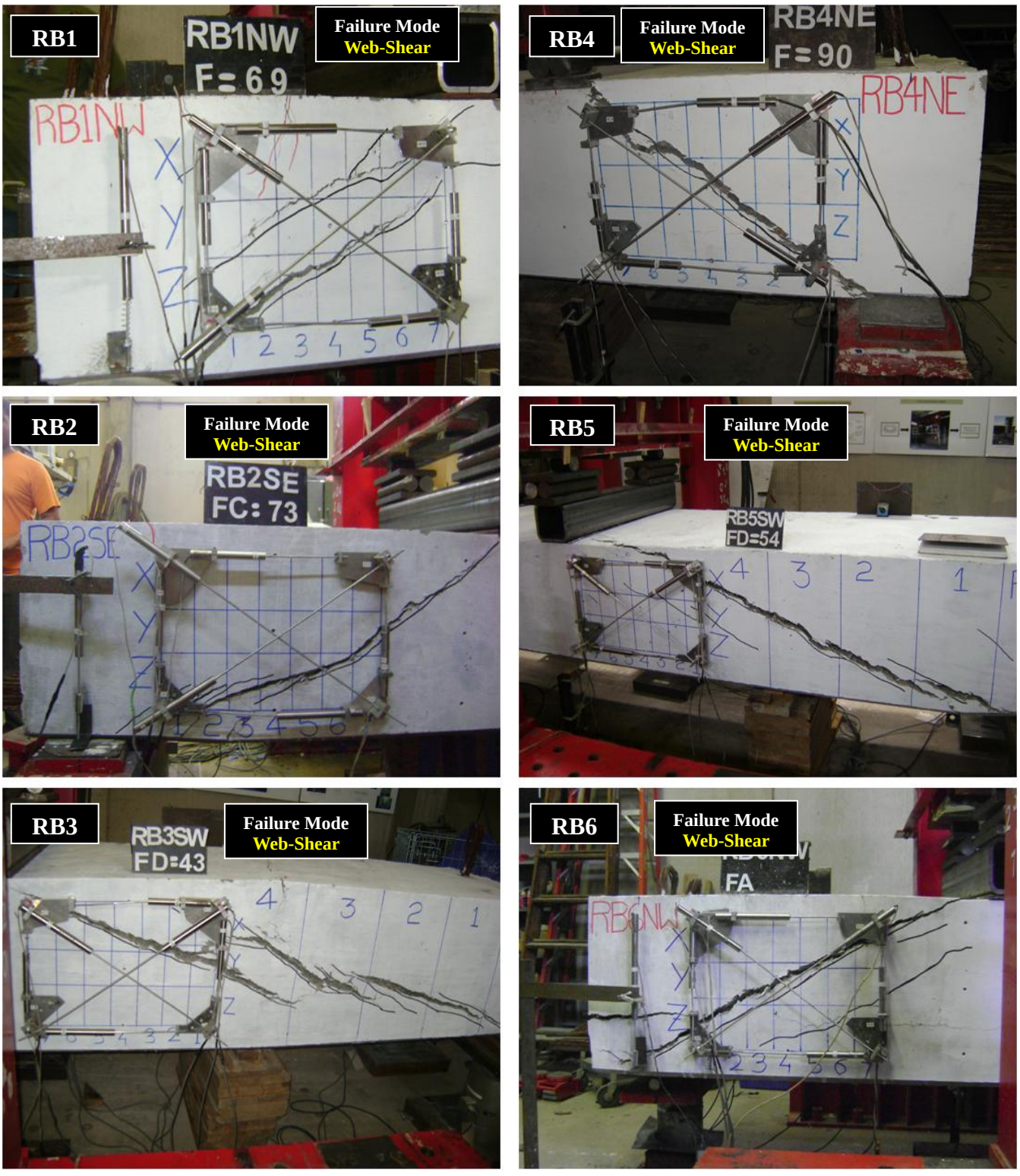

Fig. 8.13 PSFC Box-Beams at Failure

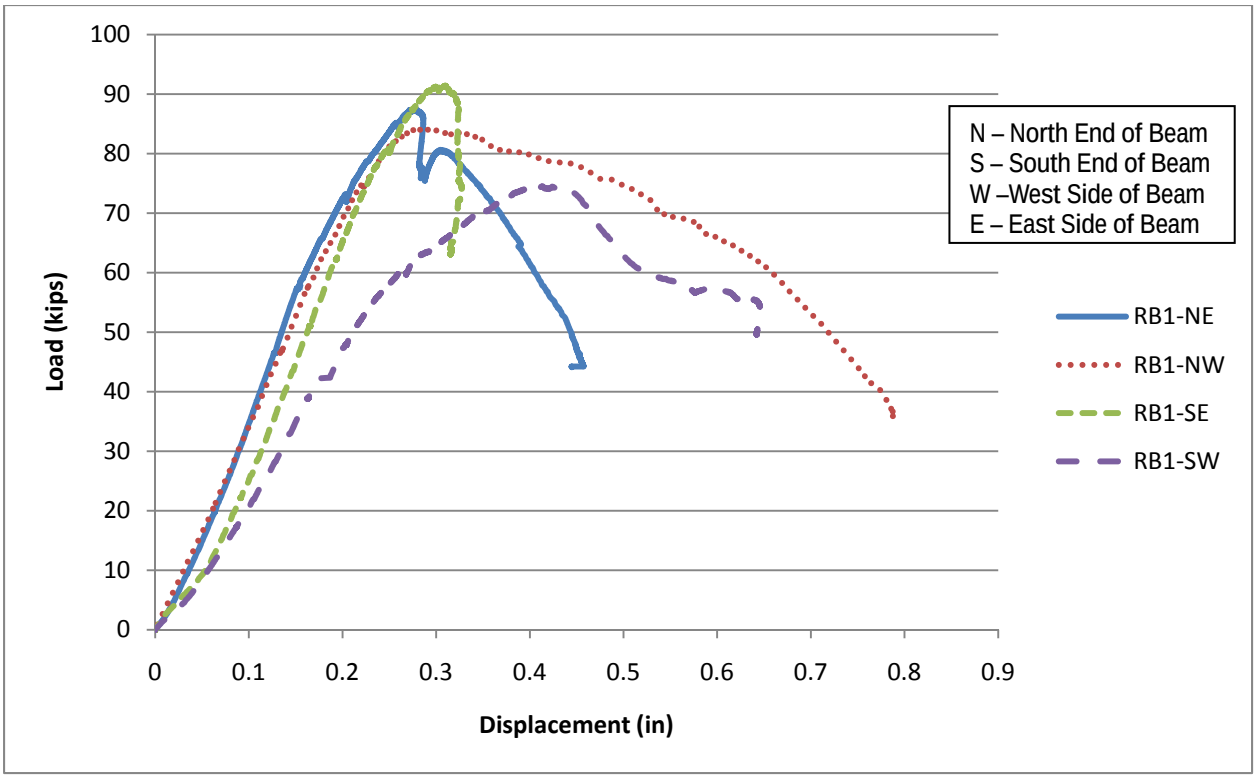

Fig. 8.14 (a) Shear Force vs. Net Deflection Curves for PSFC Box-Beam RB1

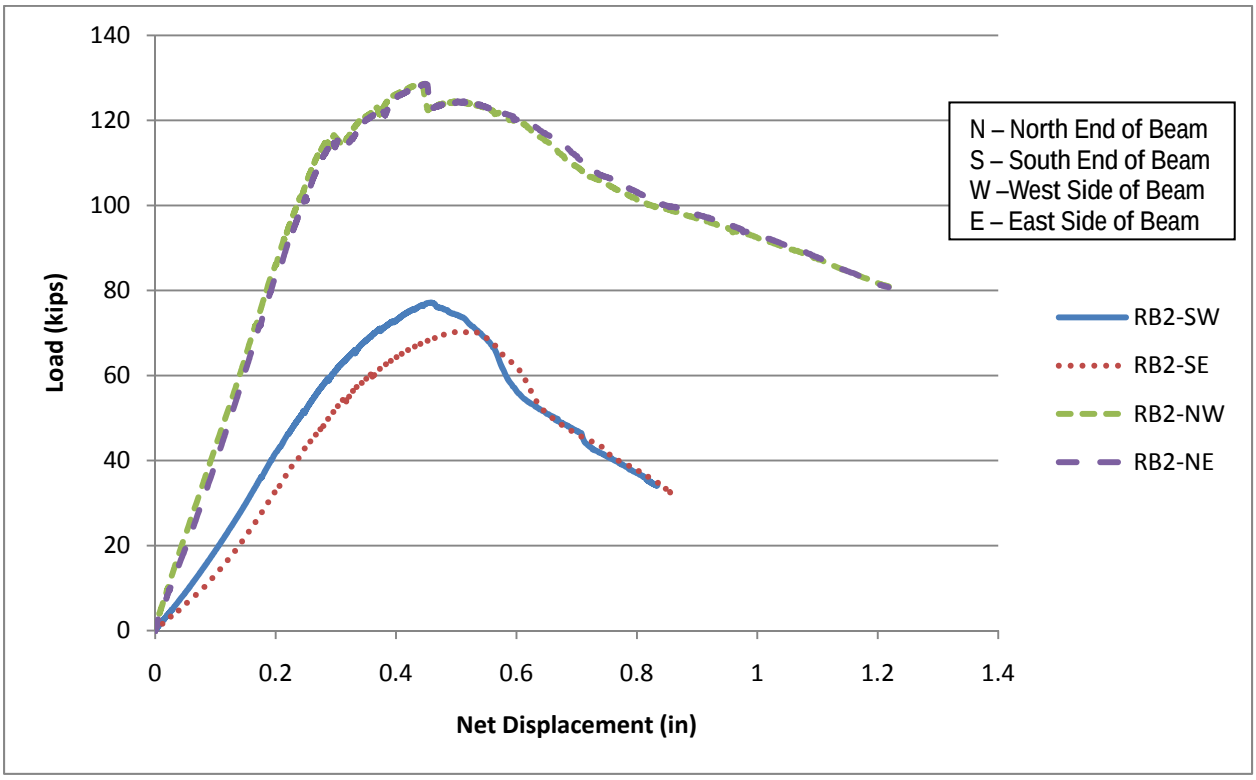

Fig. 8.14 (b) Shear Force vs. Net Deflection Curves for PSFC Box-Beam RB2

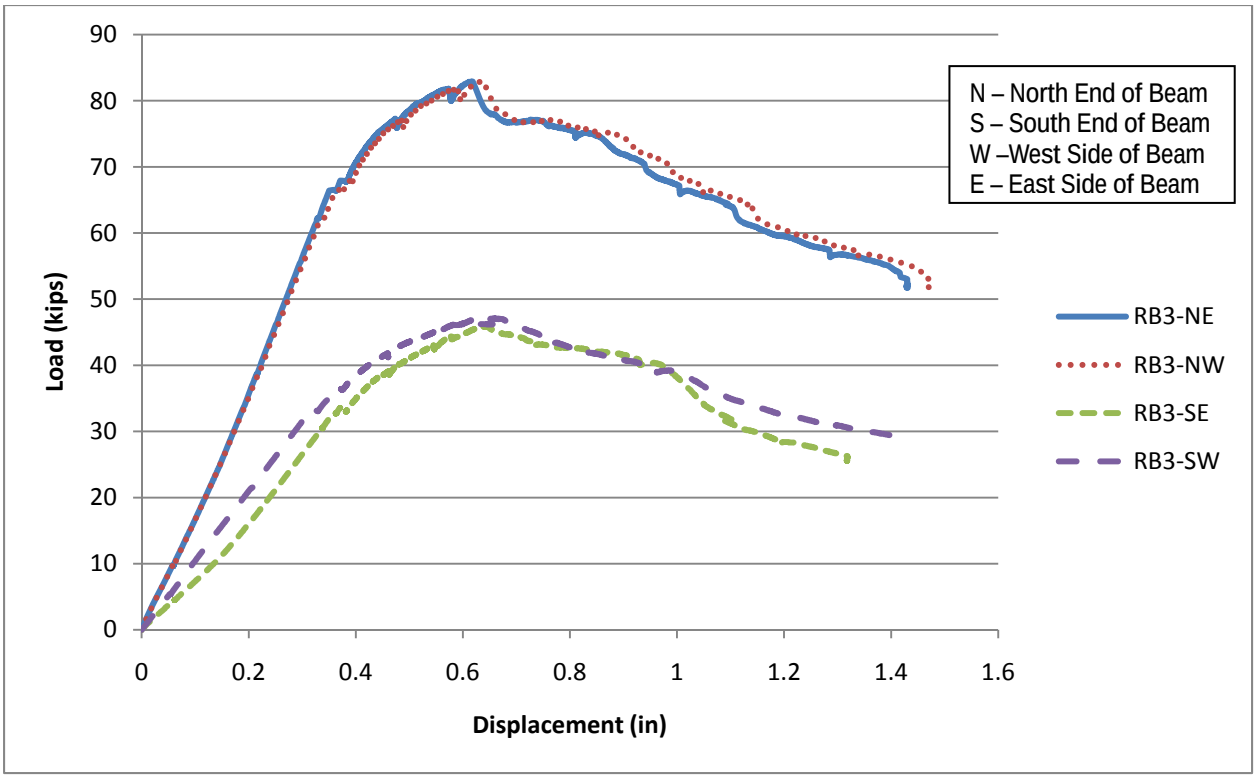

Fig. 8.14 (c) Shear Force vs. Net Deflection Curves for PSFC Box-Beam RB3

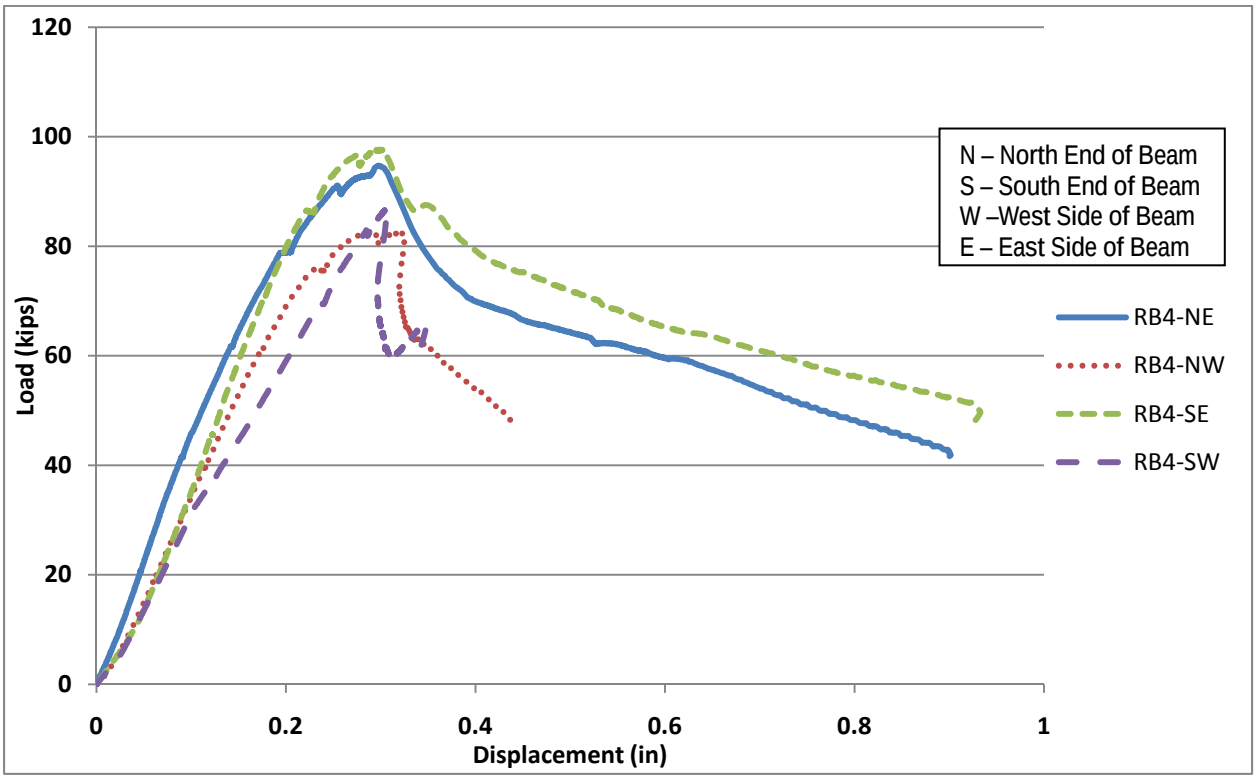

Fig. 8.14 (d) Shear Force vs. Net Deflection Curves for PSFC Box-Beam RB4

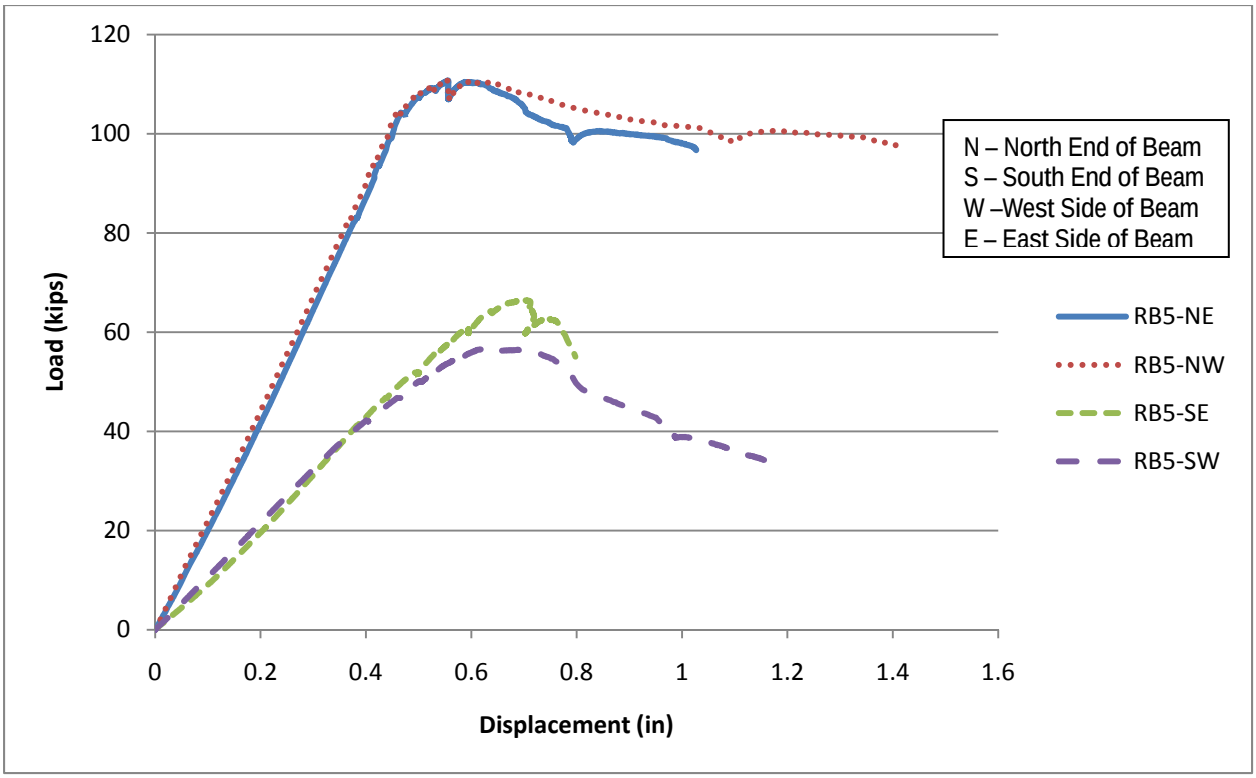

Fig. 8.14 (e) Shear Force vs. Net Deflection Curves for PSFC Box-Beam RB5

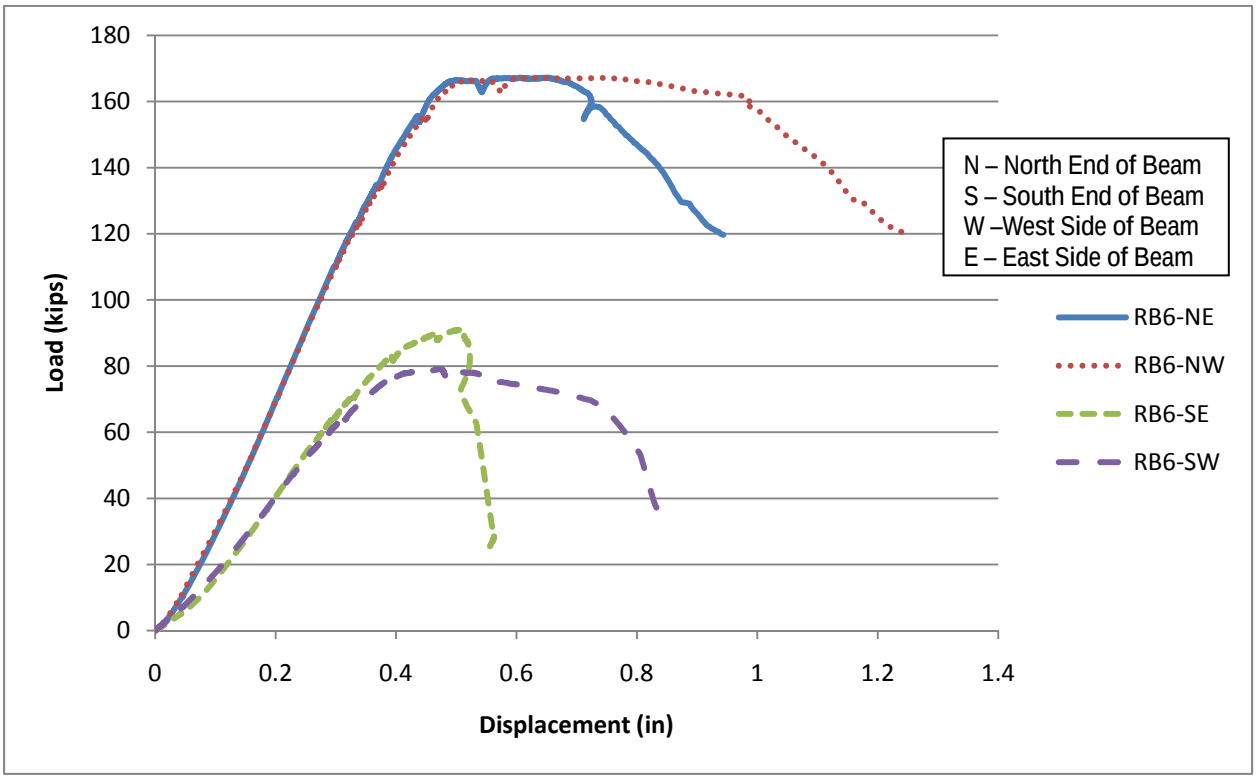

Fig. 8.14 (f) Shear Force vs. Net Deflection Curves for PSFC Box-Beam RB6

Fig. 8.14 (a) to (f) shows that the shear-force vs. net deflection curves on both sides (West and East) at either ends (North and South) of the beams matched quite well, expect in Box-beam RB1. This suggests that all the box beams had uniform shear loads in the webs and hence did not undergo torsional twisting. But in beam RB1 at South end, some possible differential shear load in webs at West and East side may have resulted in torsional twist.

The variation of shear capacity (ultimate shear load) with respect to shear span-to-effective depth ratio (*a/d*) of all the Box-beams is shown in Fig 8.15. It is clear from the figure that shear capacity of a PSFC Box-beam is sensitive to the *a/d*-ratio as also observed in the PSFC and conventional PC I-beams. The results also showed that as fiber-factor in the beams increased, the shear capacity also increased.

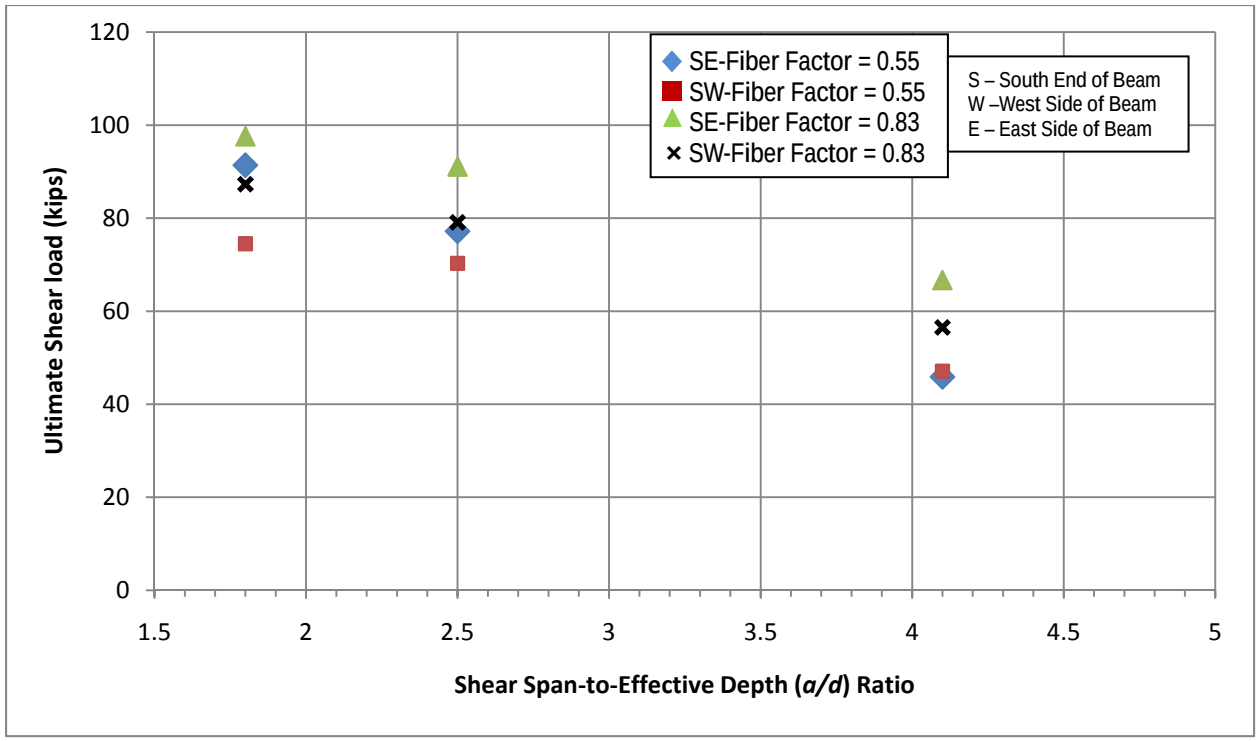

Fig 8.15 Variation of Shear Capacities of Box-Beams with Shear Span

To better understand the effectiveness of steel fibers as shear reinforcement, the load-defection curves of Box-beams with the same *a/d*-ratio but with different fiber-factors are compared. The comparisons are shown in Fig. 8.16 (a) to Fig. 8.16 (c). There is not a significant increase in the shear strength as fiber-factor is increased from 0.55 to 0.825 in the case of beams

with *a/d*-ratio of 1.8. However, for beams with *a/d*-ratios of 2.5 and 4.1, the enhancement in shear strength with increasing fiber-factor is pronounced.

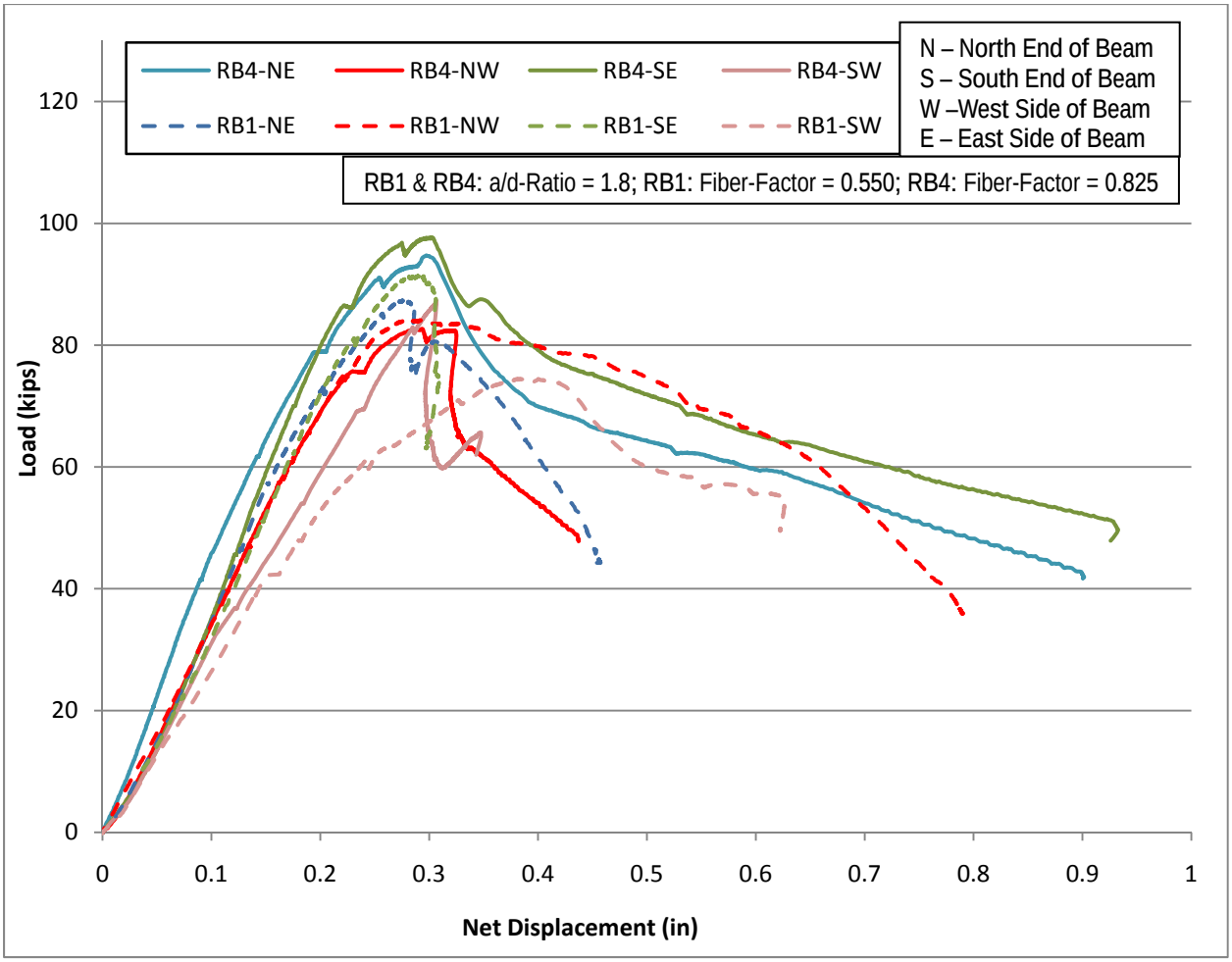

Fig. 8.16 (a) Load vs. Deflection Curves for PSFC Box-Beams RB1 and RB4

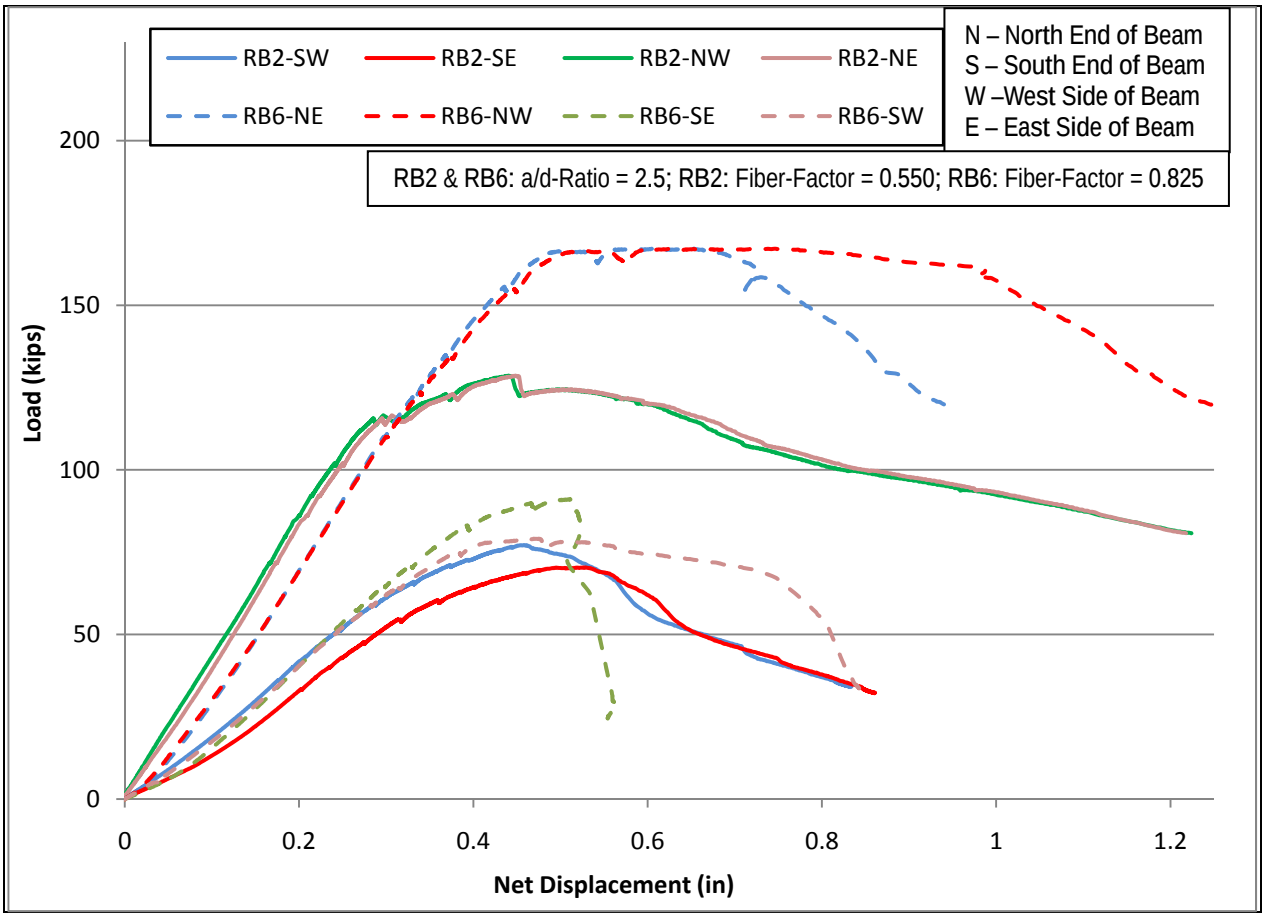

Fig. 8.16 (b) Load vs. Deflection Curves for PSFC Box-Beams RB2 and RB6

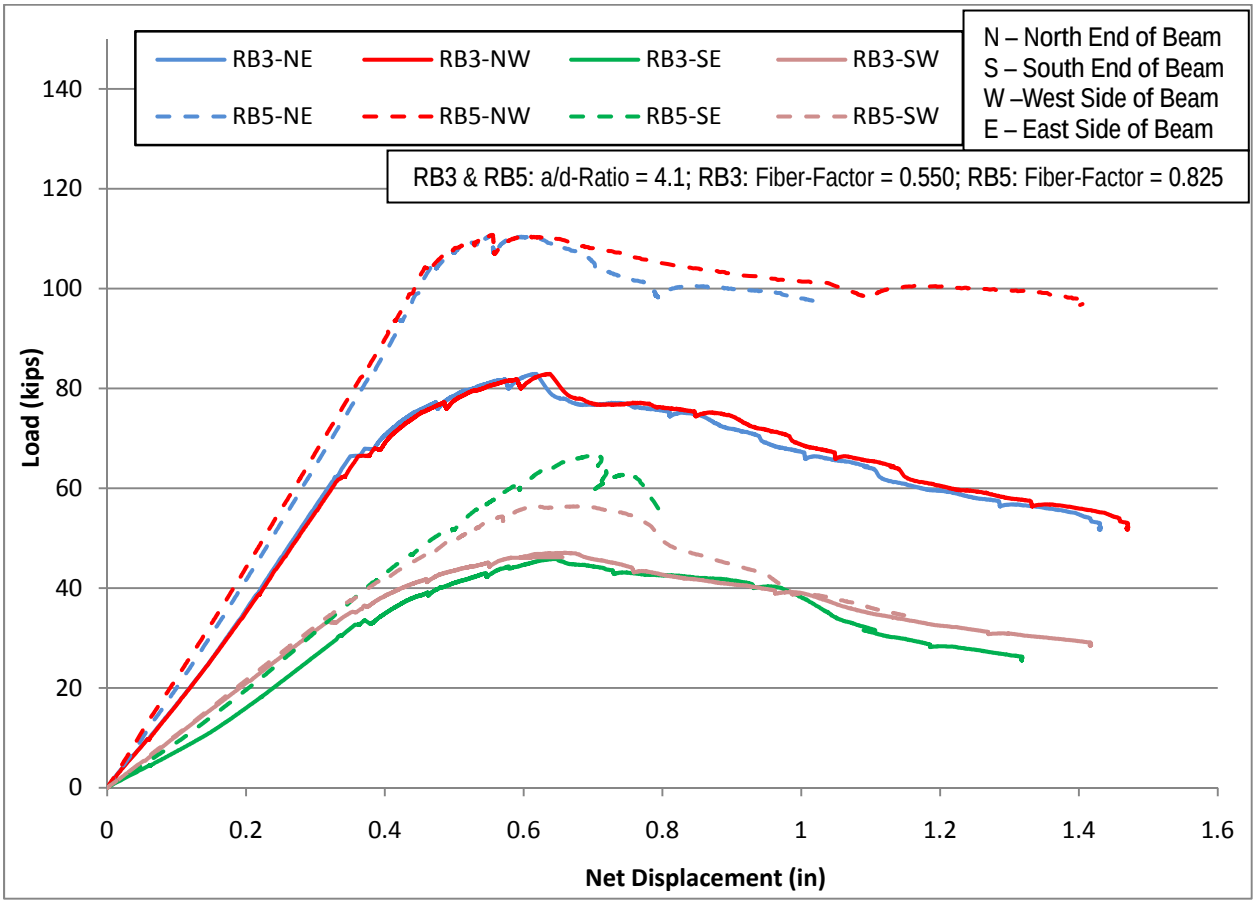

Fig. 8.16 (c) Load vs. Deflection Curves for PSFC Box-Beams RB3 and RB5

CHAPTER 9

SIMULATION OF PSFC BEAMS

9.1 Introduction

In this chapter, the PSFC beams tested in this study (Chapters 7 and 8), have been analyzed using a computer program named Simulation of Concrete Structures (SCS). The test results of PSFC beams were used to validate the SCS program, which was developed using the constitutive laws of PSFC in SMM-PSFC (Chapters 5 and 6). Since the PSFC beams were tested under monotonic loads, this validation and applicability of SCS program is only suitable in predicting the structural behavior of PSFC structures under monotonic loading. Section 9.2 describes the finite element model of the PSFC beams that was created and utilized in the SCS program to analyze the beams. A comparative study of the experimental and analytical results was conducted for the PSFC beams, in Section 9.3.

9.2 Analytical Model

Various finite element models of the PSFC beams were developed to analyze the beams using SCS program. The two (top and bottom) flanges of the beams, which were designed to resist applied bending moments, were modeled as *NonlinearBeamColumn* elements with fiber sections. The beam web, designed to resist the applied shear force, was represented by *PCPlaneStress Quadrilateral* elements. The details of the finite element models of I-Beams and Box-beams are described in Section 9.2.1, respectively. In the finite element model of the PSFC beams the prestressing loads acting on the beam were applied as nodal forces adjacent to the ends of the beams. In case of flexure-shear critical beams, a reduction of 20% in the initial prestressing force is considered to account for prestress losses. An incremental load-control was used for the prestressing loads at the start of an analysis in the model. Thereafter, the prestressing loads were kept constant and monotonic vertical loads were applied on the top flange of the beam using a predetermined displacement-control scheme.

All the concentrated loads applied on the beam in the model were through nodes. The effect of bearing plates, which were actually used in the load-test to apply vertical loads on the beam, was ignored for simplicity. The loads were distributed among three nodes adjacent to the location of the applied load. The analysis yielded similar results in the cases when (a) larger load was

applied at the node corresponding to the actual loading point and lower loads were applied at the two adjacent nodes and (b) loads were distributed equally among the three nodes. Hence, the concentrated vertical loads on the beams were modeled at a node corresponding to the actual loading point and two adjacent nodes. The results of beam analysis i.e. nodal displacement and corresponding vertical forces, were computed at every displacement step that had numerically converged. Additionally, the stresses and strains in the beam elements were also calculated by the program (Laskar, 2009).

9.2.1 Finite Element Model of PSFC Beams

9.2.1.1 I-Beams

Each of the tested PSFC I-beam was modeled using the finite element mesh as shown in Fig 9.1 and Fig 9.2. The top and bottom flanges in the beams were each divided into sixteen and fifteen *NonlinearBeamColumn* elements in the case of web-shear and flexure-shear failure modes, respectively. The bulb-shaped top and bottom flanges in beam's cross-section were modeled using rectangular *NonlinearBeamColumn* elements with equivalent area. Each *NonlinearBeamColumn* element was defined with two control sections. Each section representing the top flange was discretized into forty fibers of concrete. The configuration of the section discretization of the top flange is shown in Fig. 9.3(a). Similarly, each section representing the bottom flange was discretized into ten fibers of concrete and two fibers of tendons. The configuration of the section discretization of the bottom flange is shown in Fig. 9.3(b).

Two of the twelve tendons in the web shear specimens were provided in the *NonlinearBeamColumn* elements representing the bottom flange of the specimens. The remaining tendons were provided in the quadrilateral elements used to represent the webs of these specimens. The initial strains in the tendons were applied using the *TendonL01* constitutive module. *Concrete01*and *Steel02* material modules were used to define the concrete and steel fibers materials in the cross section, respectively.

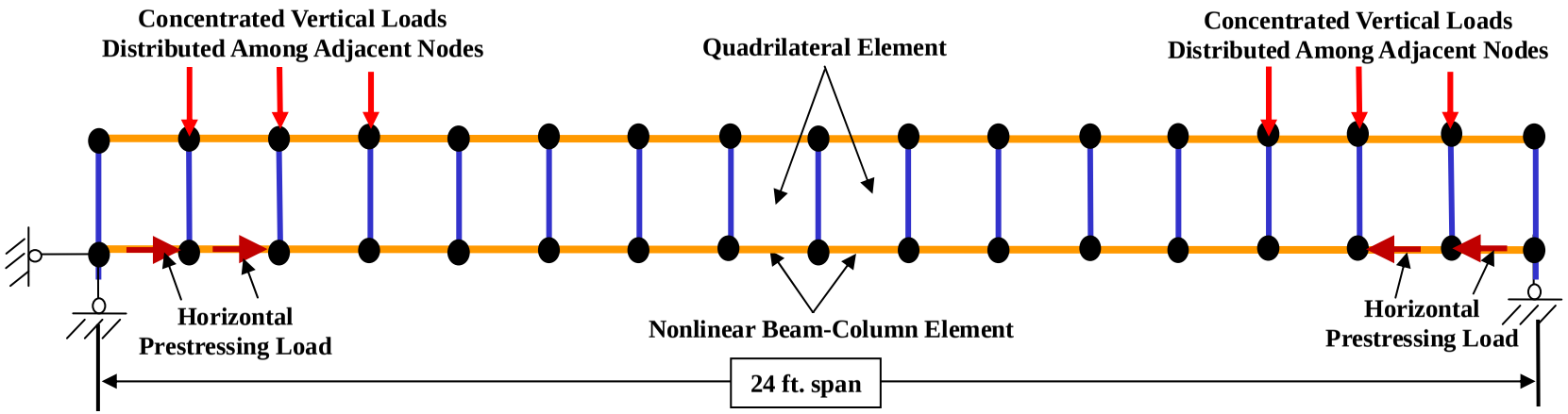

Fig. 9.1 Finite Element Model of PSFC I-Beams Tested under Web-Shear

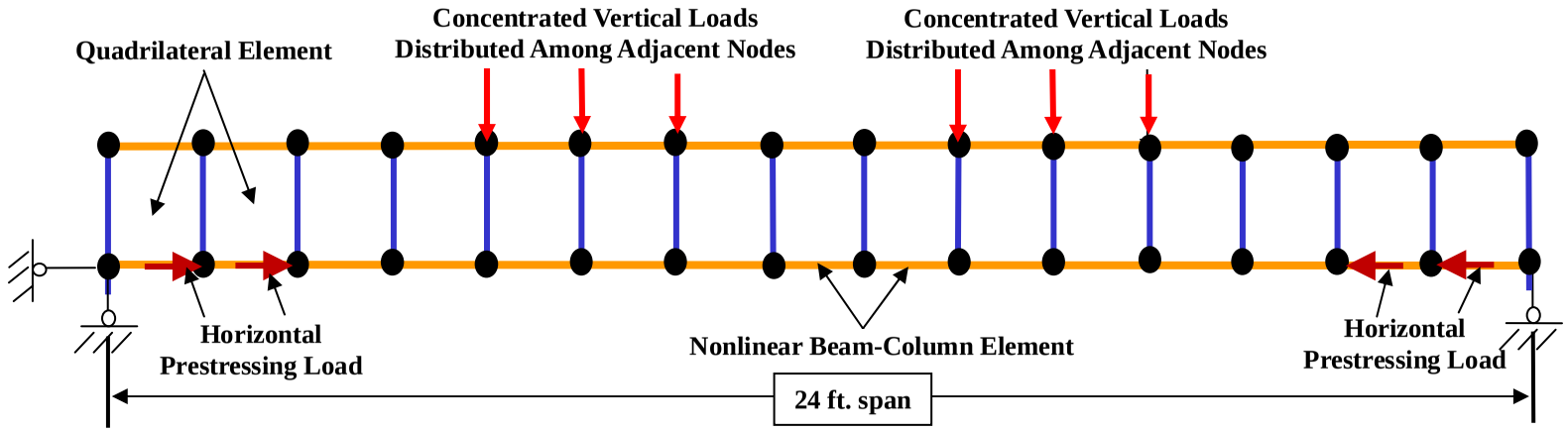

Fig. 9.2 Finite Element Model of PSFC I-Beams Tested under Flexural-Shear

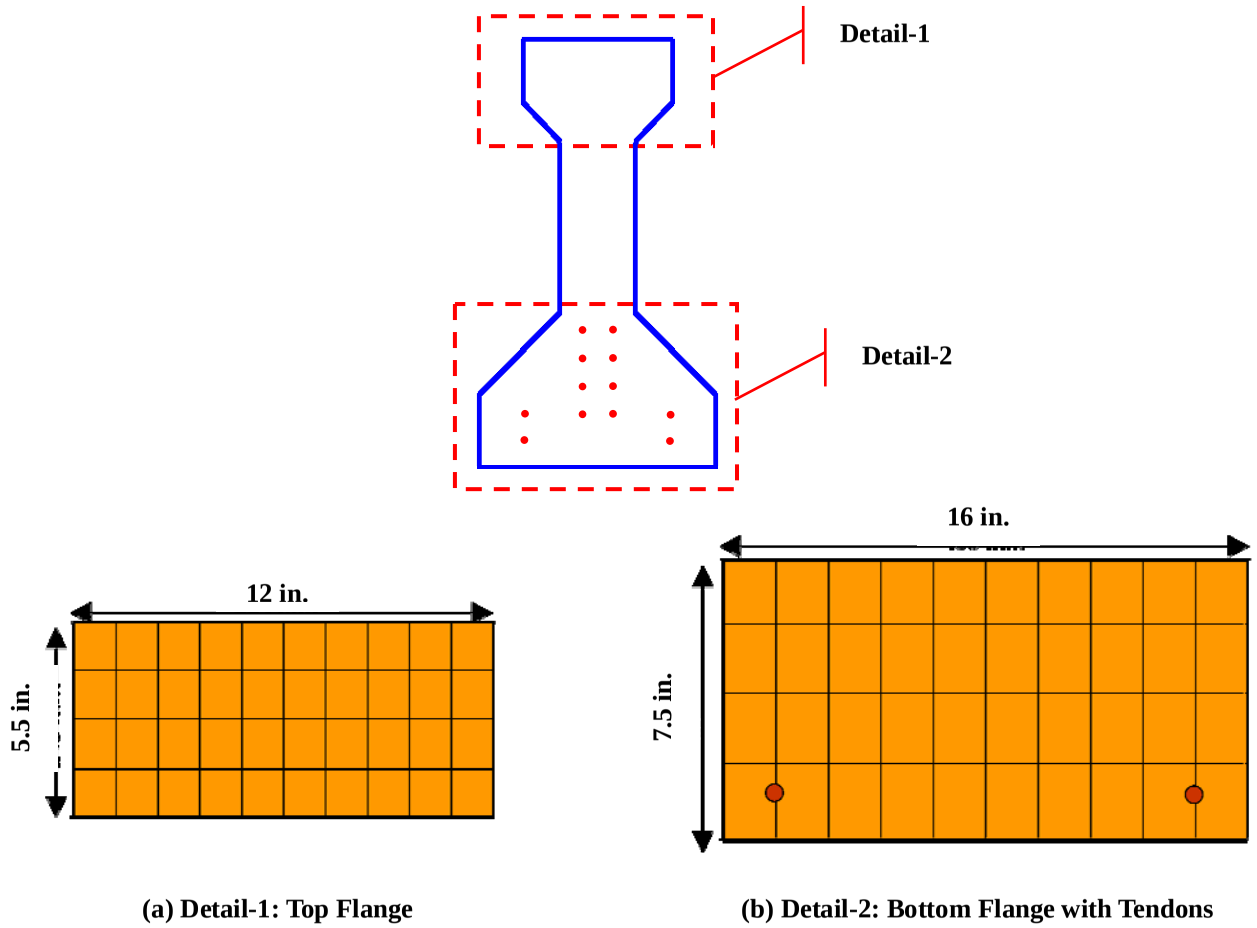

(a) Detail-1: Top Flange

(b) Detail-2: Bottom Flange with Tendons

Fig. 9.3 Cross-Section Discretization of *NonlinearBeamColumn* Elements for PSFC I-Beams Tested under Web-Shear

The *Concrete01* module used herein was a uniaxial material module of concrete previously created in OpenSees following the modified Kent and Park model (Kent and Park 1982). The *steel02* module used in this program was a uniaxial Menegotto-Pinto steel material object with isotropic strain hardening. This object also allowed user to enter the initial strain in the steel, which is useful in modeling the prestressing strands.

The web regions of the beams have been modeled by sixteen *PCPlaneStress quadrilateral* elements. The tendon orientation in the elements was defined in the horizontal direction. The steel ratio in the vertical direction was taken as a very small number to avoid numerical problems during the analysis. The tendon ratio in the horizontal direction was determined based on the area of ten prestressing tendons smeared over the entire cross section of these specimens. *ConcreteR01* and *TendonL01* were used to create the uniaxial material models of concrete and tendons in the *PCPlaneStress* material, respectively. The constant *k* used in *ConcreteL01* was to impose an upper limit to the initial stress-strain relationship of concrete in compression and which reduced the initial slope of the concrete stress-strain curve to less than $\frac{2f_c'}{\varepsilon_0}$. This initial slope of concrete stress-strain curve was taken as 1.5 for the analysis of all the beams tested under web-shear.

9.2.1.1 Box-Beams

Each of the tested PSFC Box-beam was modeled using the finite element mesh as shown in Fig 9.4 to Fig 9.6. The configuration of the section discretization of the top flange of Box-beam is shown in Fig. 9.7(a). Each section representing the bottom flange was discretized into forty fibers of concrete and two fibers of tendons. The configuration of the section discretization of the bottom flange of Box-beam is shown in Fig. 9.7(b). Only one half of the actual cross section was taken into analysis as the loads were applied on the two webs separately. The top and bottom flanges in the beams were defined as 18 *NonlinearBeamColumn* elements each. Each *NonlinearBeamColumn* element was defined with 2 control sections. Each section representing the top flange was discretized into 40 fibers of concrete.

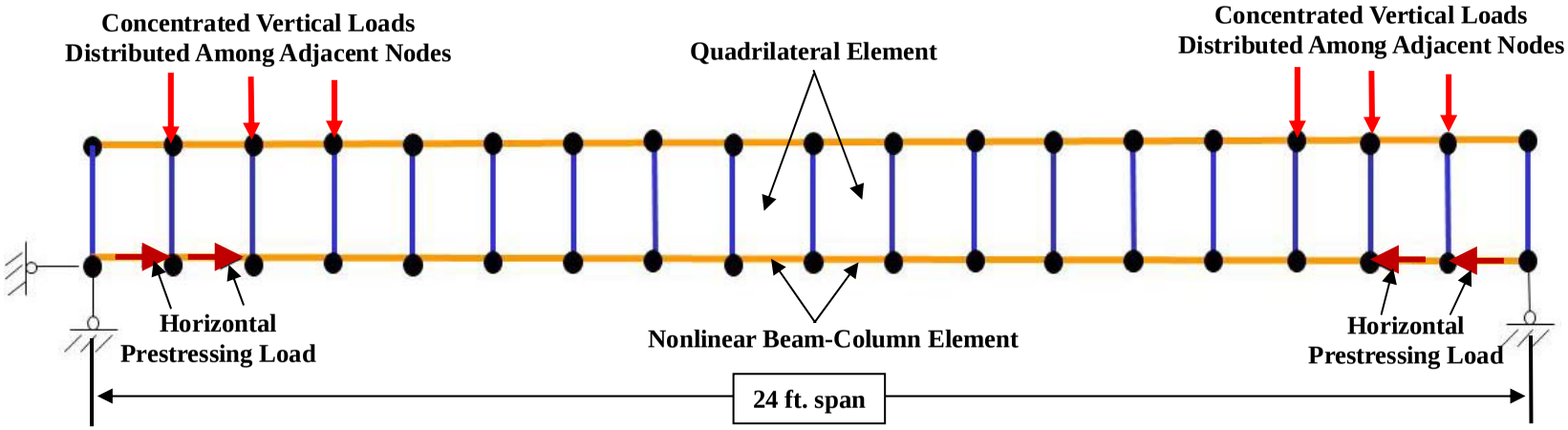

Fig. 9.4 Finite Element Model of PSFC Box-Beams Tested under Web-Shear (*a/d*=1.8)

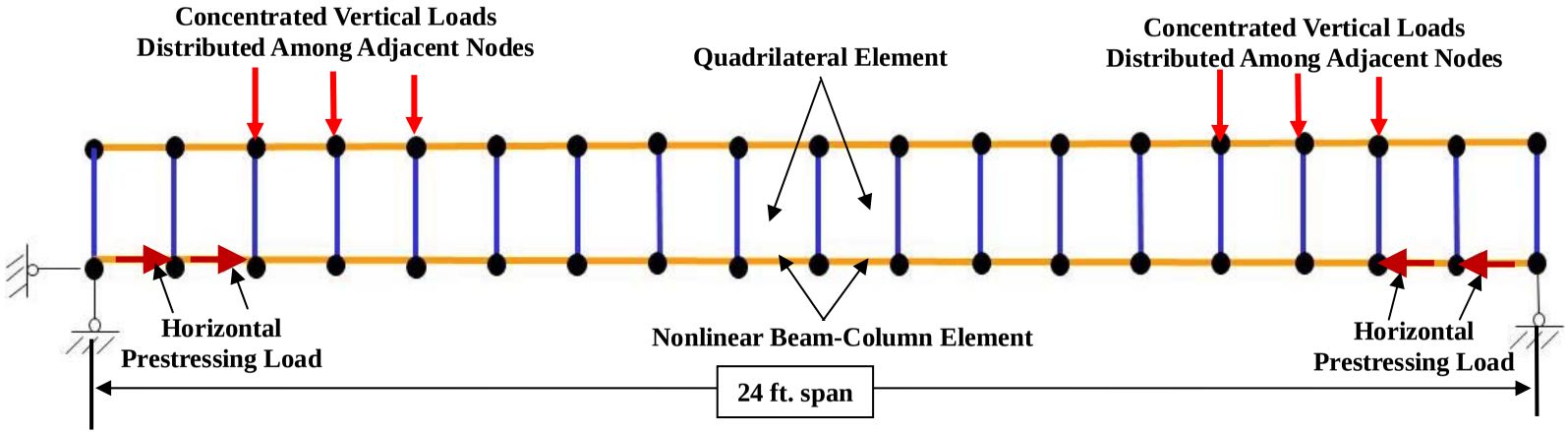

Fig. 9.5 Finite Element Model of Box-Beams Tested under Web-Shear (*a/d*=2.5)

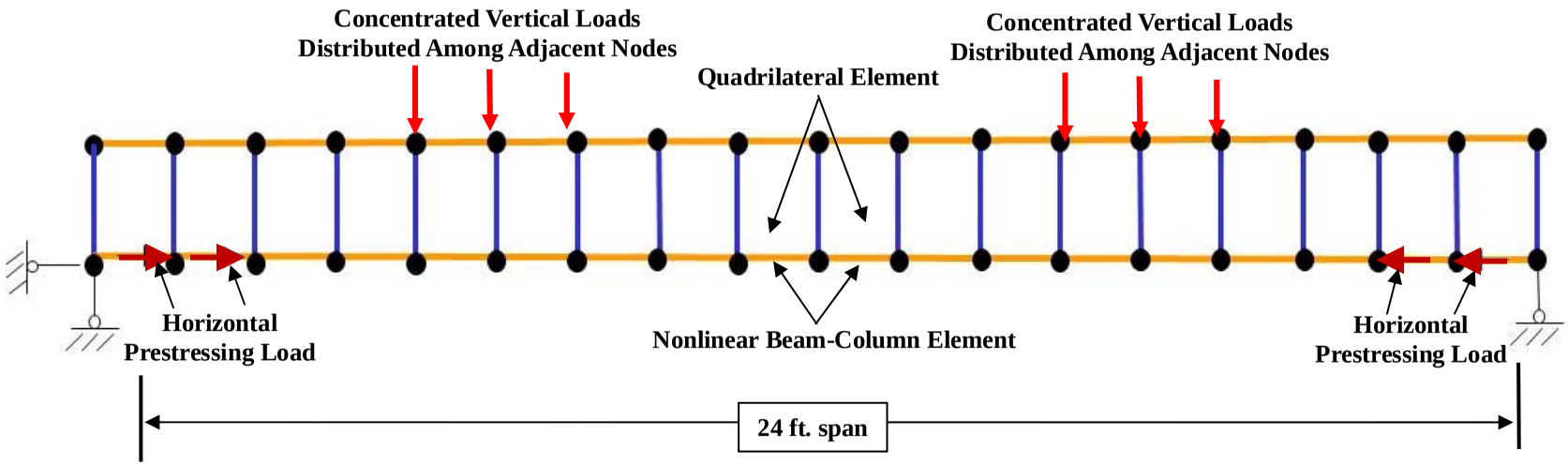

Fig. 9.6 Finite Element Model of Box-Beams Tested under Flexure-Shear (*a/d*=4.1)

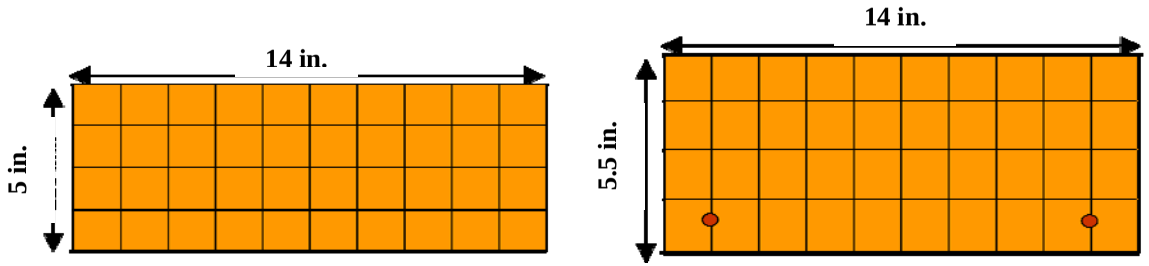

(a) Top Flange **(b) Bottom Flange with Tendons**

Fig. 9.7 Cross-Section Discretization of *NonlinearBeamColumn* Elements for Box-Beams Tested under Web-Shear

The web regions of the beams have been modeled by eighteen *PCPlaneStress quadrilateral* elements. The tendon orientation in the elements was defined in the horizontal direction. The steel ratio in the vertical direction was taken as a very small number to avoid numerical problems while analysis. The tendon ratio in the horizontal direction was determined based on the area of seventeen prestressing tendons smeared over the entire cross section of these specimens. *ConcreteR01* and *TendonL01* were used to create the uniaxial material models of concrete and tendons in the *PCPlaneStress* material, respectively.

9.3 Comparison of Analytical and Experimental Results

9.3.1 Web-Shear Failure

The measured and calculated load-displacement curves for all PSFC I-beams tested in web-shear failure mode are shown in Fig. 9.8. It can be seen that the analyses predicted reasonably well the load-displacement characteristics of the beams including initial stiffness, post-cracking stiffness, yield displacement, and ultimate strengths. The general trend observed in the beam (R1 to R4) tests, i.e. increase in load carrying capacity of beams with increase in fiber–factor, was accurately predicted by the analysis program. Fig. 9.8 also justifies the use of the constant k =1.4 (close to k = 1.5 assumed initially in the analysis) to make the initial slope of the concrete compressive stress-strain curve lower than $\frac{2f_c'}{\varepsilon_0}$.

Unlike Beams R1, R2 and R3 the prediction of the post-cracking stiffness of Beam R4 did not match well with the experimental results. All the box-beams encountered a local flexural failure at top flange and end block-out of the beams (as explained in Chapter-8), which prevented the accomplishment of expected ultimate shear failure and anticipated ductility levels. This can be clearly observed from all the curves shown in Fig. 9.9. The analysis was able to satisfactorily predict the ultimate load capacity and ductility of the box-beams tested.

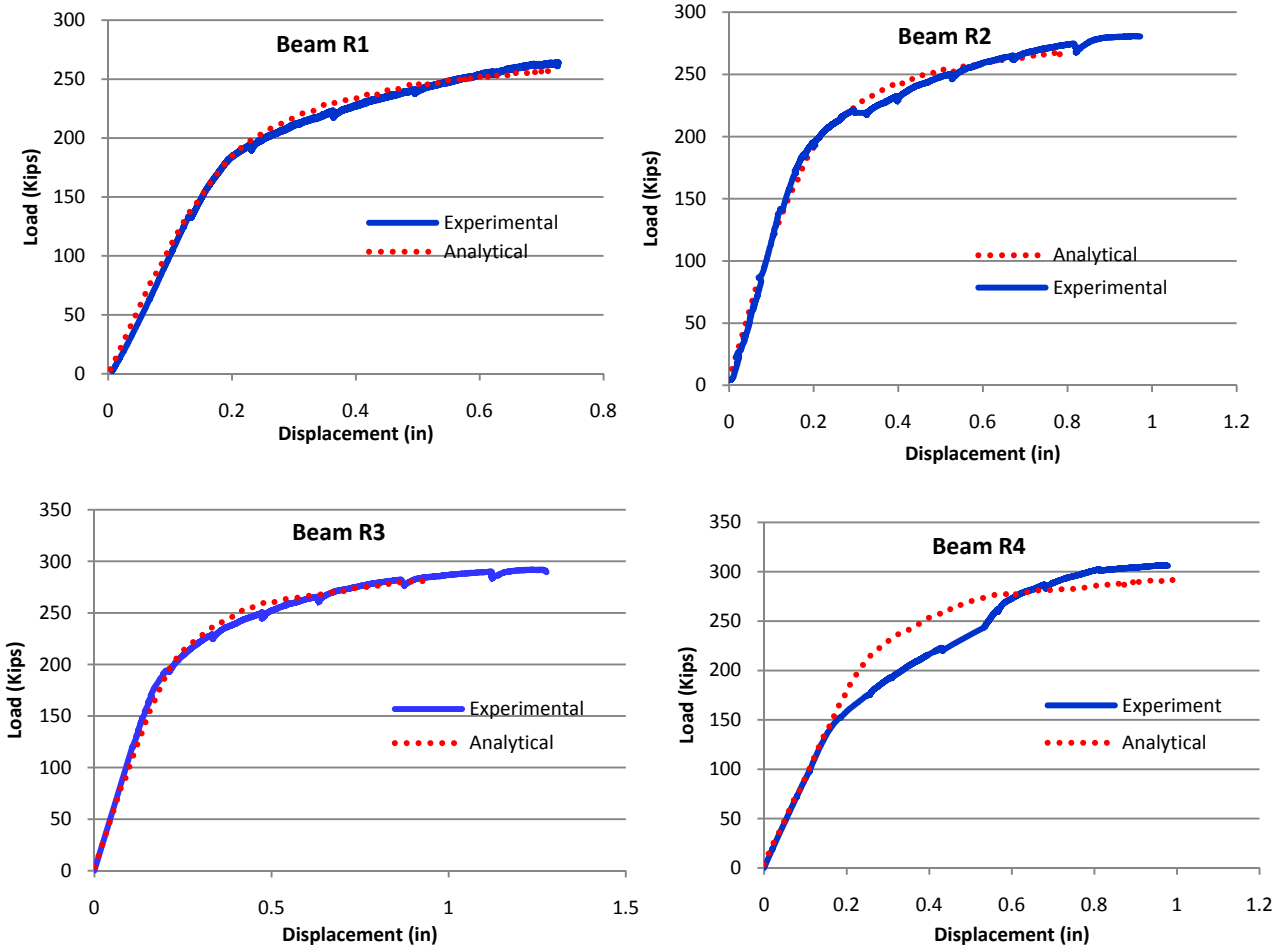

Fig. 9.8 Comparison of Experimental and Analytical Load vs. Displacement Curves of PSFC I-Beams Tested in Web-Shear Failure Mode

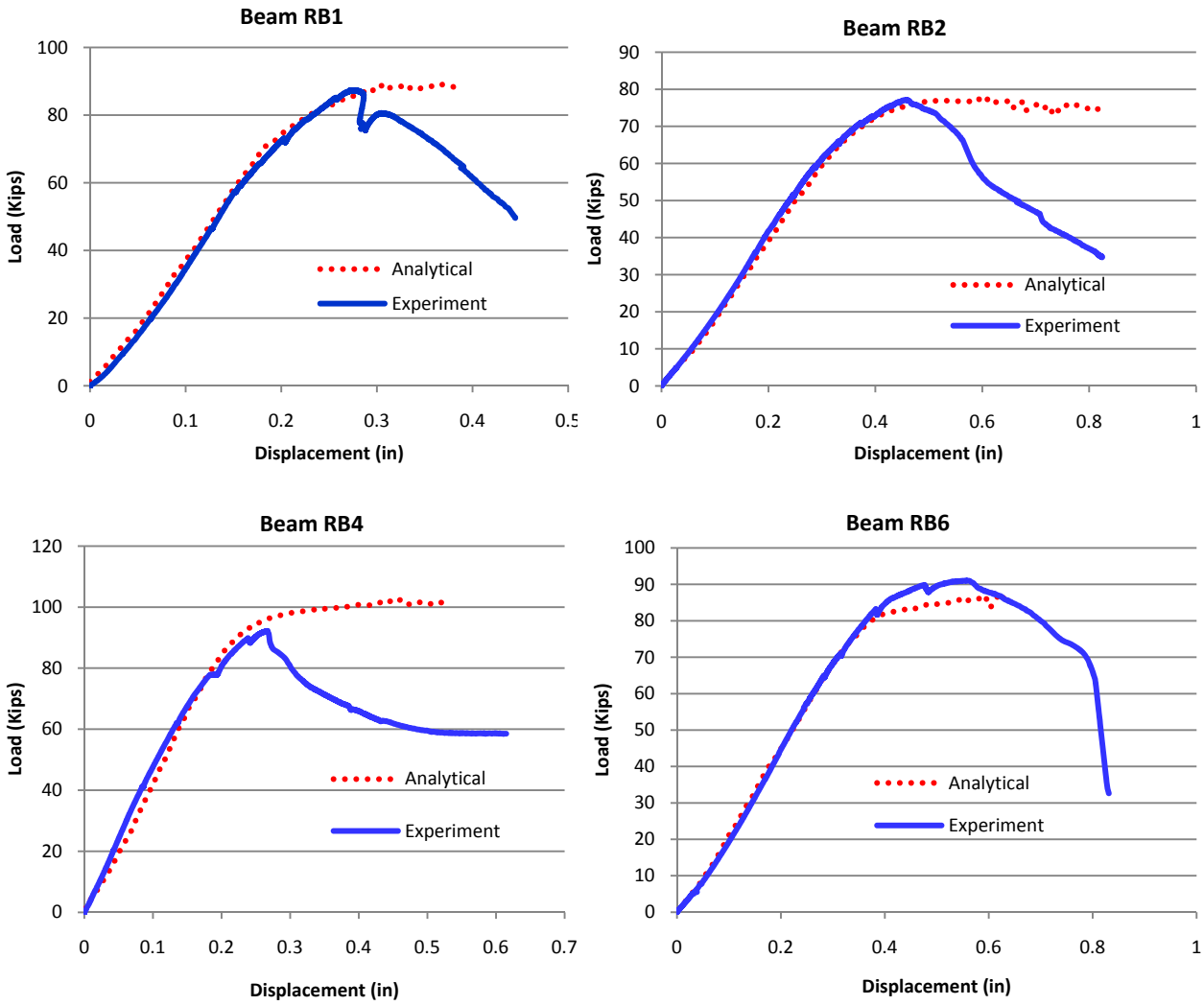

Fig. 9.9 Comparison of Experimental and Analytical Load vs. Displacement Curves of PSFC Box-Beams Tested in Web-Shear Failure Mode

9.3.2 Flexure-Shear Failure

The measured and computed load-displacement curves for beams with flexure-shear failure modes are shown in Fig. 9.10 and Fig 9.11. It can be seen that the analyses predicted reasonably well the load-displacement characteristics of the beams including initial stiffness, post-cracking stiffness, yield displacement, and ultimate strengths. The analysis could well predict the expected lower load carrying capacity of beams tested under flexure-shear in comparison to the beams tested under web-shear failure, having same amount of steel fibers. Larger ductility observed in the beams with flexure-shear failure when compared to the web-shear beams, was also well predicted in the analysis. Fig. 9.10 and Fig. 9.11 justifies the use of the constant k =1.4 (close to k = 1.5 assumed initially in the analysis) to make the initial slope of the concrete compressive stress-strain curve lower than $\frac{2f_c'}{\varepsilon_0}$.

All the box-beams encountered a local flexural failure at top flange and end block-out of the beams (as explained in Chapter-8), which prevented the accomplishment of expected ultimate shear failure and anticipated ductility levels. This can be clearly observed from all the curves shown in Fig. 9.11. The analysis was able to satisfactorily predict the ultimate load capacity and ductility of the box-beams tested.

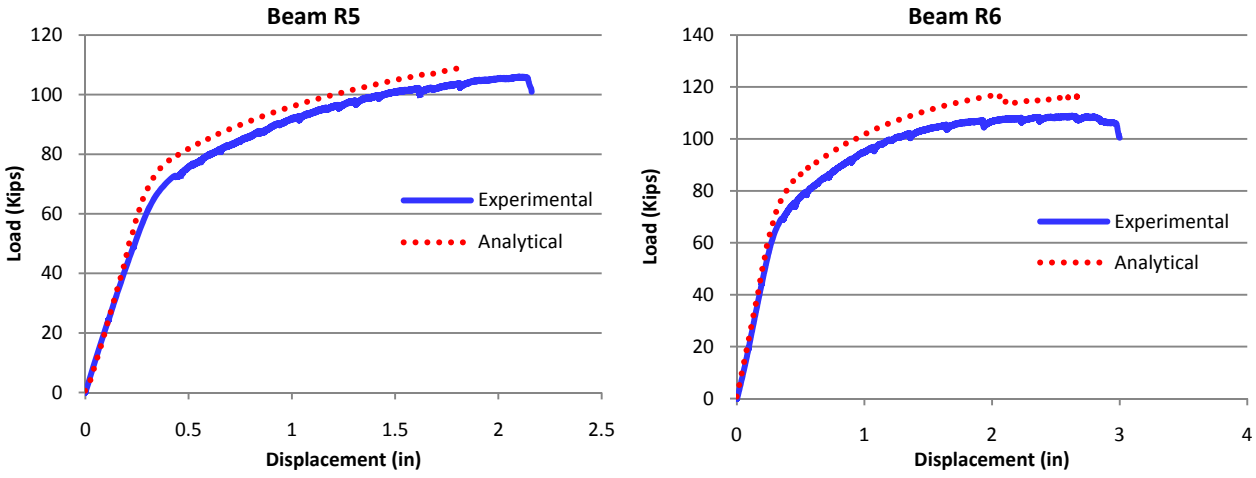

Fig. 9.10 Comparison of Experimental and Analytical Load vs. Displacement Curves of PSFC I-Beams Tested in Flexure-Shear Failure Mode

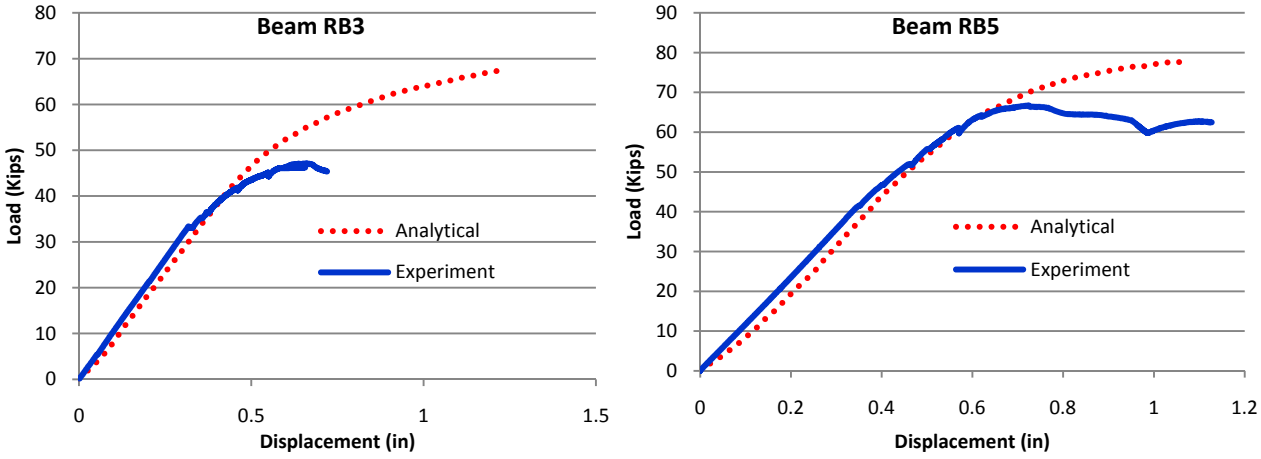

Fig. 9.11 Comparison of Experimental and Analytical Load vs. Displacement Curves of PSFC Box-Beams Tested in Flexure-Shear Failure Mode

CHAPTER 10

SHEAR DESIGN OF PRESTRESSED STEEL FIBER CONCRETE BEAMS

10.1 Design Method

A set of new design equations for shear strength of PSFC beams were developed at UH based on the test results reported in Chapter 7 and 8. In this study it was found that the shear strength of PSFC beams is a function of the shear span-to-effective depth ratio (*a/d*) and amount of steel fibers (i.e. fiber-factor, *FF*). Previous research at UH (Laskar 2009 and 2010) had established that shear strength of prestressed beams is neither a function of the prestressing force, nor dependent on the angle of failure plane. The proposed shear design method for PSFC beams is based on the equations developed by Laskar (2009 and 2010) for non-fibrous prestressed concrete.

To incorporate fiber-factor parameter in the shear design equations proposed by Laskar (2009 and 2010), it was assumed that the effect of shear span on concrete shear contribution in PSFC will be the same as in the case of prestressed concrete. The variation of the normalized concrete shear, $\frac{V_c}{\sqrt{f_c'}\, b_w d}\left(\frac{a}{d}\right)^{0.7}$ computed for the PSFC beam tested in this work, with the corresponding fiber–factor (*FF*) was studied. The relationship between the estimated normalized concrete shear strength and fiber–factor (*FF*) is shown in Fig 10.1. Considering a conservative trend (i.e. lower limit or bound) of this relationship it was observed that the *FF* term could be implemented into the V_c term of the design equation as shown in Eq. 10-1.

$$V_c = \frac{14}{(a/d)^{0.7}}\sqrt{f_c'}\, b_w d(1 + FF) \qquad (10\text{-}1)$$

where,

b_w = width of the PSFC beam's web

d = effective beam depth i.e. distance from the center-of-gravity of the tendons to the top of extreme compression fiber of the PSFC beam.

The value of *d* shall always be taken to be greater than 80% of the total depth of the beam. Also, V_c should not be greater than $10\sqrt{f_c'}\,b_w d\left(1+W_f\right)$, which is derived from $V_{c,max}$ of PC beams according to Laskar (2009 and 2010).

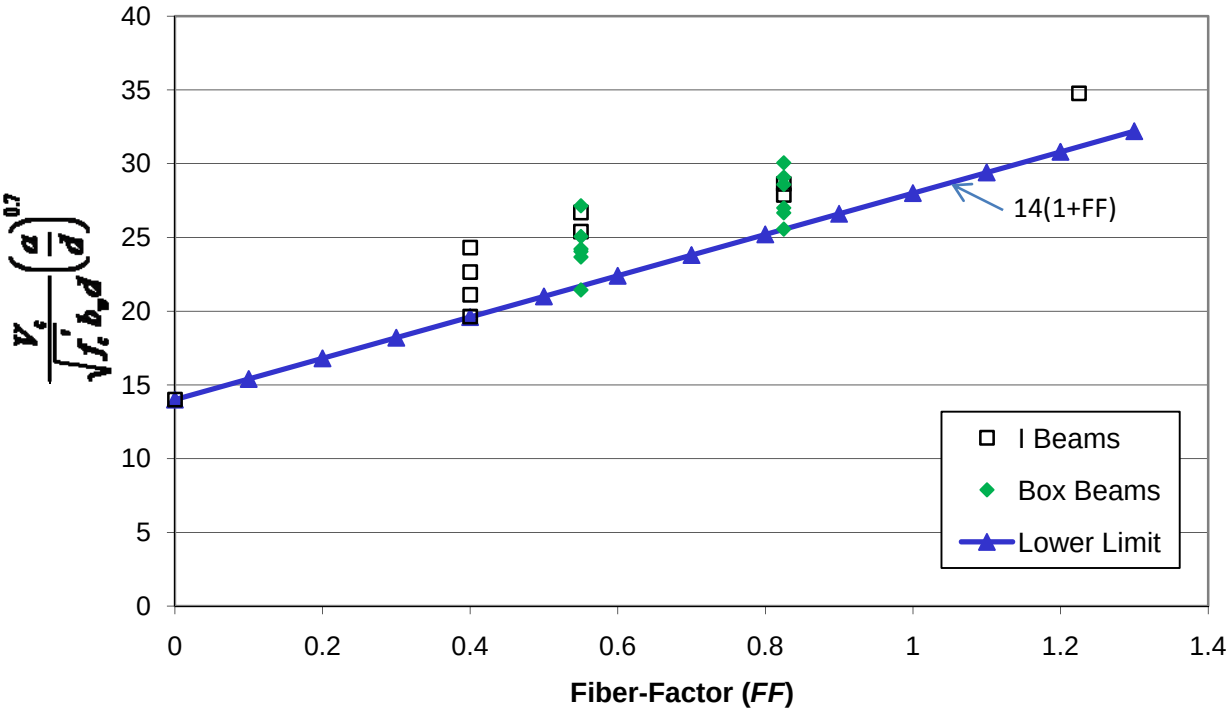

Fig 10.1 Variation of Normalized Concrete Shear Strength with Fiber-Factor for PSFC Beams

The final recommended design equation for shear capacity of PSFC beams is shown in Eq. 10-2.

$$V_u = \frac{14}{(a/d)^{0.7}}\sqrt{f_c'}\,b_w d\left(1+FF\right) \qquad (10\text{-}2)$$

Hence, the only difference in the shear design equations of the non-fibrous and fibrous beams is the term *(1+ FF)*.

For beams subjected to distributed loading, the span-to-effective depth ratio (*a/d*) varies along the length of the beam. Therefore, *a/d* must be generalized as *(M/Vd),* where *M* and *V* are

the factored applied moment and shear along the length of the beam, respectively. In short, the ultimate shear capacity of the PSFC beam can be represented as shown in Eq. 10-3.

$$V_u = 14\left(\frac{V_u d}{M_u}\right)^{0.7} \sqrt{f_c'}\, b_w d(1+FF) \qquad (10\text{-}3)$$

10.2 Design Examples for PSFC Beams

Four illustrative design examples based on the proposed shear design equations for PSFC beams are presented in this section. The first two examples the step-by-step shear design procedure for a PSFC I-beam and the last two examples explicates the shear design of Box-beams.

Example 1

TxDOT Type-A beams spaced at 8.67 feet c/c and supporting a 30 feet wide and 8 inches thick deck slab are considered (Fig. 10.2).

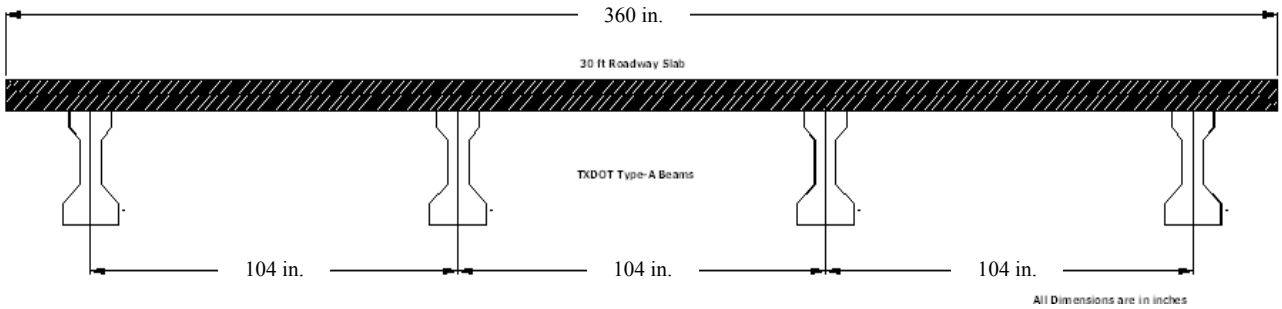

Layout of Girders and Roadway Slab considered in Design Examples

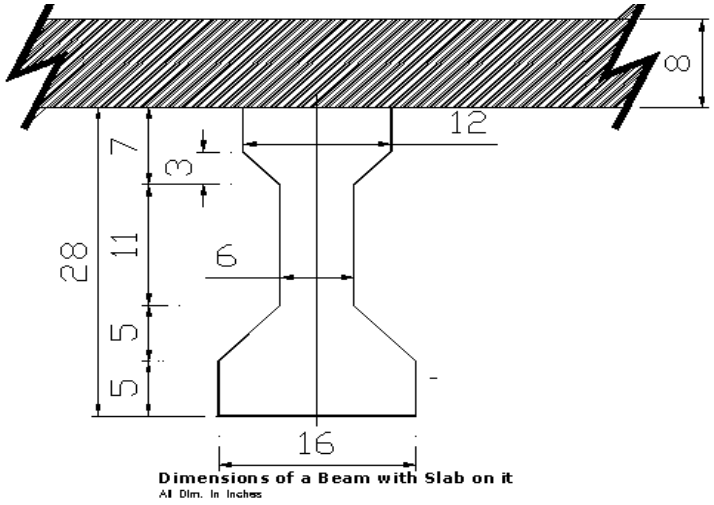

Fig. 10.2 Details of PSFC TxDOT Type-A Beam and Overlaying Slab

The values of various parameters required for design are follows:

h = 28 in	b_w = 6 in	L_n = 24 ft	f_c' = 10 ksi	FF = 0.55
f_y = 60 ksi	d_{bv} = 5/8 in	w_u = 24 kips/ft		

Maximum moment in the girder, $M_u/\phi = \frac{1}{\phi}\frac{w_u l^2}{8} = \frac{24 \times 24^2}{0.9 \times 8}$ = 1,920 kip-ft

As per calculations for flexural capacities of prestressed concrete girders, provide 18-½-inch dia. low relaxation strands.

Distance of tendon's C.G. in beam cross section from top fiber = 15.41 inches

Eccentricity of tendons from C.G. = 8.39 inches

Thickness of deck slab = 8 inches

Therefore, d = 15.41 + 8.39 + 8 = 31.8 in

Assuming the critical section of the beam in shear to be at a distance d from the support,

Shear force at critical section of the beam $V_u = \left(\frac{w_u l}{2} - w_u d\right) = \left(\frac{24 \times 24}{2} - 24 \times \frac{31.8}{12}\right)$ = 224.4 kips

Factored moment at the section, $M_u = \left(\frac{w_u l}{2} x - \frac{w_u x^2}{2}\right) = \left(\frac{24 \times 24}{2} \times \frac{31.8}{12} - \frac{24 \times \left(\frac{31.8}{12}\right)^2}{2}\right)$

∴ M_u = 678.9 kip-ft

Now, $\frac{V_u d}{M_u} = \frac{224.4 \times 31.8}{678.9 \times 12}$ = 0.876

Now, $V_c = 14\left(\frac{V_u d}{M_u}\right)^{0.7} \sqrt{f_c'}\, b_w d(1 + FF) = 14 \times 0.876^{0.7} \times \sqrt{10{,}000} \times 6 \times 31.8(1 + 0.55)$ = **377.4** kips

Maximum concrete shear capacity of the beam is given as,

$V_{c,max} = 10\sqrt{f_c'}\, b_w d(1 + FF) = 10 \times \sqrt{10{,}000} \times 6 \times 31.8(1 + 0.55)$ = 295.7 kips < 377.4 kips

∴ $V_{c,max}$ = 295.7 kips.

Consider a section in the beam at 8 feet from the support:

Factored shear force at this section, $V_u = \left(\frac{w_u l}{2} - w_u x\right) = \left(\frac{24\times 24}{2} - 24\times 8\right) = 96$ kips

Factored moment at this section, $M_u = \left(\frac{w_u l}{2} x - \frac{w_u x^2}{2}\right) = \left(\frac{24\times 24}{2}\times 8 - \frac{24\times 8^2}{2}\right) = 1536$ kip-ft

$\therefore \frac{V_u d}{M_u} = \frac{96\times 31.8}{1536\times 12} = 0.166$

Now, $V_c = 14\left(\frac{V_u d}{M_u}\right)^{0.7} \sqrt{f_c'}\, b_w d(1+FF) = 14\times 0.166^{0.7} \times \sqrt{10{,}000}\times 6\times 31.8(1+0.55) = 117.6$ kips

Maximum concrete shear capacity of the beam,

$V_{c,max} = 10\sqrt{f_c'}\, b_w d(1+FF) = 10\times \sqrt{10{,}000}\times 6\times 31.8(1+0.55) = 295.7$ kips > 117.6 kips

$\therefore V_{c,max} = 117.6$ kips at this section.

Similarly, the values of V_u, M_u, $(V_u d/M_u)$ and V_c are computed along the half-span of the I-beam, as shown in Table 10.1. It can be seen that the concrete shear capacity is greater than the applied shear force at all sections.

Table 10.1 – Computed Shear Design Parameters over Half-span of I-beam in Example-1

x (ft)	**V_u (kips)**	**M_u (kip-ft)**	$\frac{V_u d}{M_u}$	**V_c (kips)**
d=2.65	224.4	678.9	0.876	295.7
3	216	756	0.757	295.7
4	192	960	0.530	265.5
5	168	1140	0.391	214.3
6	144	1296	0.294	113.5
7	120	1428	0.223	144.6
8	96	1536	0.166	117.6
9	72	1620	0.118	92.7
10	48	1680	0.076	68.0
11	24	1680	0.037	41.2
12	0	1716	-	-

Note: The above design example has been solved considering mild steel as shear reinforcement instead of steel fibers. The details of this example are given in Tx-DOT report 0-4759-1 (Laskar

et al. 2007), Chapter 10, Design Example-1. The calculated steel shear reinforcement (stirrups) was 1.1% by volume.

Example 2

The above design Example-1 is resolved by using a uniformly distributed load of 12 kips/ft.

Maximum moment on the girder, $M_u/\phi = \frac{1}{\phi}\frac{w_u l^2}{8} = \frac{1}{0.9}\frac{12\times 24^2}{8} = 960$ kip-ft

As per calculations for flexural capacities of prestressed concrete girders, provide 8-½-inch low relaxation strands.

Distance of C.G. of beam cross section from top fiber = 15.41 inches

Eccentricity of tendons from C.G. = 10.11 inches

Thickness of deck slab = 8 inches

d = 15.41 + 10.11 + 8 = 33.52 in

Assuming the critical section of the beam in shear to be at a distance d from the support,

Shear force at critical section of the beam $V_u = \left(\frac{w_u l}{2} - w_u d\right) = \left(\frac{12\times 24}{2} - 12\times\frac{33.52}{12}\right) = 110.5$ kips

Consider a section in the beam at 5 feet from the support:

Factored shear force at the section, $V_u = \left(\frac{w_u l}{2} - w_u x\right) = \left(\frac{12\times 24}{2} - 12\times 5\right) = 84$ kips

Factored moment at the section, $M_u = \left(\frac{w_u l}{2}x - \frac{w_u x^2}{2}\right) = \left(\frac{12\times 24}{2}\times 5 - \frac{12\times 5^2}{2}\right) = 570$ kip-ft

$\therefore \quad \frac{V_u d}{M_u} = \frac{84\times 33.52}{570\times 12} = 0.412$

Now, $V_c = 14\left(\frac{V_u d}{M_u}\right)^{0.7}\sqrt{f_c'}\, b_w d(1+FF) = 14\times 0.412^{0.7}\times\sqrt{10{,}000}\times 6\times 33.52(1+0.55) =$ **234.5** kips

Maximum concrete shear capacity of the beam,

$V_{c,max} = 10\sqrt{f_c'}\, b_w d(1+FF) = 10\times\sqrt{10{,}000}\times 6\times 33.52(1+0.55) = 311.7$ kips > 234.5 kips

Consider a section in the beam at 8 feet from the support:

Factored Shear force at the section, $V_u = \left(\frac{w_u l}{2} - w_u x\right) = \left(\frac{12 \times 24}{2} - 12 \times 8\right) = 48.0$ kips

Factored Moment at the section, $M_u = \left(\frac{w_u l}{2} x - \frac{w_u x^2}{2}\right) = \left(\frac{12 \times 24}{2} \times 8 - \frac{12 \times 8^2}{2}\right) = 768$ kip-ft

$\therefore \quad \frac{V_u d}{M_u} = \frac{48 \times 33.52}{768 \times 12} = 0.175$

Now, $V_c = 14\left(\frac{V_u d}{M_u}\right)^{0.7} \sqrt{f_c'}\, b_w d\left(1 + FF\right) = 14 \times 0.175^{0.7} \times \sqrt{10{,}000} \times 6 \times 33.52\left(1 + 0.55\right) =$ **128.6** kips

Maximum concrete shear capacity of the beam,

$V_{c,max} = 10\sqrt{f_c'}\, b_w d\left(1 + FF\right) = 10 \times \sqrt{10{,}000} \times 6 \times 33.52\left(1 + 0.55\right) = 311.7$ kips > 128.6 kips

Table 10.2 shows the concrete shear resistance at different sections along half-span of the beam. It can be seen that the concrete shear capacity is greater than the applied shear force at all sections.

Table 10.2 – Computed Shear Design Parameters over Half-span of I-beam in Example-2

x (ft)	**V_u (kips)**	**M_u (kip-ft)**	$\frac{V_u d}{M_u}$	**V_c (kips)**
d=2.8	110.5	355.4	0.868	311.7
3	108	378	0.798	311.7
4	96	480	0.559	290.3
5	84	570	0.412	234.5
6	72	648	0.310	192.3
7	60	714	0.235	158.2
8	48	768	0.175	128.6
9	36	810	0.124	101.4
10	24	840	0.080	74.4
11	12	858	0.039	45.1
12	0	864	-	-

Example 3

A Box-beam (TxDOT 5B34) as shown in Fig. 10.3 is analyzed using the proposed design equation at different shear span ratios.

The values of various quantities required for design are as follows:

h = 34 in b_w = 5 in. for each web L_n = 24 ft f_c' = 10 ksi FF = 0.55

w_u = 48 kips/ft. Assume a 5" thick cast-in-place slab at top.

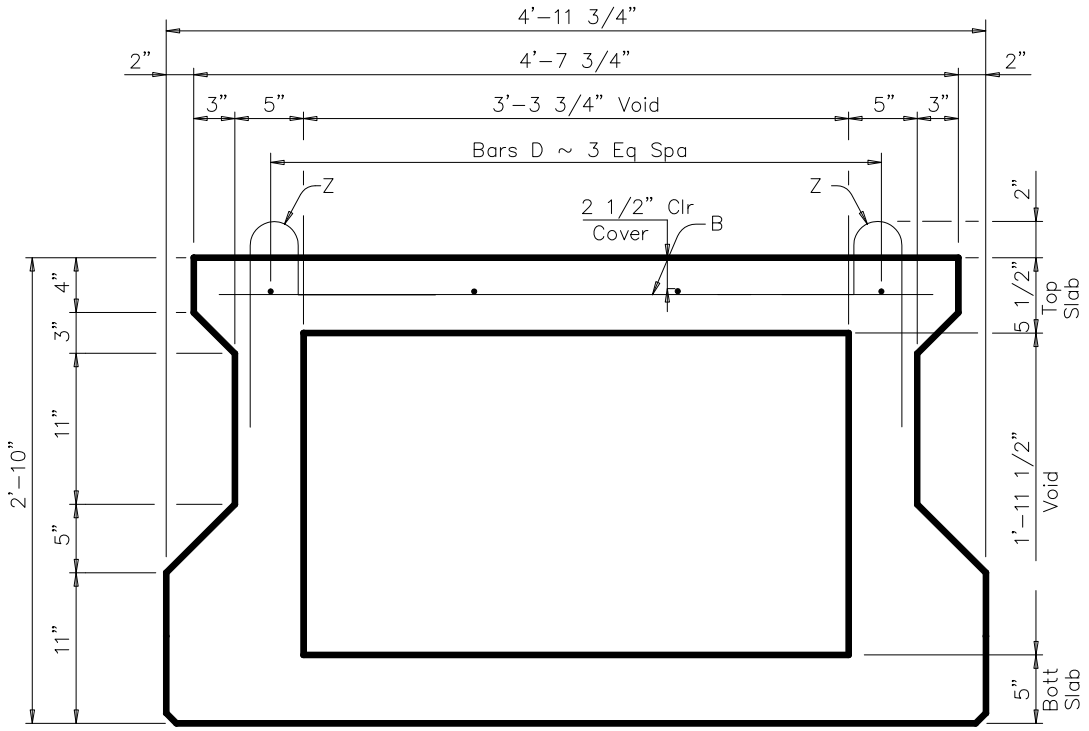

Fig. 10.3 Details of PSFC TxDOT-5B34 Box-Beam

Assuming total effective depth (beam + top slab), d

d = 30" (effective depth of beam) + 5" slab thickness = 35"

Assuming the critical section of the beam in shear to be at a distance d from the support,

Shear force at critical section of the beam, $V_u = \left(\frac{w_u l}{2} - w_u d\right) = \left(\frac{48 \times 24}{2} - 48 \times \frac{35}{12}\right) = 436$ kips

Factored moment at the section, $M_u = \left(\frac{w_u l}{2}x - \frac{w_u x^2}{2}\right) = \left(\frac{48\times 24}{2}\times\frac{35}{12} - \frac{48\times\left(\frac{35}{12}\right)^2}{2}\right)$

$= 1475.8$ kip-ft

$\therefore \frac{V_u d}{M_u} = \frac{436\times 35}{1475.8\times 12} = 0.861$

Now, $V_c = 14\left(\frac{V_u d}{M_u}\right)^{0.7}\sqrt{f_c'}\, b_w d(1+FF) = 14\times 0.861^{0.7}\times\sqrt{10{,}000}\times 10\times 35(1+0.55) =$ **684.3** kips

Also, $V_{c,max} = 10\sqrt{f_c'}\, b_w d(1+FF) = 10\times\sqrt{10{,}000}\times 10\times 35(1+0.55) =$ **542.5** kips < 684.3 kips

Consider a section in the beam at 8 feet from the support:

Factored shear force at the section, $V_u = \left(\frac{w_u l}{2} - w_u x\right) = \left(\frac{48\times 24}{2} - 48\times 8\right) = 192$ kips

Factored moment at the section, $M_u = \left(\frac{w_u l}{2}x - \frac{w_u x^2}{2}\right) = \left(\frac{48\times 24}{2}\times 8 - \frac{48\times 8^2}{2}\right) = 3072$ kip-ft

$\therefore \frac{V_u d}{M_u} = \frac{192\times 35}{3072\times 12} = 0.182$

Now, $V_c = 14\left(\frac{V_u d}{M_u}\right)^{0.7}\sqrt{f_c'}\, b_w d(1+FF) = 14\times 0.182^{0.7}\times\sqrt{10{,}000}\times 10\times 35(1+0.55) =$ **230.71** kips

Also, $V_{c,max} = 10\sqrt{f_c'}\, b_w d(1+FF) = 10\times\sqrt{10{,}000}\times 10\times 35(1+0.55) = 542.5$ kips > 230.71 kips

Table 10.3 shows the concrete shear resistance at different sections along half-span of the beam. It can be seen that the concrete shear capacity is greater than the applied shear force at all sections.

Table 10.3 – Computed Shear Design Parameters over Half-span of Box-Beam in Example-3

x (ft)	V_u (kips)	M_u (kip-ft)	$\frac{V_u d}{M_u}$	V_c (kips)
d=2.9	436	1475.8	0.86	542.50
3	432	1512	0.83	542.50
4	384	1920	0.58	520.80
5	336	2280	0.43	420.56
6	288	2592	0.32	345.13
7	240	2856	0.25	283.83
8	192	3072	0.18	230.71
9	144	3240	0.13	181.73
10	96	3360	0.08	133.38
11	48	3432	0.04	80.90

Example 4

The beam in Example-3 is redesigned below by reducing the applied uniformly distributed load on it to 12 kips/ft and increasing the span to 48ft.

Assuming the total effective depth d=35”

Assuming the critical section of the beam in shear to be at a distance d from the support,

Shear force at critical section of the beam $V_u = \left(\frac{w_u l}{2} - w_u d\right) = \left(\frac{12\times 48}{2} - 12\times\frac{35}{12}\right) = 253$ kips

Factored moment at the section, $M_u = \left(\frac{w_u l}{2}x - \frac{w_u x^2}{2}\right) = \left(\frac{12\times 48}{2}\times\frac{35}{12} - \frac{12\times\left(\frac{35}{12}\right)^2}{2}\right)$

$\therefore M_u = 788.9$ kip-ft

$\therefore \frac{V_u d}{M_u} = \frac{253\times 35}{788.9\times 12} = 0.935$

Now, $V_c = 14\left(\frac{V_u d}{M_u}\right)^{0.7}\sqrt{f_c'}\, b_w d(1+FF) = 14\times 0.935^{0.7}\times\sqrt{10{,}000}\times 10\times 35(1+0.55) =$ **724.7** kips

Also, $V_{c,max} = 10\sqrt{f_c'}\, b_w d(1+FF) = 10\times\sqrt{10{,}000}\times 10\times 35(1+0.55) =$ **542.5** kips < 724.7 kips

Consider a section in the beam at 16 feet from the support:

Factored shear force at the section, $V_u = \left(\frac{w_u l}{2} - w_u x\right) = \left(\frac{12\times 48}{2} - 12\times 16\right) = 96$ kips

Factored moment at the section, $M_u = \left(\frac{w_u l}{2}x - \frac{w_u x^2}{2}\right) = \left(\frac{12\times 48}{2}\times 16 - \frac{12\times 16^2}{2}\right) = 3072$ kip-ft

$\therefore \frac{V_u d}{M_u} = \frac{96\times 35}{3072\times 12} = 0.091$

Now, $V_c = 14\left(\frac{V_u d}{M_u}\right)^{0.7}\sqrt{f_c'}\, b_w d(1+FF) = 14\times 0.091^{0.7}\times\sqrt{10{,}000}\times 10\times 35(1+0.55) =$ **142** kips

Also, $V_{c,max} = 10\sqrt{f_c'}\, b_w d(1+FF) = 10\times\sqrt{10{,}000}\times 10\times 35(1+0.55) = 542.5$ kips > **142** kips

Table 10.4 shows the concrete shear resistance at different sections along half-span of the beam. It can be seen that the concrete shear capacity is greater than the applied shear force at all sections.

Table 10.4 – Computed Shear Design Parameters over Half-span of Box-Beam in Example-4

x (ft)	**V_u (kips)**	**M_u (kip-ft)**	**$\frac{V_u d}{M_u}$**	**V_c (kips)**
d=2.92	253	788.9	0.94	542.50
4.00	240	1056	0.66	542.50
6.00	216	1512	0.42	411.51
8.00	192	1920	0.29	320.59
10.00	168	2280	0.21	258.89
12.00	144	2592	0.16	212.45
14.00	120	2856	0.12	174.72
16.00	96	3072	0.09	142.02
18.00	72	3240	0.07	117.35
20.00	48	3360	0.04	90.24
22.00	24	3432	0.02	57.27
24.00	0	3456	0.00	0.00

CHAPTER 11

CONCLUSIONS AND SUGGESTIONS

11.1 Conclusions

The purpose of this research was to study the behavior of Prestressed Steel Fiber Concrete (PSFC) panels and beams under shear and to develop a simplified equation for the shear design of prestressed concrete girders. The following conclusions were made from this research:

1) Based on the flexural test results of small beam specimens, the recommended maximum dosage of Dramix steel fibers to be used in full-scale PSFC beams considering strength and good workability of concrete mix, is as below:

(a) Dramix Long Fibers - Dosage of 0.5% by volume of concrete

(b) Dramix Short Fibers - Dosage of 1.5% by volume of concrete

2) PSFC panel tests showed that the tensile stiffness and concrete softening characteristics of PSFC improves with an increased Fiber-Factor.

3) With regard to the PSFC panel tests steel fibers causes an increase of concrete compressive strength under sequential loading to determine the constitutive models. In the case of proportional loading for pure shear testing, a factor W_f, which is a function of fiber factor (FF) is proposed for incorporation into the softening coefficient of prestressed steel fiber concrete. W_f takes care of the effect of amount of steel fibers on concrete compressive strength.

4) The shear behavior of PSFC beams was critically examined by full-scale tests on six TxDOT Type-A beams and six modified Tx-4B20 box-beams with web-shear or flexural-shear failure modes.

5) From the experimental results of six PSFC I-beams, steel fibers were found very effective in resisting the shear loads and mild steel shear reinforcement (stirrups) can be completely replaced with steel fibers.

6) Test results of PSFC box-beams also demonstrated the effectiveness of steel fibers in resisting shear forces. It was also found that local failures in these beams, such as penetration of web-shear crack into the top flange, have to be taken care so as to achieve the ultimate shear capacity in the PSFC beam. From the test results of all twelve PSFC beams it was found that 1% by volume of Dramix short steel fibers (ZP 305) was an optimum dosage in prestress concrete beams as shear reinforcement.

7) Using the constitutive laws of PSFC established in this research, an analytical model was developed and implemented in a finite element program framework (OpenSees) to simulate the shear behavior of the PSFC beams. Using this computer program, the load-deflection curves of all the beams are simulated with acceptable accuracy.

8) A new shear design equation was developed using the results of the PSFC beam tests performed in this research. Four design examples were presented to illustrate the use of the developed design equations for PSFC girders.

11.2 Suggestions

Future research in this area are suggested as follows:

1) To obtain a better understanding of the tensile behavior of PSFC, we propose to perform a series of sequential load panel tests. A target compressive strain would be imposed on the panel and held constant. The tensile load and strain would then be increased until failure.
2) To extend the constitutive properties of PSFC for use of other types of fiber, we propose to utilize the characteristics derived from relatively simple beam tests.
3) Tendon embedded in PSFC has a greater stiffness than tendon embedded in concrete without steel fiber. To assure ductile design of PSFC, we recommend further study of ductility of embedded tendon in PSFC to preclude dominant cracking and the resulting failure of tendons at the crack.
4) Steel fiber concrete can be applied to the end zones of prestressed concrete girders, where shear bond failure may occur.

References

AASHTO T27 (1996), American Association of State Highway Transportation Officials "Sieve Analysis of Fine and Coarse Aggregates," Washington D.C.

AASHTO M43 (1998), American Association of State Highway Transportation Officials "Sizes of Aggregates for Road and Bridge Construction," Washington D.C.

Abrishami, H. H., and Mitchell, D., "Influence of steel fibers on tension stiffening," ACI Structural Journal, Vol. 94, No. 6, Nov.-Dec. 1997, pp. 769-776.

ACI Committee 318 (2008), "Building Code Requirements for Structural Concrete (ACI 318-08) and Commentary," American Concrete Institute, Farmington Hills, MI.

ACI Committee 544, "Design considerations for steel fiber reinforced concrete," ACI Structural Journal, Vol. 85, No. 5, Sept.-Oct. 1998, pp. 563-580.

ACI 544.1R (1996), "State-of-the-Art Report on Fiber Reinforced Concrete," American Concrete Institute, Farmington Hills, Michigan.

ASTM C1609 (2007), "Standard Test Method for Flexural Performance of Fiber-Reinforced Concrete (Using Beam With Third-Point Loading)," ASTM International, West Conshohocken, PA, USA.

ASTM C150 (2002), "Standard Specification for Portland Cement," ASTM International, West Conshohocken, PA, USA.

ASTM C618 (2003), "Standard Specification for Coal Fly Ash and Raw or Calcined Natural Pozzolan for Use as a Mineral Admixture in Concrete," ASTM International, West Conshohocken, PA, USA.

ASTM C494/C494M (1999), "Standard Specification for Chemical Admixtures for Concrete," ASTM International, West Conshohocken, PA, USA.

Ayoub, Amir and Filippou, Filip C. (1998), "Nonlinear Finite-Element Analysis of RC Shear Panels and Walls," *Journal of Structural Engineering*, ASCE, Vol. 124, No. 3, Mar. 1998, pp. 298-308.

Balakrishnan, S. and Murray, D. W. (1988a), "Concrete Constitutive Model for NLFE Analysis of Structures," *Journal of Structural Engineering*, ASCE, Vol. 114, No. 7, July 1988, pp. 1449-1466.

Balakrishnan, S. and Murray, D. W. (1988b), "Strength of Reinforced Concrete Panels," *Canadian Journal of Civil Engineering*, Vol. 15, No. 5, Oct. 1988, pp. 900-911.

Balakrishnan, S. and Murray, D. W. (1988c), "Prediction of R/C Panels and Deep Beam Behavior by NLFEA," *Journal of Structural Engineering*, ASCE, Vol. 114, No. 10, Oct. 1988, pp. 2323-2342.

Balaguru,P, Ramesh Narahari, and Mehendra Patel, "Flexural Toughness of Steel Fiber Reinforced Concrete", Materials Journal, American Concrete Institute , Vol 89, No 6, 1992, pp.541-546.

Balaguru,P, Dipsia, Michael G, "Properties of Fiber Reinforced High Strength Semi-Light weight Concrete", Materials Journal, American Concrete Institute , Vol 90, No 5, 1993, pp.399-405.

Bayasi, M.Z, Soroushiah, P, "Effects of Steel Fiber Reinforcement on Fresh mix Properties of Concrete", Materials Journal, American Concrete Institute , Vol 89, No 4, 1992, pp.369-374.

Belarbi, A. and Hsu, T. T. C. (1994), "Constitutive Laws of Concrete in Tension and Reinforcing Bars Stiffened by Concrete," *Structural Journal of the American Concrete Institute*, Vol. 91, No. 4, pp. 465-474.

Belarbi, A. and Hsu, T. T. C. (1995), "Constitutive Laws of Softened Concrete in Biaxial Tension-Compression," *Structural Journal of the American Concrete Institute*, Vol. 92, No. 5, pp. 562-573.

Belletti, B., Cerioni, R., and Iori, I. (2001), "Physical Approach for Reinforced-Concrete (PARC) Membrane Elements," *Journal of Structural Engineering*, ASCE, Vol. 127, No. 12, Dec. 2001, pp. 1412-1426.

Bhide, B. S. and Collins, M. P. (1989), "Influence of Axial Tension on Shear Capacity of Reinforced Concrete Members," *ACI Structural Journal*, Vol. 86, No. 5, pp. 570-580.

Chintrakarn, R. (2001), "Minimum Shear Steel and Failure Modes Diagram of Reinforced Concrete Membrane Elements," *Master's Thesis*, Department of Civil and Environmental Engineering, University of Houston, Houston, TX.

Collins, M. P., Vecchio, F. J., and Mehlhorn, G. (1985), "An International Competition to Predict the Response of Reinforced Concrete Panels," *Canadian Journal of Civil Engineering*, Ottawa, Vol. 12, No. 3, pp. 626-644.

Crisfield, Michael A. and Wills, John (1989), "Analysis of R/C Panels Using Different Concrete Models," *Journal of Engineering Mechanics*, ASCE, Vol. 115, No. 3, Mar. 1989, pp. 578-597.

Carreira DJ, Chu KH. 1986. “The moment–curvature relationship of reinforced concrete members”. *ACI Journal* **83**: 191–198.

Desayi, P. and Krishnan, S., *Equation for the stress-strain curve of concrete*, ACI J., Vol. 61(1964)345-350.

Dhonde, H.B., Mo, Y.L., and Hsu, T.C. (2006), “Fiber Reinforcement in Prestressed Concrete Beams”, *Texas Department of Transportation Report 0-4819*, March 2006.

Foster, Stephen J. and Marti, Peter (2003), “Cracked Membrane Model: Finite Element Implementation,” *Journal of Structural Engineering*, ASCE, Vol. 129, No. 9, Sept. 2003, pp. 1155-1163.

Freyssinet, E. (1956), “The Birth of Prestressing,” *Cement and Concrete Association Translation No. 29*, London.

Hognestad, *Fundamental Concepts in Ultimate Load Design*, Journal of the American concrete Institute, V 23, June 1952.

Hsu, T. T. C. (1993), *Unified Theory of Reinforced Concrete*, CRC Press, Inc., Boca Raton, FL, 336 pp.

Hsu, T. T. C. (1998), “Stresses and Crack Angles in Concrete Membrane Elements,” *Journal of Structural Engineering*, ASCE, Vol. 124, No. 12, Dec. 1998, pp. 1476-1484.

Hsu, T. T. C. (2002), “Rational Shear Design of Reinforced Concrete Bridges,” Presented at ACI 343/445 Session “Concrete Bridges in Shear,” ACI Fall Convention, Phoenix, AZ, Oct. 27 – Nov. 1, 2002.

Hsu, T. T. C., Belarbi, A., and Pang, X. B. (1995), “A Universal Panel Tester,” *Journal of Testing and Evaluations*, ASTM, Vol. 23, No. 1, pp. 41-49.

Hsu, T. T. C., Kumar, D. H., Wang, J., and Zhu, R. R. H. (2005), “Behavior of Reinforced Concrete Membrane Elements Subjected to Shear and Normal Stresses,” Submitted to *ACI Structural Journal*, 2005.

Hsu, T. T. C. and Zhang, L. X. (1996), “Tension Stiffening in Reinforced Concrete Membrane Elements,” *Structural Journal of the American Concrete Institute*, Vol. 93, No. 1, pp. 108-115.

Hsu, T. T. C. and Zhang, L. X. (1997), “Nonlinear Analysis of Membrane Elements by Fixed-Angle Softened-Truss Model,” *Structural Journal of the American Concrete Institute*, Vol. 94, No. 5, pp. 483-492.

Hsu, T. T. C., Zhang, L. X., and Gomez, T. (1995), "A Servo-control System for Universal Panel Tester," *Journal of Testing and Evaluations*, ASTM, Vol. 23, No. 6, pp. 424-430.

Hsu, T. T. C. and Zhu, R. R. H. (2002), "Softened Membrane Model for Reinforced Concrete Elements in Shear," *Structural Journal of the American Concrete Institute*, Vol. 99, No. 4, pp. 460-469.

Hu et al., "*Biaxial Failure Model for Fiber Reinforced Concrete"*, Journal of Materials in Civil Engineering, November/December 2003.

Kani, G.N.J. (1964), "The Riddle of Shear Failure and its solutions," ACI J., **61**(4), 441–467.

Kaufmann, Walter and Marti, Peter (1998), "Structural Concrete: Cracked Membrane Model," *Journal of Structural Engineering*, Vol. 124, No. 12, Dec. 1998, pp. 1467-1475.

Kirschner, U. and Collins, M. P. (1986), "Investigating Behavior of Reinforced Concrete Shell Elements", Publication No 86-09, Department of Civil Engineering, University of Toronto, Sept. 1986, 209 pp.

Kupfer, *Behavior of Concrete Under Biaxial Stress*, ACI Journal, August 1969.

Laskar, A. (2009), "Shear Behavior and Design of Prestressed Concrete Members," *PhD. Dissertation*, Department of Civil and Environmental Engineering, University of Houston, TX.

Laskar, A., Hsu, T.T.C., and Mo, Y.L. (2010), "Shear Strength of Prestressed Concrete Beams Part 1: Experiments and Shear Design Equations" ACI Journal, V. 107, No. 3, pp. 330-339.

Laskar, A., Wang, J., Mo, Y.L., Hsu, TC (2007), "Rational Shear Provisions for AASHTO LRFD Specifications", Texas Department of Transportation Report 0-4759, 2007

Limsuwan, K. (2006). "*Shear of Steel Fiber Membrane Elements*" Master's Thesis,Department of Civil Engineering, University of Houston (supervised by Thomas T.C. Hsu).

Mansour, M., Thomas T.C. Hsu, and Y.L. Mo. 2005. "Constitutive Relationships of Reinforced Concrete with Steel Fibers." Research Report, Department of Civil and Environmental Engineering, University of Houston, Houston, TX.

Meyboom, J. (1987), "An Experimental Investigation of Partially Prestressed, Orthogonally Reinforced Concrete Elements Subjected to Membrane Shear," *Thesis*, Department of Civil Engineering, University of Toronto, Toronto, Canada.

Morsch, E. (1902), "Der Eisenbetonbau, seine Anwendung und Theorie," Wayss and Freytag, A.G., Im Selbstverlag der Firma, Neustadt, A.D. Haardt, May 1902, pp. 118.

Mo,Y.L., Thomas T.C. Hsu and John Vogel (2009), "Flexural Behavior of Steel Fiber Reinforced Concrete Beams", Proceedings of the ASCE, Structures Congress 2009, Austin, TX, April 29-May 2, 2009

Pang, X. B. and Hsu, T. T. C. (1995), "Behavior of Reinforced Concrete Membrane Elements in Shear," *Structural Journal of the American Concrete Institute,* Vol. 92, No. 6, pp. 665-679.

Pang, X. B. and Hsu, T. T. C. (1996), "Fixed-Angle Softened-Truss Model for Reinforced Concrete," *Structural Journal of the American Concrete Institute*, Vol. 93, No. 2, pp. 197-207.

Ritter, W. (1899), " Die Bauweise Hennebique," Schweizerische Bauzeitung, Vol.33, No. 5, 6, and 7, Zurich, pp. 41-43, 49-52, and 59-61.

Robinson, J. R. and Demorieux, J. M. (1968), "Essai de Traction-Compression sur Modeles d'Ames de Poutre en Beton Arme," Compte Rendu Partiel I, U.T.I., Institut de Recherches Appliquees du Beton Arme, Paris, France, 43 pp.

Romualdi, J.P., and Mandel, J.A., "Tensile strength of concrete affected by uniformly distributed closely spaced short lengths of wire reinforcement," ACI Journal, Proceedings, Vol. 61, No. 6, June 1964, pp. 657-671.

Samarrai, M.A., and Elvery, R.H., "The influence of fibers upon crack development in reinforced concrete subject to uniaxial tension," Magazine of Concrete research, Vol. 26, No. 89, 1974, pp. 203-211.

Schlaich, J., Schafer, K., and Jennewein, M. (1987), "Toward a Consistent Design of Structural Concrete," *PCI Journal*, Vol. 32, No. 3, pp 74-150.

Shah, S.P. (1991). "Do Fibers Increase the Tensile Strength of Cement-Based Matrixes?," ACI Materials Journal, Vol. 88, No. 6, pp 595-602.

Stussi, F., *It Ueber die Sicherheit des einfach bewehrten Eisenbeton-Rechteck-balkens*, Publications, International Association for Bridge and Structural Engineering, Vol. 1, Zurich, April,1932, pp. 487-495.

Tadepalli, P.R., Mo, Y.L., Hsu, Thomas T.C. and Vogel, John (2009), "Flexural Behavior of Steel Fiber Reinforced Concrete Beams", *Proceedings of the ASCE, Structures Congress 2009*, Austin, TX, April 29-May 2, 2009

Tan, Murugappan, Paramasivam*, Constitutive Relation for Steel Fibre Concrete Under Biaxial Compression, Cement and Composites, Vol. 16, 1994*

Thomas, J., & Ramaswamy, A. (2007)**,** *"Mechanical Properties of Steel Fibre Reinforced Concrete", ASCE Journal of Materials in Civil Engineering, May 2007.*

Triana, Mansour*, "Biaxial Strength and Deformational Behavior of Plain and Steel Fiber Concrete", ACI Material Journal July August 1991.*

Vecchio, F. J. (1990), "Reinforced Concrete Membrane Element Formulation," *Journal of Structural Engineering*, ASCE, Vol. 116, No. 3, pp. 730-750.

Vecchio, F. J. (2000), "Disturbed Stress Field Model for Reinforced Concrete: Formulation," *Journal of Structural Engineering*, ASCE, Vol. 126, No. 9, Sept. 2000, pp. 1070-1077.

Vecchio, F. J. (2001), "Disturbed Stress Field Model for Reinforced Concrete: Implementation," *Journal of Structural Engineering*, ASCE, Vol. 127, No. 1, Jan. 2001, pp. 12-20.

Vecchio, F. and M. P. Collins (1981), "*Stress-strain characteristic of reinforced concrete in pure shear*," IABSE Colloquium, Advanced Mechanics of Reinforced Concrete, Delft, Final Report, International Association of Bridge and Structural Engineering, Zurich, Switzerland, pp. 221-225.

Vecchio, F. J. and Collins, M. P. (1982), "Response of Reinforced Concrete to In Plane Shear and Normal Stresses," *Report*, No.82-03, University of Toronto, Toronto, Canada.

Vecchio, F. J., and M. P. Collins (1986), "*The modified compression field theory for reinforced concrete elements subjected to shear,"* ACI Journal, Vol. 83, No. 2, pp. 219-231.

Vecchio, F. J., Lai, D., Sim, W., and Ng, J. (2001), "Disturbed Stress Field Model for Reinforced Concrete: Validation," *Journal of Structural Engineering*, ASCE, Vol. 127, No. 4, April 2001, pp. 350-358.

Wang, J. (2006), "Constitutive Relationships of Prestressed Concrete Membrane Elements," *Ph.D. Dissertation*, Department of Civil and Environmental Engineering, University of Houston, Houston, TX.

Wang, P.T. Shah, S.P. and Naaman, A.E. *Stress-strain curves of normal and lightweight concrete in compression*, ACI J., 75(1978)603-611.

Yin, Hsu, *Biaxia*l *Tests of Plain and Fiber Concrete*, ACI Materials Journal, Vol 83, 1989

Zhang, L. X. (1992), "Constitutive Laws of Reinforced Elements with Medium-High Strength Concrete," *Ph.D. Dissertation*, Department of Civil and Environmental Engineering, University of Houston, Houston, TX.

Zhang, L. X. and Hsu, T. T. C. (1998), "Behavior and Analysis of 100Mpa Concrete Membrane Elements," *Journal of Structural Engineering*, ASCE, Vol. 124, No. 1, Jan. 1998, pp. 24-34.

Zhu, R. R. H. (2000), "Softened-Membrane Model for Cracked Reinforced Concrete Considering Poisson Effect," PhD dissertation, Dept. of Civil and Environmental Engineering, University of Houston, Houston, TX.

Zhu, R. H., Hsu, T. T. C., and Lee, J. Y. (2001), "Rational Shear Modulus for Smeared Crack Analysis of Reinforced Concrete," *Structural Journal of the American Concrete Institute*, Vol. 98, No. 4, pp. 443-450.

Zhu, R. R. H., and Hsu, T. T. C. (2002), "Poisson Effect of Reinforced Concrete Membrane Elements," *Structural Journal of the American Concrete Institute*, Vol. 99, No. 5, pp. 631-640.